

UNCLASSIFIED

AD NUMBER	
AD338965	
CLASSIFICATION CHANGES	
TO:	unclassified
FROM:	confidential
LIMITATION CHANGES	
TO:	Approved for public release, distribution unlimited
FROM:	Distribution authorized to DoD only; Administrative/Operational Use; 07 MAR 1962. Other requests shall be referred to Defense Special Weapons Agency, Alexandria, VA 22310-3398.
AUTHORITY	
DSWA ltr, 3 Oct 1996; DSWA ltr, 3 Oct 1996	

THIS PAGE IS UNCLASSIFIED

## **REPRODUCTION QUALITY NOTICE**

**This document is the best quality available. The copy furnished to DTIC contained pages that may have the following quality problems:**

- **Pages smaller or larger than normal.**
- **Pages with background color or light colored printing.**
- **Pages with small type or poor printing; and or**
- **Pages with continuous tone material or color photographs.**

**Due to various output media available these conditions may or may not cause poor legibility in the microfiche or hardcopy output you receive.**

☐ **If this block is checked, the copy furnished to DTIC contained pages with color printing, that when reproduced in Black and White, may change detail of the original copy.**



Defense Special Weapons Agency  
6801 Telegraph Road  
Alexandria, Virginia 22310-3398

ISST

**ERRATA**

3 October 1996

*AD-338965L*

MEMORANDUM FOR DEFENSE TECHNICAL INFORMATION CENTER  
ATTENTION: OCD/Mr. Bill Bush

SUBJECT: Declassification of AD-338965L

The Defense Special Weapons Agency (formerly Defense Nuclear Agency) Security Office (OPSSI) has reviewed and **declassified** the following report:

AD-338965L      WT-1608  
OPERATION HARDTACK, April - October 1956,  
Project 1.3  
Surface Phenomena From Underwater Bursts,  
Issuance Date: March 7, 1962.

Distribution statement "A" now applies.

This office transmitted a sanitized version (WT-1608-SAN) to the National Technical Information Service (NTIS) 29 November 1995. This sanitized version is now obsolete and should no longer be sold, since the original version (AD-338965L) is **declassified and approved for public release**.

*Arduith Jarrett*  
ARDITH JARRETT  
Chief, Technical Library

copy furn:  
NTIS  
FC/DASIAC

**ERRATA**

[REDACTED]  
[REDACTED]  
AD 338 965L

DEFENSE DOCUMENTATION CENTER

FOR

SCIENTIFIC AND TECHNICAL INFORMATION

CAMERON STATION ALEXANDRIA, VIRGINIA



[REDACTED]

[REDACTED]



[REDACTED]

NOTICE: When government or other drawings, specifications or other data are used for any purpose other than in connection with a definitely related government procurement operation, the U. S. Government thereby incurs no responsibility, nor any obligation whatsoever; and the fact that the Government may have formulated, furnished, or in any way supplied the said drawings, specifications, or other data is not to be regarded by implication or otherwise as in any manner licensing the holder or any other person or corporation, or conveying any rights or permission to manufacture, use or sell any patented invention that may in any way be related thereto.

NOTICE:

THIS DOCUMENT CONTAINS INFORMATION  
AFFECTING THE NATIONAL DEFENSE OF  
THE UNITED STATES WITHIN THE MEAN-  
ING OF THE ESPIONAGE LAWS, TITLE 18,  
U.S.C., SECTIONS 793 and 794. THE  
TRANSMISSION OR THE REVELATION OF  
ITS CONTENTS IN ANY MANNER TO AN  
UNAUTHORIZED PERSON IS PROHIBITED  
BY LAW.

[REDACTED]

[REDACTED]

WT-1608

This document consists of 218 pages  
No. 1 of 175 copies, Series A

Operation

338 965L

# HARDTACK

April - October 1958

AD No. 338965

Project 1.3

SURFACE PHENOMENA FROM UNDERWATER BURSTS (U)

DDC FILE COPY

Issued under March 7, 1962

AUG 6 1963

HEADQUARTERS FIELD COMMAND  
DEFENSE ATOMIC SUPPORT AGENCY  
SANDIA BASE, ALBUQUERQUE NEW MEXICO

**FORMERLY  
RESTRICTED DATA**

Handle as Restricted Data - a form of dissemination  
Section 1406, Atomic Energy Act of 1954

This material contains information affecting  
the national defense of the United States  
within the meaning of the espionage laws,  
Title 18, U. S. C., Secs. 793 and 794, the  
transmission or revelation of which in any  
manner to an unauthorized person is pro-  
hibited by law.

EXCLUDED FROM AUTOMATIC  
DEGRADING; DOD DIR 5700.10  
DOES NOT APPLY

NO. 338965  
OF  
175 COPIES

[REDACTED]

Inquiries relative to this report may be made to

Chief, Defense Atomic Support Agency  
Washington 25, D. C.

When no longer required, this document may be  
destroyed in accordance with applicable security  
regulations.

DO NOT RETURN THIS DOCUMENT

[REDACTED]

WT-1608

OPERATION HARDTACK—PROJECT 1.3

SURFACE PHENOMENA FROM UNDERWATER BURSTS, (U)

E. Swift, Jr., Project Officer  
G. A. Young  
R. L. Willey  
J. F. Goertner  
D. E. Phillips,

U. S. Naval Ordnance Laboratory  
White Oak, Silver Spring, Maryland

#### FORMERLY RESTRICTED DATA

Handle as Restricted Data in foreign dissemination. Section 146b, Atomic Energy Act of 1954.

This material contains information affecting the national defense of the United States within the meaning of the espionage laws, Title 18, U.S.C., Secs. 793 and 794, the transmission or revelation of which in any manner to an unauthorized person is prohibited by law.

#### ABSTRACT

The primary objective was to record and measure the formation, growth, and dissipation of the visible surface phenomena during Shots Wahoo and Umbrella by means of timed technical photography. The secondary objective was to obtain a better understanding of the nature of the base surge by recording the temperature and humidity at various positions in the surge clouds formed by the collapse of the plumes on Shot Wahoo and the collapse of the column on Shot Umbrella.

The shock wave from Shot Wahoo, a 5-kt burst at a depth of 500 feet in water 3,000 feet deep, produced a primary shock wave slick over 11,000 feet in diameter and a primary spray dome 3,000 feet in diameter. (The yields used in this report are those considered most accurate as of 6 January 1960.) A pressure pulse from the collapse of the subsurface cavitating region produced a spray ring beyond the primary dome. Secondary slicks, caused by shock wave reflections from the bottom and deep strata, were also observed. The initial vertical velocities of the spray dome within 700 feet of surface zero were used to calculate underwater shock wave pressures. These values ranged from 1 to 14 percent higher than expected. Estimates of the yield based on the calculated pressures gave an average value of 11 kt. (This method is approximate but provides a useful check on radiochemical values.) The dome reached a maximum height of 840 feet in 7 seconds.

The Wahoo bubble apparently oscillated once while migrating to a position above the original surface. Its reexpansion produced a hemispherical mass of plumes about 1,600 feet high and 3,600 feet in diameter. After 20 seconds, the collapsing plumes spread out to form a base surge, which drifted with the wind and was measurable to a time of 3.5 minutes and a crosswind radius of 8,200 feet. The maximum visible surge height was about 1,400 feet.

A secondary plume formation reached a height of 850 feet about 31 seconds after the burst. When the water near surface zero had stopped rising and falling, a white foam patch remained; this was measurable until 16 minutes, when it had attained a diameter of about 10,000 feet.

Shot Umbrella was an 8-kt burst at a depth of 150 feet on the bottom of the lagoon. Light from the explosion was visible from the air for a few milliseconds. The primary shock wave produced a slick 5,400 feet in diameter and a spray dome about 3,400 feet in diameter. A second slick and a ring of spray formed beyond the primary dome at 0.53 seconds, as a result of the collapse of a cavitating region beneath the surface. Other slicks appeared at later times, caused by reflections of the shock wave from deep strata. The initial spray velocities within 200 feet of surface zero provided an estimated yield of 8.9 kt.

Plumes developed rapidly from the Umbrella spray dome, attaining a cylindrical shape and reaching a maximum height of 4,900 feet at 20 seconds. The maximum plume diameter was 3,250 feet at 22 seconds. The lower part of the plume, or column, tended to collapse at 6 seconds and a surge appeared at the base, possibly originating as a spillout from the edge of the water cavity. The visible base surge drifted with the wind and was measurable to a time of about 20 minutes and a crosswind radius of 14,600 feet. Its maximum height was about 2,100 feet. The foam patch was persistent and was measured for 22 minutes when its diameter was about 8,000 feet.

The instrumentation for recording temperature and humidity of the base surge gave limited results on Wahoo but fairly complete data on Umbrella. Both visible surges showed evidence of heating in the leading edge. The Umbrella records showed that the surge was warm for 60 seconds and at 100-percent relative humidity for 100 seconds. It

then became cooler as a result of evaporation and drier as a result of mixing. It returned to ambient conditions after 15 minutes.

Methods of predicting nuclear dome, plume, and base surge phenomena for application to the safe delivery of antisubmarine weapons are summarized. The gaps in existing knowledge are pointed out, and recommendations for future studies are included.

## FOREWORD

This report presents the final results of one of the projects participating in the military-effect programs of Operation Hardtack. Overall information about this and the other military-effect projects can be obtained from ITR-1680, the "Summary Report of the Commander, Task Unit 3." This technical summary includes: (1) tables listing each detonation with its yield, type, environment, meteorological conditions, etc.; (2) maps showing shot locations; (3) discussions of results by programs; (4) summaries of objectives, procedures, results, etc., for all projects; and (5) a listing of project reports for the military-effect programs.

## PREFACE

The authors are pleased to acknowledge the assistance provided by Robert S. Price, James R. Mitchell, and Charles R. Niffenegger of the Naval Ordnance Laboratory (NOL) in planning many of the details of the experimental operations.

The unusually high accuracy of the data obtained from the four photographic aircraft is due, in large part, to the cooperation and the conscientious efforts of the Program 5 personnel who positioned and tracked the aircraft with M-33 fire control radar systems.

The careful work of the analysis personnel at Edgerton, Germeshausen, and Grier, Inc., who handled the tedious and difficult task of measurement of the photographic records, is greatly appreciated.

In the preparation of this report, significant contributions were made by Mrs. Mary L. Milligan, Mrs. Dorothy M. Maultsby, and Mr. Joseph G. Connor, Jr., of NOL. Discussions with Dr. H. G. Snay were extremely helpful in clarifying certain aspects of the explosion phenomenology and the general scaling problem.

## CONTENTS

ABSTRACT-----	5
FOREWORD-----	7
PREFACE-----	7
CHAPTER 1 INTRODUCTION-----	15
1.1 Objectives-----	15
1.2 Experimental Background-----	15
1.3 Military Significance-----	16
1.4 Description of Phenomena and Theory of Scaling-----	16
1.4.1 Shock Wave Effects-----	16
1.4.2 Mass-Motion Effects—Deep Bursts-----	22
1.4.3 Mass-Motion Effects—Shallow Bursts-----	26
1.4.4 Base Surge-----	29
1.5 Test Conditions-----	30
CHAPTER 2 PHOTOGRAPHIC PLAN-----	33
2.1 Guiding Principles-----	33
2.2 Camera Locations, Shot Wahoo-----	33
2.3 Camera Locations, Shot Umbrella-----	34
2.4 Accuracy of Photographic Measurements-----	34
2.5 Radar Positioning and Tracking of the Photographic Aircraft-----	35
2.6 Operational and Photographic Problems-----	36
CHAPTER 3 RESULTS OF PHOTOGRAPHY, SHOT WAHOO-----	50
3.1 Spread of Underwater Shock Waves-----	56
3.2 Air Shock Waves and Condensation Clouds-----	57
3.3 Spray Dome-----	58
3.4 Trajectories of Objects near Surface Zero-----	60
3.5 Plumes-----	61
3.6 Visible Base Surge-----	62
3.7 Foam Patch-----	63
CHAPTER 4 RESULTS OF PHOTOGRAPHY, SHOT UMBRELLA-----	94
4.1 Spread of Underwater Shock Waves-----	94
4.2 Air Shock Wave and Condensation Clouds-----	95
4.3 Spray Dome-----	96
4.4 Trajectories of Objects Near Surface Zero-----	97
4.5 Plumes-----	98
4.6 Visible Base Surge-----	99
4.7 Foam Patch-----	102



CHAPTER 5 TEMPERATURE AND HUMIDITY MEASUREMENT-----	128
5.1 Theory of Temperature and Humidity Changes in a Base Surge-----	128
5.1.1 Evaporation of Drops of Pure Water -----	128
5.1.2 Effect of Salinity -----	129
5.1.3 Effect of Temperature -----	129
5.1.4 Applicability to Base Surge -----	130
5.2 Instrumentation -----	130
5.2.1 Recording Instrument-----	130
5.2.2 Power Supply -----	131
5.2.3 Mounting and Shielding of Temperature Elements -----	131
5.2.4 Assembly of Recording System-----	132
5.2.5 System Response-----	132
5.3 Field Operations -----	133
CHAPTER 6 RESULTS OF TEMPERATURE AND HUMIDITY MEASUREMENTS-	145
6.1 Shot Wahoo -----	145
6.2 Shot Umbrella -----	147
CHAPTER 7 COMPARISON OF HARDTACK RESULTS WITH HIGH- EXPLOSIVE AND NUCLEAR DATA -----	171
7.1 Spray Domes-----	171
7.2 Plumes and Visible Base Surge-----	174
CHAPTER 8 SCALING TO OTHER YIELDS AND DEPTHS FOR THE DEVELOPMENT OF SAFE DELIVERY TACTICS-----	190
8.1 General Considerations-----	190
8.2 Spray Domes-----	191
8.3 Plumes-----	192
8.4 Base Surge -----	193
CHAPTER 9 CONCLUSIONS AND RECOMMENDATIONS -----	203
9.1 Conclusions-----	203
9.2 Recommendations-----	204
APPENDIX PRINCIPLES OF HYDRODYNAMIC SCALING OF UNDERWATER EXPLOSION PHENOMENA -----	206
REFERENCES-----	212
TABLES	
1.1 Surface Weather Observations, Shots Wahoo and Umbrella -----	31
1.2 Radiosonde and Upper Wind Data, Shots Wahoo and Umbrella-----	32
1.3 Oceanographic Data, Shots Wahoo and Umbrella -----	32
2.1 Surface Camera Data, Shot Wahoo-----	36
2.2 Aircraft Camera Data, Shot Wahoo -----	39
2.3 Slant Ranges of C-54's, Shot Wahoo-----	40
2.4 Altitude of RB-50, Shot Wahoo -----	41
2.5 Target Array, Shot Wahoo-----	41

2.6 Surface Camera Data, Shot Umbrella-----	42
2.7 Aircraft Camera Data, Shot Umbrella-----	43
2.8 Slant Ranges of C-54's, Shot Umbrella-----	44
2.9 Radio Altimeter Readings for RB-50, Shot Umbrella-----	45
2.10 Target Array, Shot Umbrella-----	45
3.1 Comparison of Air Shock Wave Data Recorded at EC-2 with Observed Shock Wave Effects on Clouds, Shot Wahoo-----	66
3.2 Initial Spray Dome Velocities and Computed Yields, Shot Wahoo-----	67
4.1 Initial Spray Dome Velocities and Computed Yields, Shot Umbrella-----	104
5.1 Chart Speeds of Foxboro Recorders-----	134
5.2 Effect of Various Conditions on the Response Time of Foxboro Recorder and Elements-----	135
5.3 Temperature-Humidity Recording Stations-----	135
6.1 Summary of Temperature and Humidity Results, Shot Wahoo-----	153
6.2 Summary of Temperature and Humidity Results, Shot Umbrella-----	154
6.3 Temperature and Pressure Drops Associated with the Passage of Rarefaction Waves, Shot Umbrella-----	155
8.1 Underwater Detonation Tests-----	195
8.2 Reduced Nuclear Plume Data, Shots Umbrella, Wahoo, and Wigwag-----	195
8.3 Reduced Nuclear Plume Data, Shot Baker-----	196
8.4 Reduced Nuclear Base Surge Data-----	196

#### FIGURES

2.1 Locations of surface camera stations, Shot Wahoo-----	46
2.2 Horizontal flight path of RB-50, 24,000-foot altitude, Shot Wahoo-----	47
2.3 Horizontal flight path of C-54, 1,500-foot altitude, Shot Wahoo-----	46
2.4 Horizontal flight path of C-54, 8,100-foot altitude, Shot Wahoo-----	49
2.5 Horizontal flight path of C-54, 10,000-foot altitude, Shot Wahoo-----	50
2.6 Locations of surface camera stations, Shot Umbrella-----	51
2.7 Horizontal flight path of RB-50, 24,000-foot altitude, Shot Umbrella-----	52
2.8 Horizontal flight path of C-54, 1,500-foot altitude, Shot Umbrella-----	53
2.9 Horizontal flight path of C-54, 9,000-foot altitude, Shot Umbrella-----	54
2.10 Horizontal flight path of C-54, 10,000-foot altitude, Shot Umbrella-----	55
3.1 Primary shock wave slick, Shot Wahoo-----	68
3.2 Lateral spread of spray dome and cavitation pulse spray ring, Shot Wahoo-----	69
3.3 Bottom-reflected shock wave slick, Shot Wahoo-----	70
3.4 Aerial views of slicks, spray dome, and cavitation pulse spray ring, Shot Wahoo-----	71
3.5 Spray dome, Shot Wahoo-----	72
3.6 Spray dome height versus time curves, Shot Wahoo-----	73
3.7 Method used for determining initial spray dome velocity, Shot Wahoo-----	74
3.8 Peak underwater shock wave pressures, Shot Wahoo-----	75
3.9 Spray dome retardation factors, Shot Wahoo-----	76
3.10 Buoys and barges in the vicinity of surface zero prior to detonation, Shot Wahoo-----	77
3.11 Objects rising above spray dome, Shot Wahoo-----	78
3.12 Trajectories of objects rising above the spray dome, Shot Wahoo-----	78
3.13 Primary plumes, Shot Wahoo-----	79
3.14 Plume height versus time, Shot Wahoo-----	80

3.15 Plume radius versus time, Shot Wahoo-----	91
3.16 Dome and plume profiles, Shot Wahoo-----	92
3.17 Base surge at early times, Shot Wahoo-----	83
3.18 Base surge at late times, Shot Wahoo-----	94
3.19 Base surge radius versus time, Shot Wahoo-----	95
3.20 Base surge contours, Shot Wahoo-----	86
3.21 Base surge contours, Shot Wahoo-----	87
3.22 Base surge contours, Shot Wahoo-----	88
3.23 Base surge upwind, crosswind, and downwind, Shot Wahoo-----	99
3.24 Maximum base surge heights, Shot Wahoo-----	90
3.25 Foam patch, Shot Wahoo-----	91
3.26 Foam patch contours, Shot Wahoo-----	92
3.27 Foam patch diameter versus time, Shot Wahoo-----	93
4.1 Primary shock wave slick, Shot Umbrella-----	105
4.2 Lateral spread of spray dome, cavitation pulse slick, and spray ring, Shot Umbrella-----	106
4.3 Aerial views of slick, spray dome, and cavitation pulse spray ring, Shot Umbrella-----	107
4.4 Spread of air shock wave along water surface, Shot Umbrella-----	108
4.5 Spray dome, Shot Umbrella-----	109
4.6 Spray dome height versus time, Shot Umbrella-----	110
4.7 $P_0/U$ versus slant range, Shot Umbrella-----	111
4.8 Maximum spray dome height for radii between 500 feet and 1,500 feet at about 1 second, Shot Umbrella-----	112
4.9 Locations of ships and buoys prior to detonation, Shot Umbrella-----	113
4.10 Objects rising above the spray dome, Shot Umbrella-----	113
4.11 Trajectories of objects rising above spray dome, Shot Umbrella-----	114
4.12 Plume, Shot Umbrella-----	115
4.13 Plume height versus time, Shot Umbrella-----	116
4.14 Plume radius versus time, Shot Umbrella-----	117
4.15 Trajectories of jets in plume, Shot Umbrella-----	118
4.16 Collapse of plume and formation of base surge, Shot Umbrella-----	119
4.17 Base surge at late times, Shot Umbrella-----	120
4.18 Base surge radius versus time, Shot Umbrella-----	121
4.19 Base surge contour, Shot Umbrella-----	122
4.20 Base surge upwind, crosswind, and downwind extent, Shot Umbrella-----	123
4.21 Maximum base surge heights, Shot Umbrella-----	124
4.22 Foam patch, Shot Umbrella-----	125
4.23 Foam patch contours, Shot Umbrella-----	126
4.24 Foam patch diameter versus time, Shot Umbrella-----	127
5.1 Percentage change in size of drops of sea water versus relative humidity-----	136
5.2 Temperature elements and associated parts-----	137
5.3 Assembled element shields-----	138
5.4 Recorder in shock mount (destroyer)-----	138
5.5 Block diagram of temperature-humidity recorder-----	139
5.6 Response curves for wet and dry bulbs-----	140
5.7 Recorder in shock mount on YC barge-----	141
5.8 Washdown on YC barge-----	142
5.9 Element mountings-----	141
5.10 Temperature-humidity recording stations, Shot Wahoo-----	143

5.11 Temperature-humidity recording stations, Shot Umbrella	144
6.1 Temperature and relative humidity recorded at DD-593, Shot Wahoo	156
6.2 Temperature and relative humidity recorded at YC-9, Shot Wahoo	157
6.3 Relative humidity, Shot Wahoo	158
6.4 Temperature and relative humidity recorded at YFNB-12, Shot Umbrella	159
6.5 Temperature and relative humidity recorded at DD-474, Shot Umbrella	160
6.6 Temperature and relative humidity recorded at 55-barge, Shot Umbrella	161
6.7 Temperature and relative humidity recorded at DD-593, Shot Umbrella	162
6.8 Temperature and relative humidity recorded at Site Irwin, Shot Umbrella	163
6.9 Temperature and relative humidity recorded at Site James, Shot Umbrella	164
6.10 Temperature and relative humidity recorded at Site Keith, Shot Umbrella	165
6.11 Relative humidity, Shot Umbrella	166
6.12 Reproduction of a portion of original record obtained on YFNB-12, Shot Umbrella	167
6.13 Instrument response correction of temperatures recorded at YFNB-12, Shot Umbrella	168
6.14 Peak wet- and dry-bulb temperature changes immediately after base surge arrival, Shot Umbrella	169
6.15 Temperature and pressure drops recorded on Shot Umbrella	170
7.1 Initial spray dome velocity at surface zero versus scaled charge depth, 300-pound TNT tests in deep water	178
7.2 Spray dome retardation factor at surface zero versus scaled charge depth, 300-pound TNT tests in deep water	179
7.3 Comparison of spray dome profiles with theory, Shot Wahoo	180
7.4 Spray domes from 300-pound TNT tests bracketing the Wahoo scaled depth for shock wave phenomena	181
7.5 Comparison of spray dome profiles with theory, Shot Wigwam	182
7.6 Plume formation by a 300-pound TNT explosion at a depth of 30 feet	183
7.7 Comparison of Wahoo and Wigwam plume growth	184
7.8 Comparison of Wahoo and Wigwam average base surge growth	185
7.9 Column and smoke crown formation by HE tests approximately scaled to Shot Umbrella	186
7.10 Surface phenomena, Shot Baker	187
7.11 Comparison of Baker and Umbrella plume growth	188
7.12 Comparison of Umbrella and Baker average surge growth	189
8.1 Depths of burst for different explosion categories established for safe delivery	197
8.2 Spray dome angle versus scaled charge depth	198
8.3 Scaling of Wahoo and Wigwam plume growth	199
8.4 Scaling of Umbrella and Baker plume growth	200
8.5 Froude scaling of Wahoo and Wigwam average base surge growth	201
8.6 Froude scaling of Umbrella and Baker average base surge growth	202
A.1 Geometrically scaled model of shallow underwater explosion	210
A.2 Comparison of scaling techniques	211

# CONFIDENTIAL

## Chapter 1

### INTRODUCTION

#### 1.1 OBJECTIVES

The primary objective was to record and measure the formation, growth, and dissipation of the visible surface phenomena during Shots Wahoo and Umbrella by means of timed technical photography. The phenomena of interest included the slicks, cracks, spray domes, water columns, the shock waves, condensation clouds, plumes, fallout, visible base surge, and foam patches (Section 1.4). The purpose of obtaining these measurements was to interpret the data in terms of explosion theory and to use the results for the improvement of existing scaling techniques. These scaling methods are employed in the development of offensive and defensive tactics for military situations in which underwater nuclear weapons are used.

The secondary objective was to obtain a better understanding of the nature of the base surge by recording the temperature and humidity at various positions in the surge clouds formed by the collapse of the plumes on Shot Wahoo and the collapse of the column on Shot Umbrella. This method was expected to show the conditions within the surge, give information concerning the interaction between the base surge and the ambient atmosphere, and possibly indicate the motion of the base surge after part or all of it had become invisible because of the evaporation of water droplets.

#### 1.2 EXPERIMENTAL BACKGROUND

The U. S. Naval Ordnance Laboratory (NOL) has conducted a continuing investigation of the base surge and the related surface phenomena of underwater explosions since 1949. The experimental work has included tests with high explosives weighing from 10 pounds to 45 tons (References 1 and 2), underwater explosion tests in a vacuum tank (Reference 3), and hydraulic models of the base surge (Reference 4). Most of the data was obtained by means of photography. In addition, instrumentation was placed in the HE base surges to determine droplet and particle sizes and to record the changes in temperature and dewpoint (Reference 2). Laboratory personnel participated in Operations Castle (Reference 5) and Wistram (Reference 6) for the study of the surface phenomena of surface and underwater nuclear bursts by photographic means. Some analysis of the records of Shot Baker in Operation Crossroads has also been conducted. Scaling laws have been developed for the prediction of the surface effects of shallow underwater nuclear bursts (Reference 1).

A considerable effort has been devoted to the study of the surface phenomena of relatively deep underwater explosions by other laboratories, starting during World War I and extending through World War II. One of the main objectives during this period was the determination

CONFIDENTIAL

FORMERLY RESTRICTED DATA

of the explosion depth of depth charges by the measurement of the slick, spray dome, and plume phenomena. An extensive bibliography of this work is included in Reference 6.

### 1.3 MILITARY SIGNIFICANCE

The surface effects of conventional underwater explosions, in contrast to nuclear bursts, are not considered to be of major military importance, although some use has been made of the damaging power of the vertical jets formed by shallow explosions for the demolition of bridges (Reference 7). In addition, jets and plumes from exploding mines and shells may constitute a hazard to low-flying aircraft. However, surface phenomena have been used primarily in experimental studies as a source of information concerning the explosion. Under ideal experimental conditions, the surface effects of a conventional underwater explosion indicate the depth and position of the charge, the peak shock wave pressures at the water surface from surface zero to a considerable distance, the periods of bubble oscillation, and the phase of the bubble at the time it breaks the surface. The values calculated from photographic measurements provide a useful check on the data obtained from other types of instrumentation, if such data is available.

In contrast to conventional underwater explosion effects, the plumes and associated cloud phenomena (cauliflower cloud, fallout, and base surge) of nuclear bursts have major military significance because of the role they play as carriers of radioactive contaminants. For example, the cauliflower cloud from a shallow burst may be the source of high-energy initial gamma radiation (Reference 8). The fallout and base surge may transport contaminants several miles downwind, thereby extending the zone of airborne radiation hazard well beyond the region of physical damage from the shock wave and other effects. The close-in region in which the plumes originate is probably a zone of certain destruction for ships and aircraft because of the combined severe effects of plumes, shock, and radiation. In the case of a relatively deep burst delivered by a low-flying aircraft, the pilot must also evade a possible hazard from water rising in the spray dome.

As in conventional underwater explosions, technical photography of nuclear bursts provides information that aids in the interpretation of the records obtained with underwater pressure gages and may reveal phenomena that are not detected by other instrumentation. For example, in Operation Wigwag (Reference 6), aerial photography revealed patches of spray, well beyond the extent of the spray dome, which were caused by the focusing of the shock wave by reflection from the irregular ocean bottom. These spray patches were regions of relatively high pressure that may have significance in regard to damage to surface vessels. It is impracticable to measure such effects with gages, because it is probably impossible to predict where they will occur. However, technical photography can indicate the locations of such regions and provide an estimate of the magnitude of the peak pressures involved.

### 1.4 DESCRIPTION OF PHENOMENA AND THEORY OF SCALING

The surface phenomena of underwater explosions can be divided into two main categories: (1) those produced by the shock waves emitted at the time of the explosion and at bubble minima, and (2) those produced by the mass motion of the water, which accompanies bubble pulsation and its emergence above the surface.

**1.4.1 Shock Wave Effects.** The shock wave produced by an underwater explosion propagates outward radially at an extremely high velocity, which decreases rapidly, approaching the speed of sound. For TNT, the following expression shows the relationship between the peak pressure in the spherical shock wave and distance from the burst (Reference 9):

$$P_0 = 21,600 \left( \frac{W^{1/3}}{R} \right)^{1.13} \quad (1.1)$$

Where:  $P_0$  - peak overpressure in the shock wave, psi

$W$  - weight of explosive, pounds

$R$  - distance from center of charge, or slant range, feet

Equation 1.1 is not valid for values of  $W^{1/3}/R$  greater than about 1.1 lb<sup>1/3</sup>/ft ( $P_0 = 25,000$  psi).

The shape of the shock wave is given by the following equation (Reference 9):

$$p = P_0 e^{-t/\theta} \quad (1.2)$$

Where:  $P$  - overpressure in the shock wave, psi

$e$  - base of natural logarithms, 2.718

$t$  - time, sec

$\theta$  - shock wave decay constant (time interval for peak overpressure to decay to  $P_0/e$ ), msec

For TNT, the decay constant may be calculated from the following equation (Reference 10):

$$\theta = 0.056 W^{1/3} \left( \frac{R}{W^{1/3}} \right)^{0.22} \quad (1.3)$$

When the shock wave reaches the surface of the water, it is reflected as a tension wave. The intersection of the shock front and the surface is visible from above as a rapidly expanding ring of darkened water, sometimes called the slick (Reference 9). Following closely behind the darkened region is a white circular patch, which has been called the crack (Reference 11). Evidence exists that the surface of the water is undisturbed and, therefore, that the whiteness occurs under water, probably as a result of cavitation produced by the tension wave. Geometrical considerations indicate that the velocity of spread of the slick is a function of charge depth only, providing that the underwater shock wave has slowed down to sonic velocity and refraction effects may be neglected. Consequently, measurements of the rate of growth of the initial surface disturbance have been used to determine the depth of explosions (Reference 9).

The slick and crack are difficult to observe experimentally, and descriptions of these phenomena in the literature are not consistent. High-speed technical photography is needed for their proper resolution, and the appearance of the slick and crack is highly dependent on lighting and viewing angles. In some cases, the passage of the shock front produces only an apparent lightening of the water surface, and sometimes there is no visible effect.

Shortly after the crack appears, the water above the explosion rises vertically to form a white mound of spray called the spray dome. This rise is due to the particle velocity imparted to the water surface by the reflection of the shock wave and the subsequent breakup of the surface layer into drops of spray.

Directly above the charge, the initial vertical velocity of the surface should be approximately equal to the sum of the particle velocities in the incident and reflected shock waves, which are assumed to be equal in magnitude. At all positions, except surface zero, the

particle velocities in the shock waves have equal and opposite horizontal components, which cancel, but the vertical components are both directed upward and are additive. The resultant vertical velocity of the surface is, therefore,

$$V_0 = \frac{2(144) P_0 \cos \delta}{\rho U} \quad (1.4)$$

Where:  $V_0$  = initial vertical velocity of the surface at a point, ft/sec

$\rho$  = ambient density of the water, slugs/ft<sup>3</sup> (lb-sec<sup>2</sup>/ft<sup>4</sup>)

$U$  = shock front propagation velocity at the point, ft/sec

$\delta$  = angle with the vertical of the line from the explosion to the point on the surface (The factor of 144 is included to convert the units of  $P_0$ , which are in psi, to lb/ft<sup>2</sup>.)

Beneath the surface, the downward-moving tension wave is superimposed on the tail of the positive phase of the shock wave, which is moving upward. At some depth, the net tension becomes great enough to rupture the water and the surface layer breaks away and produces a cavitated region beneath the surface.

It is generally assumed that this layer of water rises from the surface with the initial velocity shown by Equation 1.4. However, it seems possible that the initial velocity might be reduced as a result of the work done in cavitating the water beneath the surface. Consequently, Equation 1.4 is sometimes modified to

$$V_0 = \frac{2(144) P_0 \cos \delta - 144 P_b}{\rho U} \quad (1.5)$$

Where:  $P_b$  = breaking pressure, psi

An estimate of the thickness of the surface layer may be obtained from the following formula (Reference 9):

$$L = \frac{(P_h + P_b) R U \theta}{2 P_0 c (1 - 1.13 U \frac{\theta}{R})} \quad (1.6)$$

Where:  $L$  = thickness of surface layer, feet

$P_h$  = hydrostatic pressure, psi

$c$  = charge depth, feet

Equation 1.6 shows that the thickness of the surface layer increases with distance from surface zero. The equation of motion of a horizontal layer moving upward, but decelerated by gravity and by the pressure difference between the atmosphere and the cavitated region, is

$$\frac{dv}{dt} = \frac{-144 (P_a - P_c)}{\rho L} - g \quad (1.7)$$

Where:  $v$  = upward velocity, ft/sec

$t$  = time, seconds

$P_a$  = atmospheric pressure, psi



$P_c$  = cavity pressure, psi

$g$  = acceleration due to gravity, ft/sec<sup>2</sup>

Integration of Equation 1.7 over the time of rise and descent of the surface layer shows that the closure time of the cavitated region should be

$$t_c = \frac{2 V_0}{\left[ \frac{144 (P_a - P_c)}{\rho L} + g \right]} \quad (1.8)$$

Where:  $t_c$  = time required for surface layer to rise and fall, or closure time of cavitated region, seconds.

Pressure pulses have been detected as a result of the water-hammer effect produced when the cavitated region closes. The times of occurrence of these are reported to be in reasonably good agreement with values calculated from Equation 1.8 (Reference 12). This bulk cavitation phenomenon is of considerable interest in regard to shock damage to ships.

The actual structure of the spray dome and the phenomena beneath the surface are undoubtedly more complex than indicated above. (An extension of this simple treatment would show that a series of layers of water should rise upward beneath the surface layer.)

The surface layer actually breaks up into spray, at least partially, and the cavitated region is probably a zone of cavitation bubbles so that the surface layer may not separate completely from the water beneath it. The values of  $P_b$  and  $P_c$  to be employed in Equations 1.5 through 1.8 depend upon experimental conditions, and the correct values to be employed in a given case have not been established. However,  $P_c$  cannot be less than  $P_b$  (Reference 13).

Slick, crack, and spray dome phenomena may be multiple in nature if bottom-reflected shock waves and pressure waves resulting from bubble pulsation reach the surface with sufficient intensity.

If Equation 1.4 could be used with confidence, it would be possible to calculate the peak underwater pressures along the water surface wherever spray is visible. This would permit the determination of depth of burst for a charge of known weight or the calculation of charge weight if the depth is known. This has been done successfully in some cases, but discrepancies have been observed in other experimental programs (Reference 6). These discrepancies sometimes take the form of anomalously high initial velocities (References 6 and 9).

The explanation for this probably lies in the breakup of the rising water surface into a spray. It has been shown in Reference 14 that a water surface is stable if it is accelerated in the direction of a less dense medium, such as air, but becomes unstable if the direction of acceleration is reversed. In the case of the spray dome, the motion of the upper surface of the rising layer is directed into the air but the entire layer is being decelerated by gravity and a pressure difference. Consequently, the acceleration vector is directed downward and the upper surface becomes unstable. Very small ripples and minute irregularities are stabilized by surface tension, but longer ripples and gravity waves grow in amplitude at an exponential rate as a result of the deceleration of the surface. In addition, rising spikes of water appear at the location of random disturbances, patches of foam, debris, and irregularities in the surface.

As a result of this, the surface is covered by a dense mass of water jets within milliseconds after the reflection of the underwater shock wave. These jets break up into a spray in a short time. Near the center of the dome, the entire surface of the water breaks up into a white spray, which appears to be smooth and uniform when viewed from a distance. However, closeup photographs show that the spray is more pronounced on the crests of waves, although spray is also present in the troughs. At the edge of the dome the

spray is confined to the wave crests and the original surface wave pattern can be clearly seen. Spray dome diameters are consequently greater in rough water than in smooth water.

If initial spray dome velocities are measured on a high-speed photographic record, an early extremely rapid rate of rise of jets and spray above the surface is detected. This is greater than the  $V_0$  shown by Equation 1.4. After a period of time, generally a few milliseconds, the observed velocity may drop fairly suddenly to a value that is in approximate agreement with the  $V_0$  predicted by Equation 1.4. The reason for this is not clear. Theory indicates that the early rate of growth will be exponential and will continue only until the amplitude of a disturbance is about four-tenths of the wavelength. After that time, the height-versus-time curve should be parabolic.

Some evidence that the initial bulk motion of the water beneath the spray follows Equation 1.4 was obtained during Operation Wigwag, where the weapon support barge, the YC-173, rose with an initial velocity approximately as indicated by Equation 1.4, although the leading spray rose at a more rapid rate (Reference 6).

An additional factor that may cause the initial spray dome velocity to differ from that indicated by the simple theory used above is the possibility that a shaped-charge effect may cause jetting in the troughs of waves near the center of the dome (Reference 15). It is also possible that the surface waves may focus the underwater shock wave (Reference 12).

If the high initial instability velocities are ignored, the rise of the spray in the dome can sometimes be represented by a parabolic expression of the following form (Reference 16):

$$h = V_0 t - ft^2 \quad (1.9)$$

Where:  $h$  = height of spray dome, feet

$f$  = retardation coefficient, ft/sec<sup>2</sup>

The proper value of  $f$  depends on such factors as charge size, depth of burst, position in the dome, and surface roughness. Physically, it represents half the deceleration of the spray, which results from drag forces and gravity.

Spray dome diameters increase with increasing charge depth, and, since the heights decrease, the dome profiles become flatter. Consequently, measurements of the shape of the spray dome have been used as a technique for determining the depth of explosions.

The dome is surrounded by a region called the black ring or dark ring, where small isolated jets or spikes of water can be seen. The dark appearance is an optical effect due to reduced regular reflection of light by the ruffled surface, and varies with the position of the observer. The dark ring is a relatively stationary phenomenon that does not change in size for a period of time after its formation (Reference 11).

The same shock wave surface phenomena are observed in both HE and nuclear underwater tests. However, for nuclear bursts, Equations 1.1 and 1.3 become (Reference 10):

$$P_0 = 4.38 \times 10^4 \left( \frac{Y^{1/3}}{R} \right)^{1.13} \quad (1.10)$$

and

$$\theta = 2.27 Y^{1/3} \left( \frac{R}{Y^{1/3}} \right)^{0.22} \quad (1.11)$$

Where:  $Y$  = yield, kt.

A comparison of Equation 1.1 with 1.10 and 1.3 with 1.11 shows that an underwater nuclear burst with a yield of 1 kt produces the same peak pressure at the same distance as the detonation of 0.667 kt of TNT, and produces the same time constant at the same distance as the

detonation of 0.737 kt of TNT (Reference 10).

Equation 1.10 is not valid for values of  $Y^{1/3}/R$  greater than about  $0.0016 \text{ kt}^{1/3}/\text{ft}$  ( $P_n = 3,000 \text{ psi}$ ). However, peak pressures for positions closer to a nuclear burst may be calculated from information given in Reference 17.

The scaling of shock waves is relatively simple and is based on the principle that compressibility and inertia forces govern the phenomena (see Appendix). Consequently, a change in the linear size of the charge by a factor  $k_1$  means that peak pressures and velocities will be unchanged if distances and times are multiplied by the same factor (References 9 and 18). For spherical TNT charges of a uniform density, the cube root of the charge weight is proportional to the radius and may be used as a linear scale factor. A conversion factor must be employed for the scaling of TNT data to other explosive compositions or, as shown above, to nuclear bursts.

In practice, shock wave-induced surface phenomena are scaled in terms of the depth and weight of the explosive charge, which may be expressed in the following manner:

$$\lambda_c = \frac{C}{W^{1/3}} \quad (1.12)$$

Where:  $\lambda_c$  = reduced charge depth for HE tests,  $\text{ft}/\text{lb}^{1/3}$

The following relation defines the geometrical scale factor in terms of both charge depth and the cube root of charge weight.

$$k_1 = \frac{c_m}{c_p} = \left( \frac{W_m}{W_p} \right)^{1/3} \quad (1.13)$$

Where:  $k_1$  = length scale factor

subscript m refers to the model

subscript p refers to the prototype

The initial spray dome velocities calculated from Equation 1.4 should be equal for charges exploded at the same reduced depth  $\lambda_c$  in free water if  $\rho$  and  $U$  are the same in all experiments. Spray dome heights will not be the same because of the dependence of the height on the retardation coefficient  $f$  which varies with the scale of the experiment. Spray dome diameters show approximate geometrical scaling for charges of different weights fired at the same  $\lambda_c$ .

To simulate the shock wave and the resulting slick, crack, and spray dome phenomena of an underwater nuclear burst with HE, the shock wave peak pressure equivalence factor must also be taken into account. For example: Assume that a 30-kt nuclear detonation at a depth of 1,000 feet is the prototype. Since 20-kt of TNT would produce the same peak pressure at a given distance as the 30-kt nuclear device (Reference 10), the reduced depth  $\lambda_c$  in terms of pounds of TNT is  $1,000/(40,000,000)^{1/3}$ , or  $2.92 \text{ ft}/\text{lb}^{1/3}$ . This procedure is valid for shock wave peak pressure similitude only and is not a general method.

For the comparison of different nuclear bursts, geometrical scaling of the depth of burst will be indicated as follows:

$$\Lambda_c = \frac{C}{Y^{1/3}} \quad (1.14)$$

Where:  $\Lambda_c$  = reduced charge depth for nuclear bursts,  $\text{ft}/\text{kt}^{1/3}$

If a charge is exploded in shallow water, on or off the bottom, the depth of water as well as the charge depth should be scaled geometrically in order to obtain geometrical similitude

of shock wave effects. However, the free surface and bottom produce various complicating effects on the shock wave (Reference 19), which may not scale geometrically, particularly at great distances. If a charge is fired on a rigid bottom that acts as a perfect reflector, the shock wave effects close to the charge should be the same as those produced by a charge with double the energy fired in free water. In practice, the amount of reflection depends on the nature of the bottom and is never complete (Reference 20).

Equation 1.4 was derived on the assumption that the underwater shock wave undergoes complete reflection, as a negative wave, at the surface of the water. In reality, a shock wave is transmitted to the air. However, the assumption of complete reflection is generally a good one for shots at a  $\lambda_c$  greater than 2.0 ft/lb<sup>1/3</sup>. The relative magnitudes of the shock waves are given approximately by the following expression, which applies to acoustic (low-amplitude) waves (Reference 9):

$$\frac{P_{oa}}{P_{ow}} = \frac{2 \rho_a C_a}{\rho_w C_w} \quad (1.15)$$

Where:  $P_o$  = peak overpressure in the shock wave, psi

$\rho$  = ambient density, slug/ft<sup>3</sup>

$C$  = ambient speed of sound, ft/sec

subscripts a and w refer to air and water respectively.

For example, a TNT explosion at a  $\lambda_c$  of 2.0 ft/lb<sup>1/3</sup> generates an underwater shock wave whose peak pressure drops to 10,000 psi when it reaches surface zero. Equation 1.15 indicates that the shock wave transmitted to the air would have a peak pressure of about 3 psi.

As the air shock wave propagates upward and outward, a negative, or rarefaction, phase develops behind the compression wave. The drop in air pressure that occurs during the passage of the rarefaction phase results in adiabatic cooling and possibly the formation of a condensation cloud. This phenomenon is generally considered to be of secondary importance. However, it may obscure part of the plume phenomena of interest, as during Shot Baker (Reference 21), or it may provide some indirect information concerning the strength of the air shock wave, as in Operation Wigwag (Reference 6).

**1.4.2 Mass-Motion Effects—Deep Bursts.** After the primary shock wave is emitted by a deep underwater explosion, the highly compressed gaseous sphere of explosion products pushes the surrounding water outward radially at a high velocity. The water is accelerated outward until the gas pressure drops to the level of the hydrostatic pressure. However, the motion continues because of the inertia of the water, and the bubble expands until the pressure excess in the water brings it to a stop. At this stage, the gas pressure is much lower than hydrostatic pressure and the bubble contracts. It reaches a minimum size, at which an abrupt reversal of the motion occurs and a pressure pulse is emitted (first bubble pulse). The bubble continues to oscillate and migrates toward the surface.

For the purposes of this report, "deep" bursts will be defined as explosions at a great enough depth so that the bubble completes at least one oscillation before it breaks through the surface. An explosion that is so deep that the bubble breaks up or loses its identity before reaching the surface will be called a "very deep" burst. Only bursts that are far enough from the bottom so that the bottom exerts no influence on the bubble will be considered in this section. However, the effect of the water surface will be included.

In its first expansion, the gas bubble formed by a TNT explosion grows to the maximum radius indicated by the following equation (Reference 12):

$$\lambda_{\max} = 12.6 \frac{W^{1/3}}{Z^{1/3}} \quad (1.16)$$

Where:  $\lambda_{\max}$  = maximum bubble radius, feet

$Z$  = total hydrostatic pressure at depth of burst, feet of water

The period of the first pulsation, from detonation time until the minimum radius is attained, is given for TNT by (Reference 18):

$$T_1 = 4.35 \frac{W^{1/3}}{Z^{1/3}} (1 + 0.10 \frac{\lambda_{\max}}{c}) \quad (1.17)$$

Where:  $T_1$  = first bubble period, seconds

(The last term in the equation is a correction for the effect of the water surface.)

The water surrounding the explosion is set into motion by the pulsation and migration of the bubble. In the process of migration, incompressible radial flow may be assumed, which implies that water velocities decrease inversely with the square of the distance from the center of the bubble. However, when the oscillating bubble migrates upward, the flow of the water becomes more complex and is not fully understood.

Observations have shown that the first expansion of a migrating bubble is uniform in all directions and results in a negligible displacement of the bubble center. However, because of the difference between the hydrostatic pressures at the top and bottom of the expanded bubble, the bubble collapse is not symmetrical; the bottom part moves in faster than the sides, and the sides move faster than the top (Reference 12). The bottom may impinge upon the top and penetrate the water above the bubble in the form of a jet. At this stage, the bubble has the shape of a torus, but it expands again into a roughly spherical shape.

During the collapse and reexpansion phases, the bubble moves upward. However, the bottom shows the greatest upward motion during the collapse and the top moves farthest during the expansion. The total motion of the bubble occurs during a relatively brief period before and after the time of bubble minimum.

The simulation of the migration of a large explosion bubble on a small scale is a difficult process. A depth of burst that leads to the formation of geometrically similar shock wave effects will usually not provide a true simulation of bubble migration and the consequent plume effects. As a first step, it seems reasonable to keep the ratio of the depth of burst to the maximum size of the explosion bubble constant in model and prototype. This may be expressed as a "submergence factor" (Reference 12).

$$\lambda_c^* = \frac{c}{\lambda_{\max}} \quad (1.18)$$

Where:  $\lambda_c^*$  = reduced charge depth, or submergence factor, dimensionless

If  $\lambda_c^*$  is maintained constant for different charge weights, the geometrical configuration of the bubble and water up to the end of the first expansion is reproduced. On the other hand, this does not guarantee that the subsequent behavior of the bubble will be similar in model and prototype.

When  $\lambda_c^* > 1$ , the explosion bubble becomes tangent to the original water surface when it attains its maximum size. At this depth, the water layer above the bubble should not rupture during the first bubble oscillation. However, at somewhat shallower depths rupture will take place. Consequently, this reference depth may be used to define the transition between

"shallow" and "deep" bursts. Since  $c = A_{\max}$  at this depth, it follows from Equation 1.16 that

$$c(c + 33)^{1/3} = 12.6 W^{1/3} \quad (1.19)$$

Where: 33 = normal atmospheric pressure, feet of sea water

Employing a binomial expansion, Equation 1.19 becomes approximately the following:

$$c \left( 1 + \frac{8.25}{c} \right) = 6.69 W^{1/3} \quad (1.20)$$

which indicates that for large values of  $c$ , the reference depth becomes proportional to  $W^{1/3}$ .

A different system is necessary to scale the upward migration of the bubble during its collapse and subsequent reexpansion. If it is assumed that the only force acting on the water is gravity and that the only resistance to flow is that offered by the inertia of the water, the equations of energy and motion of the bubble may be put in dimensionless form (Reference 9). In order to do this, a characteristic length having the value  $(W'/g\rho)^{1/4}$  is employed, where  $W'$  is the energy available after the emission of the shock wave. Since  $W'$  is proportional to the charge weight  $W$ , and  $g\rho$  can be treated as a constant, the following scaling parameter can be defined:

$$\lambda_c'' = \frac{z}{W^{1/4}} \quad (1.21)$$

Where:  $\lambda_c''$  = reduced charge depth, ft/lb<sup>1/4</sup>

Maintaining the equality of  $\lambda_c''$  in model and prototype provides similitude of the pressure distribution in the water surrounding the explosion bubble. Since migration is directly dependent on pressure distribution, it is seen that migration scales with  $W^{1/4}$ . Equation 1.21 can also be derived from the Froude number, since Froude scaling is valid when gravity and inertia are the only important forces (see Appendix). To obtain this result,  $A_{\max}$  is used as a characteristic length and  $T_1$  is used as a characteristic time (neglecting the surface effect). In addition, the acceleration due to gravity is assumed to be the same in model and prototype (References 22 and 23).

If the criteria expressed by Equations 1.19 and 1.21 are combined, the following result is obtained (Reference 23):

$$\frac{c_m}{c_p} = \frac{Z_m}{Z_p} \quad (1.22)$$

In expanded form, Equation 1.22 becomes

$$\frac{c_m}{c_p} = \frac{(c + P_a)_m}{(c + P_a)_p} \quad (1.23)$$

Where:  $P_a$  = atmospheric pressure, feet of water

Equation 1.23 shows that exact scaling of bubble migration is impossible with model tests conducted under normal atmospheric sea level pressure. Similitude can be approached, however, and several possibilities offer themselves. For example, if charge depths are great, the effect of atmospheric pressure becomes negligible and approximate similitude may be attained. Another technique is to conduct experimental programs in high-altitude lakes, where the atmospheric pressure is reduced, although reductions of only about 30

percent in  $P_{\text{am}}$  could be attained in this manner, and the practical difficulties would be great. However, the bubble migration of HE depth charges can be modeled successfully by reducing the air pressure in a vacuum tank (Reference 22). It is also feasible to increase the hydrostatic pressure in a model test by accelerating the test tank. In this case, the acceleration is equivalent to increasing the magnitude of  $g$ ; therefore,  $g$  becomes a variable that must be included in the scaling equations (Reference 24).

In practice, experimental difficulties arise in the modeling of explosion phenomena in the laboratory, which make the scaling problem more difficult than indicated above. These arise from such causes as the necessity for the employment of different explosives in model and prototype, the boiling of water at very low pressures in a vacuum tank, wall effects in tanks, the effects of surface tension in small-scale experiments, and the like. These are discussed in References 22 through 24.

The approach of a bubble toward the surface and its arrival and emergence produce a violent upheaval of the water, which is thrown up and outward as plumes. The upward migration of an explosion bubble from the time of detonation until the second maximum may be estimated with the following expression (Reference 23):

$$Z = 3.7 \left( \frac{A_{\text{max}}}{Z} \right)^{3/2} \left( 1 - 0.1 \frac{A_{\text{max}} Z}{C^2} \right) \quad (1.24)$$

Most of the useful studies of the plume phenomena of deep bursts have been conducted with charges weighing 200 pounds. On the basis of these tests, plumes are classified as vertical and radial, the radial plumes including those emerging at any angle with the surface except a right angle (Reference 9). In some cases, a relatively narrow vertical high-velocity plume is the first to emerge. This occurs when the migrating bubble collapses just beneath the surface and the rising bottom of the bubble penetrates the layer of water above the bubble in the form of a liquid jet. The depth for maximum velocity of this type of vertical plume is possibly at a  $\lambda_0$  of 1.2. After the appearance of the vertical jet, the bubble gases reexpand and push out a hemispherical mass of plumes that expand radially in all directions. At depths of firing that are intermediate between those yielding a narrow vertical plume, the radial plumes produced by the expanding bubble are dominant.

Since most of the migration occurs within brief intervals before and after the times of bubble minima, the times of plume emergence tend to cluster around these times. Plume times, therefore, increase in a roughly stepwise manner with increasing charge depth.

If a burst is sufficiently deep, the oscillations of the bubble will be damped out before it reaches the surface. In this case, the bubble may float upward at a constant velocity and produce relatively small plumes when it emerges. At even greater depths, it may break up into smaller bubbles that have little effect at the surface. The scaled depths at which these phenomena occur have not been established with certainty, but they probably increase with increasing charge weight.

After the plumes from a deep underwater explosion have subsided, a smooth circular expanding patch of water remains. This appears to be an upwelling of water, induced by the emerging bubble. It has been termed a "carbon slick" in some HE studies because of the presence of carbon in the patch.

The bubble formed by an underwater nuclear burst is different in composition and structure from that formed by a conventional explosion. In the latter case, a gaseous sphere of reaction products is produced, and the bubble interface consists of the same particles during the first expansion phase. A density discontinuity exists at the surface of the bubble.

In the case of a nuclear explosion, the water surrounding the burst is vaporized and a bubble of expanding steam is formed. Since water is continuously vaporized while the bubble expands, the interface is transferred from one set of particles to another. The surface of the bubble is probably not sharply defined, since the density of the moist steam at the

interface should be the same as that of the surrounding liquid (Reference 17).

In Reference 17, the maximum radius of the bubble formed by a 30-kt nuclear burst (expected Wigwam yield) at a depth of 2,000 feet ( $Z = 2,033$  feet of sea water) was calculated to be 376 feet. Assuming that a relationship of the form of Equation 1.16 is also applicable to nuclear explosions, the following equation is obtained:

$$A_{\max} = 1,500 \frac{Y^{1/3}}{Z^{1/3}} \quad (1.25)$$

Experimental evidence from Operation Wigwam showed that a 32-kt burst, at a depth of 2,000 feet, had a first bubble period of 2.87 seconds (Reference 17). If the general relationship for nuclear bubble periods is of the same form as Equation 1.17, the following result is obtained:

$$T_1 = \frac{515 Y^{1/3}}{Z^{1/3}} (1 - 0.10 \frac{A_{\max}}{c}) \quad (1.26)$$

For nuclear bursts, the transitional depth between shallow and deep bursts may also be taken as the depth at which the bubble becomes tangent to the original water surface at the end of its first expansion, as usual as in the case of HE, that the bubble is contained for at least one oscillation. Since this transitional depth is relatively great with nuclear bursts, the hydrostatic pressure due to the atmosphere (33 feet) may be neglected in Equation 1.25. Setting  $A_{\max} = c$  in this modified equation, yields the following result:

$$c = 240 Y^{1/4} \quad (1.27)$$

This equation serves as a good approximation for yields greater than 1 kt.

An oscillating steam bubble loses energy in the same manner as an oscillating gas bubble, but also loses mass because of the condensation of vapor. Consequently, the oscillations will be damped rapidly, and a migrating nuclear bubble will behave quite differently from a migrating TNT bubble after the first pulsation has ended.

For deep explosions, Equation 1.24 may be used for the migration of a nuclear bubble during its first oscillation. The subsequent bubble migration, periods, and maximum radii may be calculated with methods given in Reference 23.

The Wigwam results and data obtained with steam bubbles in the laboratory indicate that a nuclear bubble probably exists only through three pulsations. Reference 23 establishes a depth at which three complete bubble cycles are possible as the transitional depth between deep and very deep nuclear explosions. This depth is given as:

$$c = 600 Y^{1/4} \quad (1.28)$$

**1.4.3 Mass-Motion Effects—Shallow Bursts.** When a shallow burst occurs, a spray dome is formed, but the mass-motion of water produced by the expanding bubble gases follows closely behind the snook front and the rising dome is penetrated rapidly by a water column. It is difficult to distinguish one effect from the other in the early stages, since there is no marked discontinuity in the motion.

As in deeper bursts, the expanding bubble causes an upward and outward acceleration of the water surrounding the explosion. If the burst is shallow enough, the layer of water above the charge ruptures while the gases are at a high pressure and the explosion products are released to the atmosphere. For these very shallow TNT explosions, the blowout or outward venting of the contents of the bubble produces a dark smoke crown that expands rapidly (Reference 1). Although the internal pressure is reduced by the blowout, the water



at the sides of the bubble continues to move outward because of its inertia. The resultant motion forms a vertical column, which rises and penetrates the smoke crown. The continued expansion of the water results in an underpressure in the gases within the column. At this stage, the rising water at the top of the column is pushed inward by atmospheric pressure, and converges to form a vertical liquid jet that rises well above the smoke crown. The jet carries the smoke and spray at the inside of the crown upward, sometimes forming a ring vortex in the crown.

If the water above a shallow explosion has not ruptured by the time the bubble pressure drops to atmospheric pressure, the water should start to decelerate, and blowout will not occur. A water column and jet will be formed, but no smoke crown will be produced. In a TNT explosion at this condition, the jet may have a dark appearance, indicating the presence of carbon.

It is clear that the relationships between bubble pressure, depth of burst, and atmospheric pressure are important for determining the nature of the surface phenomena of shallow underwater bursts.

The adiabatic relation for the gaseous products of a TNT explosion is given as (Reference 9):

$$P_B = 1.47 \left( \frac{W}{V} \right)^{1.25} \quad (1.29)$$

Where:  $P_B$  = pressure of gas in bubble (feet of sea water)

$W$  = charge weight, pounds

$V$  = volume of gas in bubble, ft<sup>3</sup>

Setting  $P_B$  equal to one atmosphere (33 feet of sea water) and solving for bubble radius,  $A$ , yields

$$A = 1.71 W^{1/3} \quad (1.30)$$

If the bubble radius is equal to the depth of burst ( $A = c$ ), it follows that

$$c = 1.71 W^{1/3} \quad (1.31)$$

and

$$\lambda_c = 1.71 \quad (1.32)$$

for the scaled depth at which bubble pressure is equal to atmospheric pressure when the bubble gases reach the original surface level. On this basis, the ratio of bubble pressure to atmospheric pressure, when the bubble gases rise above the original surface, is constant for all charge weights at the same scaled depth  $\lambda_c$ .

The radial growth of the water column produced by a shallow burst should depend upon the difference between atmospheric pressure and the pressure inside the column and on the inertia of the water. For this type of phenomenon, the length and time scale factors for the motion are the same (Appendix). If the cube root of charge weight ( $W^{1/3}$ ) is employed as a length and time scale factor, radius-versus-time curves for the growth of columns from charges at the same geometrically-scaled depth,  $\lambda_c$ , should agree, if all radii and times are divided by  $W^{1/3}$ . This scaling method is substantiated by HE data, except for late times when the column breaks up into spray.

The maximum column diameter  $D_{max}$  has been measured on a large number of tests using TNT charges ranging from 10 to 4,200 pounds in weight (Reference 1). It is a relatively reproducible dimension, and is a function of  $W^{1/3}$  for bursts at a constant  $\lambda_c$ . The following

two equations show this dependence; Equation 1.33 is for explosions at mid-depth and Equation 1.34 is for explosions on the bottom.

$$D_{\max} = 6.75 W^{1/3} \quad (1.33)$$

(valid for  $\lambda_c \approx 0.26 \text{ ft/lb}^{1/3}$ )

$$D_{\max} = 8.01 W^{1/3} \lambda_d^{0.166} \quad (1.34)$$

(valid for  $0.25 < \lambda_d < 2.22 \text{ ft/lb}^{1/3}$ )

Where:  $D_{\max}$  = maximum column diameter, feet

$\lambda_d$  = reduced water depth, for bottom explosions,  $\text{ft/lb}^{1/3}$

The mechanism of rupture of the layer of water above a charge, which results in a blowout of detonation products, is not fully understood. If this process scaled geometrically, blowout would always occur at values of  $\lambda_c$  less than some critical value. For HE tests, the presence of a black sea crown at early times is considered to be evidence of blowout, and photographs of charges weighing up to 600 pounds show a possible critical  $\lambda_c$  around  $1 \text{ ft/lb}^{1/3}$  (Reference 13). However, there is some evidence that blowout will only occur at smaller values of  $\lambda_c$  for larger charges, and the phenomena in the critical depth region require further study. A possible explanation for this is found in the theory of instability (Reference 14). According to this theory, bubble gases will penetrate the layer of water above a charge only while the layer is being accelerated upward. The rate of penetration is proportional to the wavelength of the disturbances in the layer. The actual explosion process is doubtlessly more complicated than the process treated in this theory, however, due to the presence of the dome, cavitation effects in the water, turbulence, thermal effects, and the like. In addition, the wavelengths of surface disturbances may be roughly the same on explosions of different magnitudes. As a result, the penetration of the thick layer of water above a large charge may take longer, scalewise, than the penetration of the thin layer above a small charge at the same  $\lambda_c$ . If this occurs, the bubble pressure in a large bubble may drop below atmospheric pressure before rupture takes place, and blowout will be prevented.

Shot Baker in Operation Crossroads was the only shallow underwater nuclear test available for study prior to Operation Hardtack and has been used for the development of nuclear prediction methods. Since a well-developed cauliflower cloud was observed during Shot Baker, it is believed that a blowout of detonation (fission) products occurred. Using a radiochemical yield of 23.5 kt and a depth of 90 feet for Baker gives a  $\lambda_c$  of  $0.249 \text{ ft/lb}^{1/3}$  or a  $\lambda_c$  of  $31.5 \text{ ft/kt}^{1/3}$ . Equation 1.33 predicts a  $D_{\max}$  of 2,440 feet for Baker. The observed value was 2,030 feet, which implies that the Baker TNT equivalence, in terms of column formation, was 13.6 kt. Accordingly, for nuclear bursts scaled to Shot Baker, the following expression has been employed:

$$D_{\max} = 710 Y^{1/3} \quad (1.35)$$

(valid for  $\lambda_c \approx 31.5 \text{ ft/kt}^{1/3}$ )

If the same equivalence factor is valid for shallow bottom shots, the following expression may be obtained from Equation 1.34 for bottom bursts:

$$D_{\max} = 377 Y^{1/3} \Lambda_d^{0.166} \quad (1.36)$$

(valid for  $\Lambda_d > 31.5 \text{ ft/kt}^{1/3}$ ;  $\Lambda_d < 1$ )

This equation is possibly valid for all shallow depths, as indicated. Although  $D_{\max}$  scales geometrically in terms of  $\lambda$ , the transition from shallow to deep bursts does not occur at the same  $\lambda$  for all charge weights.

The maximum overall heights of the surface phenomena of shallow bursts scale geometrically in the same manner as maximum column diameters over the range of weights studied (21 to 4,200 pounds). The expressions for the maximum height of the central liquid jet are (Reference 1):

$$J_{\max} = 65.8 W^{1/3} \quad (1.37)$$

(valid for  $\lambda_c \approx 0.26 \text{ ft/lb}^{1/3}$  at middepth)

$$J_{\max} = 4.8 W^{1/3} \lambda_d^{0.232} \quad (1.38)$$

(valid for  $0.1 < \lambda_d < 1.1 \text{ ft/lb}^{1/3}$ , bottom shots)

Where:  $J_{\max}$  = maximum jet height, feet.

There is evidence that small HE charges produce the highest jets at a  $\lambda_c$  of about  $1.1 \text{ ft/lb}^{1/3}$ .

The technique of using the ratio of observed nuclear to extrapolated TNT values may also be applied to maximum jet heights for prediction purposes. However, as there is little physical basis for this method, the resulting equations are considered to very approximate. There was no central liquid jet during Shot Baker, though a hollow white cylindrical plume was observed rising above the cauliflower cloud. Maximum jet heights are determined by initial jet velocity and the retardation of the jet due to gravity and atmospheric resistance. Since the observed jets are often multiple in nature and may be different in structure, which leads to differences in breakup and retardation, it may be purely fortuitous that geometrical scaling holds for small HE charges.

Equation 1.37 predicts a maximum jet height of 23,800 feet for the Baker condition. The observed maximum height of the white plume was 8,000 feet. Assuming that this ratio is generally valid for shallow nuclear bursts, the following equations are obtained:

$$J_{\max} = 2,800 Y^{1/3} \quad (1.39)$$

(valid for  $\Lambda_c \approx 31.5 \text{ ft/kt}^{1/3}$ )

$$J_{\max} = 1,200 Y^{1/3} \Lambda_d^{0.232} \quad (1.40)$$

(valid for  $12.6 < \Lambda_d < 139 \text{ ft/kt}^{1/3}$ )

**1.4.4 Base Surge.** The column from a shallow burst and the plumes from a deep burst both break up into spray and collapse to form a toroidal cloud called the base surge, which expands radially along the surface of the water. The surge consists of spray droplets, with entrained air and explosion products, and behaves initially in the same manner as a homogeneous fluid.

In a nuclear burst, part of the radioactive fission debris becomes intimately mixed with the water droplets in the visible base surge. When the water evaporates, the fission products

remain as an invisible cloud or aerosol that continues to expand. The term "base surge" applies to both the visible and invisible clouds.

It is convenient to consider the surge behavior as consisting of three stages. During the first, or gravity flow stage, the surge does not mix appreciably with the ambient atmosphere. During the second, or mixing, stage, the surge engulfs ambient air and the flow is gradually retarded. In the final, or diffusion, stage, the surge has lost its kinetic energy and has become a cloud of fine droplets, which drifts with the wind. There is probably a slow growth due to eddy diffusion until the surge can no longer be identified.

During the first stage, the main forces governing the surge flow are gravity and inertia (Reference 4). Consequently, the motion at different scales may be reduced by the use of Froude scaling parameters, in which the time scale factor is equal to the square root of the length scale factor (Appendix). In shallow explosives work, the maximum column diameter  $D_{max}$  has been used as a characteristic length, and surge radius-versus-time data has been reduced by dividing the values by  $D_{max}$  and the square root of  $D_{max}$  respectively (Reference 1). Reduced curves for the base surges are similar for charges weighing from 100 to 4,200 pounds at depths geometrically scaled to Shot Baker, and on the bottom at scaled depths  $A_d$  ranging from about 0.26 to 1.1 ft/lb<sup>1/3</sup>.

Prior to Operation Hardtack, the Shot Baker base surge was used as a prototype for shallow underwater nuclear bursts. Since scaled HE surge radius-versus-time data did not agree with the nuclear data at late times. For other yields and depths, maximum column diameter was predicted with Equation 1.35 or 1.36. The predicted  $D_{max}$  and its square root were used to convert the scaled Baker surge radius-time data to the values for the expected burst conditions (Reference 1).

It was assumed that the Wigwam surge was typical for deep nuclear bursts, and rough estimates of the surge dimensions for other yields were made by using the cube root of yield as a linear scale factor.

HE test data shows that the air entrained by the water droplets in the base surge is cooled to the ambient wet-bulb temperature by the evaporation of the droplets (Reference 2). The surge is, therefore, cooler and more humid than the surrounding air and can be detected with temperature-humidity instrumentation. As the surge mixes with the ambient air, its temperature and humidity gradually return to the ambient level. The rapidity of mixing depends on the degree of turbulence in the base surge and the mechanically and thermally induced turbulence of the atmosphere.

In HE tests, the base surges evaporated in relatively short times, ranging from about 6 seconds for shallow 100-pound shots to about 30 seconds for shallow 4,200-pound shots (Reference 1). The surges from deep 300-pound TNT shots were brief in duration and were so tenuous that they often were not measurable on photographs.

The Shot Baker base surge was large enough to lift the ambient air to its condensation level, which caused the formation of new clouds. At the same time, rainfall developed in the surge, and much of the original material was probably removed by this process (Reference 2). The clouds formed by the explosion were visible for over an hour after the shot.

The Wigwam base surge, which was smaller in size and probably less dense, became invisible from the surface about 4 minutes after the shot (Reference 6) as a result of the evaporation of the liquid water droplets, though the radioactivity it carried was detected downwind between H + 13 and H + 22 minutes (Reference 26).

#### 1.5 TEST CONDITIONS

Shot Wahoo was a 9-kt (+1.5 kt, -0.5 kt) device fired at a depth of 500 feet in water about 3,000 feet deep. (The yields used in this report are those considered most accurate as of 6 January 1960 and not necessarily those currently considered as best estimates.) The

detonation occurred south of Eniwetok Atoll at 1330 local time on 16 May 1958 at a position about 3 nautical miles west of Site Glenn (Igurin Island). Shot Umbrella was an 8-kt (+2.5 kt, -1.5 kt) device fired on the bottom of Eniwetok lagoon at a depth of about 150 feet. This detonation occurred at 1115 local time on 9 June 1958 at a position about 2 nautical miles north-northwest of Site Glenn.

Shot Wahoo was in the category of deep bursts (Section 1.4.2). The Wahoo bubble was expected to oscillate once before breaking through the surface. Shot Umbrella was a shallow burst (Section 1.4.3).

The 150-foot depth indicated for Shot Umbrella is nominal; the exact depth at the point of burst was possibly 148 to 149 feet. The bottom surface was irregular, ranging from 134 to 150 feet in depth within 300 feet of the device (Reference 27).

The meteorological and oceanographic conditions reported for the two shots are summarized in Tables 1.1 through 1.3.

TABLE 1.1 SURFACE WEATHER OBSERVATIONS, SHOTS WAHOO AND UMBRELLA

Shots:	Wahoo	Umbrella
Sea level pressure, mb	1,013.1	1,010.8
Air temperature, °F	87.5	88.0
Wet-bulb temperature, °F	77.3	76.0
Dewpoint temperature, °F	73.0	72.0
Relative humidity, percent	63	63
Wind direction, degrees	090	050
Wind speed, knots	15	20
Visibility, miles	10	10
Cumulus clouds:		
Amount	0.3	0.2
Base altitude, feet	2,300	2,000
Top altitude, feet	4,000	4,000

TABLE 1.2 RADIOSONDE AND UPPER WIND DATA, SHOTS WAHOO AND UMBRELLA

Height	Wind Direction	Wind Speed	Pressure	Temperature	Relative Humidity
feet	degrees	knots	mb	°F	percent
Shot Wahoo:					
Surface	090	15	1,013	87.5	63
390	-	-	1,000	79.2	70
1,000	090	19	-	-	-
2,000	090	19	-	-	-
2,953	-	-	913	66.6	94
3,000	090	17	-	-	-
4,000	090	15	-	-	-
4,272	-	-	874	65.3	49
4,967	-	-	851	62.2	-
5,000	0	11	-	-	-
5,010	-	-	850	62.2	71
Shot Umbrella:					
Surface	050	20	1,010	86.0	-
310	-	-	1,000	76.1	-
1,000	050	23	-	-	-
2,000	060	21	-	-	-
2,986	-	-	-	-	-
3,000	070	21	-	-	-
4,000	080	22	-	-	-
4,200	-	-	873	67.6	65
4,940	-	-	850	66.6	36
5,000	080	24	-	-	-
5,118	-	-	845	66.6	29

TABLE 1.3 OCEANOGRAPHIC DATA, SHOTS WAHOO AND UMBRELLA

	Wahoo	Umbrella
Surface water temperature, °F	82.0	82.0
Surface current direction, degrees	302	-
Surface current speed, knots	0.46	-
Surface sound velocity, ft/sec	5,045	5,050
Surface salinity, parts per thousand	34.71	-
Surface density, slugs/ft <sup>3</sup>	1.98	1.98

## Chapter 2

### PHOTOGRAPHIC PLAN

#### 2.1 GUIDING PRINCIPLES

Although all of the visible surface phenomena of an underwater nuclear explosion are of scientific and practical interest, the scope of Project 1.3 was limited by budgetary considerations and it was not possible to measure all of the surface effects with the desired degree of precision. Therefore, it was decided to emphasize the recording of the visible phenomena associated with initial radiation and the spread of radioactive contaminants. Such information is currently of vital importance in the development of naval offensive and defensive tactics. Together with radiological data, it can be used to determine the safe standoff distance for a vessel or aircraft delivering a nuclear weapon; it also provides an estimate of the size of the hazardous area.

In preparation for the two shots, predictions were made concerning the times of appearance, rates of growth, and maximum sizes of the expected surface phenomena. The results of Operation Wigwam (Reference 6) and Shot Baker in Operation Crossroads (Reference 21) were scaled to the conditions of Shots Wahoo and Umbrella, respectively, according to scaling laws established with HE. It was assumed that the fallout and base surge would be carried downwind at the speed of the wind and would be visible up to 30 minutes after each shot. For planning purposes, it was also assumed that during each shot the wind from the surface up to 10,000 feet would be blowing from 75° True at a speed of 15 knots.

Personnel of Project 1.3 prepared and submitted a photographic plan, which included adequate backup cameras so that partial failure would not hamper the analysis, and which also provided extensive downwind coverage with overlapping fields of view. A coordinated technical photographic plan was then prepared by Edgerton, Germeshausen, and Grier, Inc. (EG&G) for Program 9, which had the responsibility for consolidating the requirements of the various interested projects. This was done for the purpose of eliminating duplication and reducing costs and effort.

Camera stations were established at the Eniwetok Proving Ground (EPG) by EC&G. Camera timing was accomplished with 200-cps or 12.5-cps timing dots, clocks, and intervalometers. A radio-transmitted fiducial signal was placed on the high-speed (1,000 frames/sec) camera records to indicate the actual time of detonation.

#### 2.2 CAMERA LOCATIONS, SHOT WAHOO

For Shot Wahoo, surface camera stations were established on Site Glenn (Guam Island), on two vessels (LCU-479 and DD-728), and on a 300-foot tower on Site Elmer (Parry Island). Figure 2.1 shows the locations of these stations in relation to surface zero. Two of these stations, Site Glenn and the LCU-479, were unmanned, while cameras at the other two stations were manually aimed. Camera and lens data and other pertinent data for the surface camera stations are given in Table 2.1. The single camera on Elmer apparently started late and yielded no record.

Camera stations were also located in four aircraft: one RB-50 and three C-54's.

continent camera data for the aircraft camera stations is given in Table 2.2. These cameras were all manually aimed. The RB-50 flew at an altitude of 24,000 feet in a figure-8 pattern over surface zero. The three C-54's flew at average altitudes of 1,500, 8,100, and 10,600 feet. Initially, they flew in circles about surface zero and after 7 to 10 minutes went into racetrack patterns approximately upwind or crosswind of the expected surge drift.

Figures 2.2 through 2.5 show the horizontal flight paths of each aircraft. These figures show surface zero and the horizontal plot reference point (labeled "Center of Radar Plot") as two distinct points. This discrepancy apparently was due to a change in the surface zero coordinates or the use of the wrong coordinates in setting up the radar system. On Figure 2.5, only the portions of the flight path where the cameras were facing the explosion phenomena are shown.

Slant-ranges from surface zero to the C-54's were computed by EG&G from the horizontal flight paths and average altitudes, and are listed in Table 2.3. The altitude of the RB-50, as computed from the radar tracking data (Brush recorder records), is given in Table 2.4. The altitude of the RB-50, computed from photographs when the aircraft was directly over surface zero, using known distances of ships in the target array, was only 0.5 percent lower than that computed from the Brush recorder data at the same time.

Position information for the vessels in the target array was supplied by Program 9 (Table 2.5).

### 2.3 CAMERA LOCATIONS, SHOT UMBRELLA

For Shot Umbrella, surface camera stations were located on Site Glenn, two vessels (LCU-479 and LCU-1123), and on a 300-foot tower on Site Elmer. The locations of these stations in relation to surface zero are shown in Figure 2.6. Except for that on Site Elmer, all surface camera stations were unmanned. The surface camera information is summarized in Table 2.6.

Camera stations were again located in four aircraft, which flew flight paths similar to those on Shot Wahoo. The RB-50 flew at an altitude of 24,000 feet and the C-54's flew at nominal altitudes of 1,500 feet, 9,000 feet, and 10,000 feet. The aircraft cameras were all manually aimed. The photographic data is given in Table 2.7. Horizontal flight paths are shown in Figures 2.7 through 2.10. On Figure 2.9, the times shown were obtained by interpolating between marks placed along the flight path plot by the controller at 1-minute intervals. Normally, these marks were used as only a rough indication of elapsed time along the flight path and as a check on the time marker system. On the plot, however, comparison with the timed photographic records at points along the flight path showed that these marks were more accurate than those supplied by the time marker generator, which apparently was not functioning properly.

Because no Brush recorder records were obtained on this shot, slant ranges for the C-54's were computed from the nominal altitudes and horizontal flight paths by EG&G personnel and are given in Table 2.8. These slant ranges were checked, where possible, against ranges calculated from the timed aerial photographs and were found to agree within  $\pm 1.5$  percent. Radio altimeter readings were recorded by a member of the RB-50 crew and are listed in Table 2.9. Table 2.10 gives the distance and bearing of each vessel in the target array relative to surface zero. These values were obtained by EG&G from a photo mosaic taken about 30 minutes prior to the time of the shot.

### 2.4 ACCURACY OF PHOTOGRAPHIC MEASUREMENTS

Nearly all the analysis of the photographic records was done by EG&G at Boston, Mass. The original data will be published separately by EG&G (Reference 28). Photogrammetric



scales on the records were established by using the distance between camera and subject and the calibrated focal lengths of the lenses. The camera-to-subject distances of surface stations were obtained from photo mosaics and surveys and are accurate to within 1 percent. Lens calibrations were performed at EG&G and are accurate to 0.01 percent.

Measurements were made on the original films at EG&G using a microcomparator and the data were reduced by means of a Burroughs computer. Some measurements were also made with a light table and a Bausch and Lomb hand magnifier.

Some measurements were also made by Project 1.3 personnel. At NOL, measurements were made on duplicate positive prints of the 35-mm records using a Telereadex, manufactured by Telecomputing Corporation, North Hollywood, California. Additional measurements were obtained from tracings made on a modified Recordak microfilm reader and from contact paper prints of the 70-mm records. Moviola film viewers were used at both NOL and EG&G for viewing the 35-mm film and obtaining arrival times. Neither establishment had equipment for viewing the 70-mm films.

As the measurements of surface phenomena involved a certain amount of subjective judgment, spot checks of the work done by EG&G were made by NOL personnel. In addition, EG&G checked some of its measurements for observer error by having more than one person measure the same phenomenon on the same record.

Shrinkage of the original film, which can amount to 0.5 percent, was neglected in the photogrammetric measurements. In addition, an undetermined error was introduced in making the duplicate copies of 35-mm film records used for the measurements at NOL. However, it is doubtful that this source of error was more serious than those introduced by uncertainties in camera distances and poorly or irregularly defined phenomena.

## 2.5 RADAR POSITIONING AND TRACKING OF THE PHOTOGRAPHIC AIRCRAFT

Positioning and tracking of the four photographic aircraft used on Shots Wahoo and Umbrella were carried out by Program 5 personnel. Four M-33 fire control tracking radar systems, which had been modified for positioning and tracking experimental aircraft, were used to control the flight paths and to obtain aircraft position-versus-time data. These modified M-33 radar systems have a range of about 60 miles and are capable of providing position-versus-time data with an accuracy of  $\pm 200$  feet.

On Shots Wahoo and Umbrella, each photographic aircraft was tracked by a separate radar, which was locked on the aircraft to lessen the possibility of shifting targets. (Radar beacons, to prevent such target shifts, were not provided for the aircraft, although they were requested.) The position-versus-time data was recorded in two different forms: as a plot of the horizontal component of the flight path relative to a preselected reference point (in this case, surface zero) and as Brush recorder records (obtained on Shot Wahoo only) of aircraft range, azimuth, and elevation relative to the radar van. The slant range of the aircraft from surface zero, necessary to analyze the photographic records, could be computed from either or both sets of data.

Positioning of the aircraft was accomplished by means of the horizontal flight path plotter. By noting the position of the plotting pen relative to a scaled drawing of the planned flight pattern on the plotting board, the controller for each aircraft could detect and correct, by radio communication, deviations from the planned flight path. Trial runs prior to the tests enabled the controllers and pilots to execute the planned flight paths with considerable precision. Slant ranges to surface zero obtained from the horizontal flight paths, Brush recorder data, and by scaling known distances on the photographic records, all agreed to within  $\pm 1.5$  percent. Angular measurements from the same sources agreed to  $\pm 1^\circ$ . These errors were approximately double on portions of the flight paths where the original plotting scale had been reduced in order to keep the pen on the plotting board. Such portions of the

flight paths are noted on the appropriate figures.

## 2.6 OPERATIONAL AND PHOTOGRAPHIC PROBLEMS

The technical photographic effort was a marginal one, because only limited equipment and manpower were available. However, a considerable amount of useful data was obtained because of two fortunate circumstances: the light cloud cover and the availability of Program 5 radar equipment and personnel.

The aircraft photography was planned on the expectation of more than 50-percent cloud coverage at low levels (2,000 to 4,000 feet); therefore, the possibility existed that only the C-54 flying at a 1,500-foot altitude would obtain complete records. In the event that the plumes penetrated the low cloud layer, the higher C-54's would record plume height-versus-time data at levels above the cloud tops. In addition, the two higher C-54's and the RB-50 would obtain photographs of the surface only when they flew over breaks in the clouds.

Because only scattered clouds were present at low levels on both shots, the three high-altitude aircraft obtained more extensive coverage than was anticipated. This was particularly fortunate, because the surface photography proved to be inadequate for determining the overall movement of the base surge for more than about 2 minutes on Shot Wahoo and 1 minute on Shot Umbrella. It was also fortunate that Program 5's radar equipment and personnel were available at APO for positioning and tracking the photographic aircraft on Shots Wahoo and Umbrella.

On Shot Wahoo, 41 cameras were used, seven of which were color documentaries and had no timing. Two cameras failed to operate and yielded no records; one of these was the important 500 frames/sec Fastax in the RB-50. Timing failed on one record; one camera started late; and the four 70-mm cameras located in the aircraft were not cleared of the fogged leader, which resulted in the loss of the first 1 to 1½ minutes of these records.

On Shot Umbrella, 46 cameras were used, seven of which contained color film and had no timing. Only one camera failed to operate. One record contained no timing; on another record, the timing dots appeared only intermittently along the edge of the film. Two cameras started late. Individual records were also beset by such problems as poor resolution, distortion, erratic camera speed, and shutter malfunction. For example, the images on Films 52263 and 52281, which were to be used for measuring the downwind motion of the base surge, were so distorted that they were not measurable. The reason for this has not been determined.

Probably the greatest photogrammetric problem encountered in the analysis of the Hard-tack data arose in efforts to determine detailed base surge contours. This proved to be impossible with the limited surface photography and the only photographs possibly suitable for this purpose were the 70-mm Maurer records obtained on the aircraft. However, these did not provide continuous coverage of the entire surge clouds, and the distortion of shapes on most of the available prints made it impracticable to attempt to rectify the images by conventional methods. As stated in Sections 3.6 and 4.6, it was decided to measure only the maximum surge diameter as seen from the photographic aircraft because of the effort required to obtain complete contours. A few contours were obtained from the RB-50 records on both shots when the aircraft was directly above the surge.

The contours are of particular importance in the analysis of radiological data. Since a base surge is usually extremely irregular, the time of arrival at a station cannot be obtained accurately without detailed knowledge of its shape. (It would be desirable in future tests to have most of the photographic aircraft, spaced a few minutes apart, fly figure-8 patterns directly above the base surge. With cameras aimed vertically downward, the surge, and also the fallout and foam patch, could be accurately mapped. An aircraft at a safe distance but at a low altitude, such as 1,500 feet, would also be needed to act as a general backup

and provide details not visible from surface camera stations.)

Another photogrammetric problem arose in the analysis of photographic records obtained on floating platforms. On these records, nearly every frame required a correction for camera tilt and horizontal shifting of the optic axis. In some cases, fixed reference points were obscured by the explosion phenomena, and quantitative measurements could not be obtained because the motion of the camera was not known. (Island stations should be utilized to the maximum possible extent in future work of this nature. The data from these fixed stations can be analyzed quickly and can serve as checks on the less accurate results obtained from floating or airborne stations.)

On Operation Hardtack, an ideal site for an island camera station (Site Keith) was passed up on Shot Wahoo in favor of a moored barge, because the barge station could be used again on Shot Umbrella. Although this probably reduced costs in the field, it increased the cost and effort in the analysis.

The color documentaries would have proved more valuable if timing had been provided, since some phenomena were more distinctly seen on these records than on the black-and-white photographs.

It would also be desirable to utilize F-56 cameras at the surface stations. These proved to be invaluable on Operation Wigwag. They are not only useful for measuring relatively slow phenomena, such as the base surge, but, because of their excellent resolution, are helpful in establishing camera distances and positions of target vessels. They are also useful for reestablishing times on interrupted records.

The 70-mm cameras, used in Operation Hardtack are smaller and lighter than the F-56, making them more suitable for use in aircraft. However, the F-56 records are much more readily analyzed.

It should be pointed out that the 70-mm cameras had not been fully tested and evaluated prior to their use in Operation Hardtack. The lack of experience with these cameras probably accounts for the failure of personnel to clear the leader on the four aircraft Mauters used on Shot Wahoo. The shutter malfunction on the RB-50 Mauter on Shot Umbrella and the distortion of phenomena on the surface Hulchers, which were aimed downwind of surface zero, could probably have been avoided if operating personnel had tried these cameras under similar conditions prior to the tests. In addition, the 70-mm records showed evidence of film slippage, a result that greatly reduces the value of the cameras for technical photography.

In general, the best results were obtained with cameras that had a prior history of successful technical use. It is essential that all new techniques and cameras be fully evaluated and tried under field conditions before their employment on any experiment as unique as a nuclear test.

TABLE 2.1 SURFACE CAMERA DATA, SHOT WAHOO

Camera Station	ICGO Film Number	Camera Model	Nominal Frame Rate frames/sec	Calibrated Focal Length mm	Approx. Duration of Record (After SZT)*	Aiming		Timing	Remarks
						Horizontal	Vertical		
						deg/min	deg/min	cps	
Site Glenn Station 940 N 20.589 f E 79.659 (18,151 feet and 80° 17' T from SZ)	51337	16-mm EHS	1.350	152.22	0.05	0.00	+0:55	200	No timing
	51338	35-mm Mitchell	100	160.5	1.00	R3:00	-3:50	200	
	51339	35-mm Traid	24	21.78	4.05	0.00	-7:20	12.5	
	51340	35-mm B&H	2 1/2	54.62	30.00	R16:00	+10:20	12.5	Camera aimed at reef
	51341	70-mm Hulcher	3 1/2	78.17	2.00	0.00	+14:00	1	
	51342	70-mm Hulcher	1 1/2	47.12	30.00	L21:00	+21:45	1	
	51343	16-mm GSAP	64	69.1	0.30	0.00	+2:30	Noise	Kodachrome
	51344	35-mm Mitchell	100	216.7	0.55	0.00	+1:45	200	Tilting erratic
	51345	35-mm Mitchell	59	(520)	1.70	R5:37	+0:25	12.5	Camera aimed at EC-2
	51346	K-17 (8" x 9")	1/2	151.7	1.50	-	-	1	
LCU-479 Station 941 N 51.147 f E 56.860 (22,160 feet and 348° T from SZ)	51328	16-mm Faa-ax	1.575	50.85	3.65	0.00	0.00	200	
	51329	35-mm Mitchell	100	50.37	2.45	0.00	+4:50	200	
	51330	21-mm Traid	24	21.93	4.05	0.00	+10:20	12.5	
	51331	35-mm B&H	2 1/2	25.91	26.30	L6:15	+10:20	12.5	
	51332	70-mm Hulcher	3 1/2	149.81	2.00	0.00	+6:00	1	
	51333	70-mm Hulcher	1 1/2	39.15	33.00	R27:00	+27:45	1	
	51334	16-mm GSAP	16	(25)	2.00	0.00	+5:55	Noise	Kodachrome
	51335	35-mm Mitchell	100	152.4	1.00	0.00	+2:25	200	No record
	51336	70-mm Hulcher	3 1/2	(500)	1.00	L6:15	0.00	1	Aimed at LC-2; poor resolution
	51372	35-mm Mitchell	100	152.5	1.00	Manually aimed	Manually aimed	200	Poor focus in frames
N 17.500 f E 70.150 (14,600 feet and 154° T from SZ) Warner Tower SR 409 1511 L 54.195 f E 137.065 Z ~ 300 feet (75,002 feet and 71° T from SZ)	51373	35-mm Eclair	24	32.87	4.30	Manually aimed	Manually aimed	Clock	9: to 14)
	51374	70-mm Cloud	1/4	(105)	20.05	Manually aimed	Manually aimed	Clock	Overexposed
	51375	16-mm GSAP	32	(50)	1.00	Manually aimed	Manually aimed	Poor	Kodachrome
	51412	70-mm Cloud	1/4	(315)	-	Manually aimed	Manually aimed	-	No record
	51413	70-mm Cloud	1/4	(315)	-	Manually aimed	Manually aimed	-	No record
	51414	70-mm Cloud	1/4	(315)	-	Manually aimed	Manually aimed	-	No record
	51415	70-mm Cloud	1/4	(315)	-	Manually aimed	Manually aimed	-	No record
	51416	70-mm Cloud	1/4	(315)	-	Manually aimed	Manually aimed	-	No record
	51417	70-mm Cloud	1/4	(315)	-	Manually aimed	Manually aimed	-	No record
	51418	70-mm Cloud	1/4	(315)	-	Manually aimed	Manually aimed	-	No record

\* surface Zero time (SZT) is the time of appearance of stable surface effects. † Holmes and Narver coordinates. ‡ Nominal frame rate, reset.  
 (1) Servo-drive. ‡ Parentheses indicate nominal focal length.

TABLE 2.2 AIRCRAFT CAMERA DATA, SHOT WAHOO

Camera Station	EG&G Film Number	Camera Model	Nominal Frame Rate frames/sec	Calibrated Focal Length mm	Approx. Duration of Record (after SZT) * min & sec	Timing	Remarks
RD-50	51392	16-mm F-11	500	100.8	-	200	No record
Station 944.01	51393	35-mm Mitchell	100	75.17	1:25	200	
24,000-foot altitude	51394	35-mm F-11	48	19.00	1:50	12.5	Possible discontinuity in record. 42 feet from Frame 0
Over surface zero	51395	70-mm Maurer	1/6	38.25	25:00	1	Record started ~ 1 min 40 sec late
	51396	16-mm GSAP	16	(9.5) 1	2:00	None	Kodachrome
C-54	51384	35-mm Mitchell	100	152.6	1:00	200	
Station 944.02	51385	35-mm Eclair	24	16.9	1:00	Clock	
1,500-foot altitude	51386	70-mm Maurer	1/6	36.33	25:00	1	Record started ~ 1 min 40 sec late
~ 25,000-foot slant range	51387	16-mm GSAP	64	(50)	2:00	None	Kodachrome
C-54	51380	35-mm Mitchell	100	99.16	0:55	200	
Station 944.03	51381	35-mm Eclair	24	18.9	4:00	Clock	Phenomena were distorted
10,000-foot altitude	51382	70-mm Maurer	1/6	38.47	24:00	1	Record started ~ 1 min late
~ 25,000-foot slant range	51383	16-mm GSAP	16	(9.5)	2:00	None	Kodachrome
C-54	51376	35-mm Mitchell	100	99.62	1:00	200	
Station 944.04	51377	35-mm Eclair	24	13.9	4:00	Clock	
8,100-foot altitude	51378	70-mm Maurer	1/6	36.35	22:00	1	Record started ~ 1 min 30 sec late
~ 25,000-foot slant range	51379	16-mm GSAP	16	(9.5)	2:00	None	Kodachrome

\* Surface Zero Time (SZT) is the time of appearance of visible surface effects. † Nominal frame rate preset on intervalometer ‡ Nominal focal lengths are given in parentheses.

TABLE 2.3 SLANT RANGES OF C-54's, SHOT WAHOO

Time sec	Slant Range feet	Time sec	Slant Range feet	Time sec	Slant Range feet	Time sec	Slant Range feet
1,500 feet:							
20	19,620	100	23,280	20	23,200	135	24,400
30	19,910	110	23,630	25	23,290	160	24,170
40	20,220	120	24,080	30	23,380	165	24,070
50	20,570	130	24,250	35	24,090	170	23,200
60	20,980	140	24,250	60	24,220	175	23,200
70	21,570	150	24,230	65	24,410	180	23,000
80	22,000	160	24,210	70	24,670	185	22,900
90	22,670			75	24,810	190	22,760
8,100 feet:							
20	22,280	260	21,340	10,000 feet:			
25	22,540	265	21,270	20	23,200	135	24,400
30	22,720	270	21,210	25	23,290	160	24,170
35	22,900	275	21,150	30	23,380	165	24,070
40	23,120	280	21,050	35	24,090	170	23,200
45	23,340	285	20,900	60	24,220	175	23,200
50	23,530	290	20,870	65	24,410	180	23,000
55	23,610	295	20,790	70	24,670	185	22,900
60	24,050	300	20,720	75	24,810	190	22,760
65	24,260	305	20,710	100	25,300	200	22,770
70	24,510	310	20,710	105	25,360	205	22,790
75	24,590	315	20,710	110	25,400	210	22,800
80	24,630	320	20,720	115	25,600	215	22,850
85	24,620	325	20,740	120	25,620	220	22,970
90	24,620	330	20,730	125	25,630	225	22,970
95	24,420	335	20,700	130	25,630	230	21,150
100	24,180	340	20,670	135	25,530	235	22,810
105	23,940	345	20,670	140	25,540	240	22,860
110	23,940	350	20,670	145	25,160	245	21,860
115	21,470	355	20,690	150	25,340	250	21,360
120	21,470	360	20,690	155	25,260	255	21,360
125	21,400	365	21,140	160	25,100	260	21,360
130	21,380	370	21,140	165	24,930	265	21,360
135	21,380	375	21,140	170	24,720	270	21,360
140	21,380	380	21,140	175	24,510	275	21,360
145	21,380	385	21,140	180	24,300	280	21,360
150	21,380	390	21,140	185	24,090	285	21,360
155	21,380	395	21,140	190	23,880	290	21,360
160	21,380	400	21,140	195	23,670	295	21,360
165	21,380	405	21,140	200	23,460	300	21,360
170	21,380	410	21,140	205	23,250	305	21,360
175	21,380	415	21,140	210	23,040	310	21,360
180	21,380	420	21,140	215	22,830	315	21,360
185	21,380	425	21,140	220	22,620	320	21,360
190	21,380	430	21,140	225	22,410	325	21,360
195	21,380	435	21,140	230	22,200	330	21,360
200	21,380	440	21,140	235	22,000	335	21,360
205	21,380	445	21,140	240	21,800	340	21,360
210	21,380	450	21,140	245	21,600	345	21,360
215	21,380	455	21,140	250	21,400	350	21,360
220	21,380	460	21,140	255	21,200	355	21,360
225	21,380	465	21,140	260	21,000	360	21,360
230	21,380	470	21,140	265	20,800	365	21,360
235	21,380	475	21,140	270	20,600	370	21,360
240	21,380	480	21,140	275	20,400	375	21,360
245	21,380	485	21,140	280	20,200	380	21,360
250	21,380	490	21,140	285	20,000	385	21,360
255	21,380	495	21,140	290	19,800	390	21,360
260	21,380	500	21,140	295	19,600	395	21,360
265	21,380	505	21,140	300	19,400	400	21,360
270	21,380	510	21,140	305	19,200	405	21,360
275	21,380	515	21,140	310	19,000	410	21,360
280	21,380	520	21,140	315	18,800	415	21,360
285	21,380	525	21,140	320	18,600	420	21,360
290	21,380	530	21,140	325	18,400	425	21,360
295	21,380	535	21,140	330	18,200	430	21,360
300	21,380	540	21,140	335	18,000	435	21,360
305	21,380	545	21,140	340	17,800	440	21,360
310	21,380	550	21,140	345	17,600	445	21,360
315	21,380	555	21,140	350	17,400	450	21,360
320	21,380	560	21,140	355	17,200	455	21,360
325	21,380	565	21,140	360	17,000	460	21,360
330	21,380	570	21,140	365	16,800	465	21,360
335	21,380	575	21,140	370	16,600	470	21,360
340	21,380	580	21,140	375	16,400	475	21,360
345	21,380	585	21,140	380	16,200	480	21,360
350	21,380	590	21,140	385	16,000	485	21,360
355	21,380	595	21,140	390	15,800	490	21,360
360	21,380	600	21,140	395	15,600	495	21,360
365	21,380	605	21,140	400	15,400	500	21,360
370	21,380	610	21,140	405	15,200	505	21,360
375	21,380	615	21,140	410	15,000	510	21,360
380	21,380	620	21,140	415	14,800	515	21,360
385	21,380	625	21,140	420	14,600	520	21,360
390	21,380	630	21,140	425	14,400	525	21,360
395	21,380	635	21,140	430	14,200	530	21,360
400	21,380	640	21,140	435	14,000	535	21,360
405	21,380	645	21,140	440	13,800	540	21,360
410	21,380	650	21,140	445	13,600	545	21,360
415	21,380	655	21,140	450	13,400	550	21,360
420	21,380	660	21,140	455	13,200	555	21,360
425	21,380	665	21,140	460	13,000	560	21,360
430	21,380	670	21,140	465	12,800	565	21,360
435	21,380	675	21,140	470	12,600	570	21,360
440	21,380	680	21,140	475	12,400	575	21,360
445	21,380	685	21,140	480	12,200	580	21,360
450	21,380	690	21,140	485	12,000	585	21,360
455	21,380	695	21,140	490	11,800	590	21,360
460	21,380	700	21,140	495	11,600	595	21,360
465	21,380	705	21,140	500	11,400	600	21,360
470	21,380	710	21,140	505	11,200	605	21,360
475	21,380	715	21,140	510	11,000	610	21,360
480	21,380	720	21,140	515	10,800	615	21,360
485	21,380	725	21,140	520	10,600	620	21,360
490	21,380	730	21,140	525	10,400	625	21,360
495	21,380	735	21,140	530	10,200	630	21,360
500	21,380	740	21,140	535	10,000	635	21,360
505	21,380	745	21,140	540	9,800	640	21,360
510	21,380	750	21,140	545	9,600	645	21,360
515	21,380	755	21,140	550	9,400	650	21,360
520	21,380	760	21,140	555	9,200	655	21,360
525	21,380	765	21,140	560	9,000	660	21,360
530	21,380	770	21,140	565	8,800	665	21,360
535	21,380	775	21,140	570	8,600	670	21,360
540	21,380	780	21,140	575	8,400	675	21,360
545	21,380	785	21,140	580	8,200	680	21,360
550	21,380	790	21,140	585	8,000	685	21,360
555	21,380	795	21,140	590	7,800	690	21,360
560	21,380	800	21,140	595	7,600	695	21,360
565	21,380	805	21,140	600	7,400	700	21,360
570	21,380	810	21,140	605	7,200	705	21,360
575	21,380	815	21,140	610	7,000	710	21,360
580	21,380	820	21,140	615	6,800	715	21,360
585	21,380	825	21,140	620	6,600	720	21,360
590	21,380	830	21,140	625	6,400	725	21,360
595	21,380	835	21,140	630	6,200	730	21,360
600	21,380	840	21,140	635	6,000	735	21,360
605	21,380	845	21,140	640	5,800	740	21,360
610	21,380	850	21,140	645	5,600	745	21,360
615	21,380	855	21,140	650	5,400	750	21,360
620	21,380	860	21,140	655	5,200	755	21,360
625	21,380	865	21,140	660	5,000	760	21,360
630	21,380	870	21,140	665	4,800	765	21,360
635	21,380	875	21,140	670	4,600	770	21,360
640	21,380	880	21,140	675	4,400	775	21,360
645	21,380	885	21,140	680	4,200	780	21,360
650	21,380	890	21,140	685	4,000	785	21,360
655	21,380	895	21,140	690	3,800	790	21,360
660	21,380	900	21,140	695	3,600	795	21,360
665	21,380	905	21,140	700	3,400	800	21,360
670	21,380	910	21,140	705	3,200	805	21,360
675	21,380	915	21,140	710	3,000	810	21,360
680	21,380	920	21,140	715	2,800	815	21,360
685	21,380	925	21,140	720	2,600	820	21,360
690	21,380	930	21,140	725	2,400	825	21,360
695	21,380	935	21,140	730	2,200	830	21,360
700	21,380	940	21,140	735	2,000	835	21,360
705	21,380	945	21,140	740	1,800	840	21,360
710	21,380	950	21,140	745	1,600	845	21,360
715	21,380	955	21,140	750	1,400	850	21,360

TABLE 2.1 ALTITUDE OF RB-50, SHOT WAHOO

Time is referenced from radio zero time. Altitudes were computed from Brush recorder data.

Time min and sec	Altitude feet	Time min and sec	Altitude feet	Time min and sec	Altitude feet
Zero					
Time	24,250	7:20	24,050	15:40	23,950
0:10	24,070	7:40	24,150	16:00	23,920
0:20	24,030	8:00	23,840	16:20	23,830
0:30	24,160	8:20	23,980	16:40	23,340
0:40	24,170	8:40	23,840	17:00	24,060
0:50	24,180	9:00	23,750	17:20	23,940
1:00	23,980	9:20	23,820	17:40	23,990
1:20	24,060	9:40	23,650	18:00	24,200
1:40	23,810	10:00	23,800	18:20	23,980
2:00	23,850	10:20	23,880	18:40	24,150
2:20	24,210	10:40	24,030	19:00	24,010
2:40	23,940	11:00	23,750	19:20	24,060
3:00	23,930	11:20	23,930	19:40	23,980
3:20	24,440	11:40	24,150	20:00	23,860
3:40	24,490	12:00	24,170		
4:00	24,410	12:20	24,130		
4:20	24,440	12:40	24,290		
4:40	23,730	13:00	24,060		
5:00	23,850	13:20	24,230		
5:20	24,020	13:40	24,120		
5:40	24,075	14:00	24,060		
6:00	24,080	14:20	24,060		
6:20	23,970	14:40	24,080		
6:40	23,980	15:00	24,030		
7:00	24,150	15:20	24,120		

TABLE 2.5 TARGET ARRAY, SHOT WAHOO

Vessel	Distance from Surface Zero *	Bearing from Surface Zero	Heading
	feet		
FC-2	2,346	25° 5'	208° 30'
DD-474	2,915	245° 4'	249° 30'
DD-592	4,833	250° 45'	329° 00'
DD-593	6,687	245° 56'	242° 00'
YC-1	3,413	31° 38'	-
YC-2	1,915	29° 58'	-
Zero Buoy	674	244° 01'	-
YC-4	2,014	251° 15'	-
YC-5	4,337	251° 01'	-
YC-6	6,250	248° 52'	-
YC-7	7,843	247° 39'	-
YC-8	10,106	218° 02'	-
YC-9	9,893	219° 52'	-

\* Distance is measured from the Zero Buoy to the amidships centerline of each vessel.

CONFIDENTIAL

TABLE 2.6 SURFACE CAMERA DATA, SHOT UMBRELLA

Camera Station	EC&G Film Number	Camera Model	Nominal Frame Rate frames/sec	Calibrated Focal Length mm	Approx. Duration of Record (after ZT)* min sec	Shaking		Timing Remarks
						Horizontal deg/min	Vertical deg/min	
Site Glenn Station 940	52258	16-mm EHS	1/60	101.8	0.02	0.00	0.00	200
	52259	35-mm Mitchell	1/60	51.75	0.40	123.45	0.00	200
N 30.370 f	52260	35-mm Traud	2 1/2	18.62	4.15	0.00	19.43	12.5
E 79.370	52261	35-mm B&H	2 1/2	34.52	32.00	143.35	10.15	12.5
(12,093 feet and	52262	70-mm Hulcher	2 1/2	79.17	2.00	0.00	14.14	1
162-16' T from SZ)	52263	70-mm Hulcher	1/4	39.33	30.00	127.00	27.35	1
	52264	16-mm GSAP	6 1/2	(63) f	0.70	0.30	1.50	None
	52265	35-mm Mitchell	100	216.7	0.72	0.00	1.51	200
	52266	K-17 (9" x 9")	1 1/2	5.97"	-	113.00	21.00	Clock
	52267	K-17 (9" x 9")	1 1/2	11.96"	-	11.00	17.00	1
	52268	35-mm Mitchell	4 1/2	(500)	1.34	0.00	0.10	12.5
LCU 1123	52270	35-mm Eclair	24	32.67	4.05	0.00	8.00	Clock
Station 940.02	52271	70-mm Cloud	1 1/4	(105)	10.00	0.00	10.00	Clock
N 41.208 f	52272	16-mm GSAP	16	(23)	2.66	0.00	3.25	None
E 96.147	52273	35-mm Mitchell	100	74.65	1.10	0.00	2.00	200
(20,173 feet and	52274	K-17 (9" x 9")	1 1/2	13.03"	-	6.00	20.00	Clock
92-39' T from SZ)	52275	K-17 (9" x 9")	1 1/2	24.45"	-	110.30	10.30	Clock
LCU 479	52276	16-mm Farax	1/200	101.4	-	0.00	1.20	200
Station 947	52277	35-mm Mitchell	100	50.27	1.00	87.40	3.25	200
N 25.383 f	52278	35-mm Traud	24	70.11	1.25	0.00	7.20	12.5
E 3.547	52279	35-mm B&H	16	23.81	3.50	0.00	14.20	12.5
(44,002 feet and	52280	70-mm Hulcher	2 1/2	149.61	2.00	0.00	1.25	1
347' T from SZ)	52281	70-mm Hulcher	1 1/2	28.15	10.00	827.00	27.10	1
	52282	16-mm GSAP	6 1/2	(63)	0.70	0.30	1.51	None
	52283	35-mm Mitchell	100	152.4	1.00	-	2.25	200
	52284	70-mm Mitchell	14	(500)	1.00	0.00	5.50	1
	52285	K-17 (9" x 9")	1 1/2	12.08"	0.05	16.00	20.00	Clock
	52286	K-17 (9" x 9")	1 1/2	24.45"	-	0.00	10.30	Clock
Elmer Tower	52289	70-mm Cloud	1 1/4	(205)	30.40	22.00	aimed	Clock
Station 1611								Portions of film are exposed

\* for a Zero Time (SZT) is the time of appearance of visible surface effects. † Holmes and Narver coordinates. ‡ Nominal frame rate present on inter-camera for  
 † Parentheses indicate nominal focal length.



TABLE 2.7 AIRCRAFT CAMERA DATA, SHOT UMBRELLA

All cameras were manually aimed.

Camera Station	EGG Film Number	Camera Model	Nominal Frame Rate, frames/sec	Calibrated Focal Length, mm	Approx. Duration of Rec- ording, min:sec	Tinting	Remarks
RB-56 Station 944.01 24,000-foot altitude over surface zero	52253 52254 52255 52256 52257	16-mm Fastax 35-mm Mitchell 35-mm Trid 70-mm Maurer 16-mm GSAP	1,000 100 43 1/6 13	100.8 75.17 19.00 38.28 (8.5)†	2:10 2:00 1:50 23:00 2:00	200 200 12.5 † None	Record blurred but usable Kodachrome
C-54 Station 944.02 1,500-foot altitude ~25,000-foot slant range	52249 52250 52251 52252	35-mm Mitchell 35-mm Eclair 70-mm Maurer 16-mm GSAP	100 21 1/6 61	152.6 18.9 38.33 (50)	1:50 4:10 30:00 0:30	200 Clock † None	Kodachrome
C-54 Station 944.03 10,000-foot altitude ~25,000-foot slant range	52245 52246 52247 52248	35-mm Mitchell 35-mm Eclair 70-mm Maurer 16-mm GSAP	100 21 1/6 13	99.16 18.9 38.47 (8.5)	0:36 4:10 25:00 2:00	200 Clock † None	Kodachrome
C-54 Station 911.01 9,000-foot altitude ~25,000-foot slant range	52241 52242 52243 52244	35-mm Mitchell 35-mm Eclair 70-mm Maurer 16-mm GSAP	100 21 1/6 13	99.62 18.9 38.35 (8.5)	1:00 4:55 30:00 2:00	200 Clock † None	Kodachrome

\* Surface Zero Time (SZT) is the time of appearance of visible surface effects. † Nominal frame rate preset on intervalometer.

‡ Parentheses indicate nominal focal length.

CONFIDENTIAL

TABLE 2: A SLANT RANGES OF C-51\* SHOT PISTOLLLA

[illegible]

TABLE 2.9 RADIO ALTIMETER READINGS FOR R3-30,  
SHOT UMBRELLA

Time is referenced from radio zero time.

Time	Altitude	Time	Altitude
min and sec	feet	min and sec	feet
-1:00	24,400	5:30	23,425
-50	24,500	6:00	23,525
-40	24,550	6:30	23,525
-30	24,350	7:00	23,475
-20	24,225	7:30	23,375
-10	24,375	8:00	23,450
Zero Time	24,400	8:30	23,525
:10	24,450	9:00	23,475
:20	24,425	9:30	23,200
:30	24,550	10:00	23,400
:40	24,275	11:00	23,500
:50	24,200	11:30	23,475
1:00	24,100	12:00	23,550
1:10	23,775	12:30	23,375
1:20	23,775	13:00	23,575
1:30	23,775	13:30	23,600
1:40	23,700	14:00	23,675
1:50	23,725	14:30	23,650
2:00	23,875	15:00	23,625
2:15	23,950	15:30	23,450
2:30	23,925	16:00	23,625
2:45	23,850	16:30	23,525
3:00	23,850	17:00	23,525
3:15	23,875	17:30	23,575
3:30	23,300	18:00	23,425
3:45	23,100	18:30	23,325
4:00	23,200	19:00	23,375
4:30	23,275	19:30	23,325
5:00	23,475	20:00	23,325

TABLE 2.10 TARGET ARRAY, SHOT UMBRELLA

Vessel	Distance from Surface Zero *	Bearing from Surface Zero	Heading
	feet		
EC-2	1,680	158° 01'	80° 56'
YFNB-12	2,340	68° 05'	70° 08'
DD-474	1,892	245° 41'	255° 06'
DD-592	2,969	248° 27'	334° 23'
DD-593	7,823	249° 12'	242° 37'
17-barge	1,669	262° 32'	-
21-barge	2,070	237° 57'	-
45-skiff	4,739	248° 40'	-
55-barge	5,704	251° 19'	-
65-skiff	7,015	250° 20'	-
100-skiff	10,056	248° 28'	-
Skiff	11,468	246° 37'	-

\* Distance is measured from the Zero Buoy to the amidships centerline of each vessel.

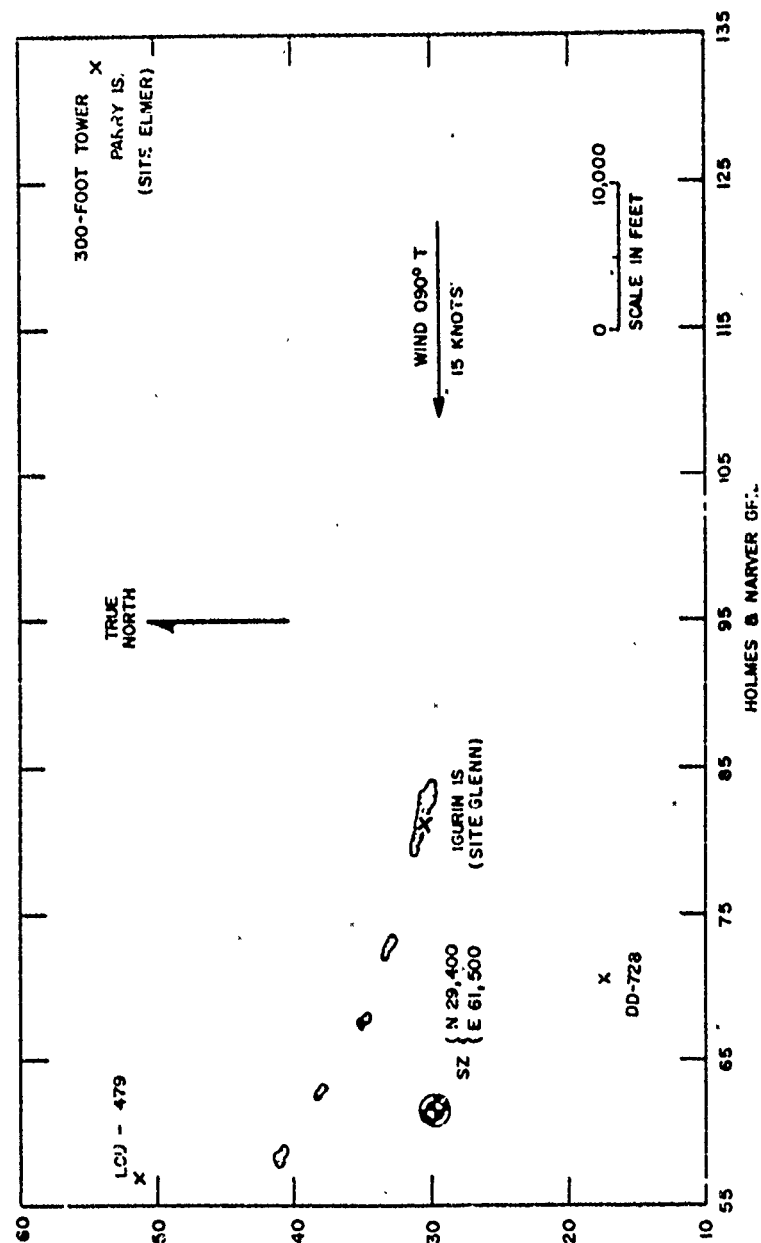


Figure 2.1 Locations of surface camera stations, Shot Wahoo.

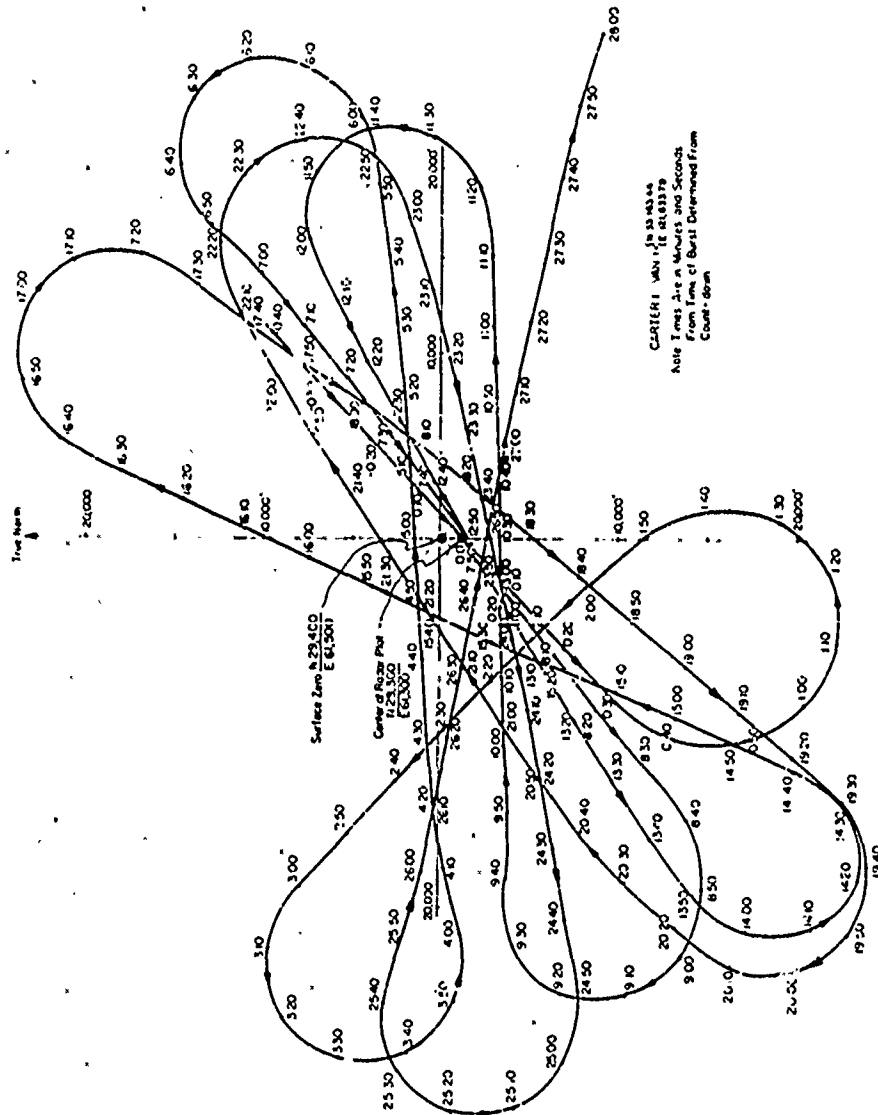
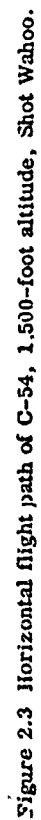


Figure 2.2 Horizontal flight path of RB-50, 24,000-foot altitude, Shot Wahoo.









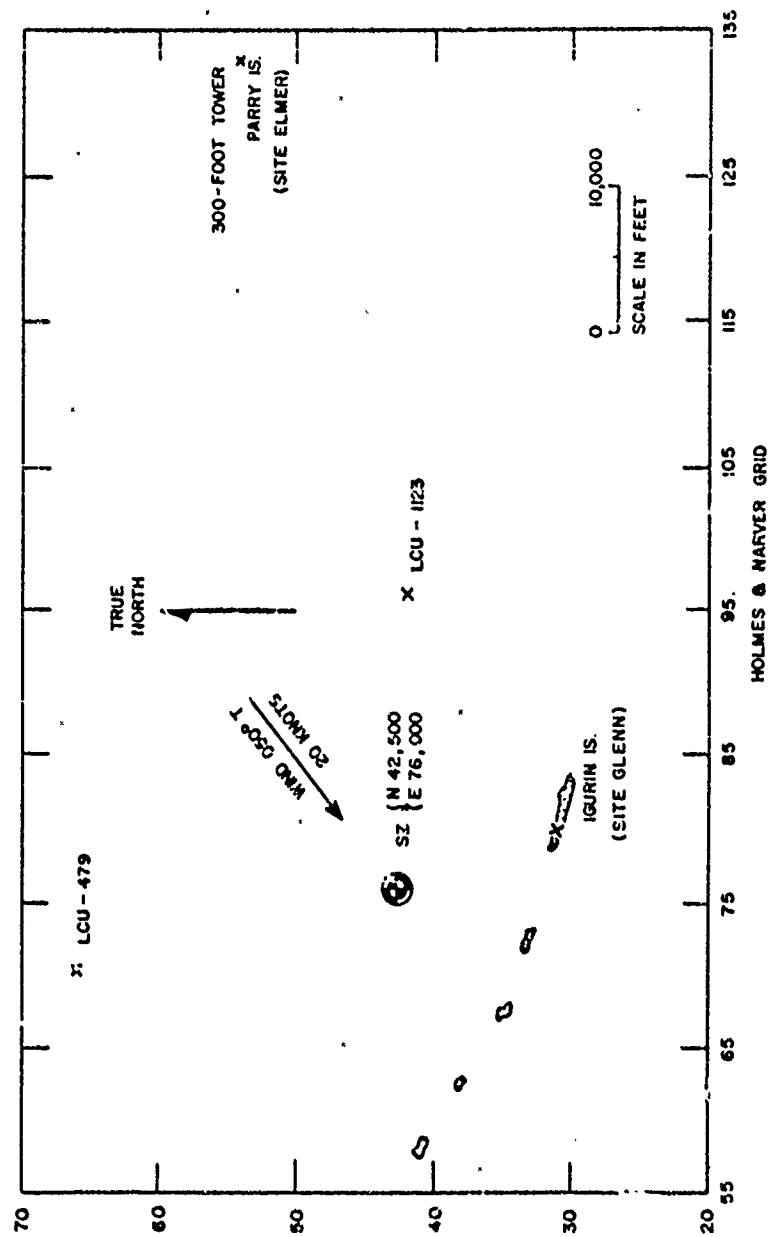


Figure 2.6 Locations of surface camera stations, Shot Umbrella.









## Chapter 3

### RESULTS OF PHOTOGRAPHY, SHOT WAHOO

#### 3.1 SPREAD OF UNDERWATER SHOCK WAVES

Viewed from the air; the first visible evidence of Shot Wahoo was an expanding disk on the surface of the water, which indicated the arrival of the primary underwater shock wave (EG&G Films 51393, 51394, and 51376). The edge of the disk was darker than the surrounding water, and the expanding darkened zone was undoubtedly the direct shock wave slick, similar to those observed in Operation Wigwam and in HE tests. This slick was visible from the air until about 1 second after surface zero time (SZT) when it had reached a radius of 5,500 feet. (SZT is the time of appearance of visible surface effects.) It could be seen for longer times from the surface camera stations.

The spread of an underwater shock wave along the water surface may be described by the following expression (Reference 2):

$$r^2 = 2cUt + U^2t^2 \quad (3.1)$$

Where:  $r$  = distance from surface zero along the water surface, feet

$c$  = depth of burst, feet

$U$  = shock-front propagation velocity, ft/sec

$t$  = time, seconds

The calculated spread, based on a constant shock-front velocity of 5,050 ft/sec, is shown in Figure 3.1. Slick measurements obtained from the RB-50 and the 10,000-foot C-54 are also shown in the figure and range from 1 to 3 percent higher than the calculated values. This difference is not significant and is probably due primarily to measurement difficulties. If a burst occurs at an unknown depth, Equation 3.1 can be used to obtain an approximate depth, providing slick measurements are available.

An expanding white circular patch was observed within the area of the slick. This patch grew at a slower rate than the slick and reached a maximum radius of about 2,500 feet at 0.6 second after SZT. Except possibly for a few milliseconds during which the whiteness may have been due to underwater cavitation, the white region seen from the air may be considered to be the primary spray dome that results from the reflection of the direct shock wave at the surface.

The dome contained a central area of spray, which was entirely white in appearance from surface zero to a radius of about 1,000 feet. The density of spray then gradually decreased at increasing distances and, near the outer edges, the whiteness appeared only on the crests of waves. The periphery of the dome was jagged and poorly defined. Radius-versus-time measurements of the central spray area and outer edge of the spray dome, as seen from the air, are presented in Figure 3.2.

At about 0.58 second after SZT, slicks were observed to move rapidly inward and outward from a radius of about 2,100 feet. Following the passage of the slicks, a white annulus of spray was formed surrounding the primary dome. This spray was produced by a pressure

pulse that was generated by the collapse of the cavitated region beneath the surface. Measurements of the cavitation pulse spray ring are included in Figure 3.2. The sudden expansion of the central dense spray region at 0.52 second is not understood. It is possible that this was not associated with the cavitation pulse.

Additional slicks and patches of spray were visible in the neighborhood of the EC-2 and YC-2 about 1 second after SZT (Reference 29). One distinct slick was seen, followed by several faint brief slick passages. The leading slick expanded unsymmetrically, growing more rapidly in the offshore direction than onshore. This slick was produced by the bottom-reflected shock wave; its lack of symmetry can be attributed to the slope of the bottom. It could be seen from the air to a radial distance of about 10,000 feet from surface zero but was visible to at least 13,800 feet on the surface camera records from the Observer Ship at a distance of 14,800 feet from surface zero. Measurements obtained from aerial photographs are presented in Figure 3.3. The less distinct slicks were due to other reflections, possibly from strata beneath the ocean floor. The patches of spray resulted from focusing of the bottom-reflected shock by irregularities in the bottom and indicated local regions of high pressure (Reference 6).

Two late slicks were observed on documentary color film taken on Site Henry by Lookout Mountain Laboratory (LM Film MOF 41). Although no timed technical photography was available from this location, a comparison with cameras on Site Glenn indicates that these slicks appeared at about 29.7 and 30.7 seconds after SZT. Two slicks arrived at the EC-2 at about 30.6 and 31.9 seconds (Reference 19). Because the Site Henry measurements are not precise, these observations probably represent the same slicks. They present visual evidence of the passage of the second and third of four pressure pulses reported by Project 1.1 as arriving at the EC-2 between 28 and 33 seconds after the burst. These pulse times indicate a possible relation to the closure and upwelling of the cavity at surface zero after the primary plumes collapsed (Section 3.5). However, the relative arrival time of each pressure pulse at the EC-2 gages shows a possible origin at a great depth. The available information is probably not adequate to identify the origin of these pulses.

The appearance of the slicks, spray dome, and spray ring is shown in Figure 3.4. These views were selected from aerial photographs.

A fiducial mark indicating the time of detonation was recorded on the Eastman high-speed record at Site Glenn (EG&G Film 51337). This gave an interval of 77.9 msec between the detonation and the first visible surface effects. The agreement with a calculated value of 78 msec (Reference 17) is excellent.

A direct shock wave arrival time of 434 msec at the EC-2 was obtained by extrapolating Project 1.1 values obtained from a gage string extending from 300 to 1,875 feet in depth (Reference 19). The slick arrival time obtained from photographic measurements was 372 msec after SZT, giving a difference of 62 msec between detonation and the first visible surface effects. Since the Project 1.1 value was obtained 2,300 feet from surface zero and was, therefore, affected by environmental conditions, 78 msec is considered to be the most reliable value of the interval between detonation and the first visible surface effects.

### 3.2 AIR SHOCK WAVES AND CONDENSATION CLOUDS

The first air shock wave, which resulted from the transmittal of a small fraction of the energy of the primary underwater shock wave across the air-water boundary, was visible on a few surface camera records (EG&G Films 51337, 51338, 51344, and 51372). It could be seen for about 35 msec, disappearing first in the center at about 26 msec and finally at the edges near the water surface. A peak pressure of 0.19 psi was recorded on the EC-2 from this air shock wave 480 msec after the burst (Reference 29).

The passage of positive and negative pressure pulses through the cumulus cloud layer,

which extended from 2,300 to 4,000 feet in altitude, was evidenced by momentary shrinking and enlargement of the clouds. This effect was most clearly seen on aircraft color film (EG&G Films 51379, 51383, and 51396). The compression in the positive pulses produced an adiabatic warming of the air at the cloud level and a temporary evaporation of the cloud droplets. The negative, or rarefaction, pulses led to adiabatic cooling and a consequent growth of the droplets.

Cloud effects were noticed at three distinct times. These are indicated in Table 3.1 in conjunction with air shock wave data. The times of observation of cloud changes depended on the distance of the cloud from surface zero. Since these distances were not known, and it is not likely that the same clouds were observed from different camera stations, the observed times of cloud effects have little quantitative significance, though it is possible to identify the origin of most cloud changes with confidence.

No condensation cloud was observed on Shot Wahoo, other than the enlargement of the existing clouds. The greatest reported pressure drop at the EC-2 was 0.18 psi. This was evidently not large enough to lower the ambient temperature to the dewpoint and bring about condensation in the relatively dry air near sea level.

### 3.3 SPRAY DOME

The Wahoo spray dome was visible from surface camera stations within 1 to 2 msec after the appearance of the air shock wave. Initially, the spray dome had a smooth outline, which became more irregular as the dome developed. When it had reached its maximum height of 840 feet at 7 seconds, individual jets of spray could be clearly seen. Rising above the main dome was a central cluster of gray jets produced by rising objects. The behavior of these objects will be discussed in Section 3.4. The appearance of the spray dome at various times is shown in Figure 3.5.

As the dome reached its full size before plume effects occurred, it was possible to study its behavior thoroughly. Height-versus-time measurements were made at surface zero and at 100-foot intervals to the right and left of surface zero on photographic records obtained at the three surface camera stations. These measurements extended to a dome radius of 1,600 feet but showed considerable scatter at radii beyond 1,000 feet. At 1,600 feet, the maximum measured height of spray was 23 feet. This result is consistent with the aircraft data, which indicates continuous spray to a radius of 1,000 feet and patches of spray extending as far as 2,500 feet. Smoothed spray dome height-versus-time curves obtained at Station 940 (Site Glenn) are shown in Figure 3.6 as examples of the type of data obtained.

Equations of the form of Equation 1.9 were fitted to the data at early times in an effort to determine the initial dome velocities and spray retardation factors. To simplify the process, Equation 1.9 was used in linear form, as follows:

$$\frac{h}{t} = V_0 - ft \quad (3.2)$$

When spray dome values are plotted in the form of height/time versus time, they can be fitted with a straight line whose zero intercept is equal to  $V_0$  and whose slope is equal to  $f$ , providing the height-versus-time curve is parabolic (Reference 16). In reality, the height/time values are erratic at early times because of a strong sensitivity to slight timing errors, the difficulty in measuring height at early times, and the possible occurrence of high instability (Reference 14) velocities for brief intervals.

In practice, a straight line was drawn through the reduced height data points over a time interval as close to zero time as possible. This time interval generally started between



1 and 2 seconds after SZT. At later times, the points also deviated from a straight line in some cases because of variations in the retardation factor. An example of this treatment of the Igurin Island data is shown in Figure 3.7.

Values of the initial spray dome velocity at 100-foot intervals along the water surface were used to calculate the peak pressures in the underwater shock wave on the basis of Equation 1.4. (It was assumed here that  $P_b$  is negligible. This subject is discussed in Section 7.1.) These values and their means and standard deviations are listed in Table 3.2. Since the Wahoo shock wave had practically reached acoustic velocity when it reached the surface (Reference 17), Equation 1.4 was reduced to

$$P_0 = \frac{34.7 V_0}{\cos \delta} \quad (3.3)$$

for this purpose.

Figure 3.8 shows the mean values of the computed peak pressures together with peak pressures predicted for yields of 8.5, 9, and 10.5 kt by Equation 1.10 for pressures less than 2,500 psi and by Reference 17 for pressures above 3,000 psi. Peak pressures obtained by Project 1.1 are also shown.

The peak pressures calculated from initial spray dome velocities were consistently higher than those predicted by theory for a 9-kt yield, varying from 1 to 7 percent between radii of 100 and 400 feet (slant ranges of 510 to 640 feet) to about 11 to 14 percent for radii of 500 to 700 feet (slant ranges of 707 to 860 feet). An effort was made to measure the smoothed spray dome at surface zero. No consistent values could be obtained, however, because of the influence of the high central jet. At radii beyond 700 feet, the data became increasingly unreliable because of measurement difficulties.

The pressures measured by Project 1.1 were lower than indicated by theory, in some cases, probably because of the effect of refraction at the distance of the gages. Since the gages were at depths ranging from 90 to 1,875 feet below the EC-2, the presentation in Figure 3.8 tends to simplify the actual results. The spray dome data indicates that the peak pressures at the surface were not influenced by refraction, at least to a slant range of 860 feet.

Table 3.2 includes estimated values of the Wahoo yield, based on a comparison of the calculated underwater peak pressures with theoretical values. These results, and the presentation in Figure 3.8, indicate that spray dome velocities are useful for estimating the yield of an underwater nuclear burst, providing that the depth of detonation is known. Although the calculated yields average 11 kt between slant ranges of 510 and 860 feet, the four close-in values average 10.2 kt and tend to lie within the range of 8.5 to 10.5 kt indicated for the radiochemical yield. It therefore appears that yields calculated on the basis of spray dome velocities are reasonable when they are obtained relatively close to surface zero, for bursts similar to Shot Wahoo. It is to be expected that, in general, yields calculated in this manner on field tests will be high because of surface roughness.

Values of the Wahoo spray dome retardation coefficient  $f$  were selected from dome height-versus-time data in which  $f$  remained constant until the spray stopped rising. These values are shown as a function of distance from surface zero in Figure 3.9. The scatter is greater than the scatter shown by calculated peak pressures, though the trend toward decreasing retardation with increasing distance from the center of the dome is clear. This indicates the presence of larger drops near the edge of the dome. The variation of  $f$  with distance for Shot Wahoo can be expressed as

$$f = 30 e^{-0.001 r} \quad (3.4)$$

The retardation factor,  $f$ , must reach a lower limit of  $16 \text{ ft/sec}^2$  due to the invariable effect of gravity. Consequently, Equation 3.4 is valid only to a spray dome radius of 630 feet for Shot Wahoo.

### 3.4 TRAJECTORIES OF OBJECTS NEAR SURFACE ZERO

Several narrow jets of spray rose above the Wahoo dome, trailing behind objects that were propelled into the air when the underwater shock wave arrived at the surface. With the exception of one black jet, which was located in a cluster of jets near surface zero, all the spray jets were white.

Figure 3.10 shows the region in the vicinity of surface zero prior to the time of detonation. The Zero Buoy was a modified Navy telephone buoy about 10 feet in diameter. A steel Army Transportation Corps barge section, which was 22 feet in length and 9 feet 10 inches wide, was moored approximately 30 feet from the Zero Buoy and contained Project 1.11 electronic equipment (Reference 20). A modified LCM, which housed the firing racks, was moored 674 feet from the Zero Buoy at a  $244^\circ$  bearing. Small plastic buoys and a steel net buoy supported the instrument cable that led to the device. The steel buoy was possibly 300 feet from surface zero; the plastic buoys were at greater distances.

A white jet rose at the position of the LCM, and smaller jets could be seen along the instrument cable, probably caused by the rising plastic buoys. The black jet in the cluster near surface zero appeared to originate at the Project 1.11 barge.

The trajectories of three of the rising objects were measured on Films 5237 (Site Glenn) and 51328 (LCU-479). Two of these objects are indicated on Figure 3.11. The trajectories for all three are shown in Figure 3.12 and, in each case, a parabolic equation of the same form employed for the spray dome heights was fitted to the data. In all cases, the lateral component of motion was negligible.

The photographic resolution was not adequate for the identification of the objects, and the estimates of the points of origin are probably not accurate because of measurement difficulties. Object No. 1 appeared to come from a position between 63 and 110 feet from surface zero between bearings of  $239^\circ$  and  $247^\circ$ . It had an initial velocity of about  $500 \text{ ft/sec}$ .

Object No. 2 seemed to originate 100 feet from surface zero at a bearing of  $259^\circ$ . It had an initial velocity of about  $440 \text{ ft/sec}$ .

Object No. 3 possibly originated 50 feet from surface zero between bearings of  $168^\circ$  and  $190^\circ$ . Since these determinations are very approximate, it seems likely that this object came from the Project 1.11 barge. It had a greater initial velocity (about  $577 \text{ ft/sec}$ ) than the others but decelerated at a much greater rate (Figure 3.12). Its lateral motion was about  $65 \text{ ft/sec}$  toward the southwest.

As seen from Site Glenn, the jets near the center of the Wahoo dome appeared to merge into a broad gray jet that was about 100 feet wide at 1.1 seconds after SZT. In general, the objects in the cluster appeared to originate in a region between the zero buoy and a position on the array somewhat beyond the Project 1.11 barge. The breakup of the barge probably discolored the water in this area. In addition, the possibility that some of the contents of the expanding Wahoo bubble were ejected along the firing and instrument cable should be considered.

Assuming a 9-kt yield, Reference 17 indicates that the peak pressure at surface zero was 10,400 psi. On this basis, Equation 3.3 predicts an initial spray dome velocity of  $300 \text{ ft/sec}$ . The initial velocities of the rising objects that could be measured ranged between 1.5 and 1.9 times the expected spray dome velocity.

Similar results have been observed in HE tests in which buoys or drums located at surface zero rose rapidly above the spray dome. It is believed that no study of this phenomenon has been made, but additional information could be extracted from the Wahoo

records if such a study is undertaken. Useful data could also be obtained from the photographic records of Operation Wigwam.

### 3.5 PLUMES

The primary plumes became visible at the edge of the spray dome about 6 seconds after SZT. By 7 seconds, a rapidly expanding mass of radial plumes was clearly visible, and at 8 seconds, the plumes had expanded well beyond the limits of the dome. The assemblage of plumes had an overall spherical shape at early times. At about 12 seconds, the vertical growth had begun to decelerate rapidly while the lateral plumes continued to spread at an almost constant rate.

From then on, the shape of the mass of plumes flattened, and the plumes gradually spilled over and broke up into spray. A maximum overall plume height of about 1,600 feet was reached at 15 seconds after SZT. By 20 seconds, the lateral plumes had collapsed on the surface, attaining a maximum diameter of about 3,800 feet. The descent of the top surface of the plumes was measurable for about 27 seconds. Starting at 20 seconds, much of the spray which formed in the plumes spread out radially along the surface as a base surge.

The development and collapse of the primary plumes is illustrated in Figure 3.13. A secondary plume formation (Figure 3.17) became visible above the top of the collapsing primary plumes about 21 seconds after SZT. This formation reached a maximum height of about 950 feet approximately 31 seconds after SZT. The secondary plumes were not symmetrical. Their entire shape could not be determined, as only a portion of the top was visible.

The vertical rise and fall of the top of the Wahoo primary and secondary plumes is shown in Figure 3.14, as measured from the three surface camera stations. Each curve represents an average of data obtained at one position. Maximum and average heights are shown for the primary plumes, since a relatively small spike rose above the bulk of the plumes. The maximum values were obtained at the top of this spike. The scatter in the original data was about  $\pm 6$  percent for the primary plumes and  $\pm 7$  percent for the secondary plumes, due to such factors as the varying degrees of resolution obtained with different cameras, the differences in appearance from different stations, small asymmetries, the judgment required in the determination of average heights, movement of plumes outside of the plane of measurement, and the like. Such scatter is normal in measurements of this type of phenomenon. Because of this uncertainty, the maximum heights of the primary and secondary plumes on Wahoo should be considered to be 1,700 feet and 1,000 feet, respectively, for aircraft safety considerations (Chapter 8).

Figure 3.15 shows the right and left radial growth of the plumes, measured to the extremities, as seen from the three surface camera stations. The curves show a high degree of symmetry and indicate an almost linear rate of lateral growth from about 8 to 20 seconds, at which time the plumes reached the surface. The average maximum collapsed plume radius was about 1,850 feet, with an extreme measured value of 1,910 feet.

The behavior of the nuclear explosion bubble and the subsequent formation of the plumes is not well understood. Equations 1.25 and 1.26 indicate that the bubble reached a maximum radius of 384 feet at 2.64 seconds after the burst. If the bubble expanded uniformly without migrating upward, and pushed the surrounding water outward radially, the surface above the burst would be lifted to a height about 87 feet above its original level. However, at the time this possibly occurred, the spray in the dome had reached a height of 640 feet and bulk motion of the surface was hidden.

The calculated bubble period was 5.28 seconds. Equation 1.24 indicates a migration to the second bubble maximum of 1,050 feet. This implies a migration of about 525 feet up to

the time of the first bubble minimum, which would place the bubble center near the original surface at this time. Other equations predict a migration of 915 feet (Reference 9) and 916 feet (Reference 19) during the first bubble pulsation. Although the latter equations were based on HE data and all have doubtful validity for a burst near the surface, the general result that the Wahoo bubble migrated to a position above the original surface is supported by the absence of a bubble pulse on the underwater pressure records (Reference 19).

When individual plumes were traced back in an effort to determine their origin, a region above the original surface was indicated. In addition, Figures 3.14 and 3.15 show that the vertical and lateral components of plume velocities were almost constant and about the same magnitude between about 8 and 10 seconds after SZT. The average velocity of expansion of the plumes during this interval was about 160 ft/sec. At later times, the vertical rate of rise was reduced by gravity and atmospheric drag while the lateral growth remained almost linear, with some small retardation by atmospheric drag.

The initial uniform plume growth is also shown by the profiles in Figure 3.16. The shape at 8, 9, and 10 seconds indicates that a hemispherical mound of water was probably pushed above the surface by the bubble. The rapid expansion of the bubble within the mound then threw this water out in all directions with the same initial velocity. Since the surface had been roughened by the form, in the spray dome, the deceleration of the surface led to the rapid formation of the large plumes that were observed. This concept is supported by photographs of small-charge phenomena in a vacuum tank with firing conditions scaled approximately to shot Wahoo (Reference 30). A rough extrapolation shows that the mound of water, which developed into the plumes, possibly had an initial diameter of about 1,000 feet.

The expansion of the bubble and outbreak of the primary plumes generated an air shock wave. This was detected at the EC-2 at 7.25 seconds and reached a peak value of 0.215 psi at 8.27 seconds. This may be interpreted as being a measurement of the first bubble pulse. An extrapolation to surface zero indicates a first bubble period between 5 and 6 seconds.

It seems likely that considerable mixing of water and fission products took place at the time of bubble collapse, because the base surge that developed from the plumes was highly contaminated (Reference 31).

The secondary plumes are believed to have been caused by the oscillation of the water surface at surface zero following the collapse of the primary plumes. Aerial photographs showed that the collapse of the secondary plume formation contributed material to the interior of the surge cloud (EG&G Film 51395).

### 3.6 VISIBLE BASE SURGE

As the plumes traveled outward and downward through the air they broke up into spray, just as the stream from a firehose breaks up into small droplets if it follows a long trajectory. When the plumes collapsed on the surface, the larger drops and coherent masses of water probably dropped back into the ocean. However, the fine drops that had been formed in the plumes remained airborne because of their small mass and continued to flow outward radially, as a result of the momentum imparted by the expanding plumes. Since the drops entrain air as they move outward, the suspension of drops in air behaves similarly to a dense homogeneous fluid. The aerosol that spreads out from the plumes is called a base surge.

The development of the Wahoo base surge from the primary plumes was a fairly continuous process, but the surge could be distinguished from the collapsing plumes by 20 seconds after SZT. The surge was roughly circular, but was not smooth in outline and showed several lobes. As it spread outward along the surface the lobes separated and the surge became increasingly irregular and tenuous in appearance. It was also noted that the surge

was retarded when it moved over a target vessel, which contributed to the distortion. Although patches of the surge cloud were faintly visible from the air for possibly 25 minutes, it was not possible to make reliable measurements of the surge boundaries beyond about 3.5 minutes. The appearance of the base surge at various times is shown in Figures 3.17, 3.18, and 3.25.

Right and left radii of the surge in relation to surface zero were measured from the three surface camera stations. The average curves from each station are presented in Figure 3.19. The original measurements showed a scatter of  $\pm 4$  percent. Since the surge was distorted and was transported away from surface zero by the wind, the curves in Figure 3.19 do not show exact dimensions beyond about 30 seconds after SZT. However, Station 940 (Site Glenn) was almost exactly upwind and Station 941 (LCU-479) was approximately crosswind from the burst. Consequently, the Station 941 radius-versus-time curves in Figure 3.19, with bearings of  $78^\circ$  and  $258^\circ$ , are approximately along the upwind and downwind axes of the surge. The Station 940 curves are on the crosswind axis of the surge.

The curves shown in Figure 3.19 represent the extremities of the base surge. They do not necessarily indicate the correct time of surge arrival at a ship or instrument station. This could be obtained by studying the photographs or by preparing detailed contour plots of the surge as it traveled downwind. The latter proved to be impossible to obtain for this report; however, partial contours of the base surge and foam patch were obtained from RD-50 Film 51395 when the aircraft was almost directly above the burst. These are shown in Figures 3.20 through 3.22 for the period from 110 through 270 seconds.

In many places, the contours in Figures 3.20 through 3.22 are incomplete because of obscuration by the natural clouds in the area. However, the irregular nature of the base surge is clearly shown. In particular, a pronounced retardation of the surge on a line downwind of the DD-474 can be observed. As a result, two large lobes extended downwind from surface zero on bearings of about  $245^\circ$  and  $285^\circ$ . Because these lobes blocked the view, the  $258^\circ$  curve in Figure 3.19 is not accurate beyond about 50 seconds after SZT. Lobes in the upwind direction obscured the view of the  $78^\circ$  axis, so that this curve also is unreliable.

Measurements of the upwind, crosswind, and downwind extent of the Wahoo base surge were made on the contours in Figures 3.20 through 3.22. Since the surface and 1,000-foot winds were from the east, upwind and downwind measurements were made perpendicular to a north-south line through surface zero, and crosswind measurements were made perpendicular to an east-west line through surface zero. All measurements were made to the surge extremities; therefore, the contours show the maximum extent of the surge. At 118 seconds and later, the surge extended farther to the south than to the north; thus, the geometrical center lay about 200 feet south of the east-west axis between 118 and 149 seconds.

In addition, measurements of both the drift of the geometrical center of the surge and the surge diameter perpendicular to the optic axis were made from the photographic aircraft until 204 seconds after SZT. Since the center of the surge was difficult to locate, particularly at late times, the drift measurements showed considerable scatter and in some cases, were not usable. The data from Films 51378 and 51282 appeared to be reasonable, however, and indicated a drift to the west of about 15 knots between about 70 and 170 seconds, with the center of the surge approximately 400 feet south of the east-west axis. At later times, an apparent drift to the southwest was shown. However, this was probably a result of the large lobe extending toward the southwest, as it seems probable that the surge moved bodily in that direction.

Because of the limitations of Figure 3.19, all of the available measurements and combined in Figure 3.23 to obtain the best possible estimate of the downwind, upwind, and crosswind curves for the extremities of the Wahoo base surge. The downwind curve is based mainly

on the contour measurements in Figures 3.20 through 3.22. At times up to 50 seconds, the Station 941 right surge radius measurements are used.

The approximately upwind curve from Station 941 is also shown with the limited upwind contour measurements. The latter are considered to be more reliable at late times than the surface camera data, because the surge was more clearly visible from the air. The crosswind curve in Figure 3.23 from 20 to 105 seconds after SZT was obtained by averaging the left and right radii measured from the Station 940 records (Figure 3.19) and correcting the data for a 12-knot movement away from the cameras. Between 110 and 170 seconds, the crosswind curve is based on contour measurements. From 173 to 240 seconds, the crosswind curve is an extrapolation based on a few contour crosswind measurements south of the east-west axis.

The average surge radius curve shown on Figure 3.23 is based on aircraft measurements to the outer edges of the lobes. These values represent measurements from the center of the base surge. Aircraft measurements that were made between lobes and some that were doubtful because of obscuration by clouds were not used. The distances between the aircraft and the surge were estimated by assuming a constant drift of .5 knots toward the west. The average aircraft-curve is in good agreement with the crosswind data and, for practical purposes, the difference between the average radius and crosswind extent is negligible.

It may be noted that the downwind leading edge moved at an almost constant speed of 21 knots between 110 seconds and the final measurement time of 270 seconds. The downwind curve, between 20 and 240 seconds, can be obtained by adding a 10-knot drift to the crosswind curve. At later times, the crosswind curve leveled off, but the rapid downwind motion continued, probably because of the 18-knot wind speed at altitudes above the surface. It seems likely that the speed of drift increased as the surge cloud increased in height and encountered wind speeds stronger than at the surface. The trailing upwind edge of the surge was difficult to measure. Its motion showed evidence of frictional retardation by the surface.

Figures 3.18 and 3.20 through 3.22 show the toroidal shape of the Wahoo surge. Measurements of the horizontal thickness of the surge were made at some positions in Figures 3.20 through 3.22. The thickness proved to be highly variable. For example, it ranged between 2,000 and 3,000 feet on the 335° axis and between 1,500 and 2,000 feet on the 285° axis.

Figure 3.24 shows the maximum height of the base surge as seen from the surface camera stations. Although the surge appeared about 20 seconds after SZT, the curves start at about 40 seconds because it was not possible to determine realistic surge heights until the surge had moved outward and could be clearly distinguished from the collapsing plumes. The height data from any one station showed scatter as great as 17 percent, due in part to measurement difficulties at late times. When the highest part of the surge became indistinct and evaporated, the measurement was shifted to the next highest lobe. The disagreement between the three curves in Figure 3.24 probably results from the measurement of the highest point, as seen from each camera station. No effort was made to correct these values for distance from the object planes through surface zero. For example, an error as great as 40 percent could have occurred at 110 seconds from this cause.

The curves indicate that the surge top rose rapidly at first, at about an average rate of 15 ft/sec between 45 and 80 seconds. Between 80 and 140 seconds, the height fluctuated between 1,100 and 1,400 feet. The measurements after 140 seconds are unreliable because of the tenuous nature of the surge at these late times. In particular, the rapid decrease in height shown by the Station 941 curve is not believed to be realistic.

### 3.7 FOAM PATCH

After the plumes had subsided, and as the surge cloud dissipated and drifted downwind, a clearly defined, white, roughly circular area was observed at the location of surface zero. This is referred to as the foam patch, and is shown in Figures 3.18 and 3.25. It is believed to result from a strong, probably vortical, circulation caused by the gravity rise of the bubble. Evidently, as was also observed during Wigwam (Reference 6), an upward flow of water occurred in the vicinity of surface zero. This water spread out radially and sank, resulting in an accumulation of foam and debris at the edge of the patch, as illustrated in Figure 3.25. The radial structure of the Wahoo patch and the occurrence of small waves, which appeared to originate at its edge, lend support to this hypothesis (EG&G Film 51395 at about 140 seconds). The whiteness of the patch was due to foam produced by the violent agitation of the water during the explosion.

The foam patch expanded slowly and was measured for about 16 minutes, after which the entire outline was no longer discernible on aerial photographs. However, the north edge was still visible at 25 minutes, when one of the largest photographic records ended (EG&G Film 51395).

Contours of the foam patch up to 4.5 minutes after SZT are included in Figures 3.20 through 3.22 and are shown for later times in Figure 3.26. Measurements of the diameters were made on these contours along six axes. In addition, major diameters were measured on the U-54 photographic records. These measurements are shown in Figure 3.27. Because of the scatter in the data, due at least in part to the fact that the surge cloud partially obscured the foam patch, no attempt was made to draw curves through the data. However, a definite drift of the foam patch in the direction of the surface current is evident in the contours presented in Figure 3.26.

A region of radioactively contaminated water was detected on Shot Wahoo by Project 2.3 (Reference 31). This project had five underwater gamma intensity recorders (UW-GITR's), four of which recorded the passage of the contaminated water. These UW-GITR's were located on conical buoys and had a probe depth of about 6 feet. They were positioned at distances of from 4,100 feet to 8,000 feet from surface zero and recorded arrival times of from 5 to 15 times, which were generally consistent with the spread of the foam patch. It seems reasonable to assume that the region of contaminated water corresponded to the foam patch; however, the measurements are insufficient to resolve this question with certainty.

The motion of two of the ships in the target array was measured on the contours presented in Figures 3.20 through 3.22. The DD-474, which was 2,915 feet from surface zero at a bearing of 249° 30' T prior to the shot, was found to be 3,200 feet from surface zero at 110 seconds and 3,350 feet at 151 seconds. No change in its bearing was found. The UC-2, 2,346 feet from surface zero at a bearing of 29° 13' T prior to the shot, was 2,800 feet from surface zero at 110 seconds and 3,050 feet at 151 seconds. A bearing of about 34° T was measured during this time interval.

TABLE 3.1 COMPARISON OF AIR SHOCK WAVE DATA RECORDED AT EC-2  
WITH OBSERVED SHOCK WAVE EFFECTS ON CLOUDS, SHOT WAHOO

Air Blast Measured By Project 1.2 Time	Pressure psi	Probable Origin of Pulse	Cloud Effects	
			Approximate Time of Observation sec	Approximate Duration sec
0.48	+0.19	Primary shock		
1.10	-0.12	Bottom- reflected	2.8	Shrinking) 1
1.90	+0.17	Zero crossing shock		Enlargement)
2.40	-0.01			Shrinking)
7.25	Zero crossing	Primary plumes	8.1	Shrinking) 4
8.27	+0.22			Enlargement)
10.23	-0.14			Shrinking)
11.16	+0.14			Shrinking)
25.92	+0.070	Second plumes	28.1	Shrinking) 5
27.57	+0.20			Enlargement)
28.75	-0.18			Shrinking)
31.60	0.04			Enlargement)



TABLE 3.2 INITIAL SPRAY GUN VELOCITIES AND COMPUTED YIELDS (MILS) 14800

Distance from Surface Zero	Chart Range, ft	Station	Initial Spray Gun Velocity ft/sec	Peak Pressure, psi	Mean Pressure, psi	Standard Deviation of $P_0$ , psi	Coefficient of Variation of $P_0$ , %	Computed Yield lb	Mean Yield lb	Standard Dev- iation of Yield lb	Coefficient of Variation of Yield, %
ft	ft			psi	psi	psi	psi	lb	lb	lb	lb
0	500	846.01	313	10,900	15,100	3,650	24.2	10.0	21.7	10.2	47.0
0		940	186	16,000				26.7			
0		941	504	17,200				22.5			
100L	510	846.01	290	10,300	10,300	115	1.1	9.4	9.5	0.93	9.8
100R		846.01	175	9,730				8.3			
100L		940	293	10,400				9.7			
100R		940	285	10,300				9.7			
100L		941	311	11,000				9.7			
100R		941	293	10,400				9.7			
200L	519	846.01	268	10,000	10,100	514	5.1	10.7	10.7	1.29	12.1
200R		846.01	277	9,800				10.7			
200L		940	255	9,640				10.7			
200R		940	263	9,830				10.7			
200L		941	277	10,200				10.7			
200R		941	296	11,100				13.2			
300L	583	846.01	238	9,630	9,000	575	6.4	11.9	10.2	1.50	13.7
300R		846.01	217	8,950				11.7			
300L		940	210	8,400				8.9			
300R		940	212	8,400				8.9			
300L		941	239	9,110				10.6			
300R		941	227	8,330				8.6			
400L	640	846.01	193	8,280	8,100	408	5.0	12.0	10.5	1.24	11.8
400R		846.01	170	7,590				8.9			
400L		940	175	7,780				9.4			
400R		940	180	8,000				10.2			
400L		941	193	8,130				10.6			
400R		941	172	8,530				11.9			
500L	707	846.01	155	7,610	7,140	421	5.7	12.8	11.6	1.75	15.1
500R		846.01	130	7,360				11.3			
500L		940	135	7,120				10.4			
500R		940	143	7,020				10.0			
500L		941	149	7,110				11.1			
500R		941	167	8,190				11.5			
600L	781	846.01	128	6,940	6,760	360	6.3	13.2	12.4	2.17	15.9
600R		846.01	118	6,940				13.2			
600L		940	117	6,940				10.4			
600R		940	130	7,960				9.1			
600L		941	125	6,780				12.4			
600R		941	140	7,990				16.2			
700L	850	846.01	108	6,510	5,890	641	11.1	15.0	12.0	2.94	21.1
700R		846.01	100	5,970				13.4			
700L		940	92	5,400				10.6			
700R		940	95	5,670				10.8			
700L		941	94	5,570				10.8			
700R		941	91	5,430				9.8			

\* L and R denote measurements to left and right of surface zero, respectively

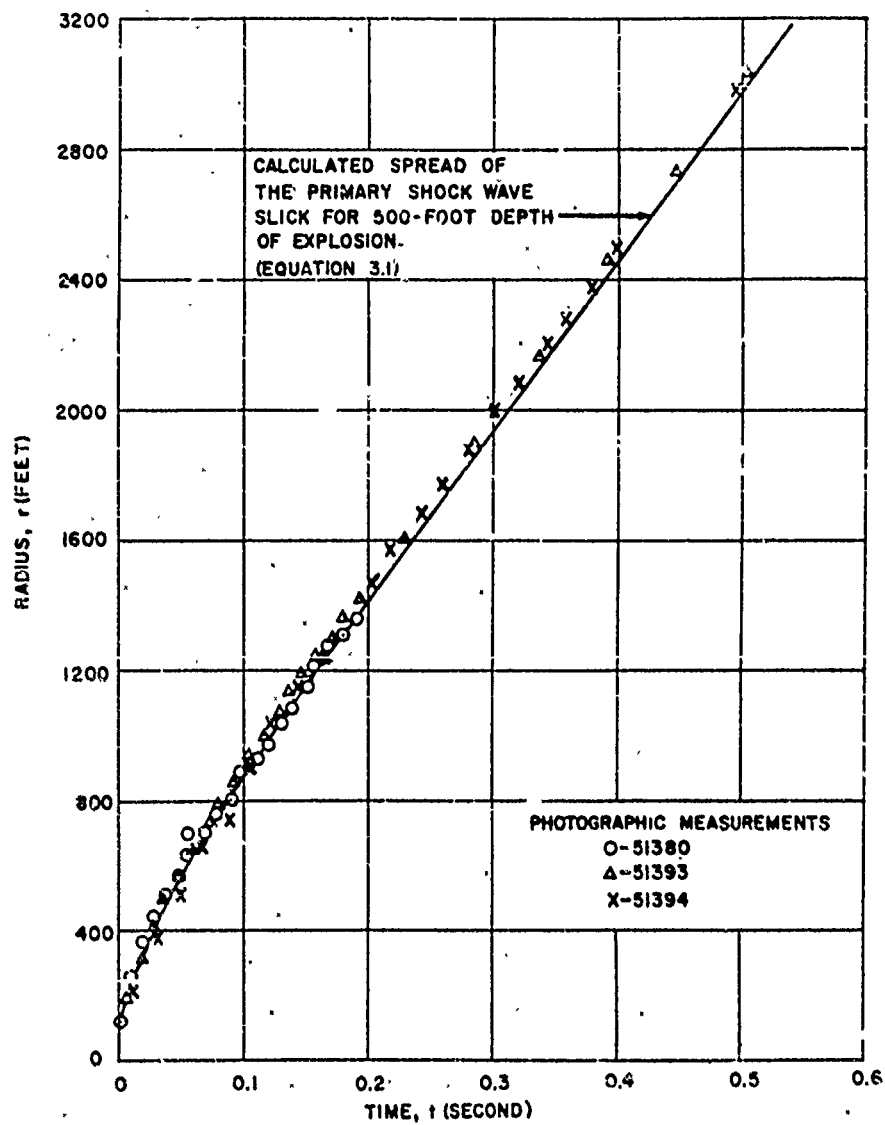


Figure 3.1 Primary shock wave slick., Shot Wahoo.

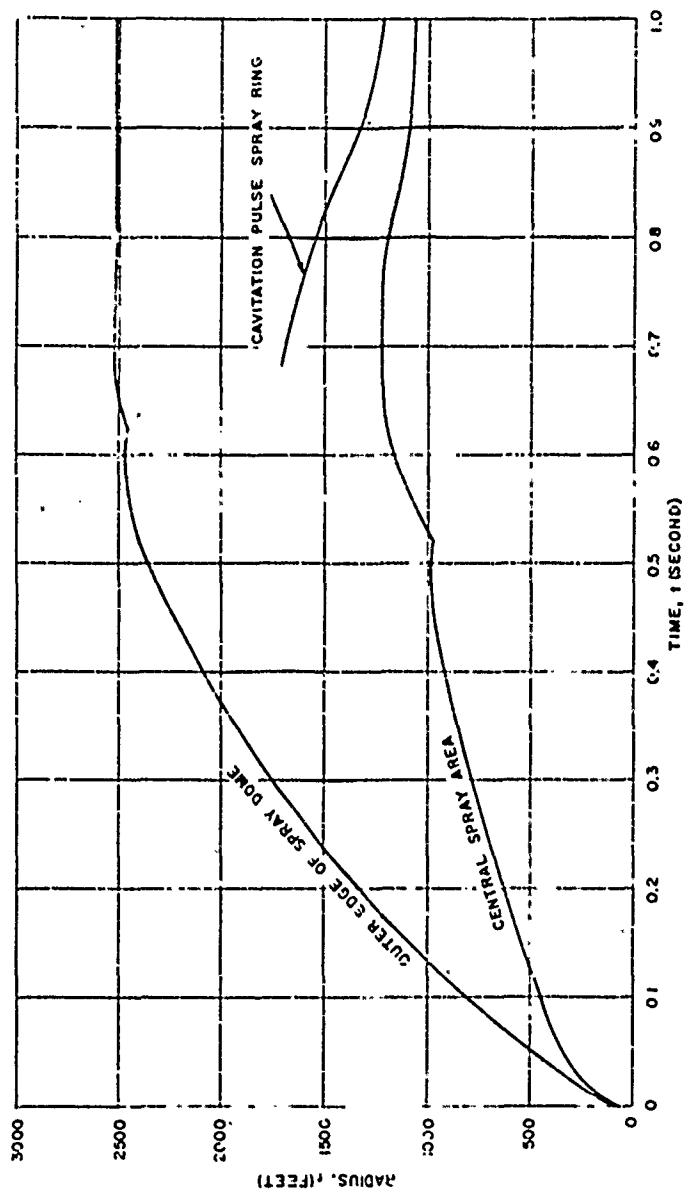


Figure 3.2 Lateral spread of spray dome and cavitation pulse spray ring, SI of Wahoo.

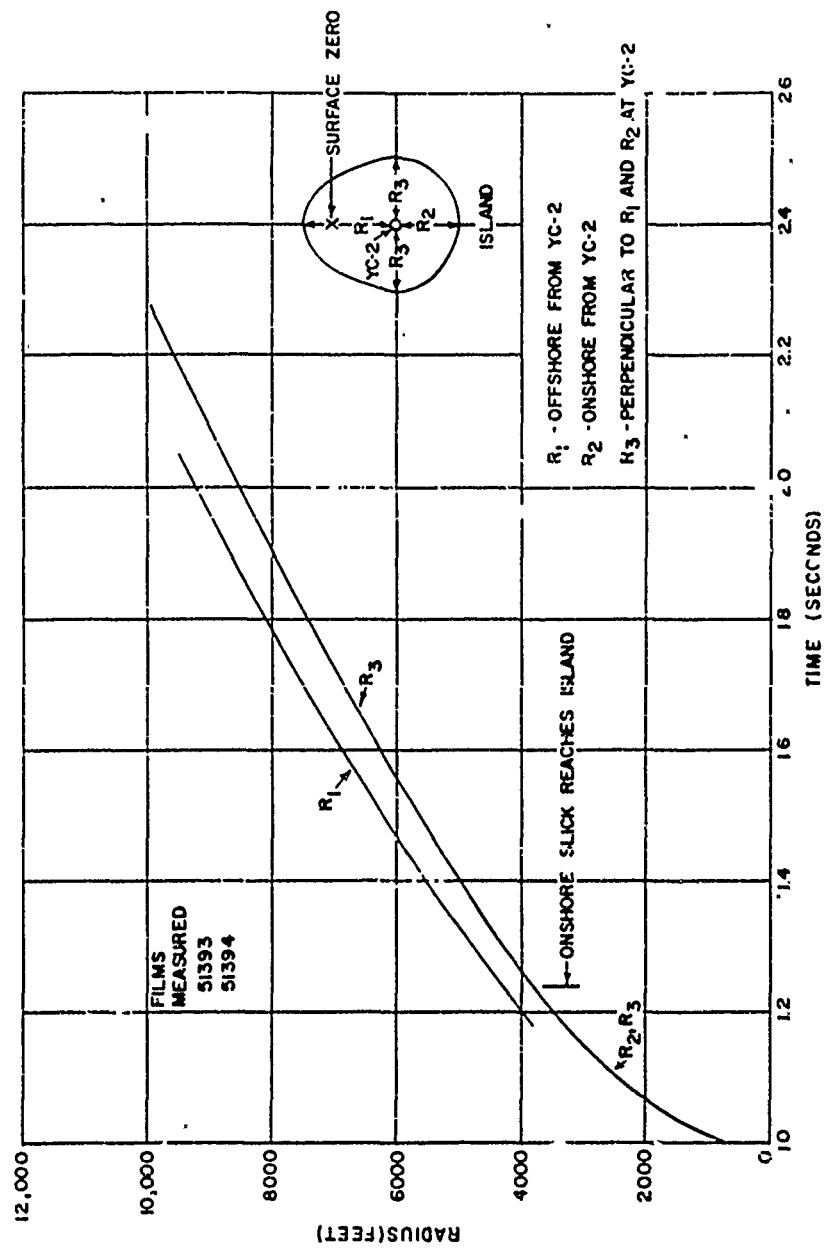
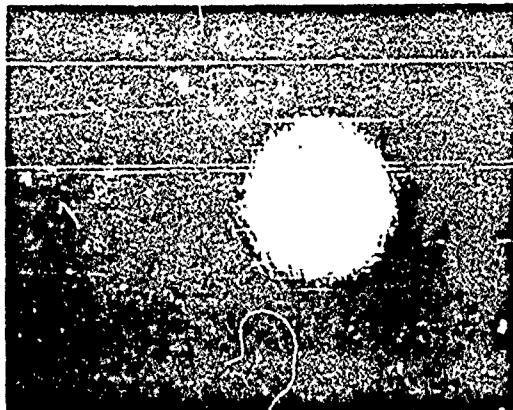
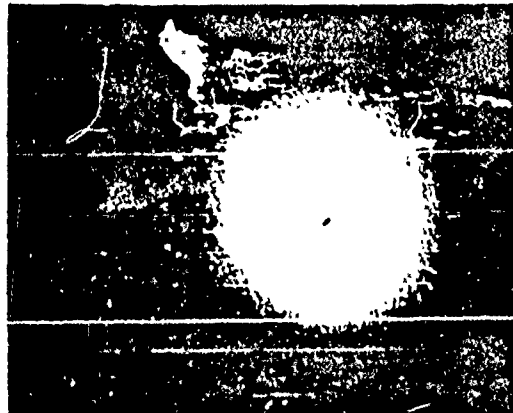


Figure 3.3 Bottom-reflected shock wave: slick, Shot Wahoo.



PRIMARY SHOCK WAVE SLICK  
AND SPRAY DOME  
0.28 SECOND  
FILM NO. 51393

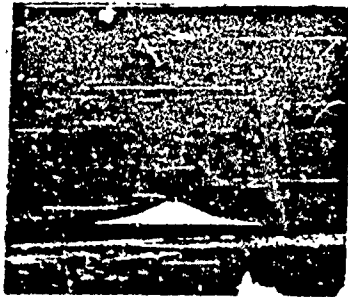


CAVITATION PULSE SLICK  
AND SPRAY RING  
0.73 SECOND  
FILM NO. 51393



BOTTOM-REFLECTED  
SHOCK WAVE SLICK  
1.38 SECONDS  
FILM NO. 51394

Figure 3.4 Aerial views of slicks, spray dome, and cavitation pulse spray ring, Shot Wahoo.



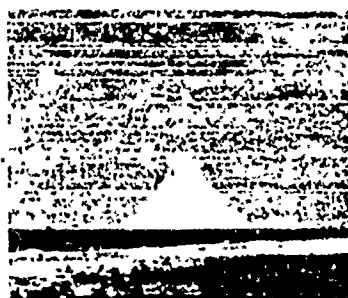
1.7 SECONDS



3.3 SECONDS



5.3 SECONDS



7.0 SECONDS

FILM NO. 51341

Figure 3.5 Spray dome, Shot Wahoo.

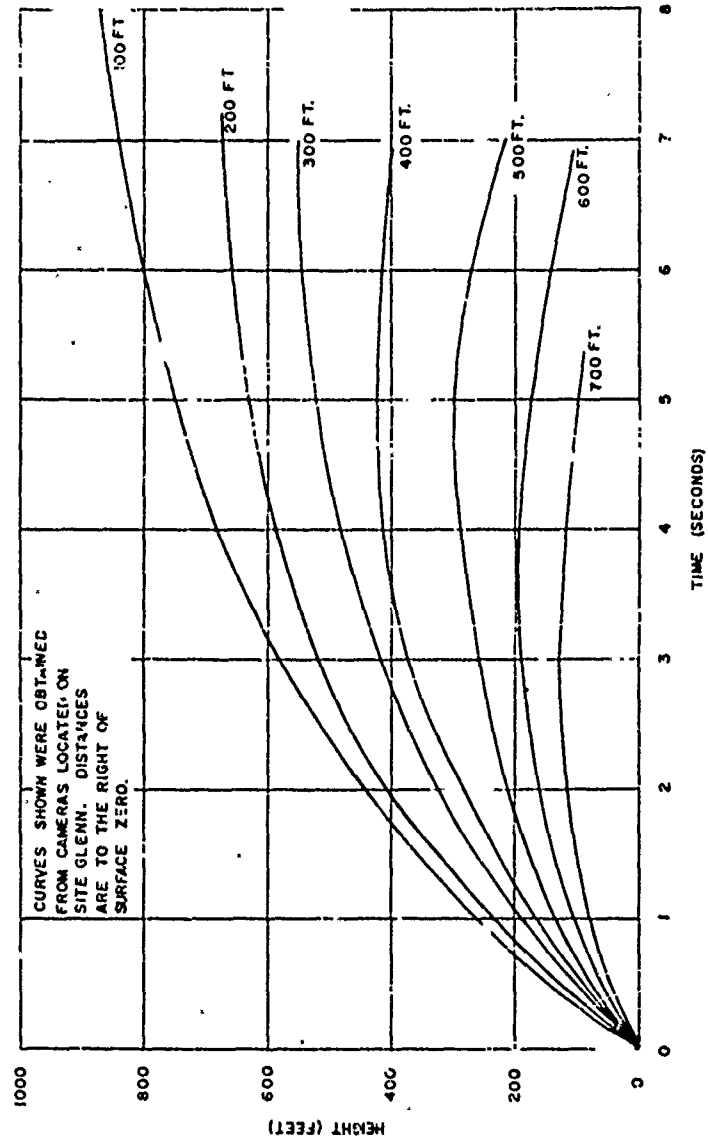


Figure 3.6 Spray dome height versus time curves, Shot Wahoo.

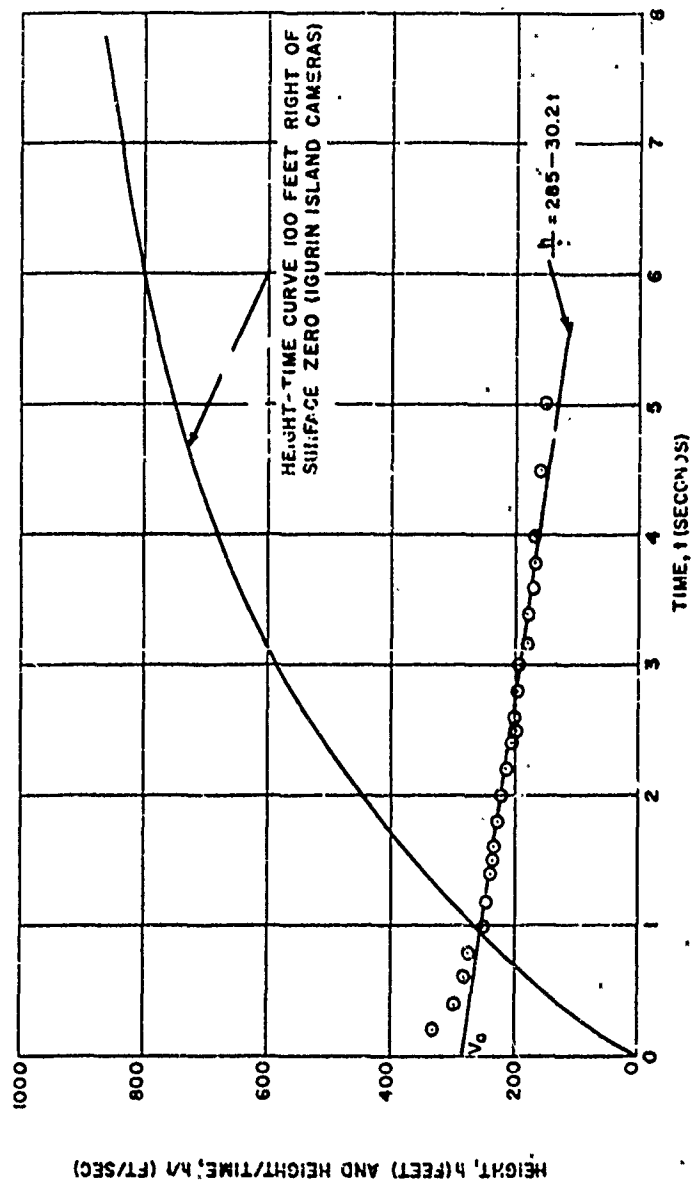


Figure 3.7 Method used for determining initial spray - one velocity, Shot V/shoo.



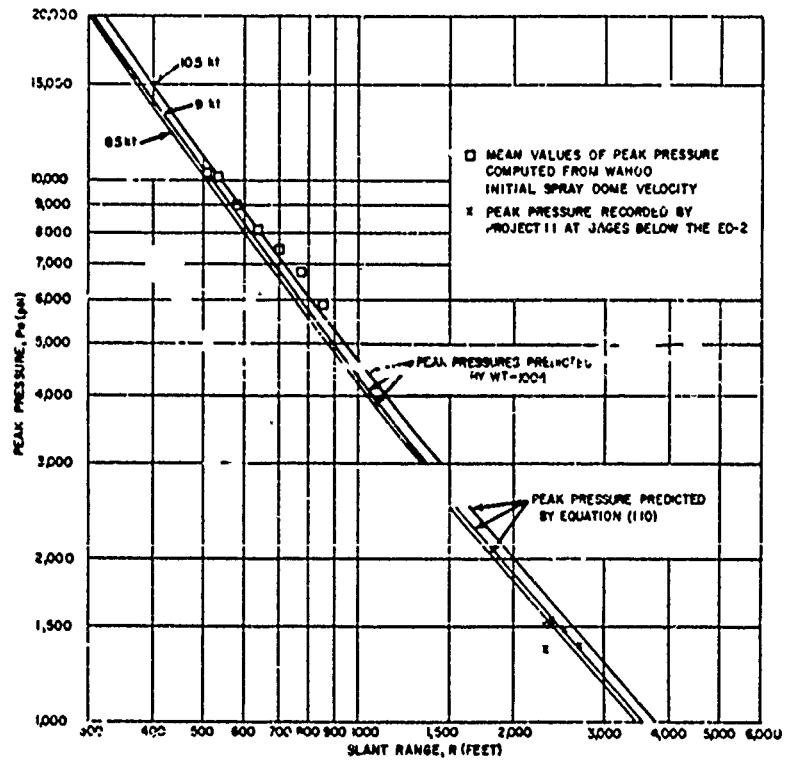


Figure S.8 Peak underwater shock wave pressures, Shot Wahoo.

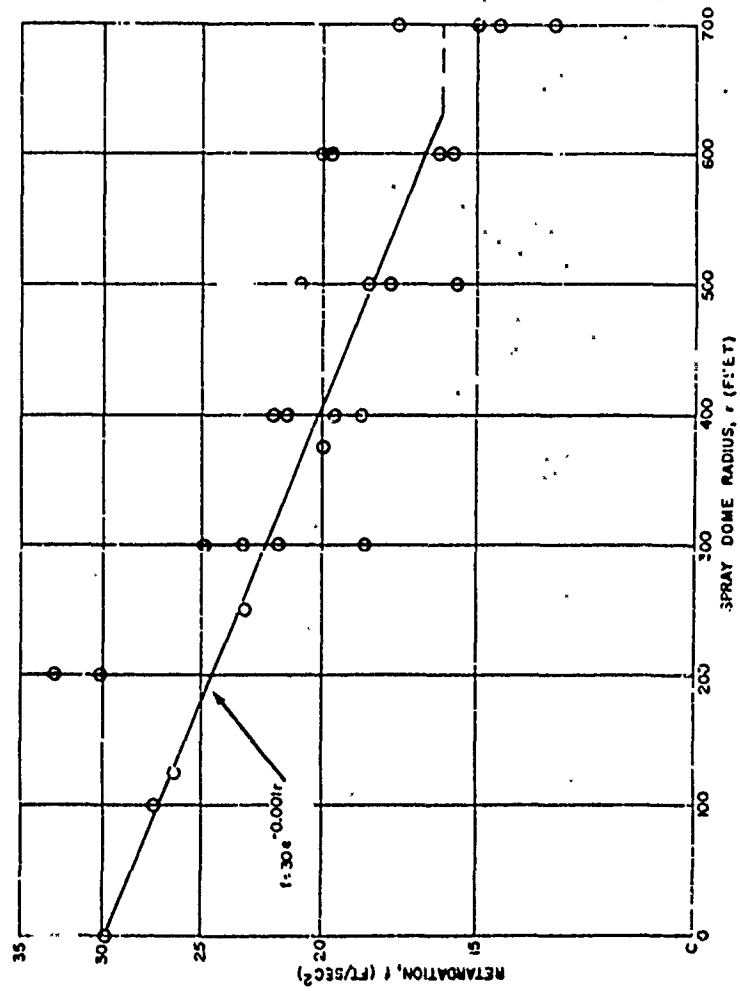


Figure 3.9 Spray dome retardation factors, Shot Wahoo.

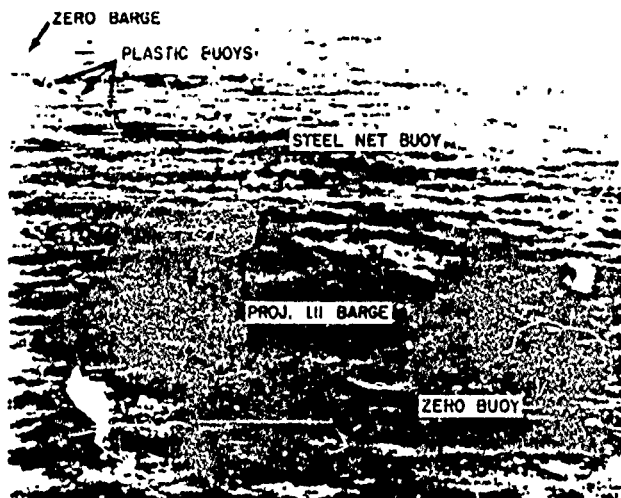


Figure 3.10 Buoys and barges in the vicinity of surface zero prior to detonation, Shot Wahoo..



FILM NO 51337

1.16 SECONDS

Figure 3.11 Objects rising above spray dome, Shot Wahoo.

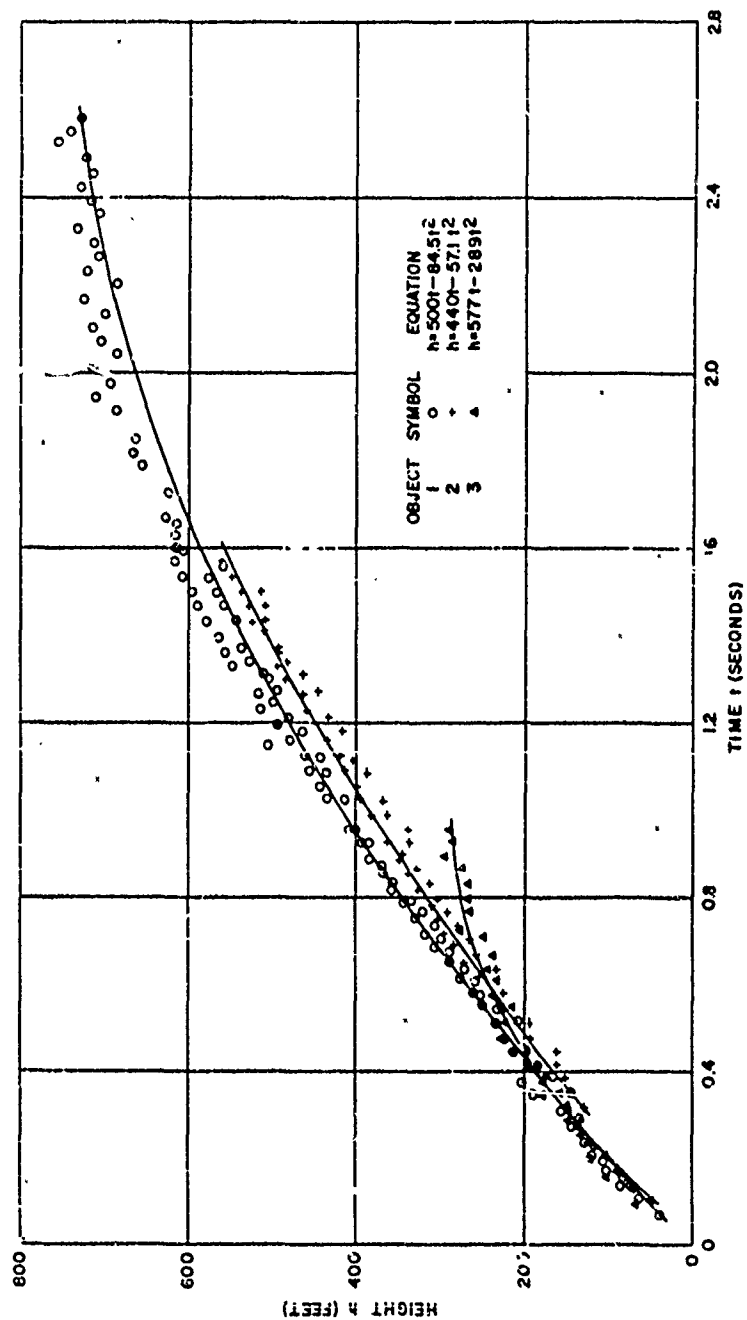
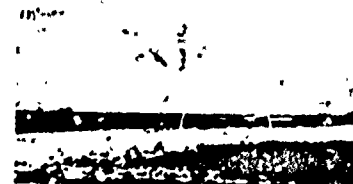


Figure 3.12 Trajectories of objects rising above the spray dome; Shot Wahoo.



8.3 SECONDS



11.7 SECONDS



15.0 SECONDS



18.7 SECONDS

FILM NO. 51341

Figure 3.13 Primary plumes, Shot Wahoo.

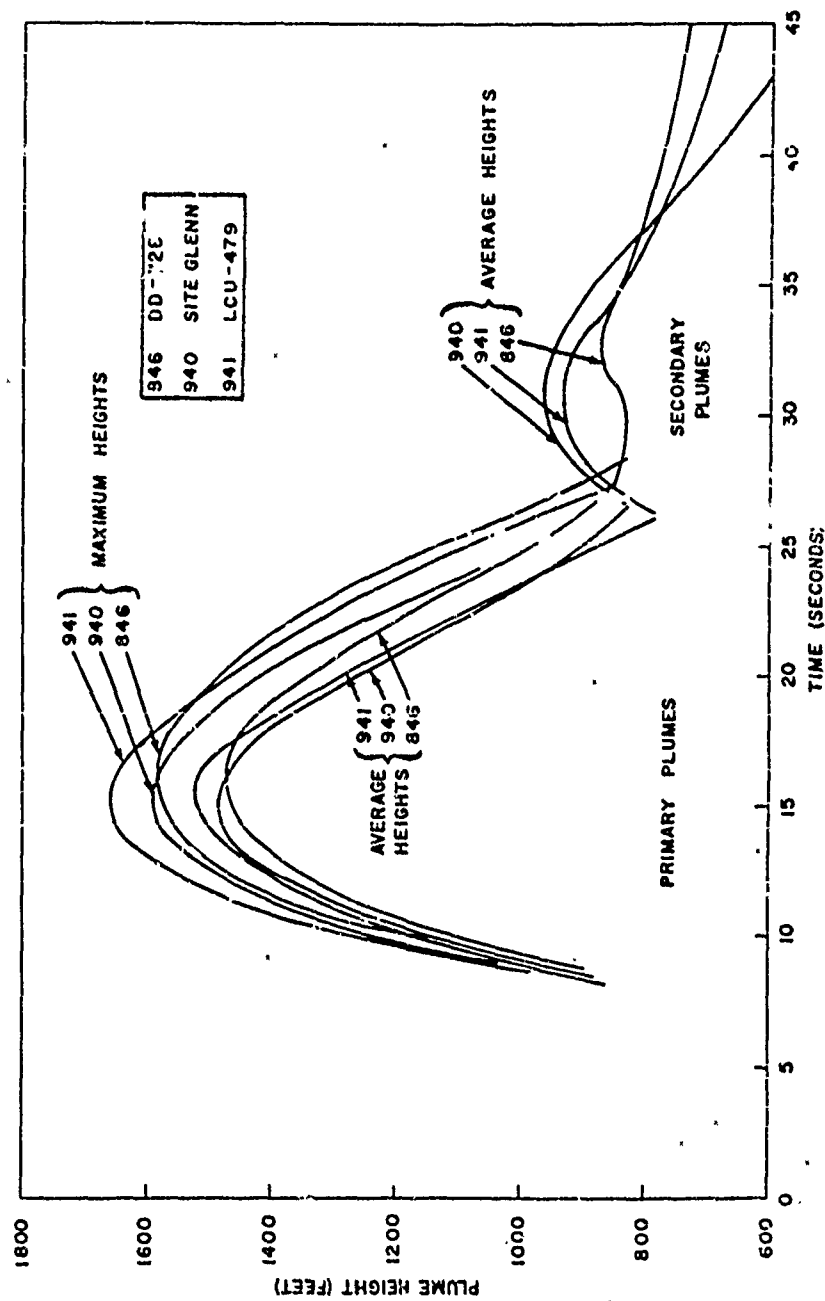


Figure 3.14 Plume height versus time, Shot Wahoo.

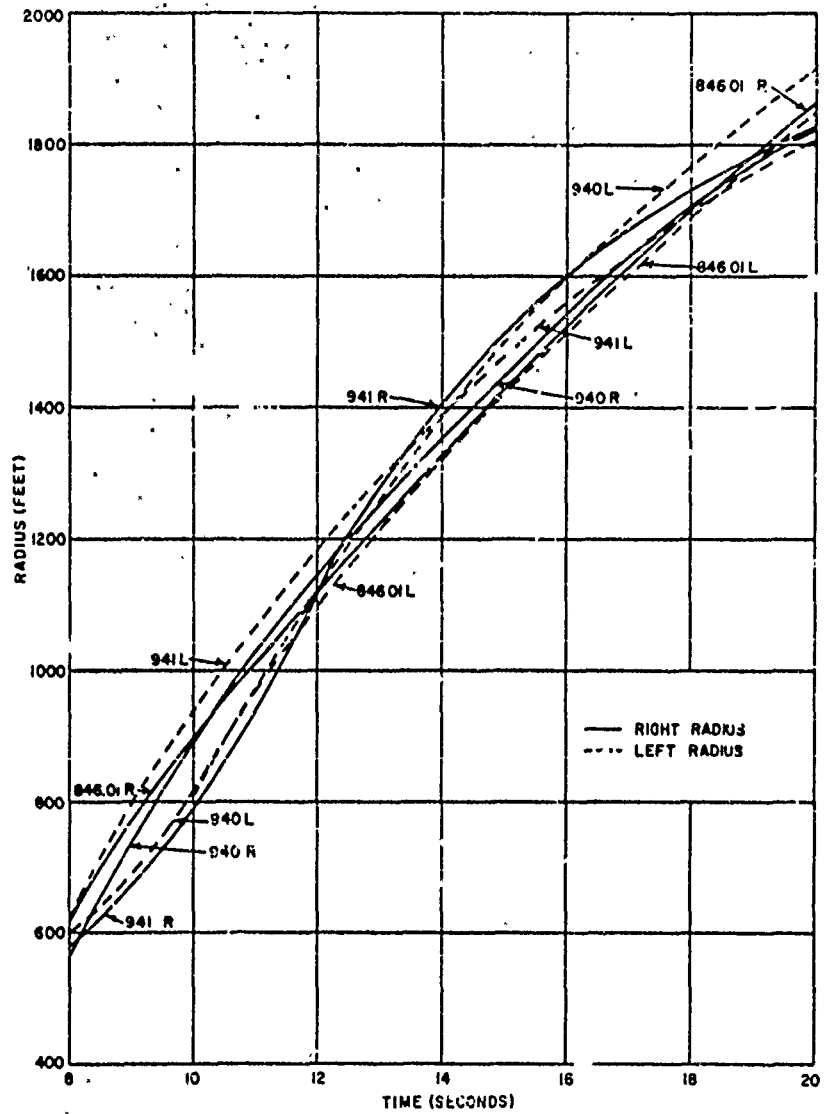
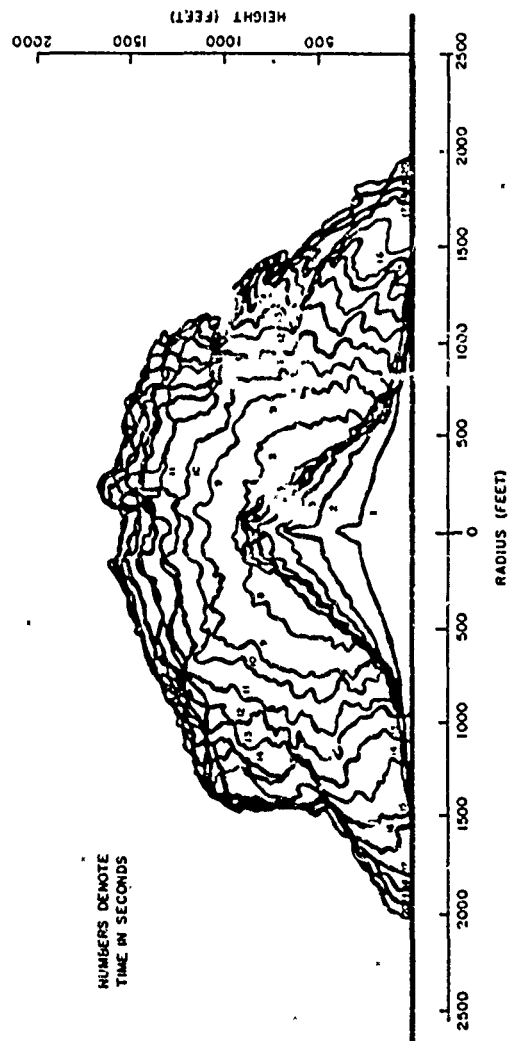


Figure 5 15 Plume radius versus time, Shot Wahoo.



FILM NO. 51339  
IGURIN ISLAND

Figure 3.16 Dome and plume profiles, I.C. Wahoo.



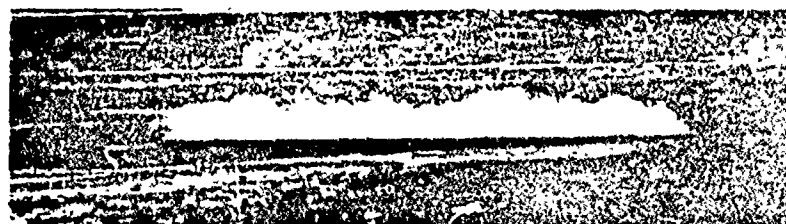


24 SECONDS

SECONDARY PLUMES



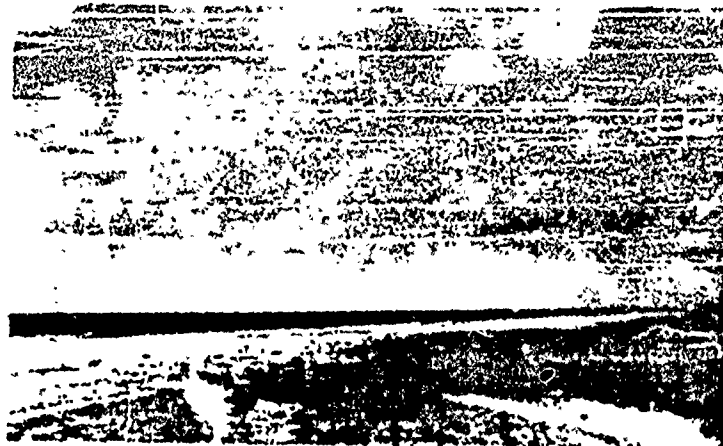
32 SECONDS



45 SECONDS

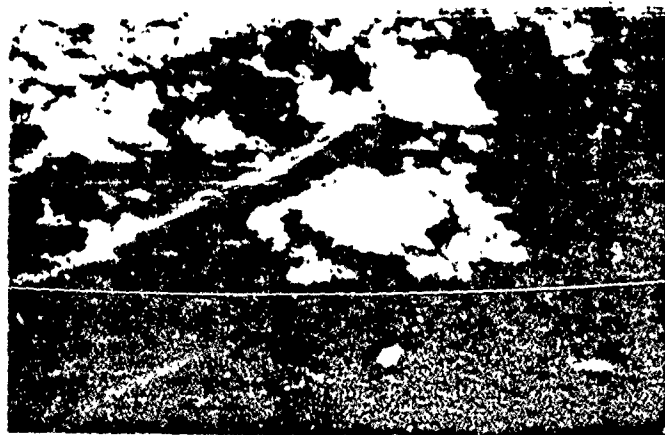
FILM NO 51541

Figure 3.17 Base surge at early times. Shot Wahoo



FILM NO. A-141

93 SECONDS



FILM NO. 51582

100 SEC.

Figure 3-11 Base surge at late times - Shot Wave

CONFIDENTIAL

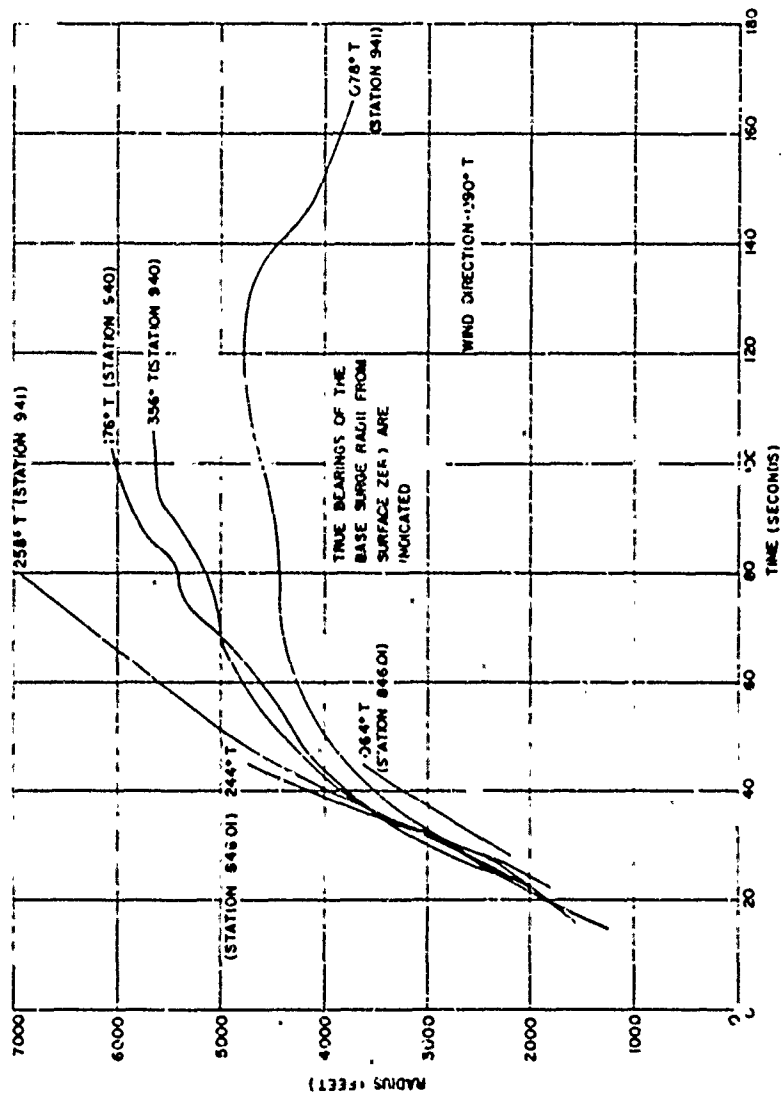
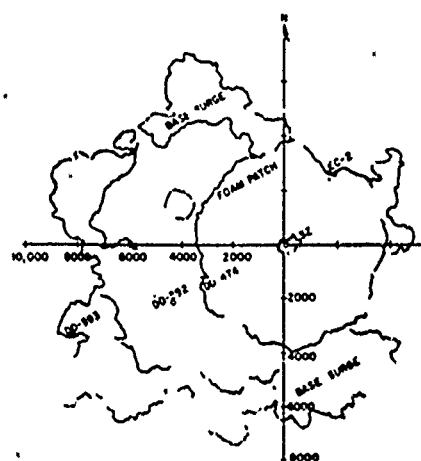
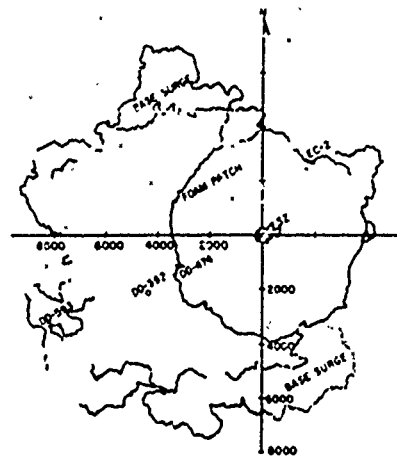


Figure 3.19 Base surge radius versus time, Shot Wahoo.

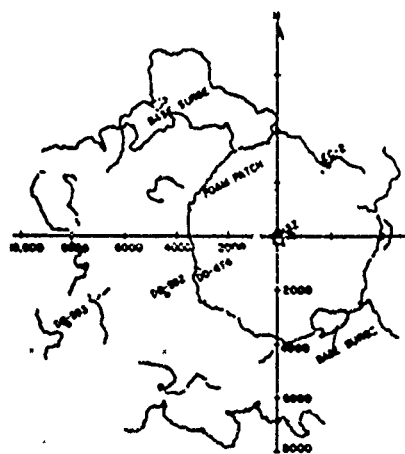




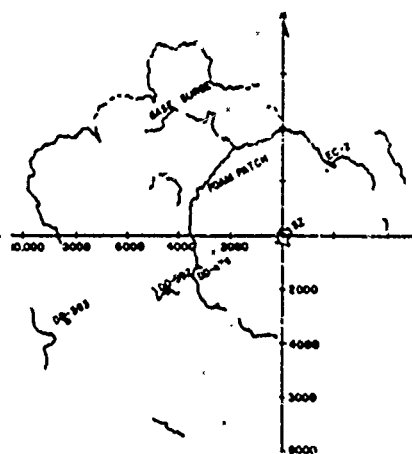
141 SECONDS



149 SECONDS

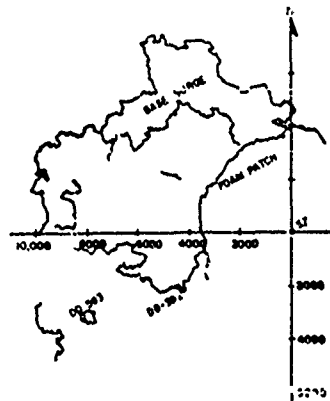


157 SECONDS

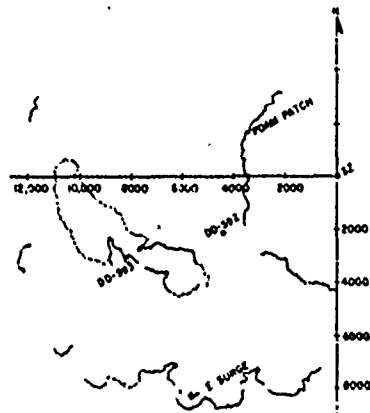


165 SECONDS  
FILM NO 5:335

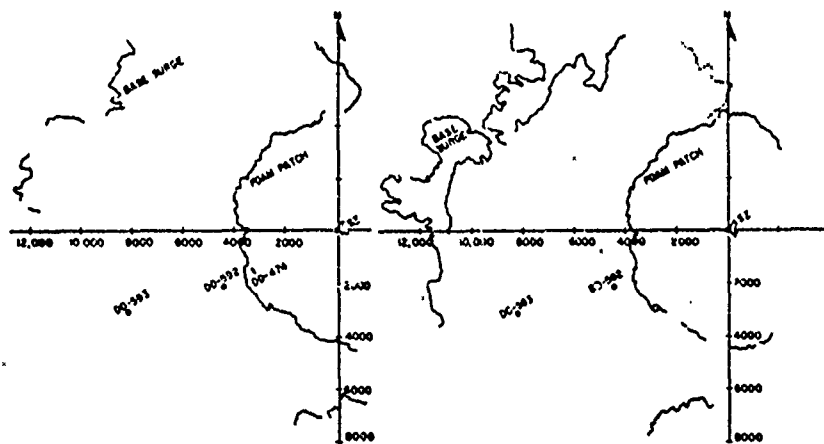
Figure 3.21 Base surge contours, Shot Wahoo.



173 SECONDS



237 SECONDS



253 SECONDS

270 SECONDS

FILM NO. 51395

Figure 3.22 Base surge contours, Shot Wahoo.

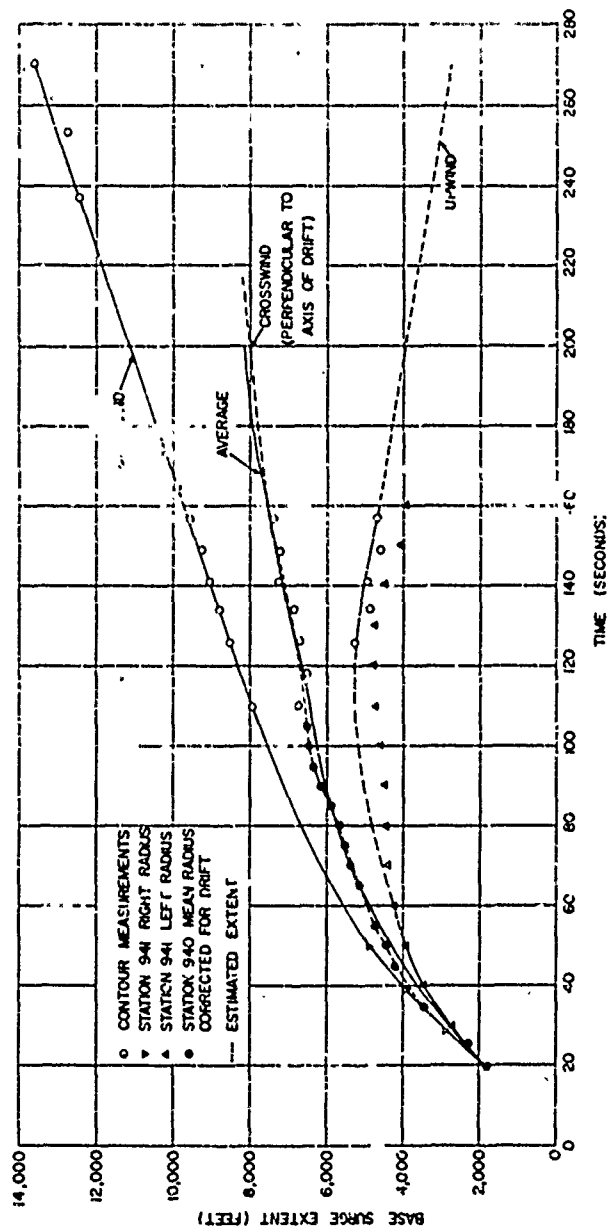


Figure 3.23 Base surge upwind, crosswind, and downwind, Sho: Wahoo.

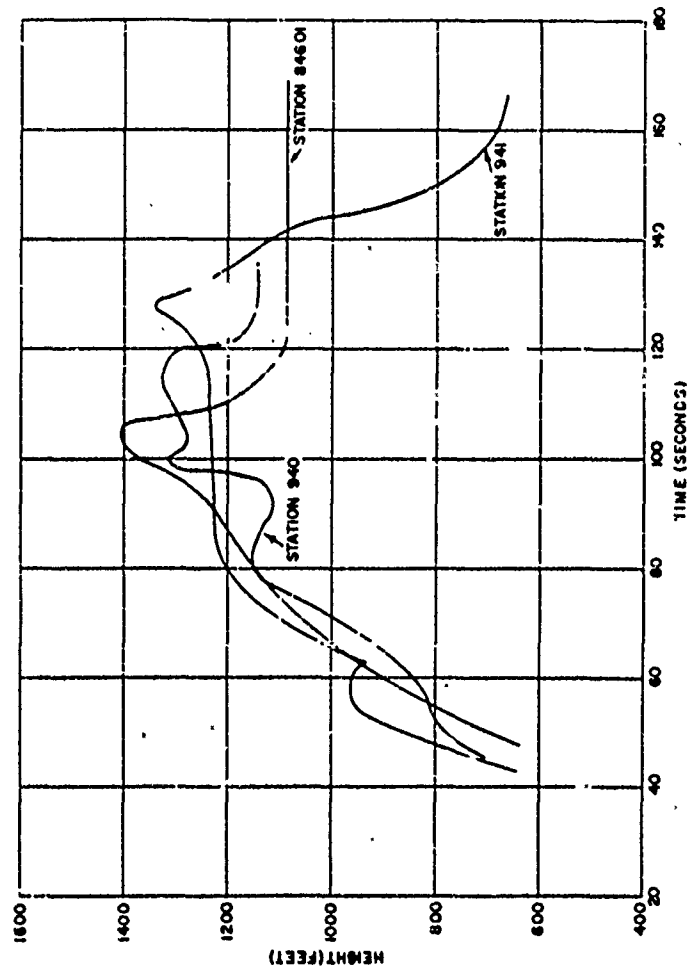


Figure 3.24 Maximum base surge height, Shot W-4hco.





141 SECONDS

FILM NO. 51396



63 MINUTES

FILM NO. 51382

Figure 3.25 Foam patch, Shot Wahoo.

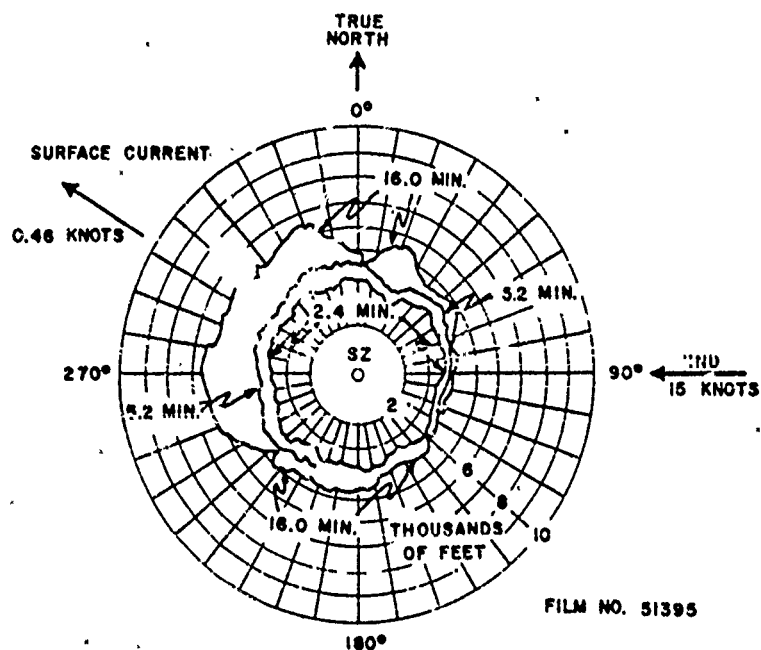


Figure 3.26 Foam patch contours, Shot Wahoc.

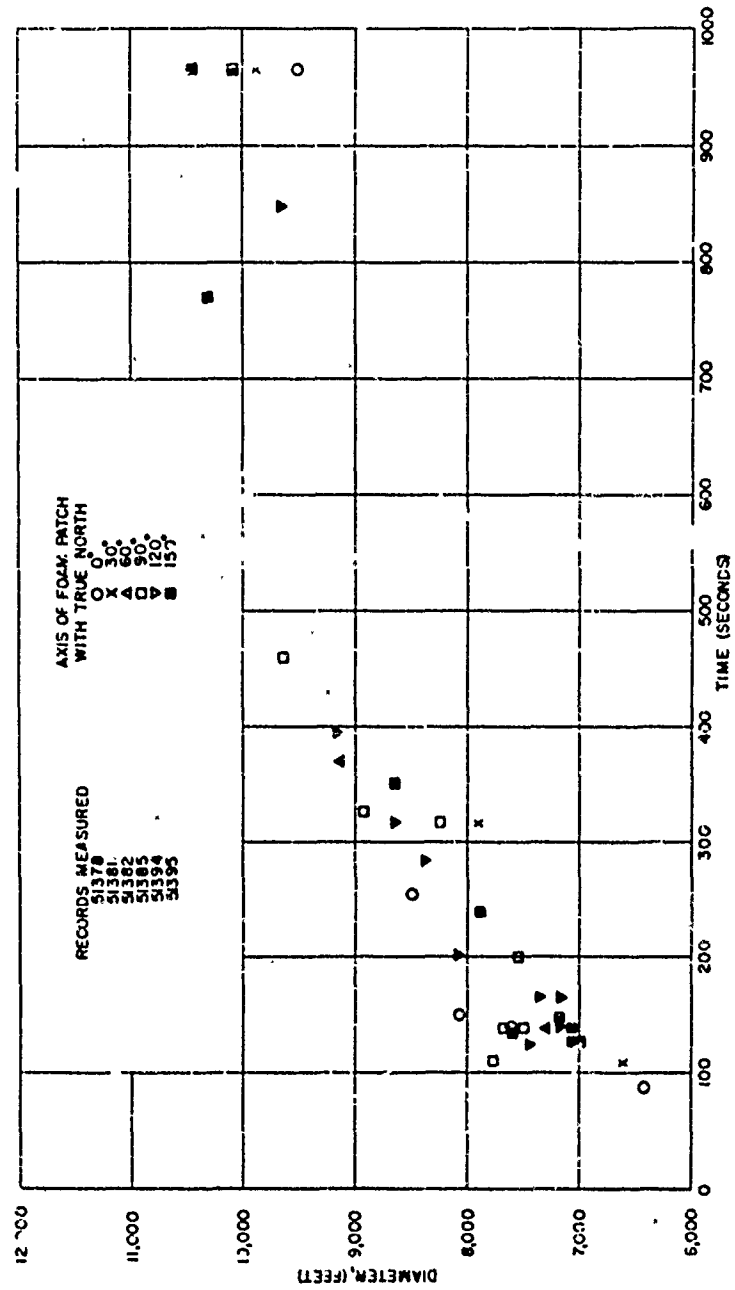


Figure 3.27 Foam patch diameter versus time, Shot 14 hoo.

## Chapter 4

### RESULTS OF PHOTOGRAPHY, SHOT UMBRELLA

#### 4.1 SPREAD OF UNDERWATER SHOCK WAVES

As viewed from the air, the first evidence of Shot Umbrella was an underwater flash of light resulting from the detonation of the device. This light persisted for somewhat less than 10 msec; however, the exact time could not be determined, because the flash was visible on only one frame in each of four photographic records, all of which had a frame rate of 100 frames/sec or less (EG&G Films 52241, 52245, 52254, and 52255).

A few milliseconds later an expanding white patch with a dark ring appeared, similar to that observed on Shot Wahoo. The dark ring, indicating the intersection of the primary underwater shock wave with the water surface, was visible to a radius of 2,700 feet. Its rate of spread, as measured from the free of the aircraft, together with the calculated spread of the slick for a depth of burst of 150 feet (Reference 9) and the time of arrival of the underwater shock wave measured by Project 1.1 (Reference 19), is shown on Figure 4.1. The agreement between the calculated spread, photographic measurements, and Project 1.1 data is excellent.

The expanding white disk followed closely behind the slick at early times, being about 30 feet behind at 0.1 second. Initially, the whiteness was possibly caused by cavitation beneath the surface, but the spray dome undoubtedly developed rapidly thereafter. The time lag between the appearance of whiteness and the rise of spray was possibly as great as 10 msec, although this could not be determined accurately.

The lateral growth of the spray dome is shown as the upper curve in Figure 4.2. As can be seen in Figure 4.3, the outer edge was poorly defined, with patches of spray occurring only on wave crests. The density of the spray increased toward the center, where the dome was a continuous mass of spray, appearing as a white disk with a fairly well defined edge. The lateral expansion of this dense central area is shown as the lower curve in Figure 4.2. Both the central region and the outer area stopped growing at about 0.5 second; the radii at this time were approximately 750 feet and 1,900 feet.

At approximately 0.53 second after SZT, a slick, followed by the formation of spray, was seen to move inward toward surface zero from a radius of about 1,900 feet. At about the same time and about the same radius, another slick, lighter in color than the surrounding water but with a dark border, moved outward rapidly. A comparison of arrival times of these slicks with the arrival times of the cavitation pulse at the Project 1.1 underwater pressure gages showed good agreement, as can be seen in Figure 4.2.

A dense ring of spray formed immediately after the appearance of these slicks and grew outward briefly to a maximum radius of about 2,100 feet from surface zero at 0.6 second. It also spread inward while the primary inner dome expanded outward along the surface. At about 1 second after SZT, these areas had merged to form a continuous white dome. The outer radius decreased to 1,900 feet at 0.7 second and remained fairly static to the end of the 1-second period of measurement. These results are included in Figure 4.2. Most of the original spray data showed a scatter of about 5 percent with extreme values up to 10 percent about the mean. The appearance of the primary slick, spray dome, and cavitation

pulse spray ring, as seen from the air, is shown in Figure 4.3.

In addition to the primary shock wave slick, several less intense slicks radiated from surface zero at extremely high velocities. These first appeared beyond the primary slick approximately 0.58 second after SZT and were probably caused by reflections of the shock wave from various strata beneath the bottom of the lagoon.

A radio fiducial mark, indicating the exact instant of detonation, was recorded on the 1,000-frames/sec record taken from Site Glenn (EG&G Film 52258). Unfortunately, surface zero was obscured from this station by the EC-2. It was, therefore, not possible to determine from this record the time after detonation that the first surface effects were visible.

A cluster of flashbulbs was set off on the Zero Barge at zero time, and these are visible on some of the photographic records. On the records taken at speeds of approximately 100 frames/sec, the flash bulbs were visible one to two frames before the first visible surface effects. This would indicate an interval of about 15 msec ( $\pm 5$  msec) between the time of detonation and the first visible surface effects.

If it is assumed that the burst had an effective hydrodynamic yield of 8 kt multiplied by a factor of 1.6, because of the presence of the bottom (Reference 20), the time of arrival of the shock wave to the surface, as calculated according to Reference 17, is 13.7 msec. This calculation is relatively insensitive to yield for shallow bursts but gives a time that is consistent with the experimental result.

#### 4.2 AIR SHOCK WAVE AND CONDENSATION CLOUDS

The air shock wave that appeared above surface zero was visible on two photographic records taken from Site Glenn; a 100-frame/sec Mitchell record and the 1,000-frame/sec Eastman high speed record (EG&G Films 52265 and 52258). Surface zero was obscured on these records by the EC-2, so that only a portion of the shock wave could be seen. This portion, on the side of the dome off the stern of the EC-2, was visible until approximately 70 msec after SZT.

A faint light ring, which indicated the intersection of the air shock wave with the water surface, was visible on some of the RB-50 films (EG&G Films 52254, 52255, and 52257). This ring appeared dark when viewed from the C-54's. It moved radially outward from surface zero and was visible to a radius of about 10,000 feet. The radial growth of the leading edge is shown in Figure 4.4. The measurements are consistent with the times of arrival of the peak of the second air pressure pulse at the DD-592 and the 55-barge (Reference 23). These values are included in Figure 4.4.

A condensation cloud appeared on the downwind side of the column at about 1.8 seconds after SZT (Figure 4.12). Its lower edge was at a height of about 800 feet, and its maximum altitude was approximately 1,400 feet. By 4.3 seconds, the cloud had disappeared, apparently engulfed by the expanding plumes. An enlargement and whitening of a few clouds in the cumulus cloud layer, 2,000 feet above the surface, was also observed. This effect was faint and could be detected on only a few records, primarily the aerial color documentaries. A patch of cloud near surface zero was affected at 4.4 seconds after SZT, and a patch at a greater distance was affected about 8 seconds after SZT. In both cases, the brightening and enlargement persisted for about 3 seconds. As on Shot Wahoo, this was caused by the passage of the rarefaction phase of an air shock wave. The phenomenon is discussed in greater detail in Section 6.2.

### 4.3 SPRAY DOME

Following the air shock wave, a bell-shaped dome of spray rose above the water surface. Several large jets, resulting from the action of the shock wave on buoys near surface zero, were visible at the center. These are discussed in Section 4.4. A prominent feature was a large black patch that appeared on the side of the dome where the Zero Barge, an LCU, had been moored about 50 feet from the Zero Buoy. The blackness was probably caused by debris from the breakup of the barge by the primary underwater shock wave. The appearance of the dome is shown in Figure 4.5.

Measurements of spray height versus time were made at surface zero and at 100-foot intervals to the right and left of surface zero on the photographic records from the three surface camera stations. Measurements were made to the top of the spray in all cases. As an example, smoothed curves for positions extending to 400 feet left of surface zero, as seen from the LCU-479, are shown in Figure 4.6. Measurements were made to a radius of 1,500 feet, but the scatter of data points made it impossible to fit a smooth curve to the measurements with confidence at distances beyond 600 feet. At a 1,500-foot radius, the maximum measured height was 10 feet.

The spray height-versus-time curves showed discontinuities at early times. A particularly abrupt change at 0.38 sec. is shown on the 200-foot radius curve in Figure 4.6. A sudden increase in velocity of this nature appeared on some surface zero records between 0.5 and 0.6 second, but only slight changes, occurring between 0.2 and 0.5 sec., were detected at the 100-foot radii. At distances beyond 600 feet, the discontinuities appeared at later times. These sudden changes indicated the appearance of plume effects. At this time, the mass motion of the water produced by the expanding bubble rapidly overtook the shock-wave-induced spray effects, and the water rose upward to form a cylindrical plume.

Because of the short duration of the spray dome on Shot Umbrella, it was necessary to use care in the determination of initial velocities by the method given in Section 3.3. In some cases, the height-versus-time curves were linear until plume effects appeared, and the slopes of the lines were assumed to represent initial velocities. These constant velocities were observed on some records at the 200- and 400-foot radii and on all records at the 300-foot radii. The measured values are listed in Table 4.1. Means, standard deviations, and coefficients of variation are also shown; the latter indicate an increasing scatter with increasing distance from surface zero. Initial velocities were not measured at radii beyond 600 feet because of the scatter of the data points.

By means of Equation 1.4, it is possible to calculate peak underwater shock pressures and, hence, the yield from initial spray dome velocity, if the depth of burst and shock velocity are known. For a shallow burst, such as Umbrella, the shock velocity is changing rapidly near the surface and a constant value cannot be assigned to it.

However, it is possible to estimate the yield from the spray dome data by using the ratio of peak pressure to shock velocity  $P_0/U$  as a variable. For Umbrella, Equation 1.4 reduces to:

$$\frac{P_0}{U} = \frac{V_0}{145 \cos \delta} \quad (4.1)$$

Values of  $P_0/U$  were found from the spray dome velocity data and are shown in Table 4.1. The means are compared with theoretical values for yields of 5, 8, 10, and 15 kt in Figure 4.7. An interpolation of the individual calculated values indicates effective hydrodynamic yields of 12.8, 13.4, and 15.6 kt at surface zero and horizontal radii of 100 and 200 feet (150-, 180-, and 250-foot slant ranges). The average of all individual yield determinations in this region is 14.2 kt. At greater distances, the values are unreasonably high, probably because of difficulties in measuring the smaller heights and the possible occurrence

of high instability (Reference 14) velocities for brief intervals. Table 4.1 includes all of the yield values obtained from initial spray dome velocities.

The calculated yields based on this method are considerably greater than the radiochemical yield, because the burst occurred on the bottom of the lagoon. It has been estimated that the presence of the bottom would produce an effective hydrodynamic yield 1.6 times that obtained from the same burst in free water (Reference 20). Dividing this factor into the surface zero value of 12.8 kt gives a total yield of 8.0 kt, and applying it to the average value of 14.2 kt gives a total yield of 8.9 kt. The standard deviation is 3 kt for the individual yield determinations at the three radii given above, so that, within the limits of scatter, the average total yield of 8.9 kt is in good agreement with the reported radiochemical yield of 8 kt.

It should be noted that the reflection factor of 1.6 was calculated on the basis of an assumed energy partition between water and coral and is subject to some uncertainty. It could vary between the extreme limits of 1.0 and 2.0, but neither of these is likely.

No reliable data on the spray retardation coefficient  $f$  could be obtained on Umbrella, because the plume phenomena obscured the later behavior of the spray. The measured values showed wide variability, they averaged 590 and 340 ft/sec<sup>2</sup> at surface zero and the 100-foot radii, respectively, which is probably only a rough order of magnitude. In cases where the velocity was constant during the short period of measurement, no retardation could be determined.

A curve of maximum observed spray dome height for radii between 70 and 1,500 feet at about 1 second after SZT is shown in Figure 4.8. The plume undoubtedly increased the values nearer the center, but this effect cannot be evaluated quantitatively.

#### 4.4 TRAJECTORIES OF OBJECTS NEAR SURFACE ZERO

Shortly after the appearance of the first visible surface effects, several objects, followed by trails of spray, could be seen rising above the central portion of the spray dome. These objects were probably buoys, portions of barges, and the like near surface zero, which were propelled upward by the underwater shock wave. The location of some of these objects prior to detonation is shown in Figure 4.9. The Zero Buoy was a modified Navy telephone buoy about 10 feet in diameter. A Zero Barge, which consisted of an LCM placed in the well of an LCU, was moored about 50 feet from the buoy. The barge contained firing racks and Project 1.11 electronic equipment.

Figure 4.10 shows the appearance of the objects rising above the spray dome. It was possible to measure the trajectories of three of these objects from the three surface camera stations (Figure 4.11). A parabolic equation of the form used in the Waloo spray dome analysis (Equation 3.2) was fitted to the data. The fitted curves are shown in the figure, together with their equations. Because of the relatively short duration of the trajectory of Object No. 3, no attempt was made to fit a curve to these values. With the exception of Object No. 3, the lateral component of motion was negligible.

The resolution of the photographic records was inadequate to identify the objects, and triangulation of the trajectories from the three camera stations was probably not accurate because of measurement difficulties. However, this method provided estimates of the locations of the objects prior to the shot. Object No. 1 was estimated to be 18 feet from surface zero, at a bearing of 65°. This object had a large gray spray trail and was still rising when the period of measurement ended. An initial velocity of 1,320 ft/sec was indicated.

Object No. 2 was approximately 37 feet from surface zero at a bearing of 40°. Its initial velocity was 2,260 ft/sec, and it had a high retardation factor. Therefore, its trajectory

leveled off during the period of measurement. Its spray trail was also gray.

Object No. 3 was 29 feet from surface zero at a bearing of 186°. It rose out of the black patch produced on the side of the spray dome by the breakup of the Zero Barge. This object was followed by a narrow white spray trail. A lateral component of velocity of 370 ft/sec and a vertical component of 1,950 ft/sec were shown by the data, giving an initial velocity of about 1,985 ft/sec.

A theoretical peak pressure of 74,300 psi at surface zero is predicted by Reference 17 for a yield of 12.8 kt (8 kt multiplied by a factor of 1.6 because of the effect of the bottom, as discussed in Section 4.3). This would give an initial spray dome velocity of 1,570 ft/sec at this point. The initial velocities of the objects measured were from 1.2 to 1.4 times the expected spray dome velocity, probably as a result of a different mechanism of initiation of the motion.

In addition to those that were measured, other objects were seen to fall from the upper plumes (EG&G Film 52249). Because of the greater importance of other measurements for this report, all the trajectories were not measured, and all the photographic records were not analyzed. Should the need for more information exist, additional data can be obtained from the record.

#### 4.5 PLUMES

Since the development of the plumes from the spray dome on a relatively shallow burst like Shot Umbrella is a fairly continuous process, it is difficult to distinguish the two phenomena. However, the spray dome height-versus-time curves in Figure 4.6 show discontinuities, which indicate that new jets originated in the sides of the Umbrella dome about 0.4 second after SZT. Close examination of the photographs shows that these jets had strong lateral components of motion, indicating that they were produced by the expanding explosion bubble. At this stage, the water pushed out by the gases and vapors was probably decelerating.

The plume continued to rise and expand laterally, attaining a roughly cylindrical shape, as shown in Figure 4.12. The plume was wider near the top than at the bottom, with the narrowest portion, or neck, at an average height of 300 to 400 feet above the surface.

Figure 4.12 shows that the plume consisted of a mass of jets, which broke up into spray. The jets in the upper part of the plume started out in an almost vertical direction from positions close to the burst and had broken up into a fine cloudlike mist by the time the plume reached its maximum height. The height-versus-time data showed slight discontinuities as rising jets overtook and passed jets above them. Since a narrow jet rose a few hundred feet above them. Since a narrow jet rose a few hundred feet above the top of the bulk of the plume, the curves in Figure 4.13 are for both maximum height and average height. The vertical growth had virtually ceased at 20 seconds after detonation, when a height of about 4,900 feet was reached. For aircraft safety considerations, it may be stated that the maximum plume height for Umbrella was 5,000 feet. The scatter in plume-height data for a camera station and the spread of the curves in Figure 4.13 about the mean never exceed  $\pm 5$  percent. In some cases, the measured average height exceeded the reported maximum, particularly at late times. This can probably be attributed to measurement difficulties.

Because of the random nature of the jets, the lateral growth of the plume was not entirely symmetrical. Plume radii relative to surface zero were measured to the outermost jets, as seen from the three surface camera stations; these curves are shown in Figure 4.14. The jets in the plume started to spill over and fall between 10 and 11 seconds after the burst. The maximum measured plume diameter, as seen from the LCU-1123, was about 3,250 feet at 22 seconds after SZT. By this time, the plume had lost its sharp outline and had become



a roughly cylindrical diffuse mass of spray.

At early times, the lower part of the plume resembled the column observed during HE tests. The lower jets that formed the column followed relatively short trajectories and left the surface at larger angles with the vertical than the jets that rose to the top of the plume. Trajectories of individual jets that could be followed on the records for several seconds are shown in Figure 4.15. The top of the column could not be clearly distinguished from the lighter material above it.

Measurements of the lateral growth of the column neck are included in Figure 4.14. This region was measured for scaling purposes because of its smooth appearance at early times. However, jets became clearly visible in the column neck about 3.5 seconds after SZT. These reached a maximum height about 6 seconds after SZT.

The gradual settlement of the plume material, which started about 20 seconds after the shot, may be called fallout. The plume was divided into three large masses of falling material; the largest at the bottom and the smallest at the top. Figure 4.14 shows a rapid decrease in diameter between 35 and 40 seconds when the lowest mass settled out, and measurements were shifted to a higher level. The plume, or fallout, diameter decreased continuously thereafter as material dropped to the surface, leaving a relatively narrow cylindrical mist. Measurements of the motion showed that the fallout moved in the direction of and at about the speed of the wind from 20 seconds until it was no longer visible. A fall-out contour at 146 seconds is included in Figure 4.19. Figure 4.13 shows that the mist at the top of the plume settled at an average rate of about 23 ft/sec. The appearance of the plume during its collapsing stage is shown in Figure 4.16.

The mist remaining from the Umbrella plume was visible for a longer time from the air than from the ground. However, the reported time of disappearance varied with the point of observation and the observer. In general, the mist was visible on aerial photographs until 3 to 4 minutes after SZT and on surface camera records only until 100 to 120 seconds after SZT.

It is interesting to note that a string of ball-crusher gages, which was suspended from a buoy about 590 feet from surface zero by Project 1.1, was recovered intact after the burst (Reference 19). This probably indicates that the radius of the cavity produced in the water by the explosion was less than 590 feet. Measurements show that the outside edge of the column extended well beyond the edge of this cavity.

A movement of spray into the column was observed on Film 52268 about 4 seconds after SZT. This probably indicated a rupture of the column wall and a subsequent inflow of air because of the low pressure inside the column. The column neck radius was 565 feet at this time.

#### 4.6 VISIBLE BASE SURGE

The leading edge of the Umbrella base surge emerged from the base of the column about 7.4 seconds after SZT. This surge front was possibly a spillover of material at the edge of the water cavity. A similar phenomenon was observed during Shot Baker of Operation Crossroads and in HE tests. In some cases, bottom material was observed to spill out of the base of the column. As the Umbrella surge moved radially, the collapsing column fed material into it. After the column had subsided, the surge continued to spread along the surface as a ring-shaped cloud. The surge was irregular in outline but did not form separate lobes as rapidly as during Shot Wahoo. At the end of the longest available photographic record (Film 52247), which was at 25 minutes the Umbrella surge was still visible from the air as a well-defined toroidal cloud.

Figure 4.16 shows the collapse of the Umbrella plume and the formation of the base surge. The surge structure, as seen from the air when the plume was no longer visible, is illustrated in Figure 4.17.

Figure 4.18 includes the measurements of right and left surge radii as seen from the three surface camera stations. The bearing of each radius, in reference to surface zero, is indicated on the figure. The longest and most useful record was that obtained from Station 940 (Site Glenn). The right and left radii seen from these cameras lay on the 72°-to-252° axis of the surge, which was approximately parallel to the reported surface wind direction (from 55°). The surge velocity was initially about 57 knots on the 252° radius, which was approximately downwind. At 50 seconds after SZT, the velocity had decreased to 61 knots. The curve for the 72° radius levels off at about 4,200 feet between 90 and 100 seconds after SZT, and then indicates an approximately downwind motion, which seems to maintain a constant velocity of about 11 knots after 200 seconds following SZT. However, measurements taken near the top of the surge, on the 72° bearing, showed a motion of about 20 knots at 135 seconds, which is in agreement with the reported surface wind speed.

Photographs show that the upwind trailing edge of the Umbrella base surge lagged behind the main body of the surge, probably because of retardation by surface friction. It also is possible that the surge was denser near the surface and, therefore, less subject to the influence of the wind. As the surge moved downwind, it appeared that spray from the surface of the foam patch was stripped off by the wind. This mist was not distinguishable from the surge, and added to the difficulty of obtaining surge measurements upwind after about 190 seconds, when the upwind trailing edge was in the foam patch. It possibly moved beyond the foam patch about 520 seconds after SZT.

Figure 4.19 shows the only base surge contour available for Shot Umbrella. It was obtained at 140 seconds after SZT from Film 52256. The surge had a slightly elliptical shape at this time, and its irregular outline can be clearly seen. The disruption of the surge by the downwind target vessels is also evident in Figure 4.19. These effects illustrate the limitations of surface photography for establishing the true shape and dimensions of the base surge.

An attempt was made to determine the drift of the Umbrella surge on the aerial photographic records by measuring the distance between the center of the surge and the center of the foam patch. This proved to be extremely difficult because of the irregular shapes of both phenomena, the diffuse nature of the surge at late times, and the distortion introduced in some records by the proximity of the surge to the edge of the frame.

An additional photogrammetric problem also existed in measuring the drift from the 1,500-foot C-54, as it was at nearly the same altitude as the top of the surge. The most useful and reliable records appeared to be Films 52243 and 52247, from the 9,000- and 10,000-foot aircraft, respectively. Although the drift measurements showed scatter, the average motion measured between 100 and 1,200 seconds was about 20 knots along the 235° bearing from surface zero. This differed by 5° from the 230° drift expected on the basis of the reported wind direction. However, this is not unreasonable, as the surface wind direction is reported in 10° increments and consequently could have been anywhere between 225° and 235°. In order to obtain consistent data, all base surge measurements obtained from aircraft were adjusted for a steady drift of 20 knots along the 235° bearing, starting at 10 seconds after SZT. This movement was added to, or subtracted from, the camera distances from surface zero as determined on the radar plots.

The aircraft measurements showed varying degrees of scatter, depending on such factors as the trailing mist, measurements between lobes, indefinite edges of the surge, and the like. However, using aircraft bearings, it was possible to determine approximate curves for the average and crosswind surge radii to 1,159 seconds after SZT. For the first 100 seconds, the scatter was negligible. It increased to ±10 percent at 400 seconds. The later surge values are questionable because of the limited data after 500 seconds.

The crosswind and average surge radii are shown in Figure 4.20. In addition, the upwind and downwind motion of the surge along the 55°-to-235° axis through surface zero is shown.

The curves are based on aerial measurements, the contour plot in Figure 4.19, visual determination of the surge arrival and departure times at temperature-humidity stations, and the surface measurements shown in Figure 4.18. Two curves are shown for the upwind trailing edge; one represents the main body of the surge and the other the shallow mist, which probably included some spray from the foam patch. This mist faded after the surge left the foam patch and was no longer visible at 600 seconds after SZT, when the surge was beyond the Island stations. The disappearance of the trailing mist probably helps to account for the agreement between the average and crosswind radius curves at 1,200 seconds in Figure 4.20. At this late time, the surge was ring shaped and was moving with the wind; it was probably no longer subject to surface frictional effects. The crosswind radius-versus-time curve shows a 3-knot radial growth at the end of the record, indicating a continued slow growth of the surge.

In general, the leading downwind edge was more clearly defined than the trailing upwind edge. The inner edges of the surge ring were also not clearly defined, and the enclosed area contained mist from fallout and probably spray from the foam patch. Figure 4.17 shows a greater vertical development of the surge on the downwind semicircle than on the upwind. The greater wind shear on the upwind half of the surge, where the surge was moving against the wind at early times, probably accounts for this.

What apparently was the arrival of the base surge was detected on some of the Project 1.2 airblast gage records. A short positive pulse followed by a slightly negative phase was recorded at 19.5 seconds at the EC-7. A second gage on the EC-2 recorded a negative phase, starting at 19.0 seconds. In both cases, the trace was wavy during the negative phase. The data recorded at the DD-474 showed a slight waviness of the trace beginning at 18 seconds, with a short positive pulse at 19.2 seconds. After the positive pulse, the trace was wavy until the end of the record. No negative phase was discernible during this period. At the 21-barge, the trace became negative and very irregular 20.8 seconds after SZT. These times are in agreement with the radius-versus-time curves shown in Figure 4.18.

The maximum height of the Umbrella base surge was measured from the three surface camera stations. The data obtained from different cameras at individual stations did not show excessive scatter; the range approached  $\pm 10$  percent from the mean in extreme cases. However, there was considerable deviation between the original average height-versus-time curves from different stations. The primary reason was the constantly changing distances between the highest peaks of the surge and the camera stations, resulting from the radial growth and downwind drift of the surge toward or away from a station. In addition, the point of measurement shifted as one lobe overtook another or a high lobe evaporated. Also, the highest lobe visible from one station might not have been seen from another. No attempt was made to positively identify the high lobes on different records, to locate them precisely in space, or to determine their exact heights. The effort involved was not believed to be justified because of the normal variation expected in this type of data. However, an approximate correction was applied where possible by estimating the positions of the high lobes and accounting for the motion of the surge.

Figure 4.21 shows the resulting maximum height-versus-time curves for the three surface stations. No correction has been applied for the first 50 seconds for Stations 942 (LCU-479) and 946.02 (LCU-1123), because the average readings from the two stations are believed to lie within 10 percent of the true values. Since Station 942 was approximately crosswind of the burst and was the greatest distance away, the error due to surge motion was minimized, and probably varied between zero and 20 percent during the period of measurement. A constant correction factor of 0.9 was, therefore, applied to the Station 942 surge heights between 50 and 146 seconds, after which measurements were no longer possible, because the surge extended beyond the field of view of the cameras. Station 946.02

was between an upwind and crosswind position. Between 50 and 64 seconds after SZT, a correction of 0.8 was applied to compensate for the measurement of surge heights about 3,600 feet closer to the camera than surface zero. At 64 seconds, the measurements appeared to shift to lobes perpendicular to the line of sight. As the surge moved downwind and away from the station, the measured heights were low after 64 seconds. The correction factors between 65 seconds and the end of the measurements at 248 seconds were based on a wind component of 15 knots along the camera line of sight. After 80 seconds, the highest lobes were on the downwind half of the surge, and an average distance from the center of the surge to the lobes was added to the wind motion to obtain the correction factor. This reached a maximum of 1.35 at 248 seconds.

Station 940 (Site Glenn) was subject to the greatest measurement error because of its proximity to the burst. For example, at 60 seconds after SZT, the highest part of the surge, as seen from Iguria, was about 6,800 feet from the cameras, and surface zero was 12,093 feet from the cameras. To compensate for the radial motion of the surge toward Station 940 and the simultaneous wind drift, the height measurements were reduced by a factor of 0.1 at 15 seconds, increasing linearly to a 0.5 reduction at 60 seconds and remaining 0.5 until 230 seconds after SZT when the surge extended beyond the field of view of the cameras.

Figure 4.21 is probably accurate, particularly at late times, but indicates the general trend and approximate magnitudes. The figure shows an average rate of rise of about 12 ft/sec between 15 and 120 seconds after SZT, which is somewhat less than the rate of rise of the Wahoo surge top. The Umbrella surge top tended to fluctuate between 1,000 and 2,100 feet after 120 seconds, probably averaging several hundred feet higher than the Wahoo surge.

An interesting feature was the development of relatively dense white cloud turrets on the tops of the surge lobes, particularly on the downwind portions of the surge. This started about 1 minute after SZT and indicated a growth of the surge droplets, probably resulting from adiabatic cooling of the surge aerosol. The droplet growth occurred at heights above about 1,000 feet.

#### 4.7 FOAM PATCH

After the plumes had fallen back to the surface, and as the surge cloud dissipated and began to drift downwind, a white circular patch could clearly be seen about surface zero. The appearance of the foam patch is shown in Figure 4.22. Its whiteness is due to pulverized coral from the bottom of the lagoon and foam produced by the violent agitation of the water. Evidently, there was an upward flow of water in the vicinity of surface zero, similar to that observed on Wigwam and Wahoo. The water spread out radially, resulting in a gradual enlargement of the patch and an accumulation of foam and debris at its edge.

The foam patch was visible and measureable until 26 minutes after SZT. A comparison of Figures 4.22 and 3.25 shows the greater persistence and density of the Umbrella patch. Contours traced from RB-30 Film 52256 are shown in Figure 4.23. Diameters of six axes, relative to surface zero, were measured on these contours and were also extrapolated from major diameters measured from the C-54 records; these are shown in Figure 4.24. A single curve was drawn up to 500 seconds, because the foam patch was partially obscured by the surge cloud, which resulted in a great deal of scatter in the data. At later times, the asymmetry became more apparent, and separate curves were drawn for each axis.

A large indentation can be seen on the southwest side of the foam patch in Figures 4.22 and 4.23. An examination of aerial records showed that the DD-592 lay at the head of this indentation. Apparently, when the patch reached this ship, about 7 minutes after SZT, it consisted only of foam and debris in a shallow layer on the surface. The DD-592 was broadside to surface zero and thus blocked further expansion of this material. The supposition

that the foam patch was primarily on the surface at late times is further supported by a distinct motion of the patch in the downwind direction, as can be seen in Figures 4.23 and 4.24.

A region of radioactively contaminated water was detected on Shot Umbrella by Project 2.3; however, the dose rate was considerably smaller than that recorded on Shot Wahoo (Reference 31). Contamination of the water adjacent to the target ships was also measured by Project 2.1 (Reference 32). The only successful record obtained by this project was at the DD-593, beyond the foam patch, where a total dose of 0.7 r was recorded for the first 8.5 hours after the shot. It is probable that the settling coral scavenged most of the radioactive debris.

TABLE A.1 INITIAL STRAY DOME VELOCITIES AND COMPUTED YIELDS, SCOT UNDERSEA

Distance From Surface Feet	Slant Range	Station	Initial Spray Dome Velocity ft/sec	Mean Spray Dome Velocity ft/sec	Standard Deviation of Velocity ft/sec	P/σ	Mean P/σ	Effective Yield kt	Mean Effective Yield kt	Standard Deviation Yield kt
0	150	940	1190	1370	68	14.7	14.7	11.4	12.8	1.3
0		942	1190			11.2	10.7	11.9		
0		946.02	1390			11.0		13.2		
100L	180	940	920	1050	117	7.60	6.70	9.65	13.4	3.5
100R		940	1030			8.31		12.5		
100L		942	1160			9.82		15.0		
100R		942	980			8.40		11.2		
100L		946.02	1010			8.35		12.0		
100R		946.02	1390			10.7		19.3		
200L	250	940	599	539	57	4.39	6.19	20.0	15.6	2.7
200R		940	517			1.26		16.0		
200L		942	517			1.97		18.0		
200R		942	562			2.84		17.2		
200L		946.02	510			5.86		23.6		
200R		946.02	500			3.75		13.0		
300L	335	940	265	290	32	4.09	4.56	13.8	19.3	4.8
300R		940	290			4.46		17.0		
300L		942	310			4.77		19.8		
300R		942	280			4.11		12.1		
300L		946.02	280			4.46		14.3		
300R		946.02	375			5.46		27.3		
400L	477	940	193	190	22	3.79	3.79	26.2	26.1	8.7
400R		940	167			3.25		17.2		
400L		942	162			3.72		15.8		
400R		942	199			7.91		28.9		
400L		946.02	200			7.93		29.4		
400R		946.02	222			1.36		29.7		
500L	522	940	89	109	15	2.16	2.62	11.3	20.0	8.5
500R		940	108			2.46		16.3		
500L		942	98			2.36		13.9		
500R		942	131			3.20		14.8		
500L		946.02	116			2.86		28.5		
500R		946.02	105			2.52		16.8		
600L	618	940	76.9	76.9	8.1	2.18	2.33	20.5	19.2	3.4
600R		940	78.0			2.05		18.6		
600L		942	78.6			2.73		21.4		
600R		942	79.3			2.26		17.5		
600L		946.02	71.3			2.08		17.5		
600R		946.02	69.2			1.97		14.8		

\* L and R denote measurements to left and right of surface zero, respectively

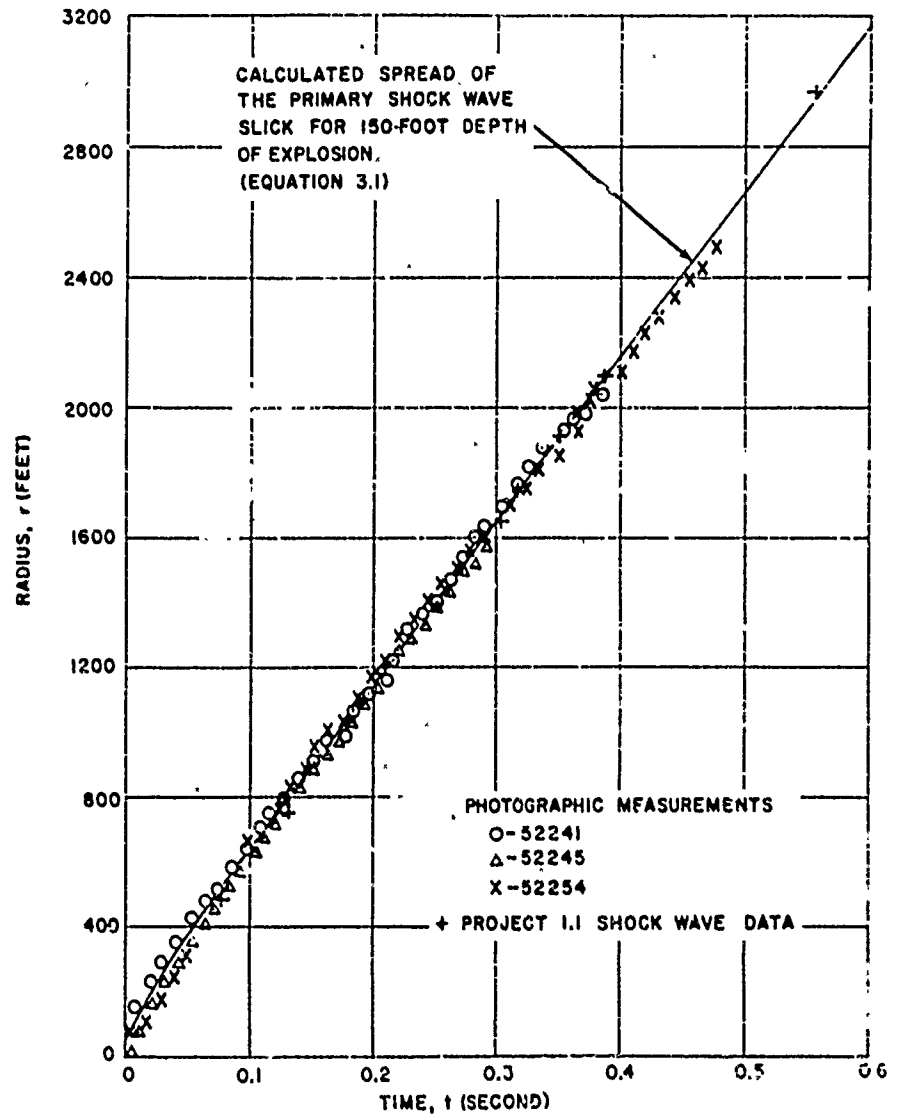


Figure 4.1 Primary shock wave slick, Shot Umbrella.

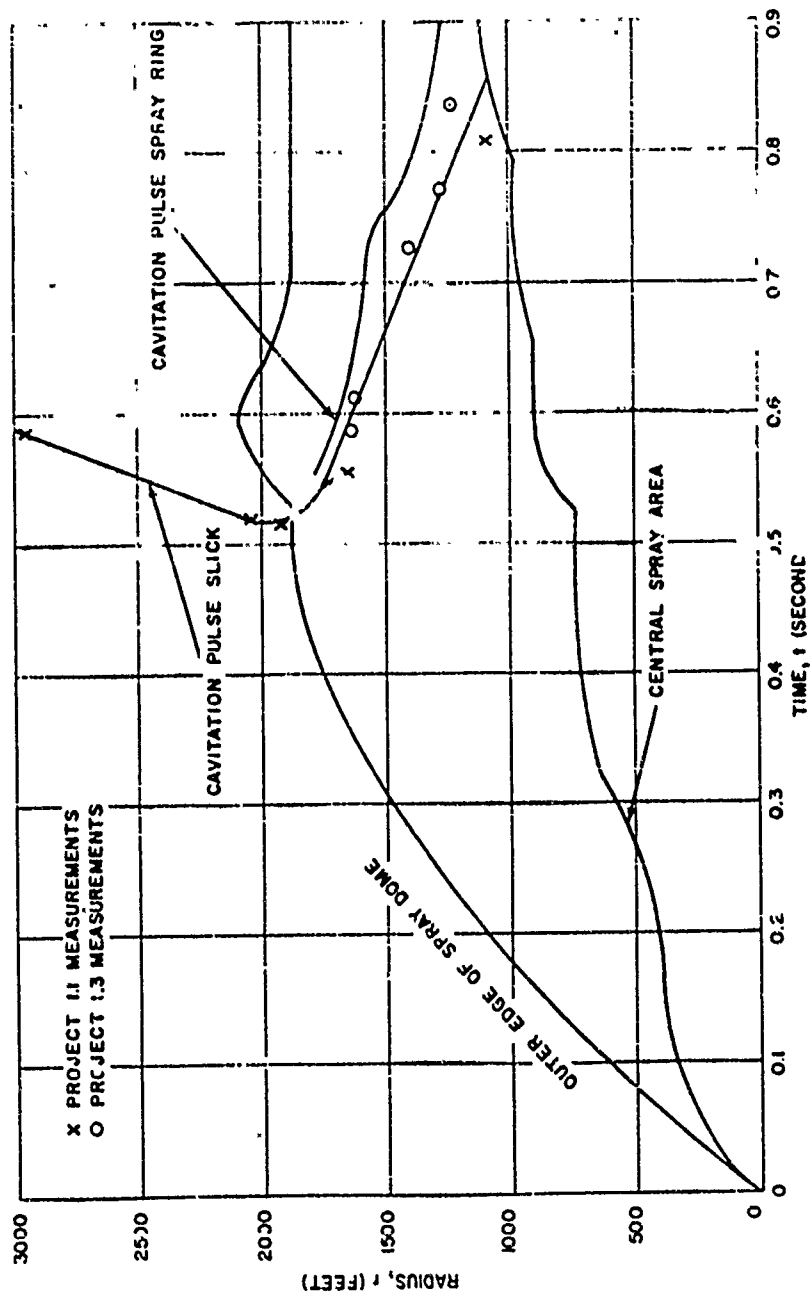
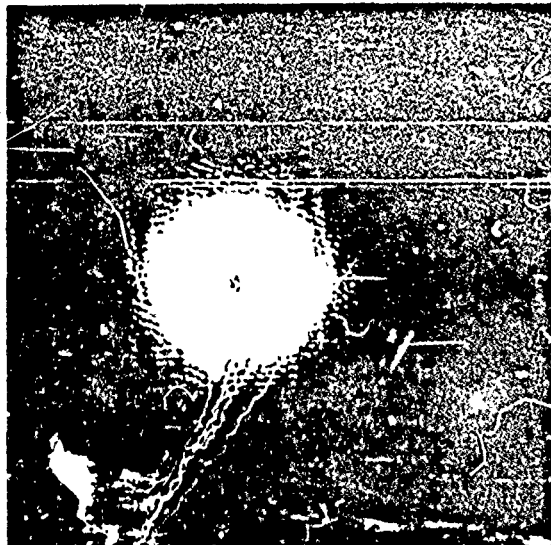


Figure 4.2 Lateral spread of spray dome, cavitation pulse slick, and spray ring, Shot Umbrella.





PRIMARY SHOCK WAVE SHOCK AND SPRAY DOME  
0.37 SECOND



CAVITATION PULSE SPRAY RING  
0.77 SECOND

Figure 4.3 Aerial views of slick, spray dome,  
and cavitation pulse spray ring, Shot Umbrella.

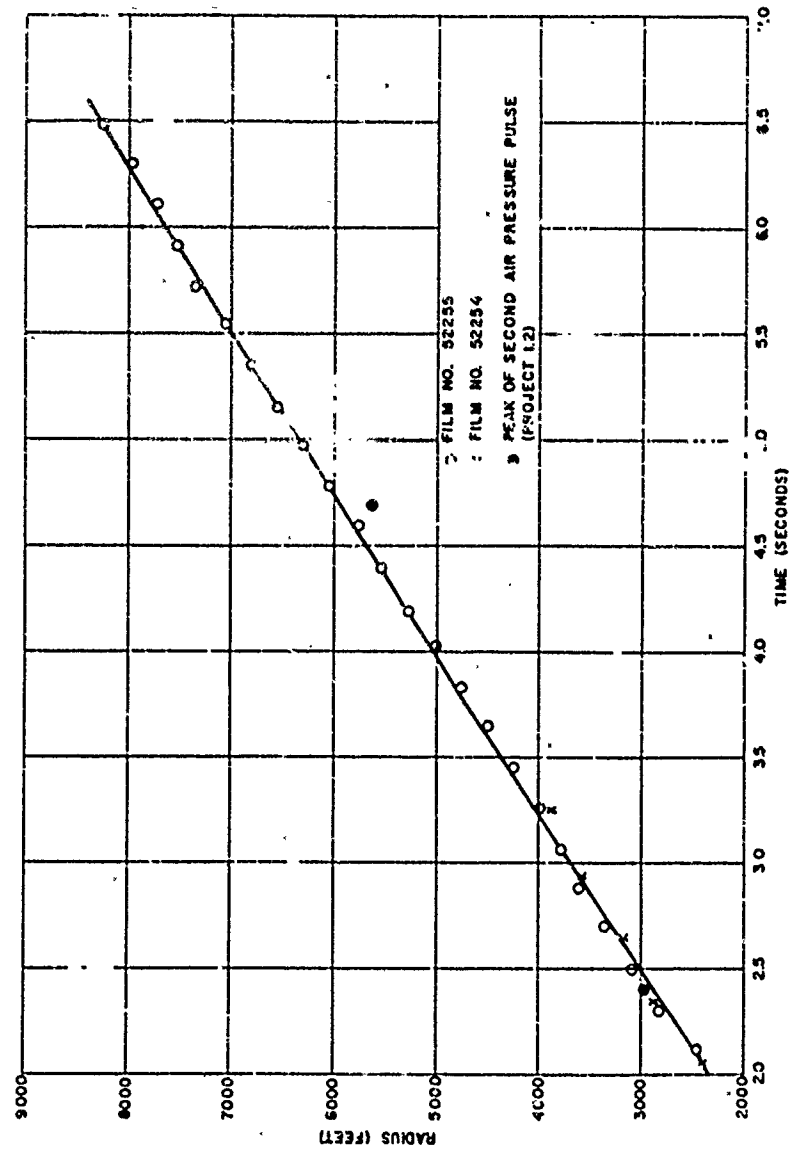
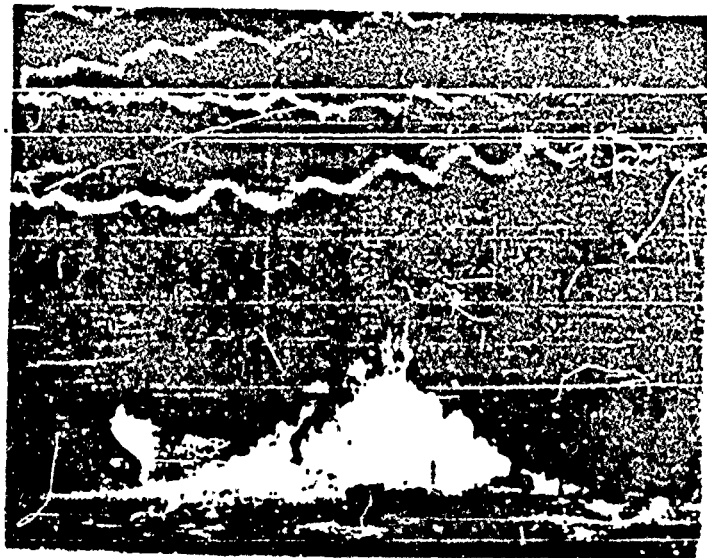
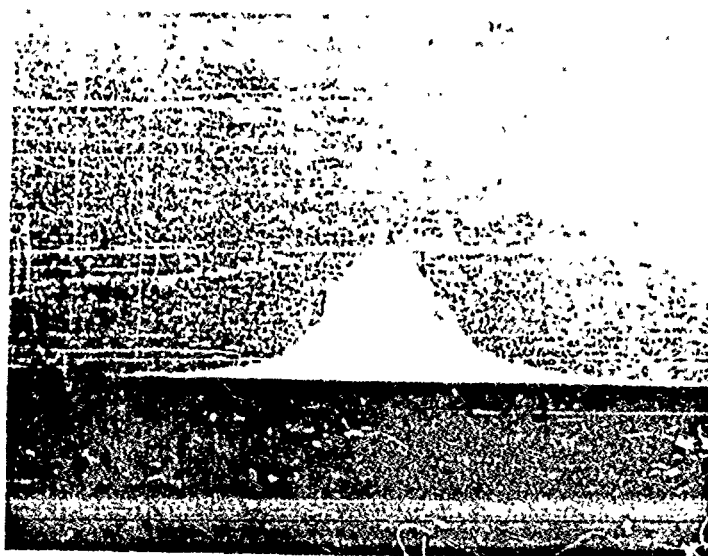


Figure 4.4 Spread of air shock wave along water surface, Shot Umbrella.



016 SECOND



037 SECOND

Figure 4.5 Spray dome, Shot Umbrella.

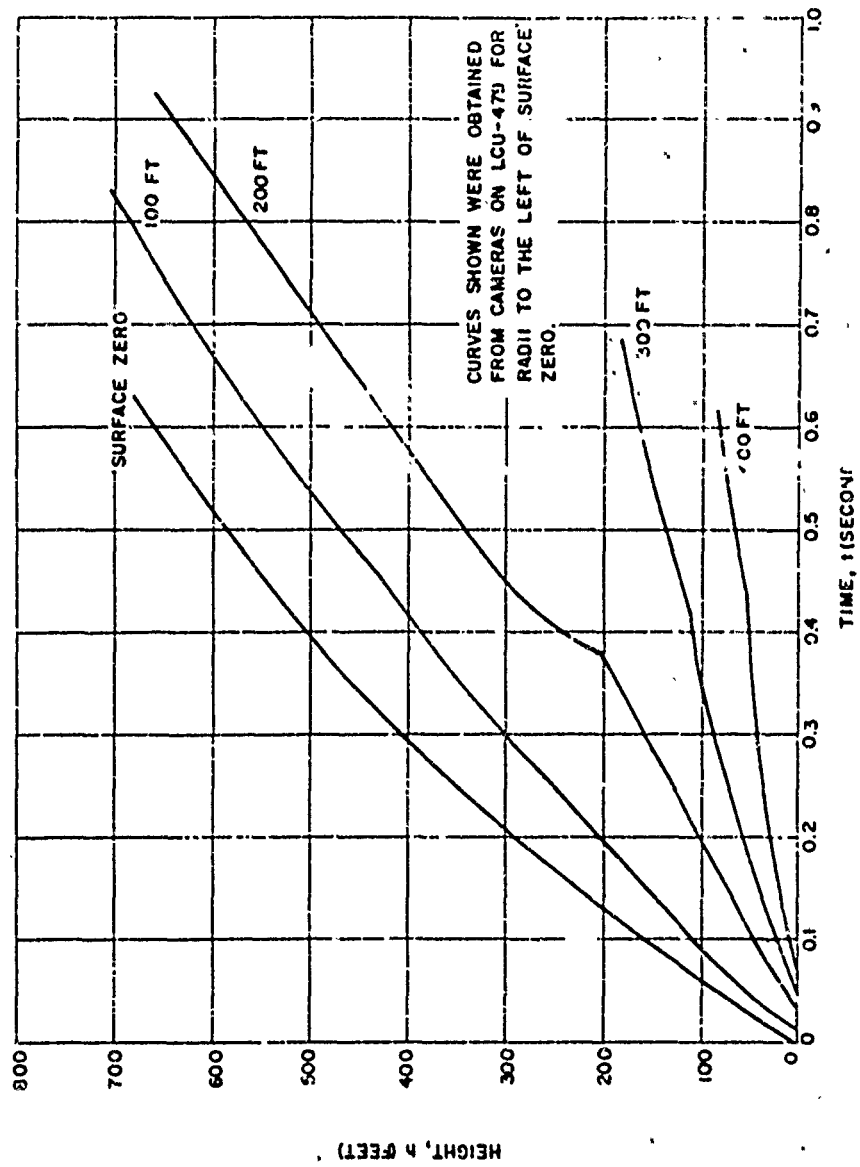


Figure 4.6 Spray dome height versus time, Shot Umbrella.

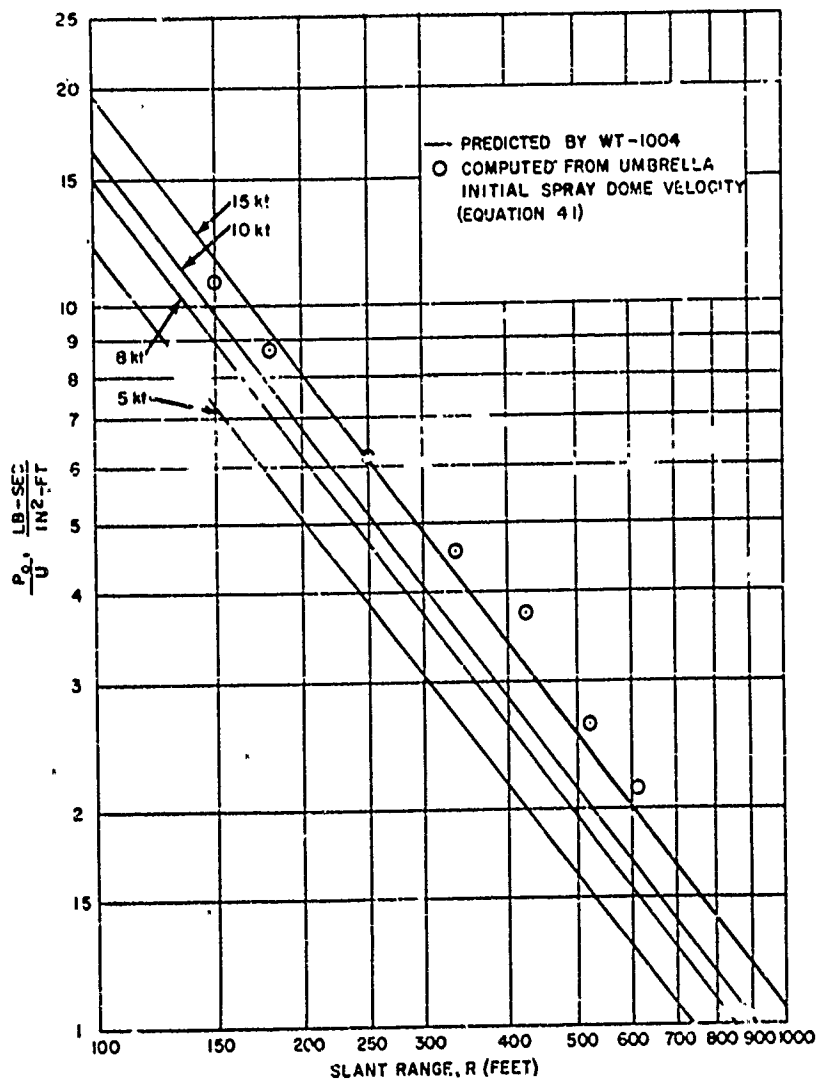


Figure 4.7  $P_0/U$  versus slant range, Shot Umbrella.

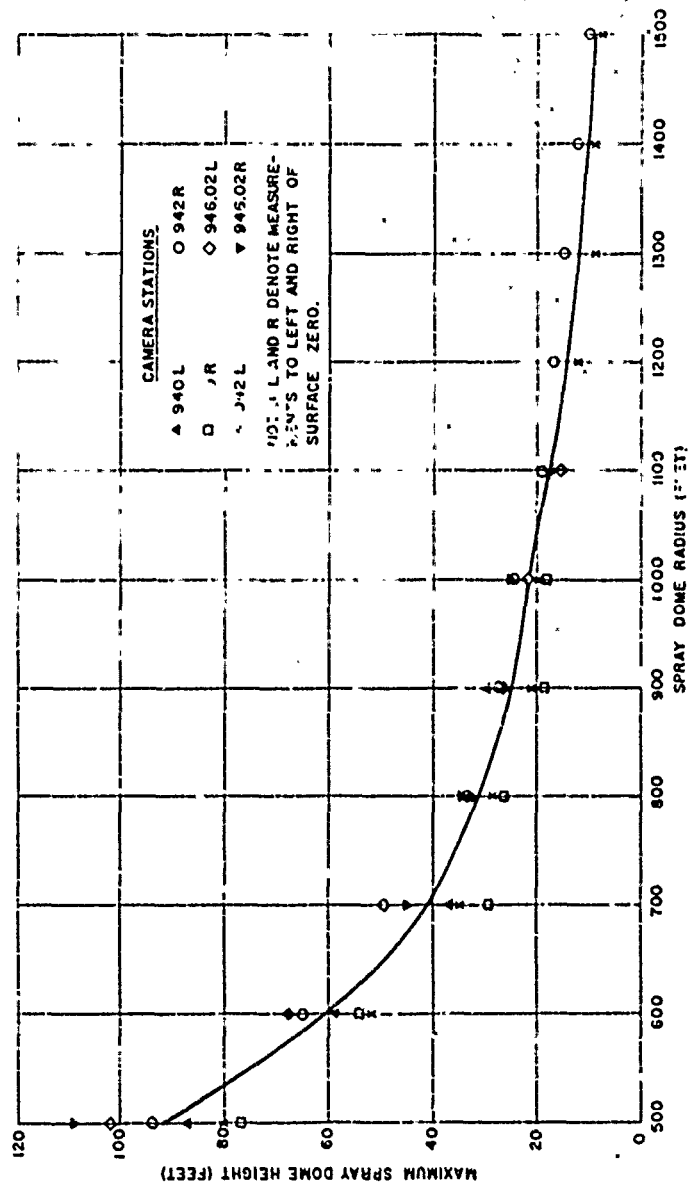


Figure 7: Maximum spray dome height for radii between 500 feet and 1,500 feet at about 1 second, Shot Umbrella.

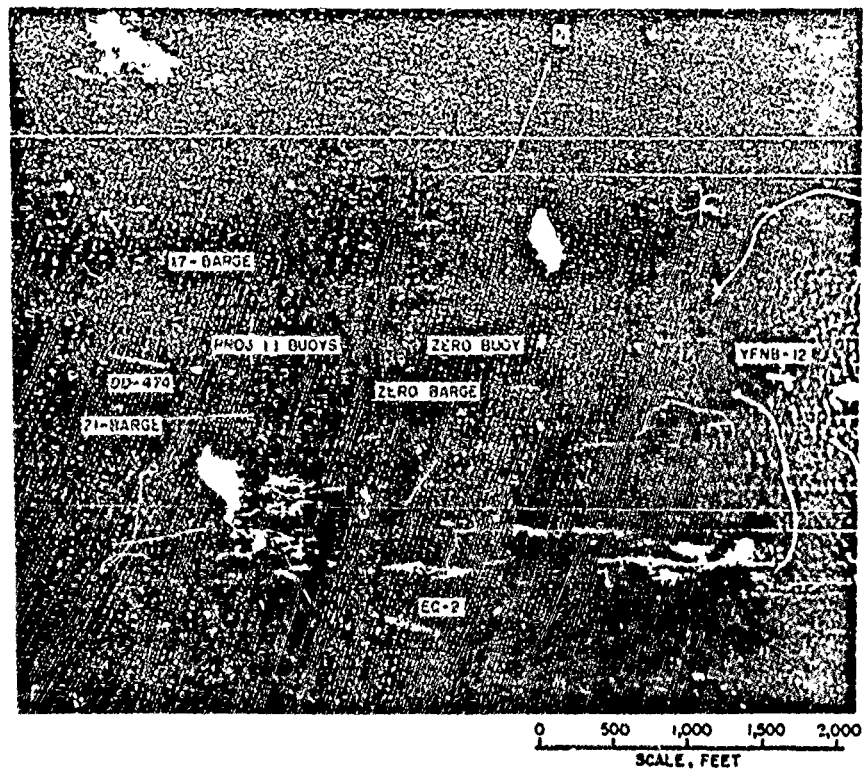


Figure 4.9 Locations of ships and buoys prior to detonation, Shot Umbrella.

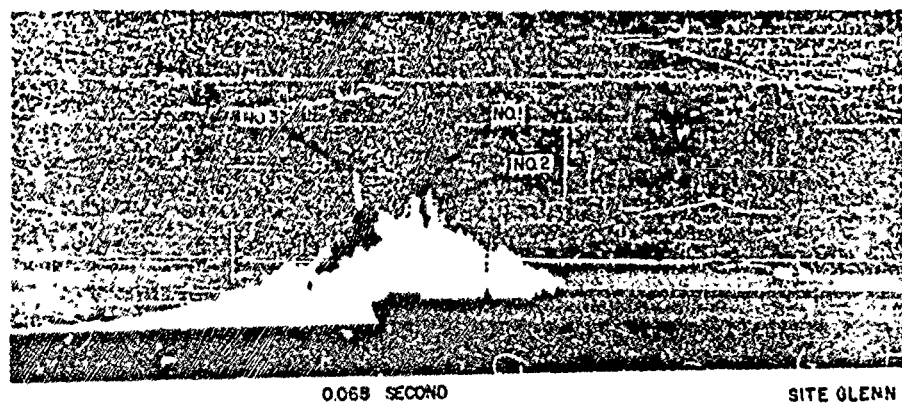


Figure 4.10 Objects rising above the spray dome, Shot Umbrella.

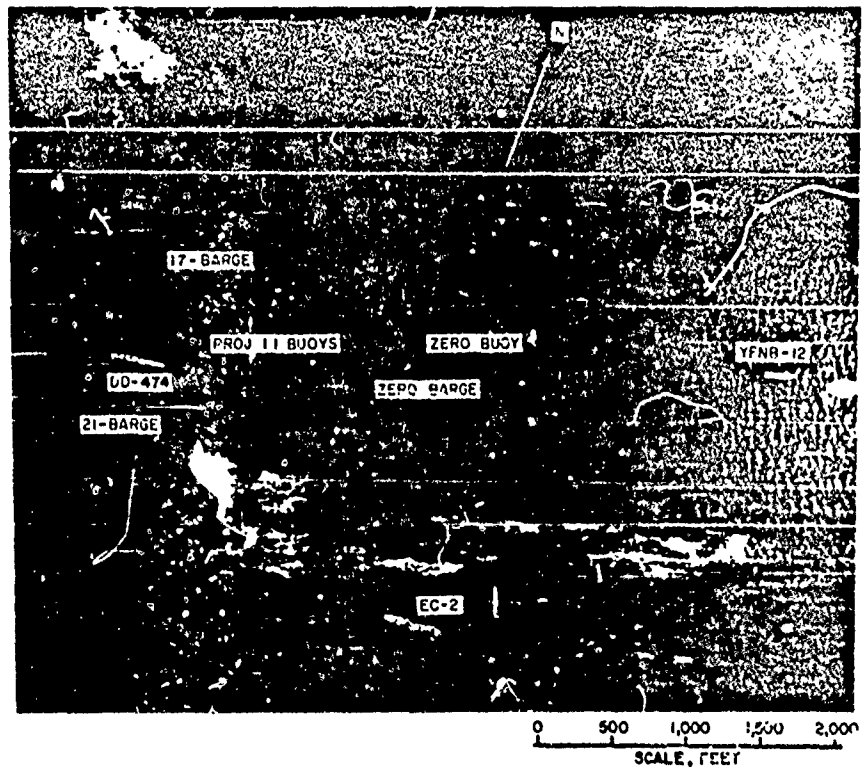


Figure 4.9 Locations of ships and buoys prior to detonation, Shot Umbrella.

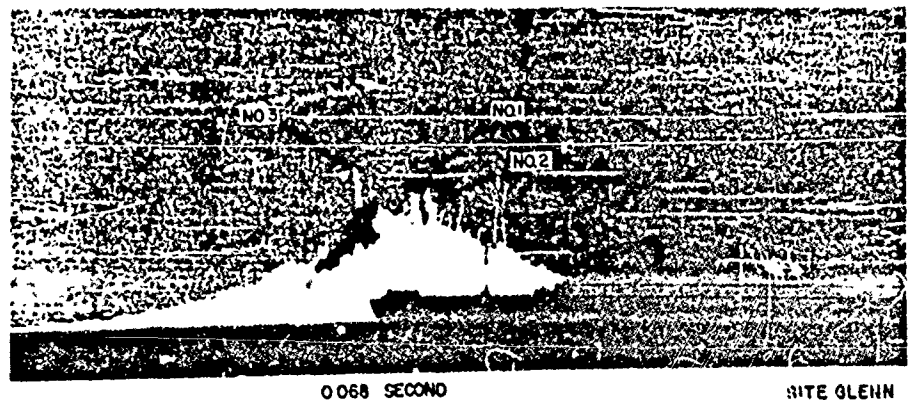


Figure 4.10 Objects rising above the spray dome, Shot Umbrella.



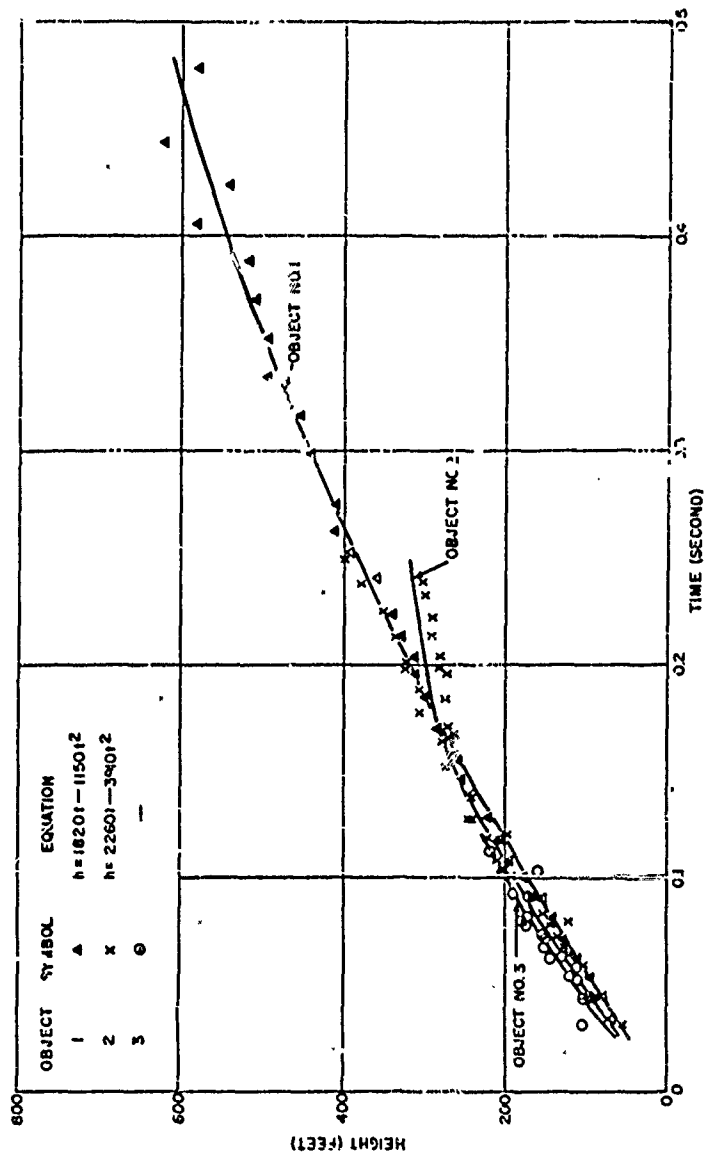


Figure 4.11 Trajectories of objects rising above target dome, Shot Umbrella.



13.380



28.370



5.2 SEC



8.2 SEC

SITE GLENN

Figure 4.12 Plume, Shot Umbrella.

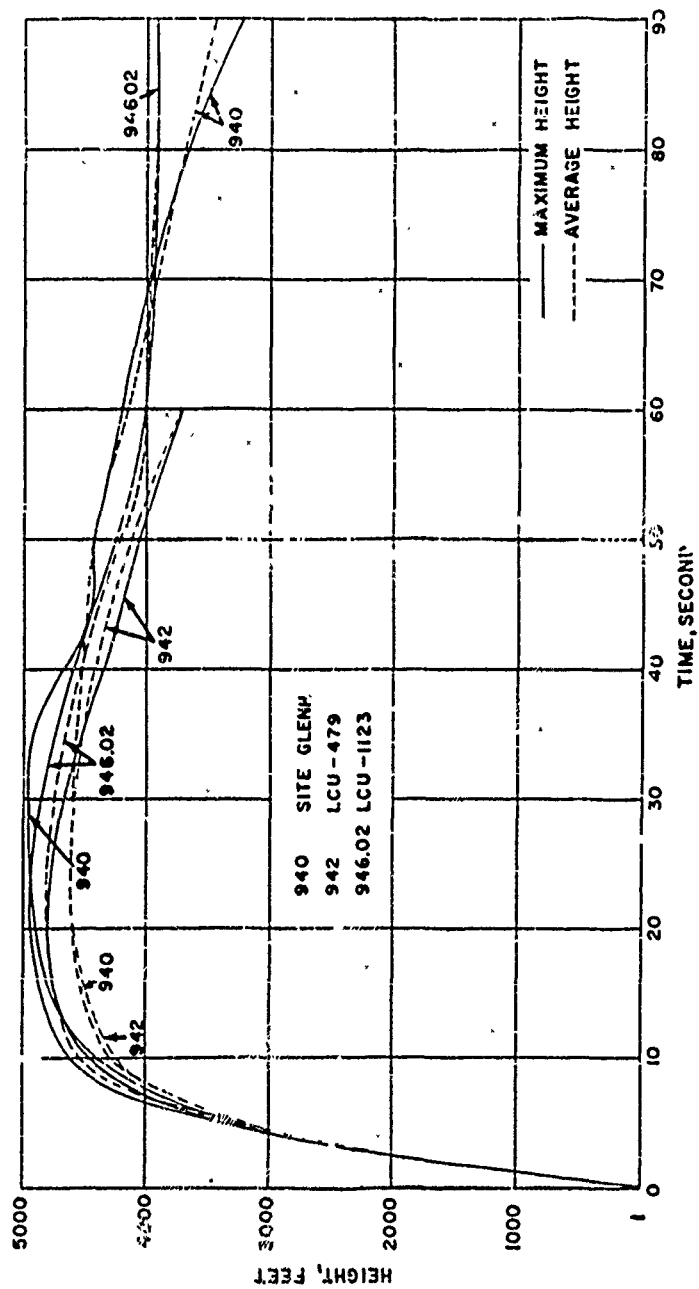


Figure 4.13 Plume height versus time, Shot Umbrella.

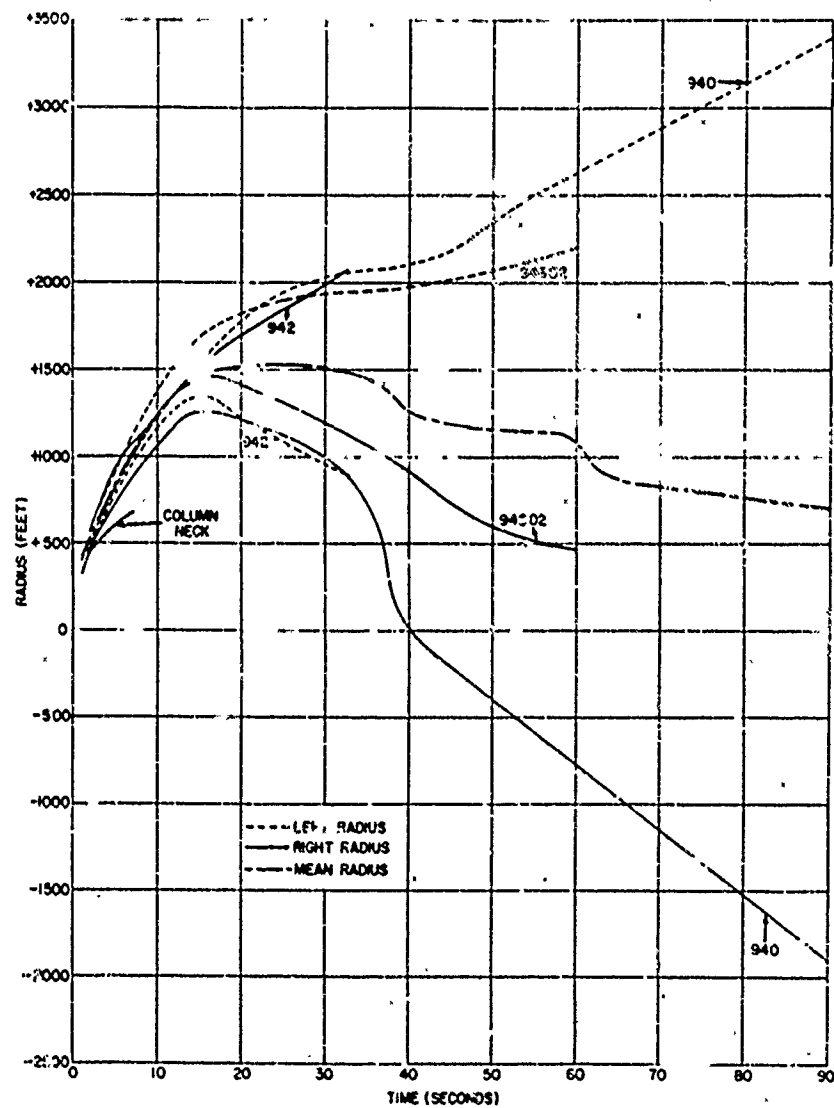


Figure 4.14 Plume radius versus time, Shot Umbrella.

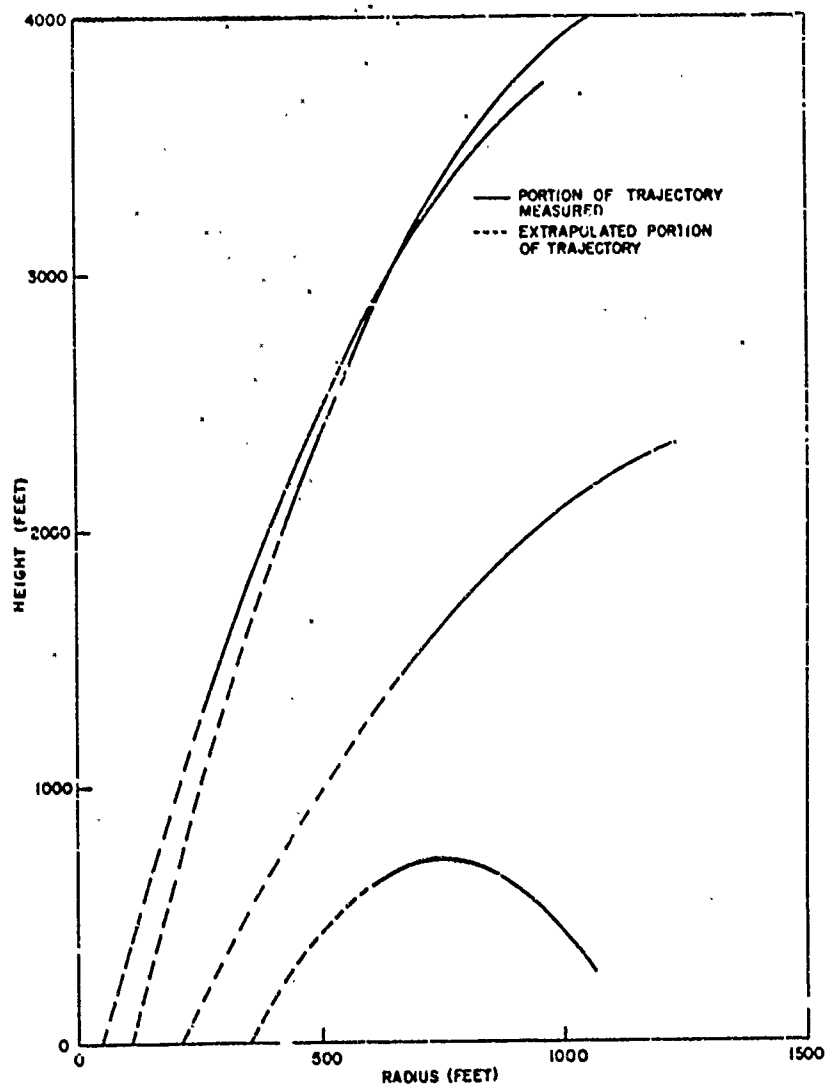


Figure 4.15 Trajectories of jets in plume, Shot Umbrella.



17 SECONDS



32 SECONDS

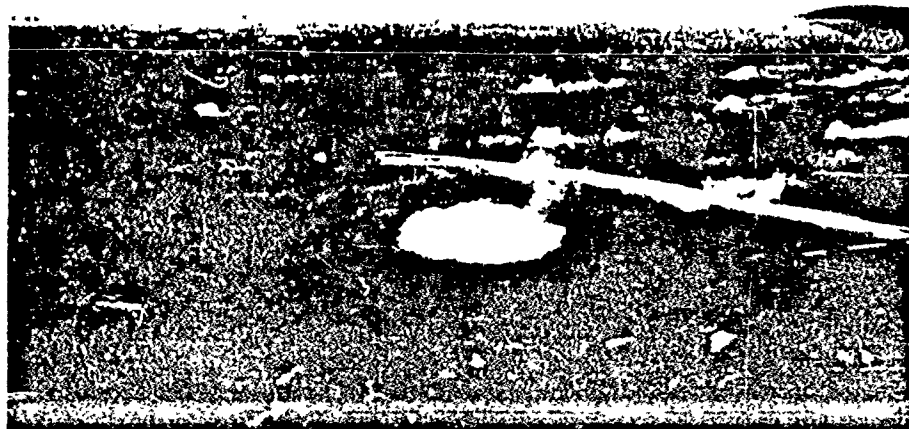


42 SECONDS

Figure 4.16 Collapse of plume and formation of base surge, Shot Umbrella.



2.6 MINUTES



6.9 MINUTES

Figure 4.17 Base surge at late times, Shot Umbrella.

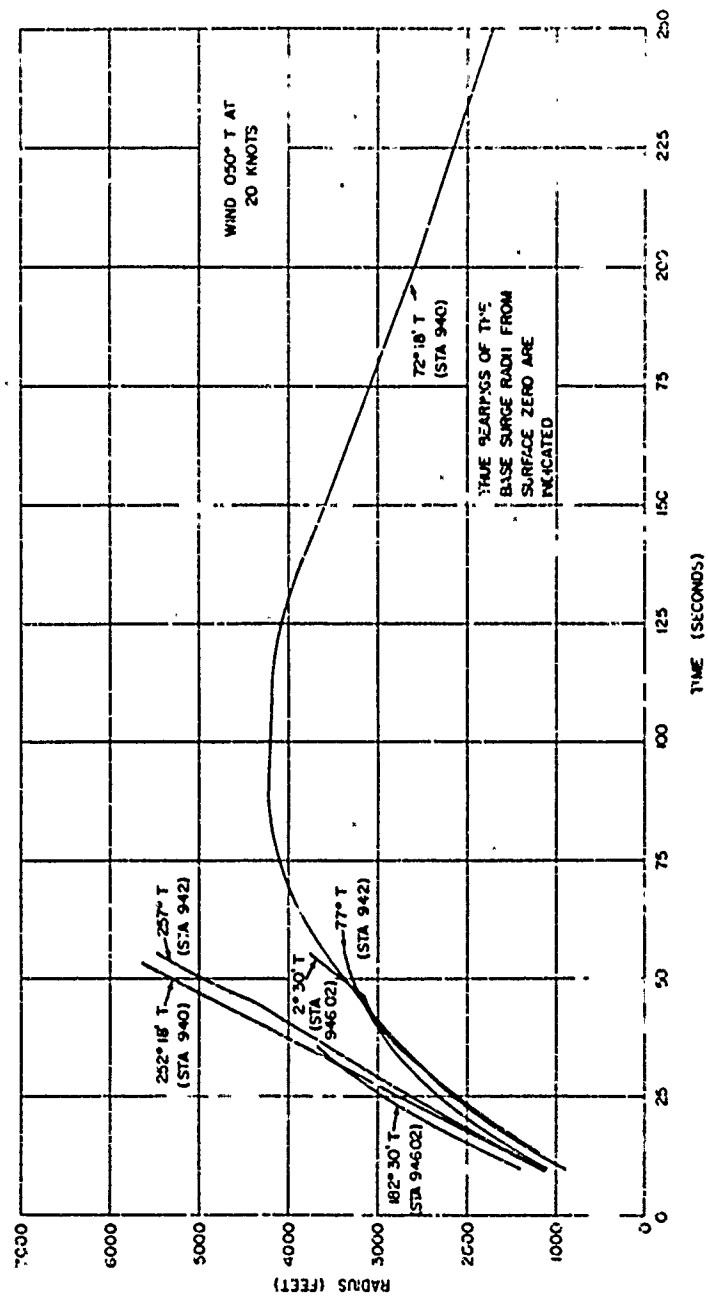


Figure 4.16 Base surge radius versus time, Shot Umbrella.



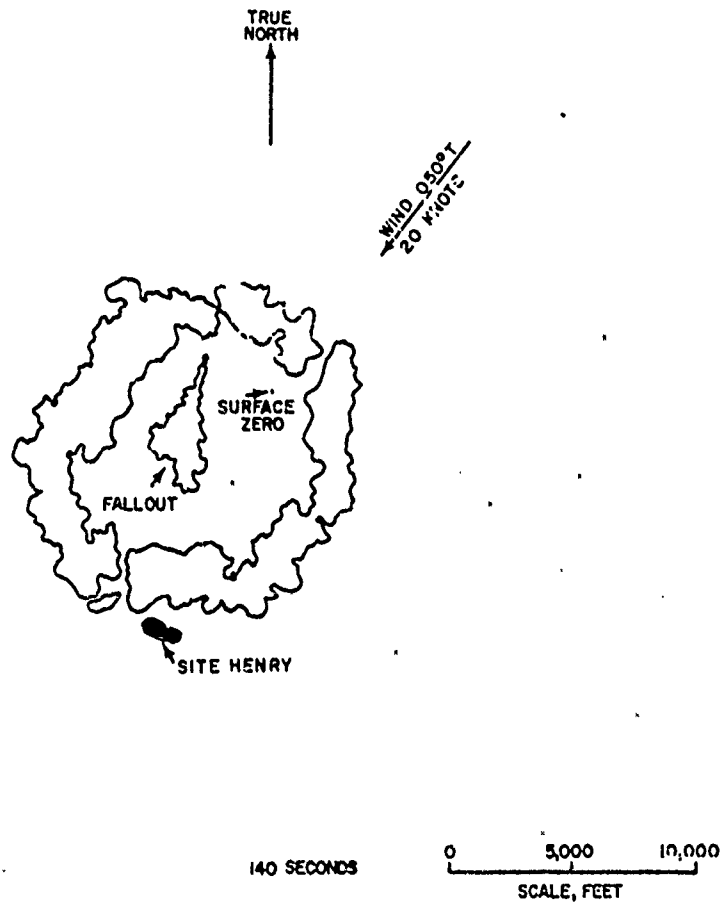


Figure 4.19 Base surge contour, Shot Umbrella.

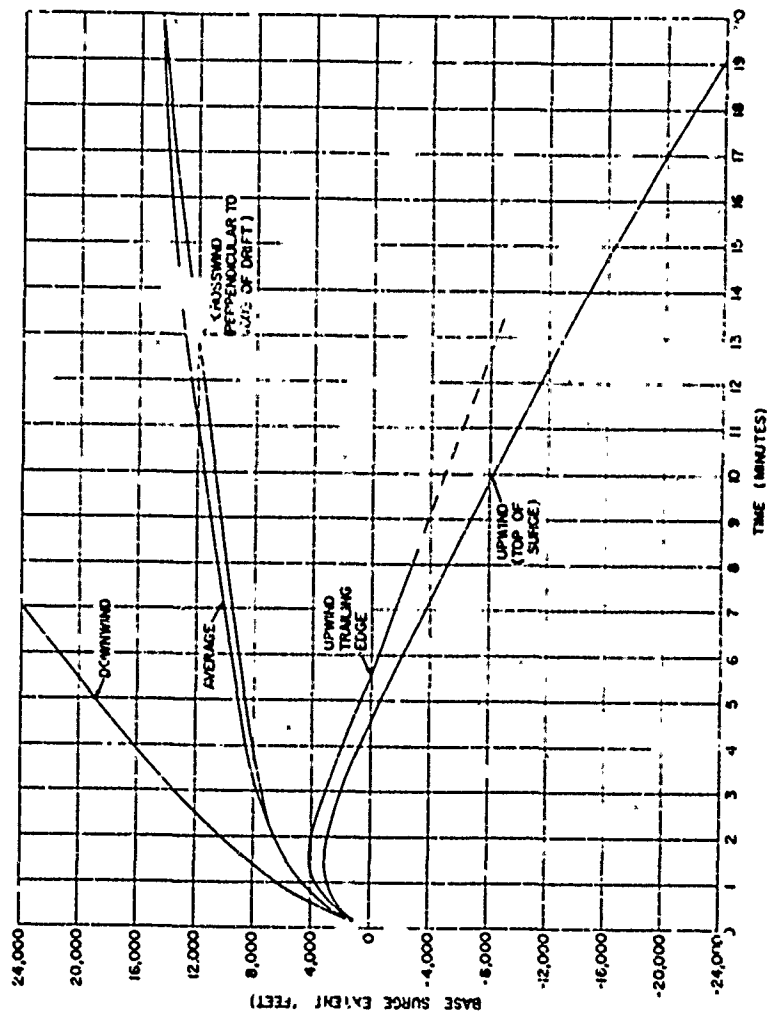


Figure 4.20 Base surge upwind, crosswind, and downwind extent, Shot no. 10.

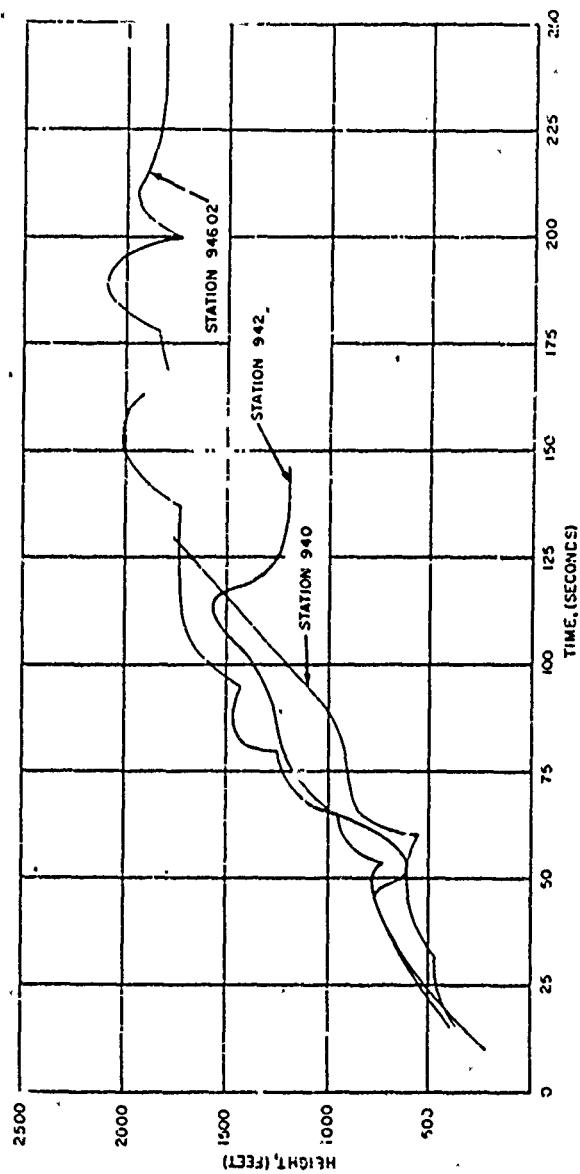
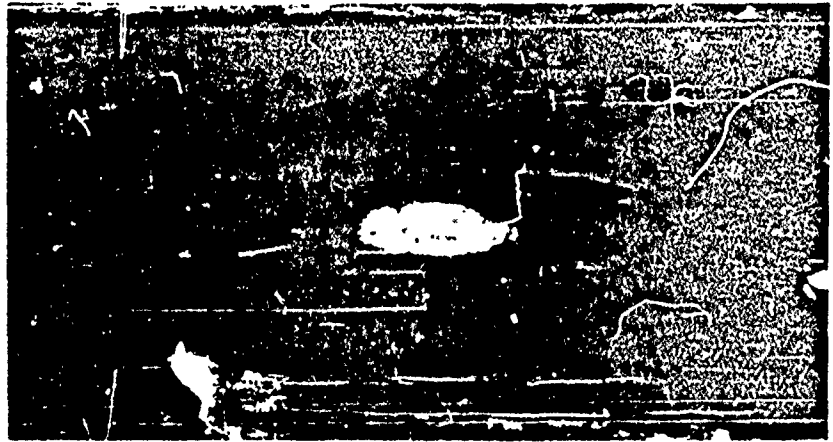


Figure 4.21 Maximum base surge height, Shot Umbrella.



69 MINUTES



146 MINUTES

Figure 4.22 Foam patch, Shot Umbrella.

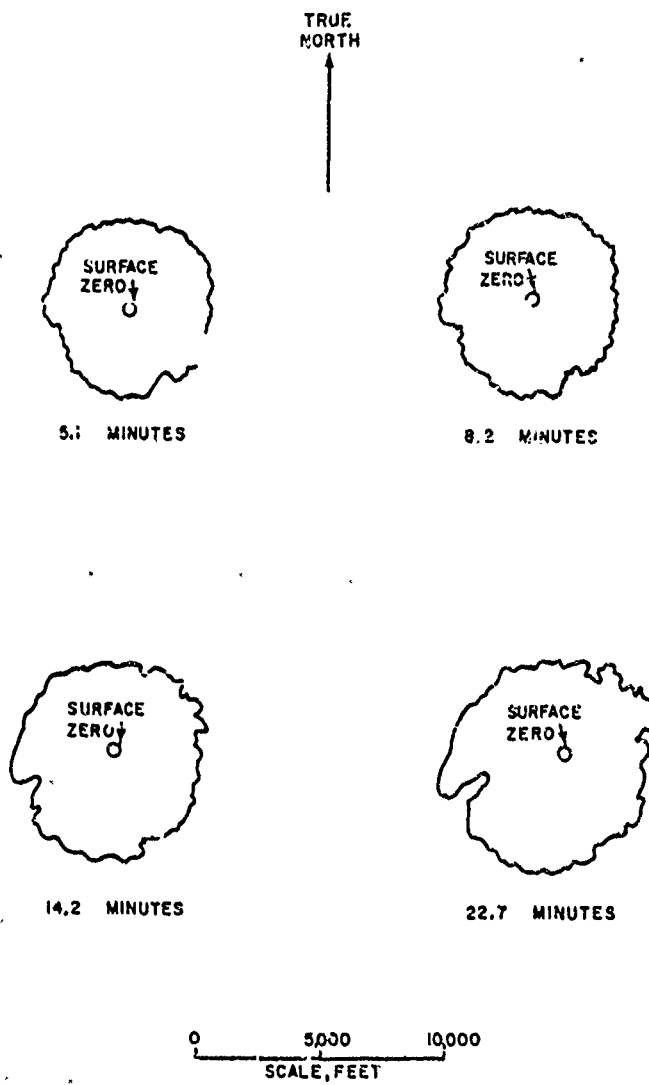


Figure 4.23 Foam patch contours, Shot Umbrella.

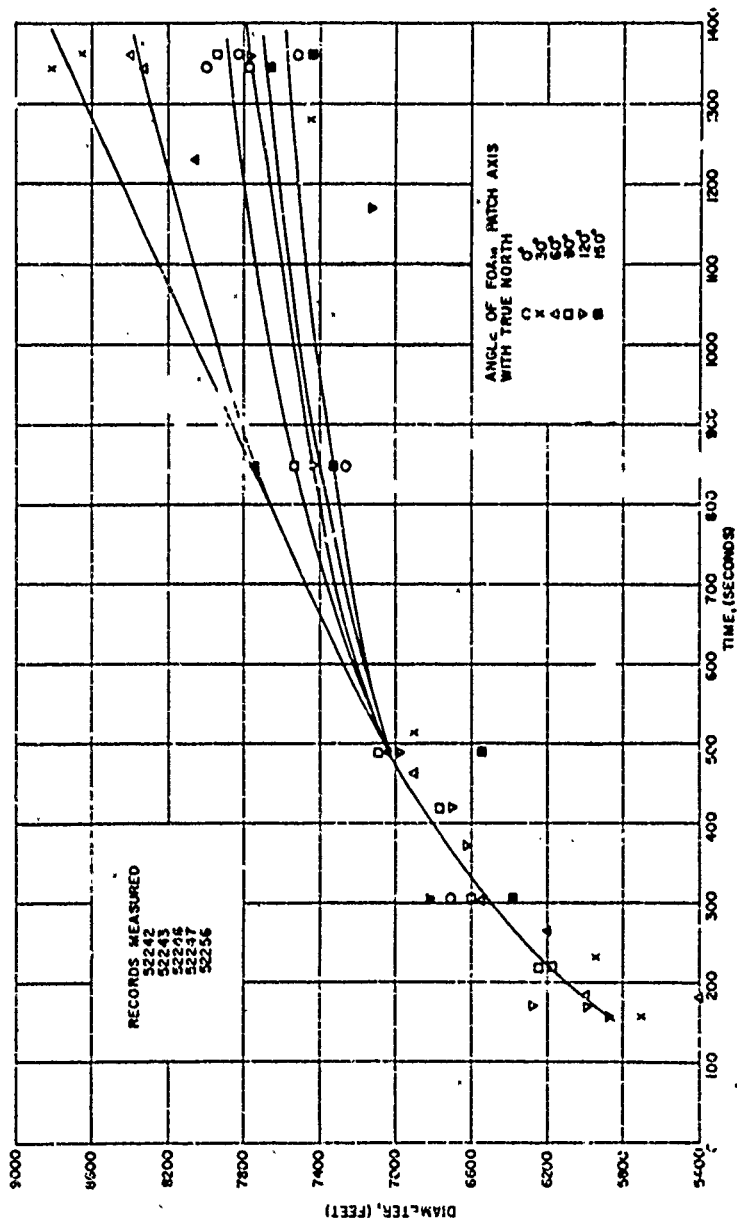


Figure 4.24 Foam patch diameter versus time, Shot Umbrella.

## Chapter 5

### TEMPERATURE AND HUMIDITY MEASUREMENT

#### 5.1 THEORY OF TEMPERATURE AND HUMIDITY CHANGES IN A BASE SURGE

When a base surge separates from the collapsing column or plumes formed by an underwater explosion, the mixture of closely spaced waterdrops and entrained air behaves like a homogeneous fluid flowing outward, because its bulk density is greater than the density of the ambient air. The drop size spectrum in the base surge has not been established, but an upper limit of 0.1 cm in diameter with possibly 50 percent of the drops smaller than 0.01 cm in diameter seen to be a reasonable rough estimate of the distribution at early times for a shallow burst (Reference 2). As the surge progresses outward, the processes of mixing, evaporation, and condensation change the drop size distribution and also the temperature in the surge, since evaporation is a cooling process, and condensation has a warming effect. The relative humidity of the entrained air is also affected.

The measurement of temperature and humidity change inside the Hardtack base surges was planned for the purpose of gaining some insight into these processes for shallow and deep nuclear bursts.

**5.1.1 Evaporation of Drops of Pure Water.** The rate of evaporation of a single stationary drop under steady state conditions is given by the following equation (Reference 33):

$$\frac{dM}{dt} = 2\pi Kd (\rho_d - \rho_a) \quad (5.1)$$

Where:  $\frac{dM}{dt}$  = rate at which mass (vapor) flows across the boundary of the drop, gm/sec

$K$  = diffusivity of water vapor in air, cm<sup>2</sup>/sec

$d$  = diameter of drop, centimeters

$\rho_d$  = water vapor density at the surface of the drop, gm/cm<sup>3</sup>

$\rho_a$  = water vapor density in the ambient air, gm/cm<sup>3</sup>

The total time required for the complete evaporation of a drop is

$$t = \frac{\rho d_0^3}{8K (\rho_d - \rho_a)} \quad (5.2)$$

Where:  $t$  = time for complete evaporation, seconds

$\rho$  = density of liquid water in the drop, gm/cm<sup>3</sup>

$d_0$  = initial diameter of drop, centimeters

Equation 5.2 indicates that the time required for drop evaporation is proportional to the square of the initial diameter and, consequently, to the initial surface area of the drop. The time for evaporation will be slightly less at high air temperatures than at low temperatures

because of the variation in the diffusivity  $K$ . This parameter increases slowly with increasing temperature in the atmospheric range, having, for example, values of 0.257 cm<sup>2</sup>/sec at 68° F and 0.273 cm<sup>2</sup>/sec at 88° F.

Equation 5.2 also shows that the evaporation time is inversely proportional to the difference between the vapor density at the drop surface and the vapor density in the ambient air. At the drop surface, the air is assumed to be saturated with vapor at the temperature of the drop. If  $\rho_d$  exceeds  $\rho_a$ , evaporation occurs; if  $\rho_d$  is less than  $\rho_a$ , water vapor condenses on the drop.

Although Equation 5.2 is correct for a steady-state condition (constant  $\rho_d$  and  $\rho_a$ ), this seldom occurs in a base surge, and the variations in  $\rho_d$  and  $\rho_a$  and drop and air temperatures can be quite complex.

In the ambient atmosphere, relative humidity may be defined as:

$$\text{R.H.} = 100 \left( \frac{\rho_a}{\rho_{as}} \right) \quad (5.3)$$

Where: R.H. = relative humidity, percent

$\rho_{as}$  = vapor density at saturation, gm/cm<sup>3</sup>

The saturation water vapor density  $\rho_{as}$  is measured in reference to a plane surface of pure water. It is a function of temperature only. If a plane surface of pure water is at the same temperature as the air above it and the air is at a relative humidity of 100 percent,  $\rho_a = \rho_{as}$ , and a state of equilibrium exists. If the relative humidity is less than 100 percent,  $\rho_a < \rho_{as}$ , and evaporation occurs.

The behavior of drops of water is more difficult to treat than the behavior of a large volume of water with a level surface. Two effects that occur with small droplets are an increase in equilibrium vapor pressure because of surface tension and a decrease in equilibrium vapor pressure if the droplets carry an electrical charge. However, both of these effects are negligible for drops greater than about  $2 \times 10^{-4}$  cm in diameter (Reference 34). Drops smaller than this size will not be considered in the following discussion, since it is believed that only a very small fraction of the drops in the surge fall in this size range.

**5.1.2 Effect of Salinity.** The salinity of sea water reduces the vapor density at the surface to a value about 98 percent of the value of  $\rho_d$  at the surface of pure water (Reference 35). Consequently, the surface of the ocean is in equilibrium with the air if the relative humidity is 98 percent, providing the water and air are at the same temperature.

If the relative humidity is less than 98 percent, a drop of sea water at air temperature will start to evaporate. As the drop shrinks, the concentration of dissolved sea salts increases, resulting in a gradual lowering of  $\rho_d$ . A saturated solution of sea salt is in equilibrium with its surroundings at a relative humidity of about 79 percent (Reference 36). At this stage the salinity is about 155 parts per thousand (Reference 37). Consequently, a drop of sea water will evaporate until it becomes a saturated solution if the ambient relative humidity is 79 percent or less. If the relative humidity is 33 percent or less, evaporation will continue until dry salt particles remain (Reference 36). The percentage change in the initial diameter of a drop of sea water as a function of relative humidity is shown in Figure 5.1. The relative humidity at the four underwater nuclear tests is also indicated.

**5.1.3 Effect of Temperature.** The process of heat exchange is important to the entire evaporation (or condensation) process and cannot be neglected. Initially, a water drop produced by an underwater explosion may be warmer or cooler than the air or it may be the same temperature. If the explosion heats the water surrounding it, heated water may enter the base surge.



If a drop is warmer than the air,  $\rho_d > \rho_a$ , and evaporation will take place. A fraction of the heat in the drop is conducted to the air and the remainder is used for evaporation. If the relative humidity is below the saturation value, evaporation will continue, with heat provided by the drop, until the drop cools to the temperature of the air. At later times, the heat for evaporation will be provided by conduction from the air. The drop then cools to approximately the ambient wet-bulb temperature  $T_w$ . In an infinite atmosphere, a steady state is reached and the drop remains at approximately  $T_w$  while it evaporates, providing  $\rho_d$  at the drop temperature exceeds  $\rho_a$ . For a drop of pure water, evaporation should be complete. With sea water, the percentage of evaporation of a drop is shown by Figure 5.1. At equilibrium, the drop temperature returns to the ambient value.

It is also possible that an explosion in cold water will produce drops that are colder than the air. In this case, evaporation will occur if the relative humidity is low ( $\rho_d > \rho_a$ ). However, high relative humidities are more common over a water surface and, if  $\rho_d < \rho_a$ , the surge drops will grow instead of evaporating. This would have a warming effect.

**5.1.4 Applicability to Base Surge.** For convenience, the changes which occur in the base surge may be divided into three stages, as discussed in Section 1.4.4. During Stage 1, the surge is assumed to be dense, highly concentrated aerosol that does not mix with the ambient air. During Stage 2, mixing occurs, and the surge is gradually diluted. During Stage 3, the surge drops are widely separated and behave as though they were in an infinite atmosphere.

For a small HE test in fresh water, Stages 1 and 2 are very brief, and, if the initial drop temperature is near the ambient wet-bulb temperature, Equation 5.2 provides a good order-of-magnitude estimate for the duration of the base surge.

For a large explosion in fresh water, the air between the drops during Stage 1 should cool to the wet-bulb temperature. In this case, the air becomes saturated, and evaporation ceases. However, during Stage 2, the relative humidity in the surge is reduced by mixing with drier air, and evaporation continues at a rate depending on the rate of mixing. During Stage 3, the drops evaporate completely.

When an explosion occurs in the ocean, similar results occur except that the drops of sea water do not completely disappear. They may remain as a concentrated solution of salts or dry salt particles, depending upon the relative humidity.

The situation was more complicated during Shot Baker of Operation Crossroads when new cloud development occurred at the top of the base surge during Stage 2. This was a result of the lifting of the humid unstable ambient air by the surge. Subsequently, a rainout occurred, possibly originating in the new upper clouds. This rainfall probably scavenged the base surge droplets and deposited the surge material on the surface of the lagoon or on target vessels.

## 5.2 INSTRUMENTATION

Temperature-humidity recording stations were established at various distances from surface zero on Shots Wahoo and Umbrella. The major component at each station was a Foxboro resistance dynamometer temperature recorder, which was modified at NOL to record both dry- and wet-bulb temperatures. Relative humidity was calculated from the two temperatures (Reference 38).

**5.2.1 Recording Instrument.** A Foxboro resistance dynamometer recorder measures temperature variations by means of the change in electrical resistance of a sensing element, through a modified Wheatstone bridge. The output of the circuit is recorded by mechanical linkage on a synchronous motor-driven chart directly as temperature in degrees Fahrenheit. The

recorders used have three ranges: 20° to 70°, 40° to 90°, and 50° to 100° F. The range depends on the values of resistors inscribed in the circuitry (Figure 5.2, Item 5). For Operation Hardtack, the 50° to 100° F range was used because of climatological conditions at EPJ.

The Foxboro recorders were checked for linearity by the use of precision resistors. An attempt was made to hold errors in linearity to  $\pm 0.1^\circ\text{F}$ , but small accumulative tolerances in the pen linkage and chart positioning from chart to chart may have increased the error to  $\pm 0.3^\circ\text{F}$ . This gave a systematic discrepancy between the actual temperature and that recorded but did not affect indicated temperature changes once the recorder was in operation. Temperature changes as small as  $0.1^\circ\text{F}$  could be seen on the records. It is believed these are real. Test readings of temperature on the same record by several persons agreed to  $\pm 0.1^\circ\text{F}$ .

**5.2.2 Power Supply.** The power supply employed in the field was a combination of 6-volt, 90 ampere-hour batteries, wired in series, and an American Television and Radio Co. (ATR) 12U/RSF inverter. The inverter changed the 12-volt dc battery power to 110 volts, 60 cps, and a rated output of 100 to 125 watts at the 110-volt level.

The frequency and voltage output of each ATR inverter were checked under the varying conditions expected in the field. Output voltages remained well within the operational limits for the Foxboro recorder ( $\pm 10$  percent). Frequency varied about 3 percent under all test conditions, but for each individual inverter unit the reproducibility was  $\pm 0.5$  percent. The reproducibility of the frequency output of each inverter was important, because the chart speed varied with this parameter. Provisions were made to record the minus 1-minute and the minus 1-second radio timing signals on the edge of each chart. From these radio signals it was possible to determine chart speed near zero time and also zero time itself with a high degree of accuracy. Chart speeds determined from these radio timing signals and those determined with a stable source in the laboratory are given in Table 5.1.

**5.2.3 Mounting and Shielding of Temperature Elements.** The Stikon sensing element (BN-2 thermometer manufactured by Arthur C. Ruge Associates, Inc., Hudson, N.H.) was a grid of fine nickel wire (0.0008-inch diameter) bonded into a paper-thin Bakelite wafer. The dimensions of the wafer were 1.5 by 0.5 by 0.005 inches. This element was bonded, in accordance with instructions of the element manufacturer, onto a strip of metal 0.013 inch thick. The metal backing strip was used to attach the element to a holder.

Two types of holder were used to position the elements; these are shown as Item 7 in Figure 5.2. A plastic holder was used for the dry element to provide as fast a response time as possible. Since the response of the wet element is inherently faster, the stronger, more simply constructed metal holder was used. After the elements were bonded to the backing strips and mounted on the holders, they were waterproofed with a very thin coating of Araldite (manufactured by Ciba Company, Inc., New York, N.Y.). The required number of these units plus an equal amount of spares were prepared and tested in the laboratory. The units were designed so that they could be easily changed in the field.

Two of these sensing elements, one dry-bulb and one wet-bulb, were connected to each recorder alternately through a cam-operated microswitch (Figure 5.2, Item 5). The cam was cut so that the dry-bulb recorded for a period about three times as long as the wet-bulb (approximately 6 seconds and 2 seconds). The wet-bulb element was covered with a wicking that extended into a reservoir of distilled water. The capacity of the reservoir permitted unattended operation for a period of several days.

The mounted elements were positioned in separate compartments in specially designed shields (Figure 5.3). These shields were designed to give the sensitive elements maximum protection from solar radiation and precipitation or fallout. An electrically driven fan.

which furnished an airflow of about 11 ft/sec, was installed below the elements in each unit to insure sufficient ventilation of the elements.

The shielding of the elements against solar radiation and precipitation was checked for effectiveness by comparing recorded data with data obtained from standard temperature-humidity measuring instruments in standard Weather Bureau instrument shelters during various climatic conditions. The system was also given in preliminary field test in the Project 3.1 trials off the coast of California during January 1958. Tests were also made on the instrumentation during dry runs and trial operations of the washdown systems. It was found that the recorded temperature and humidity were not affected by the washdown systems or by other equipment operating in the vicinity of the sensing elements.

**5.2.4 Assembly of Recording System.** The recording system (Foxboro recorder, batteries, inverter, and circuit panel) and associated components for each station were enclosed in a waterproofed sheet metal box measuring 14 by 18 by 34 inches. The inverter required mounting on Lord shock mounts to minimize oscillations that might tend to influence its vibrator. The recorder, batteries, and circuit panel were attached rigidly to the sides and bottom of the box. Eight points were provided on the sheet metal box to attach the shock cord which supported the unit. The recorder in shock mounts is shown in Figure 5.4. A block diagram of the circuitry is shown in Figure 5.5.

Each unit was checked and calibrated separately, then all units for a station were assembled and calibrated as a system. In the calibration of the complete system, the sensing elements were attached to the same cables that were to be used in the field and were immersed in agitated water at room temperature. Since the resistance of each element varied slightly, the recorder was adjusted so that the reading of the dry-bulb temperature agreed with a precision mercury-in-glass thermometer. At the same time, the value recorded by the wet-bulb was noted. The difference between the two readings, usually 2 percent or less, was applied as a correction to each of the wet-bulb temperatures. If it was necessary to replace a unit of the system in the field, the entire system was recalibrated.

**5.2.5 System Response.** When a temperature-indicating device of any kind, at an initial temperature  $T_0$ , is placed in a medium with a temperature  $T_m$ . It does not immediately assume the temperature of the medium but approaches it asymptotically at a rate depending on the properties of the device and the medium. The change in the indication of the device with time is given by Reference 39:

$$\frac{dT}{dt} = -\frac{1}{\lambda} (T - T_m) \quad (5.4)$$

Where:  $T$  = the instantaneous temperature indicated by the device, °F

$t$  = time, seconds

$\lambda$  = lag coefficient of the device, seconds

Assuming that  $T_m$  is constant, Equation 5.4 can be integrated to yield:

$$T - T_m = (T_0 - T_m) e^{-t/\lambda} \quad (5.5)$$

Where:  $e$  = base of natural logarithms, 2.718.

If  $t = \lambda$  in Equation 5.5, then

$$T - T_m = \frac{1}{e} (T_0 - T_m) \quad (5.6)$$

which indicates that  $\lambda$  is the number of seconds required for the difference between the indicated temperature and temperature of the medium to be reduced to  $1/e$ , or 37 percent of its initial value.

Another term frequently used in temperature measurements is the "time constant", which is the period of time, in seconds, required for a device to reach a given percentage of the total temperature change. As defined here, the lag coefficient  $\lambda$  is equal to the 63-percent time constant and  $2.3\lambda$  is equal to the 90-percent time constant.

If a temperature change from  $T_0$  to  $T_m$  occurs as a step function and  $\lambda$  is known,  $T_m$  can be calculated from the temperature-versus-time curve on a recorder. It is also possible to integrate Equation 5.4 and calculate the actual temperature from the recorder values, if  $T_m$  is a linear or periodic function of time.

The Foxboro recorders are capable of full-scale response in 1 second. However, the response of the recording instrument is limited by the response of the sensing elements, which, in turn, is dependent on a number of factors, such as the method of mounting, the thickness of the water proof coating, the shielding of the elements, and the velocity of the air.

The response time of the Hardtack instrumentation was determined by both a rise and a decrease in temperature. Several temperature differences were used. Two enclosures with different temperatures were employed. The assembled element and shielding were placed in one of the enclosures and allowed to stabilize at that temperature. Then, when the recorder indicated that the elements and shielding were in equilibrium, they were transferred quickly to the second enclosure. The time required for the sensing element and shielding to stabilize at the temperature of the second enclosure was obtained from the timed chart of the recorder being tested. The 63-percent and 90-percent time constants obtained for the recorders and the elements in various mountings and conditions are listed in Table 5.2. Figure 5.6 shows the response curves for the dry and wet bulbs and the recorder as used during Operation Hardtack.

### 5.3 FIELD OPERATIONS

The recorders were located singly to produce as much data as possible. For each shot, one recorder was placed as near to the burst as possible in the upwind direction from surface zero and at a location expected to be outside of the base surge. This was to be used as a control to measure ambient conditions for the duration of the recording. The remaining recorders were placed in the expected downwind direction from surface zero.

On floating stations the recorders were shock mounted on or below decks (Figures 5.4 and 5.7) with the shielded sensing elements mounted on masts above the washdown spray (Figures 3.8 and 5.9). Recorders for the island stations were placed on the ground and were sandbagged against possible wave action. The shielded sensing elements were mounted on masts about 20 feet above the ground level. The island stations were chosen so that they would be several feet above the high-tide level and clear of obstructions in the direction of surface zero.

The three target destroyers, which were to be used on both shots, were instrumented by Project 1.3 personnel during January 1958 at the Long Beach Naval Shipyard, Long Beach, California. The remaining installations were completed at EPG. Prior to installation at the station locations, each instrument, with the exception of those on the target destroyers, was completely assembled and calibrated at Site Elmer. Units aboard the target destroyers

were serviced and calibrated in their mounted position in time to participate in the various required trials and power runs. The systems were given final tests and sealed for Shot Wahoo on the last 2 days before the test. Power was turned on at all stations by the minus 30 minute radio signal. The locations of the temperature-humidity stations for Shot Wahoo are shown in Figure 5.10.

After Shot Wahoo, as soon as the instrument stations were declared radiologically safe, the paper-roll charts were removed from the recorders, and the recorders that were to be transferred for Shot Umbrella were moved to Site Elmer for checking and calibration. The recorders were then taken to the various stations. The recorders aboard the destroyers were left in position. These were also checked and calibrated prior to Shot Umbrella. All elements, fields, and cables used on Shot Wahoo were discarded because of contamination and were replaced for Shot Umbrella.

On the final two days before Shot Umbrella, the recording systems were given final tests and were sealed. After Shot Umbrella, as soon as the stations were declared radiologically safe, the charts were removed from the recorders. All installations were then disassembled and the equipment was transferred to Site Elmer and prepared for shipment to NOL.

Figure 5.11 shows the locations of the temperature-humidity stations for Shot Umbrella. The exact positions of all stations for Shots Wahoo and Umbrella are listed in Table 5.3.

TABLE 5.1 CHART SPEEDS OF FOXBORO RECORDERS

Instrument Number	Shot	Station	Calibrated Chart Speed	Chart Speed from Radio Timing
			in/min	in/min
4	Umbrella	YFNB-12	5.97	5.96
5	Umbrella	Site Henry	6.01	—
6	Umbrella	55-Barge	6.02	6.03
7	Umbrella	Site Irwin	6.02	6.00
	Radio Trial	Site Irwin	6.02*	6.06*
9	Wahoo	YC-9	5.92*	5.96*
	Umbrella	Site Keith	5.92	5.95
10	Radio Trial	Site James	—	6.04
	Umbrella	Site James	—	6.01
	Radio Trial	Site James	5.98*	5.97*
474	Umbrella	DD-474	5.99	5.98
	Radio Trial	DD-474	6.03*	5.99*
592	Radio Trial	DD-592	5.98*	5.98*
593	Wahoo	DD-593	6.05*	6.04*
	Umbrella	DD-593	6.04	6.03

\* Chart speeds calculated 30 minutes after the instrument's starting time. All other chart speeds were calculated 45 minutes after the instrument's starting time.

TABLE 5.2 EFFECT OF VARIOUS CONDITIONS ON THE RESPONSE TIME OF FOXBORO RECORDER AND ELEMENTS

	Time Constant:	63 pct	90 pct
		sec	sec
Effect of airflow on response time (element uncoated, unmounted, and unshielded):			
Still air		4.0	9.2
Airflow of 5 ft/sec		3.1	7.1
Airflow of 10 ft/sec		1.7	4.0
Effect of coating and mounting on response time (element mounted and constant airflow of 10 to 13 ft/sec):			
Element uncoated, mounted in plastic holder		9	38
Element coated, mounted in plastic holder		19	45
Element coated, mounted in metal holder		27	90 to 94
Effect of recorder system used in the field (element coated, mounted, and shielded):			
Element mounted in plastic holder		14	41
Element mounted in metal holder		39	95

TABLE 5.3 TEMPERATURE-HUMIDITY RECORDING STATIONS

Station	Distance from Surface Zero feet	Bearing from Surface Zero	Height of Elements Above Water feet
Shot Wahoo:			
YC-1	3,413	31° 38'	21.5
DD-474	2,900	245° 04'	32
YC-5	4,337	251° 04'	22.5
DD-592	4,900	250° 45'	62
YC-6	6,250	248° 52'	23
YC-7	7,815	247° 39'	22.5
DD-593	8,900	245° 56'	62
YC-9	9,883	248° 52'	24
Shot Umbrella:			
YFNB-12	2,350	68° 05'	49
DD-474	1,900	245° 41'	62
DD-592	2,000	248° 27'	62
55-Base	5,624	251° 15'	28.5
DD-593	7,900	249° 12'	62
Site Henry	10,350	20°	20
Site Irwin	13,700	231°	15
Site James	14,700	753°	20
Site Keith	18,780	265°	22

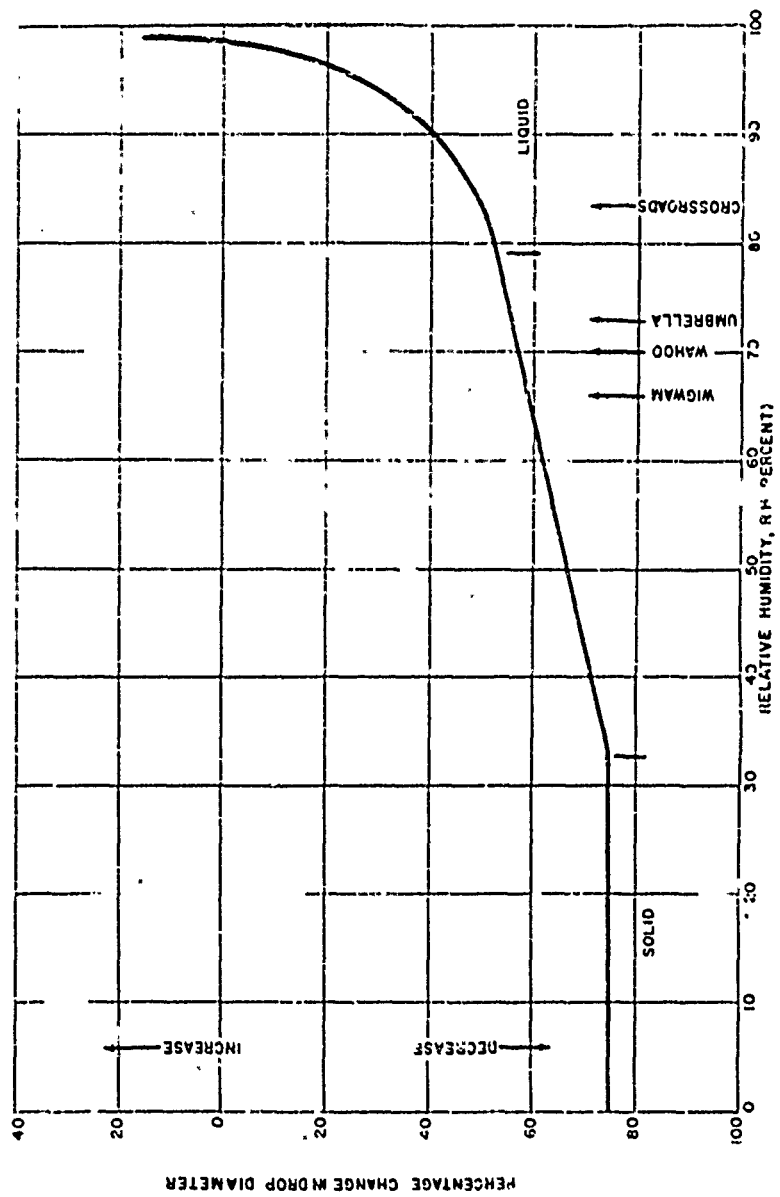
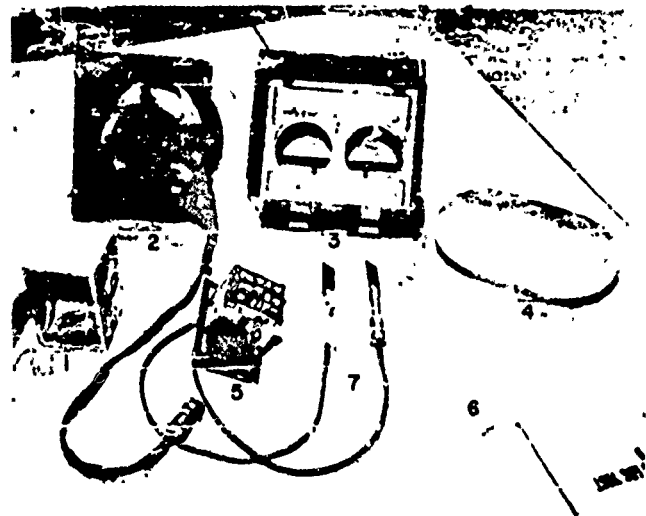
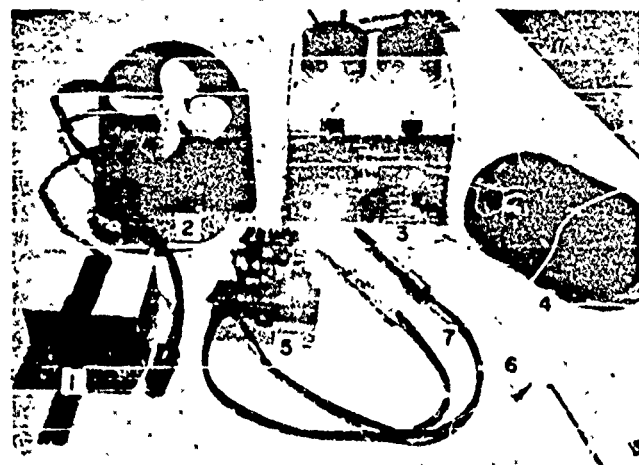


Figure 5.1 Percentage change in size of drops of sea water versus relative humidity.



1. COVER FOR SWITCHING MECHANISM AND RESISTOR BOARD
2. FAN AND BASE OF SHIELD
3. RESERVOIR AND MAIN SECTION OF SHIELD
4. TOP OF SHIELD
5. SWITCHING MECHANISM AND RESISTOR BOARD
6. WET-BULB WICKING
7. ELEMENT HOLDERS

Figure 5.2 Temperature elements and associated parts.



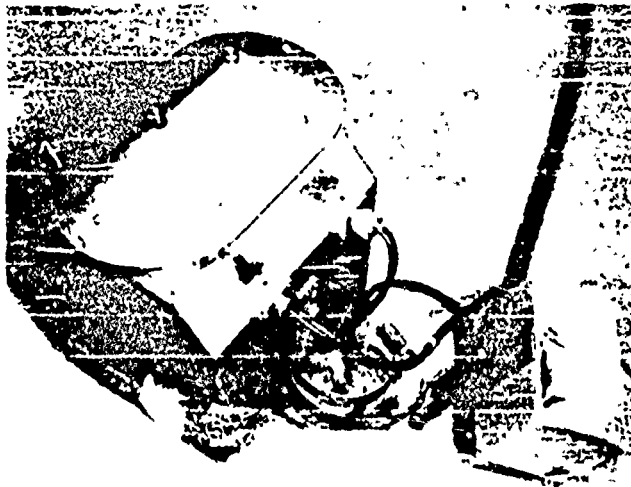


Figure 5.3 Assembled element shields.

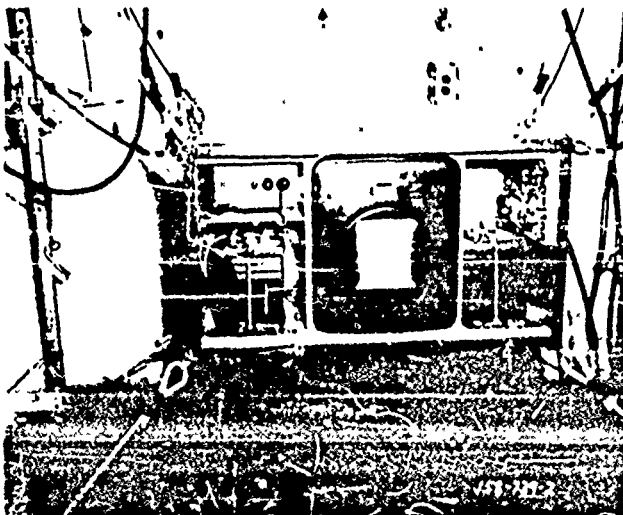


Figure 5.4 Recorder in shock mount (destroyer).

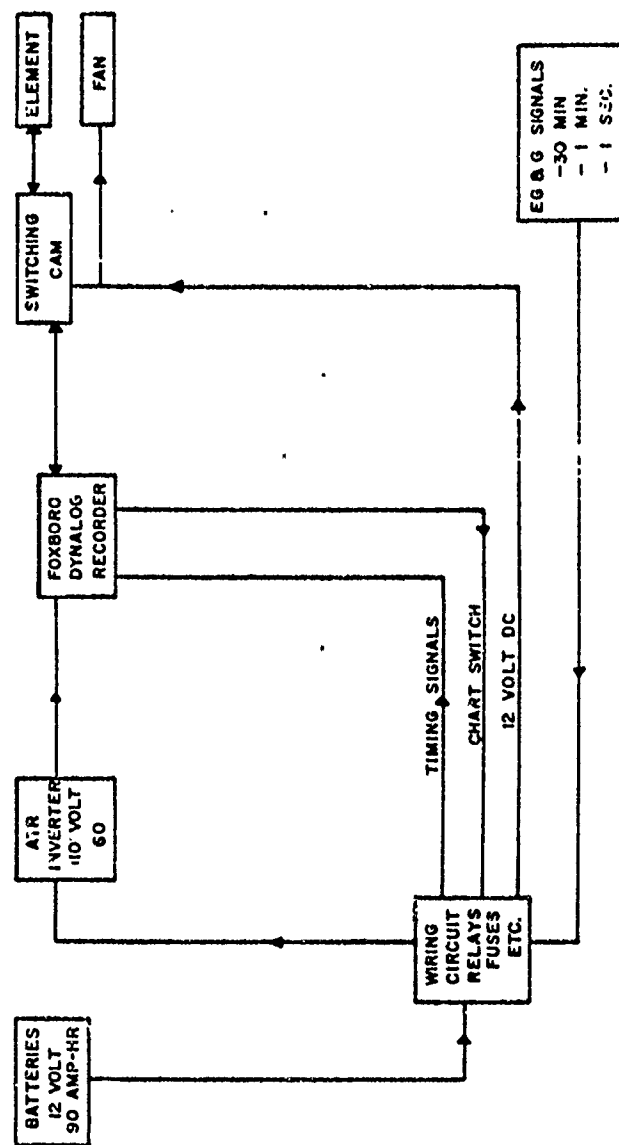


Figure 5.5 Block diagram of temperature-humidity recorder.

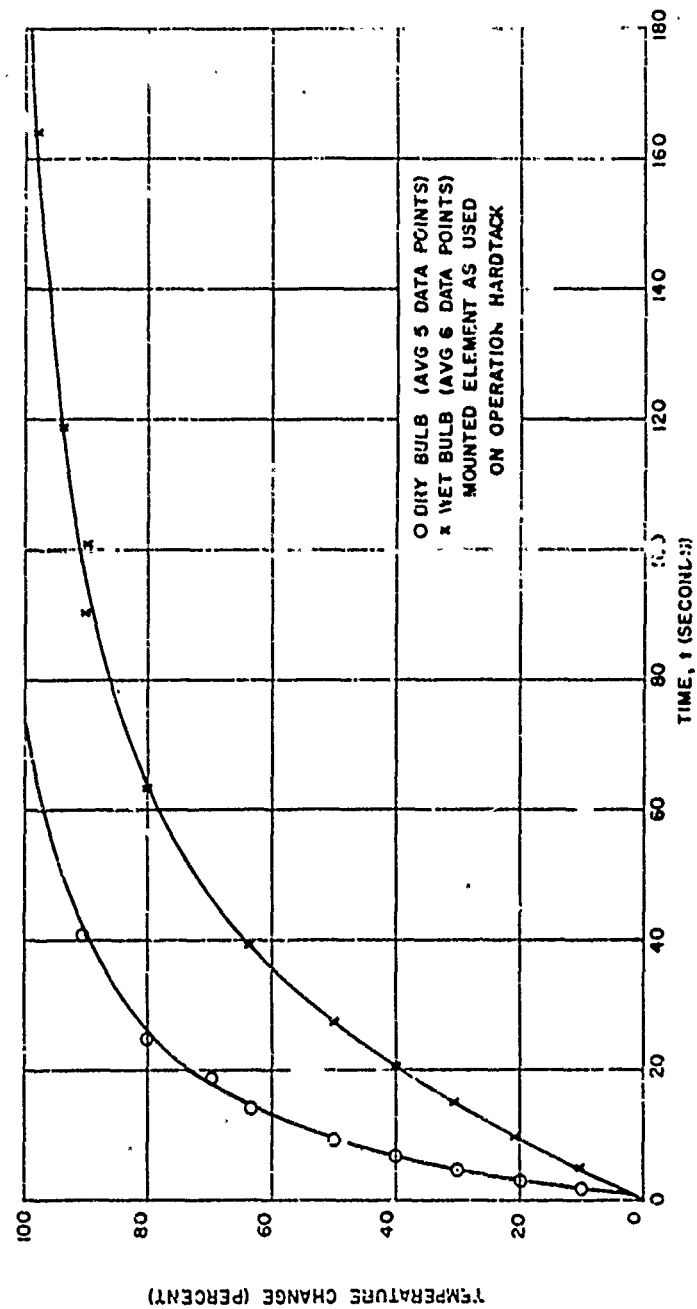


Figure 5.6 Response curves for wet and dry bulbs.

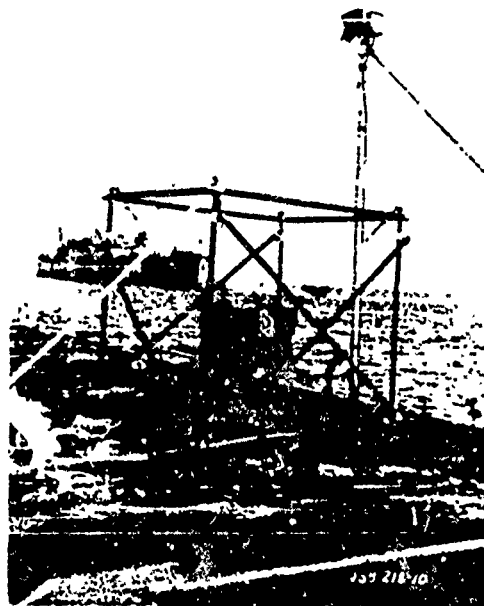


Figure 5.7 Recorder in shock mount on YC barge.

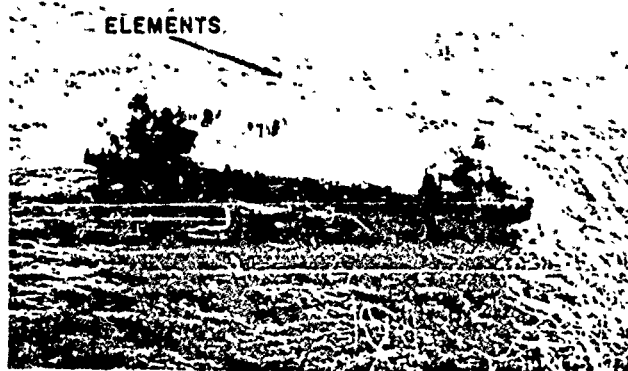
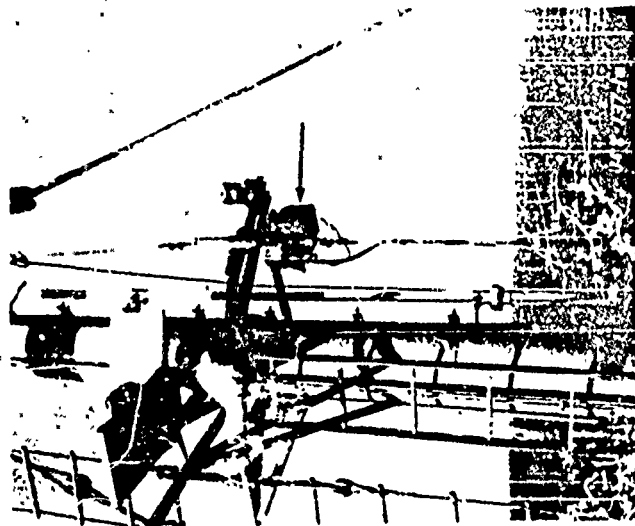
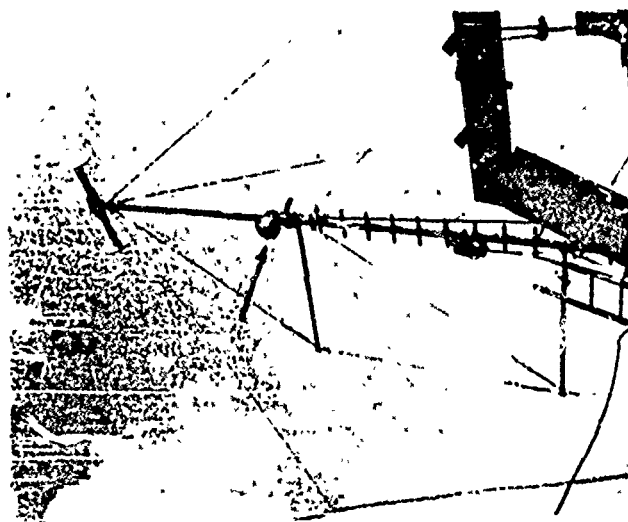


Figure 5.8 Washdown on YC barge.



DESTROYER



SS-BARGE

Figure 5.9 Element mountings

CONFIDENTIAL

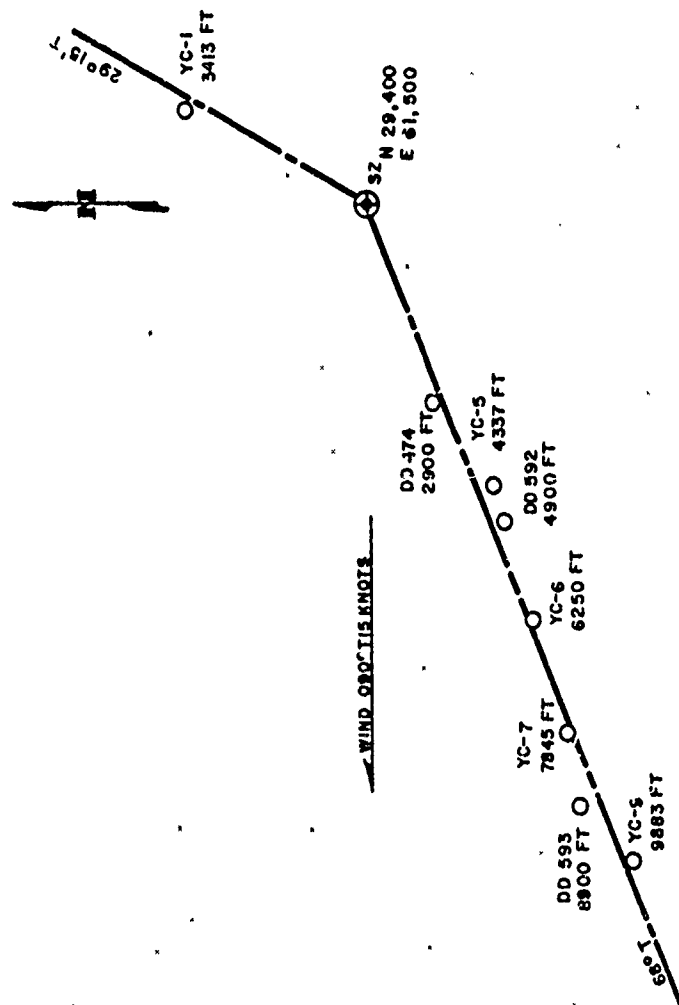


Figure 5.10 Temperature-humidity recording stations, Shot Wahoo.

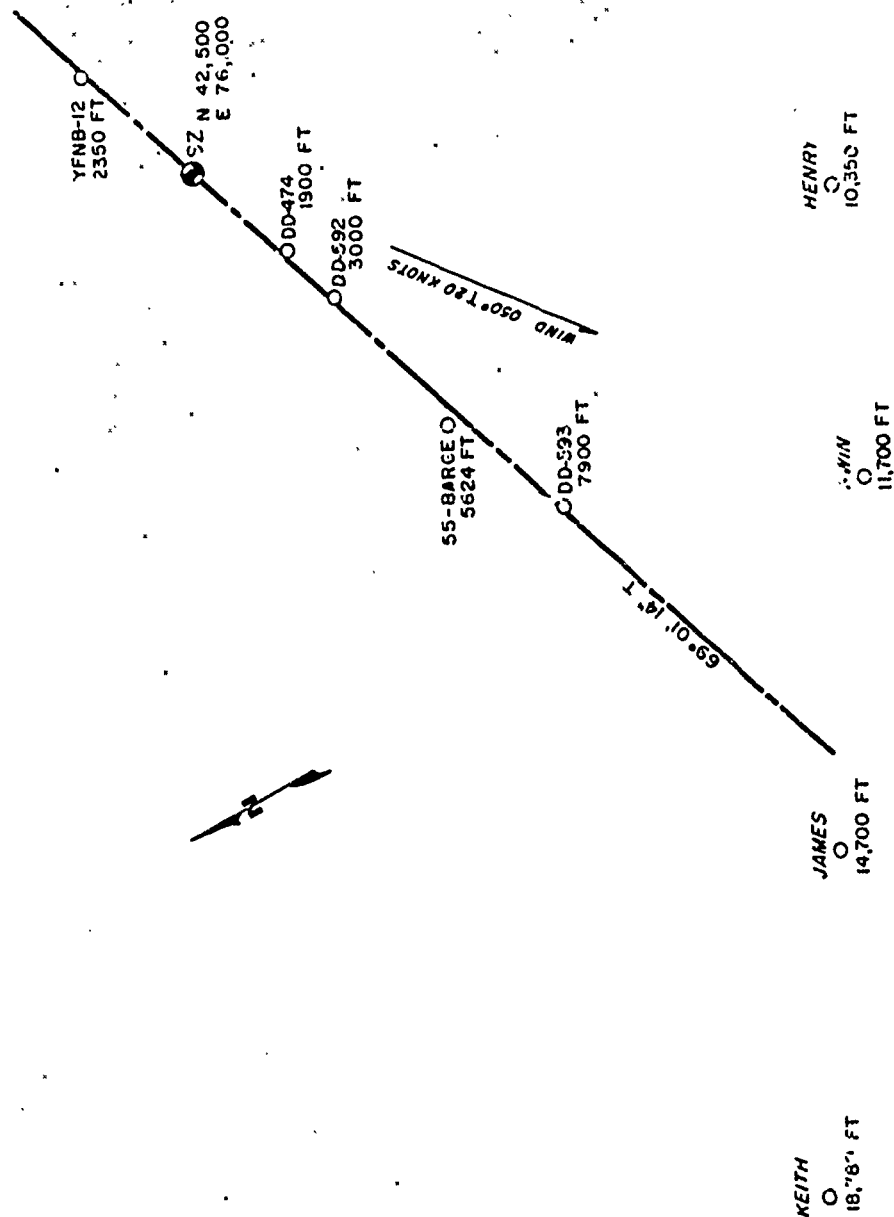


Figure 5.11 Temperature-humidity recording stations. Shot U.S. Trella.

## Chapter 6

### RESULTS OF TEMPERATURE AND HUMIDITY MEASUREMENTS

#### 6.1 SHOT WAHOO

For Shot Wahoo, the recorders throughout the array were triggered prematurely when improper radio timing signals were transmitted on the day before the shot. By the time it was learned that these signals had been transmitted, it was too late to reactivate any of the recorders. Efforts were made on D-day to put a limited number of these stations in operating condition, with priority given to the three DD's, the upwind YC-1, and the extreme downwind YC-9. recorders on the DD-592 and DD-474 did not operate during the shot because of a failure in the radio timing signals at these stations, and it is believed that the recorder on the YC-1 failed because of weak batteries. However, wet- and dry-bulb temperatures were obtained on the DD-593 and the YC-9 (Table 6.1).

Since the base surge was toroidal in shape on both shots, a station downwind from surface zero could indicate two surge arrivals and two departures. These are called the arrival of the leading edge, the departure of the downwind inner edge, the arrival of the upwind inner edge, and the departure of the trailing edge. Also, the arrival and departure of fallout could occur at a downwind station between the times of passage of the inner edges of the surge.

Times of arrival of the leading edge of the base surge at the instrument stations were determined visually on both shots by one of the Project 1.3 personnel in a photographic aircraft. These times were checked by examining the aerial photographs. In addition, times of arrival and departure of distinct portions of the surge and fallout could be estimated by photographic means and from the contour plots of Chapter 3. These times are indicated, where possible, on the figures in this chapter.

Figure 6.1 shows the wet- and dry-bulb temperatures and relative humidity recorded at the DD-593 for Shot Wahoo for the period from 1 minute prior to shot time to 23 minutes after. The readings have been corrected for the variations in time due to frequency fluctuations in the power supply. No correction for response of the system was attempted on this record because of the very large number of minute fluctuations in the dry-bulb temperature. It is believed that these fluctuations were due to hot gases from the ship's stack, which mixed with the turbulent air and passed over the elements. The sensing elements were mounted 14 feet above and 18 feet downwind of the stack. Photographs of the DD-592 taken from the DD-728 showed large amounts of dark smoke rising from the stack immediately after the burst and drifting in the general direction of the sensing elements at that station, lending support to the belief that this also occurred on the DD-593.

Visually, the surge was estimated to arrive at the DD-593 at 140 seconds after SZT. Estimates based on the photographs ranged from 130 to 169 seconds. The dry-bulb temperature curve indicated a rise of 2.8° F at 130 seconds after the burst and fluctuated sharply between extremes of about 83.0° and 87.0° F until approximately 190 seconds, when the oscillations became smaller in amplitude, at approximately preshot levels. At 3.7 minutes after the burst, the temperature rose rapidly and then oscillated between extremes of 87.8° and 95.7° F until about 12 minutes, when it dropped below 88.0° F, reaching a minimum of



86.3° F at 12.8 minutes. It then rose sharply again and exceeded the range of the instrument. It declined rapidly after 16.8 minutes and began to level off at 20 minutes, slowly returning to ambient values thereafter.

The temperature rise that occurred when the base surge arrived possibly indicated that the leading edge of the surge was warmer than the ambient air. This temperature change was on the order of magnitude that could be expected from the heating of the water by the nuclear explosion. The exact amount of heating cannot be determined, because the origin of the water in the base surge is not known. However, the source was probably a layer between the surface and the depth of burst, which included surface water at an initial temperature of 82.0° F and the colder water beneath it.

As shown in Figure 6.1, the instruments were in clear spaces between the surge lobes between 152 and 159 seconds and between 215 and 247 seconds. The temperature dropped slightly during these intervals. The time of departure of the downwind inner edge could not be determined because of the ragged nature of the surge. In general, because of the probable influence of turbulent mixing with the hot stack gases on the surge temperature, the dry-bulb record at the DD-593 cannot be considered to be quantitatively useful.

The high temperatures between 8.7 and 12 minutes can probably be attributed to a general downward motion, or subsiding airflow. This settlement was probably initiated by the falling primary and secondary plumes, and may have continued after the water in the plumes had fallen out or had evaporated. The record provides evidence that the stack gases were normally above the temperature elements, but were carried down by the fallout.

The higher temperatures recorded between 7.8 and 18 minutes can be attributed to the passage of the upwind portion of the base surge. Although it was poorly defined and barely visible from the air at these times, a greater settlement or fallout rate was indicated for the upwind surge cloud at late times than for the plumes. An extrapolation of the curve for the base surge upwind trailing edge in Figure 3.23 to the distance of the DD-593 gives a departure time of 16 minutes, which is consistent with the rapid decline in temperature starting at 16.8 minutes.

The wet-bulb temperature record was smoother because of the slower response time of the mounted element, which tended to eliminate the high-frequency fluctuations. However, the curve was similar in shape to the dry-bulb curve, indicating a rise to 77.7° F at surge arrival and showing large rises due to the fallout from the plumes and upwind base surge. These rises are not quantitatively useful for interpreting explosion effects because of the unknown influence of the stack gases. The relative humidity curve is also of very limited value because of this factor.

Wet- and dry-bulb temperature and relative humidity records obtained at the YC-9 are presented in Figure 6.2. The records have been corrected for time variations due to fluctuations in the power supply frequency. The temperature rise to 81.2° F, starting at 160 seconds, was consistent with the earliest estimated surge arrival time of 161 seconds. This small rise (0.3° F) provides further evidence that the leading edge of the surge was heated by the explosion, since the YC-9 was a barge with no stacks. The temperature then fell to a minimum of 79.7° F at 216 seconds after the burst, and showed only gradual changes thereafter, mostly between levels of 80° F and 81° F. The gradual decline in temperature, which started at 11 minutes and reached a minimum of 80.0° F at 13.1 minutes, was probably caused by the vestiges of fallout and the upwind portion of the base surge. The cooling effect was produced by the evaporation of the surge droplets. The return to the ambient value at 15.8 minutes probably indicates the departure of the surge trailing edge. Considering the diffuse, irregular nature of this boundary, particularly at late times, this result is reasonably consistent with the time of 17 minutes obtained by an extrapolation of the upwind trailing edge of the surge to a radius of 9,883 feet on the downwind axis.

Wet-bulb temperature rose at the YC-9 when the surge arrived; again, this was probably due to the early heating of the water that entered the surge. Its peak value of 75.7° F was 1.6° above the ambient level. The only significant drop in wet-bulb temperature before the final departure of the surge occurred between 4 and 5 minutes after the burst, when a minimum of 74.1° F was reached. This interval of low levels is consistent with the two periods shown on Figure 6.2, when the YC-9 was in clear spaces between surge lobes; 230 to 270 seconds and 278 to 302 seconds after SZT.

The curves in Figures 6.1 and 6.2 were not corrected for the response time of the sensing elements and shielding, since an approach to a step change probably occurred only at the arrival time of the leading edge of the base surge. Corrections for response were made at this time to prepare a corrected relative humidity curve for the YC-9, which is shown in Figure 6.3. The complete DD-593 curve is also included in this figure, though no response corrections have been made because the humidity values are not reliable. The maximum relative humidity indicated at the YC-9 was 85 percent, occurring 12 seconds after surge arrival. The relative humidity remained above the ambient level until after the surge had departed.

Within the range of error in the time determinations, the first changes at the Wahoo temperature-humidity instruments coincided with the arrival of the visible base surge. The leading edge of the surge was warmer than the surrounding air, but the exact amount of heating is not known because of the paucity of data and the uncertainty of readings at the LD-593. The evaporation of the droplets in the surge gradually produced a cooling effect and led to a lowering of temperature below ambient and a raising of relative humidity, but the limited measurements make it impossible to study these effects in detail on Shot Wahoo. In general, the extrapolated motion of the trailing upwind edge of the surge shown in Figure 3.23 seems to be verified.

## 6.2 SHOT UMBRELLA

For Shot Umbrella, all recorders were activated at the proper time, and timing signals were received at all stations. Complete records were obtained from six of the nine temperature-humidity recorders, and a partial record was obtained from the recorder located on the DD-474, where cables holding the sensing element shelter on the mast were cut by flying debris about 37 seconds after zero time. The instruments failed to record data at Site Henry and on the DD-592, because the charts jammed on the drive sprockets prior to shot time. This was caused by a combination of a malfunction of the chart takeup mechanism and the effects of the weather on the rolled paper charts.

Figures 6.4 through 6.10 are curves showing wet- and dry-bulb temperatures and relative humidity as functions of time for each station. The significant results are summarized in Table 6.2. At the surge arrival time, a rise in temperature was recorded by the wet bulb at all stations. At close-in stations, the dry bulb recorded a rise in temperature followed by a decline; at more distant stations, only a sharp decline was recorded.

In Figure 6.4, which is a plot of the data from the recorder on the YFNB-12, the only upwind station, the time of surge arrival indicated by photography was about 27 seconds after SZT. Both the dry- and wet-bulb temperatures started to rise at this time. The dry-bulb temperature rose to 84.1° F, then fell below ambient, starting its decline about 40 seconds after the burst. The wet-bulb temperature rose and fell more slowly, having a peak value of 80.4° F at 53 seconds after SZT. The illustration indicates a lower dry-bulb than wet-bulb temperature between 1 and 2.5 minutes, an effect most likely resulting from the slower response of the wet bulb. The temperature reached a plateau of 77.4° F about 3 minutes after the burst. It showed later fluctuations and slowly returned to the ambient level, which it reached at 30 minutes. The wet-bulb record fluctuated about a level a few

tenths of a degree above ambient after about 4.5 minutes. A relative humidity of 100 percent was observed at about 30 seconds following the time of surge arrival.

The 72° surge radius curve presented in Figure 4.18 indicates that the trailing upwind edge of the surge should have passed the YFNB-12, which was at a bearing of 68° T, about 214 seconds after S2T. This is consistent with the leveling-off of the temperature record after 3 minutes. However, the upwind edge of the surge was not sharply defined, and ragged patches of mist could be observed at the surface beyond the main body of the surge. In addition, the YFNB-12 was in the foam patch, which seemed to produce a considerable amount of airborne spray, possibly by the action of the wind on its foam-covered surface. This foam patch spray seemed to augment the base surge at low levels and helped to produce its long trailing edge. The trailing mist probably accounted for the failure of the instruments to show a rapid return to ambient readings.

Figure 6.5 is a plot of the data from the temperature recorder located on the DD-474, 1,900 feet downwind from surface zero. This brief record is similar to the record obtained on the YFNB-12, indicating a dry-bulb temperature rise starting at 19 seconds and reaching a value of 83.6° F. This was attained at 22 seconds; it was followed by a steady temperature decline until the clear-cut cables were cut at 37 seconds. The wet-bulb temperature started to rise between 14 and 24 seconds, and was still increasing when the instrument stopped operating. The time of surge arrival, determined visually, was 18 seconds -- a value consistent with the time of temperature rise.

Wet- and dry-bulb temperatures recorded at the 55-barge, 5,624 feet downwind from surface zero, are shown in Figure 6.6. The dry-bulb temperature started to fall at 63 seconds after the burst, reaching a minimum of 75.2° F (6.4° below ambient temperature) at 137 seconds. Starting between 60 and 66 seconds, the wet-bulb temperature began to rise, reaching 77.3° F (2.4° above ambient) by 72 seconds after the burst. It subsequently dropped, leveling off at 73.4° F at 150 seconds. The dry-bulb temperature gradually returned to ambient, which it reached 25 minutes after the burst. The wet-bulb temperature fluctuated about a value close to the ambient value after about 11 minutes following the burst. A brief period of 100-percent relative humidity was observed, starting at approximately 60 seconds after the burst. The time of surge arrival, recorded from a visual observation, was 60 seconds, which agreed reasonably well with a subsequent check of photographs. The records do not show any clear-cut indication of the passage of the downwind inner edge of the surge. However, the slight temperature oscillation between 2 and 3 minutes may indicate the passage of fallout. An extrapolation of the surge radius curve for the 72° bearing shown in Figure 4.18 to the downwind position of the 55-barge indicates a departure time of the surge trailing edge of about 10.5 minutes. This general result is similar to that attained at the YFNB-12, in that a cooling effect, probably due to the presence of mist and spray trailing well behind the main body of the surge, is indicated. This cooling effect persisted at the 55-barge for about 14 minutes after the departure of the visible surge trailing edge, possibly caused by air that had passed across the foam patch.

According to a visual observation at the test site, the base surge arrived at the DD-593 at 87 seconds after S2T. The dry-bulb temperature at this station started to drop at 85 seconds and reached a minimum of 78.2° F (3.4° below ambient) by 162 seconds after the burst, as shown in Figure 6.7. The wet-bulb temperature started to rise between 84 and 95 seconds after the burst, attaining a peak value of 76.3° F (1.2° F above ambient) by 107 seconds. The relative humidity reached 85 percent at 2 minutes, indicating that the base surge was no longer saturated at the location of the DD-593, 7,900 feet from surface zero. At this distance, the surge had doubtless become diluted by mixing with the ambient air. The departure of the downwind inner edge of the surge at about 141 seconds was not indicated by significant changes in the temperature curves.

At later times, the curves in Figure 6.7 probably do not give a correct indication of the

temperature and humidity of the surge, as this was the same station that recorded extremely high temperatures on Shot Wahoo (Figure 6.1). No such high temperatures were recorded at late times by any other station. The sharp temperature rise at about 316 seconds (Figure 6.7) was probably associated with fallout, and the larger rise at 458 seconds followed the arrival of the upwind inner edge of the surge, which occurred at 440 seconds. As in Shot Wahoo, the results are consistent with subsiding motion in both of these areas. This is expected in the fallout region. It probably indicates a decay of the turbulence in the surge several minutes after the burst and a subsequent gradual settling out of the water drops that remain. Since the temperature record did not rise at the time of surge arrival, there was probably a net upward vertical motion in the surge at early times. Inasmuch as the ambient temperatures at the DD-593 were in agreement with the values recorded at other stations, it is evident that the stack gases did not affect the readings prior to the shot. An extrapolation of the surge radius-time curve for the 72° bearing in Figure 4.18 to the downwind position of the DD-593 indicates a departure time of the upwind trailing edge of the surge of about 12.5 minutes. As at the closer stations, the temperature remained below ambient levels, and the wet-bulb temperature fluctuated near the ambient value after this time, returning to preshot values at 25 minutes after the burst.

Changes of a barometric altitude were shown by the Site Irwin records (Figure 6.5), obtained 11,700 feet almost directly downwind from surface zero. The photographically observed time of surge arrival of 141 to 145 seconds is consistent with the drop in temperature starting at 147 seconds and the rise in wet-bulb temperature starting at 147 and 156 seconds. The visually estimated time of surge arrival of 155 seconds was possibly in error because of the poorly defined leading edge of the surge. The wet-bulb temperature fell below ambient when the downwind inner edge departed at 201 seconds.

The relative humidity at Site Irwin reached a peak of 83.7 percent about 3.1 minutes after the burst.

About 4.7 minutes after the burst, the dry-bulb temperature started to climb slowly toward the ambient level. This value was not reached until 14 minutes after the shot, and the temperature remained almost constant after 14.3 minutes. However, the wet-bulb temperature fluctuated at levels slightly above ambient even after 18 minutes from the time of the shot. An extrapolation of the trailing upwind edge of the Umbrella surge, as shown in Figure 4.20, to the Site Irwin position indicates a departure time of 15.9 minutes. Though the evidence is not conclusive, it appears that the shallow trailing layer still existed at Site Irwin, though it was probably no longer visible.

It was estimated visually that the base surge arrived at Site James, 14,700 feet from surface zero, at 210 seconds (Figure 6.9). However, the first significant dry-bulb temperature drop started at 259 seconds, the temperature reaching a minimum of 80.0° F (1.7° below ambient) 70 seconds later. The wet-bulb temperature rose to 75.2° F (0.7° above ambient) at about the same time. The 49-second discrepancy between the visual arrival time and the time of temperature drop is not understood. Possibly, the leading edge of the surge was above the surface in the vicinity of the islands. As seen from the aircraft, this would give the appearance of the surge arriving at a station. In addition, the ragged, irregular nature of the surge when it reached the islands contributed to the difficulty in determining times of arrival.

The relative humidity reached 78.5 percent after the surge arrived, a value considerably less than recorded closer to the burst.

The departure of the downwind inner edge of the base surge at 336 seconds was not indicated by any sudden change on the temperature records. However, the dry-bulb temperature gradually rose, then leveled off for about 2 minutes after the arrival of the upwind inner edge of the surge at 9.3 minutes, then climbed slowly and reached the ambient value 13.6 minutes after the burst.

Between 6 and 9.5 minutes, the wet-bulb temperature fluctuated around a value possibly 0.5° below ambient, then rose from 73.6° to 74.7° F in 35 seconds with the arrival of the upwind inner edge of the surge and continued to oscillate about the ambient wet-bulb temperature thereafter.

A direct extrapolation of the surge motion along the 72°-10-252° axis, as determined from surface photography, indicates a departure of the trailing edge of the surge mist from Site James at 18.5 minutes after the burst. Since the dry-bulb temperature remained at ambient level at 13.6 minutes, it appears that this extrapolation is not warranted.

Photographs show that the visible surge was beyond the island stations by 13.3 minutes after the burst, which is consistent with the time of return of the temperature to the ambient value. It therefore appears that the shallow layer of mist, which trailed behind the main body of the surge at the closer-in stations, had dissipated when the surge passed Site James.

The station at Site Keith was the farthest from surface zero (18,780 feet) and was at a bearing of 265°, which was 30° off the axis of surge drift. A surge time of arrival of 6.7 minutes was estimated from the average surge motion, disregarding the lobes. The time of departure of the trailing edge was estimated as 11.7 minutes on the same basis. The station was in the edge of the surge during this period and, since the surge boundaries were not sharply defined, no pronounced changes in the temperature records were observed (Figure 6.10). However, the dry-bulb temperature variations exceeded the ambient variation between 8.5 and 10.3 minutes after the burst, reaching a minimum of 81.5° F (2.6° below ambient), at 9.7 minutes. These times are consistent with the extrapolated average surge motion.

Since the wet-bulb temperature fluctuated continuously, both before and after the burst, it was not possible to relate any variations to surge effects. However, there is some evidence of a gradual slight wet-bulb temperature rise during and after the surge passage.

The maximum relative humidity during the period when the surge was known to be at the station was 76 percent, recorded at 10 minutes after the burst. The peak value of 77 percent, indicated at 19 minutes after the burst, is difficult to explain, as photographs show clearly that the surge was well beyond the island stations at this late time.

Relative humidity versus time for all stations is given in Figure 6.11. Times of surge arrivals and, where possible, the surge departures at each station as determined from the photographic records and/or visual observation are indicated in the figure.

Although the times are not exact because of the different response times of the elements, Figure 6.11 shows qualitatively that the relative humidity in the base surge was at, or close to, saturation until the surge reached the 55-barge. It then decreased fairly rapidly with distance from the burst. The long persistence of high relative humidity at the YFNB-12 and 55-barge may have resulted from airborne mist, or cooled air, from the foam patch. The YFNB-12 was within the patch, but the 55-barge was about 2,000 feet downwind of its edge.

A reproduction of a portion of the original record obtained at the YFNB-12 station is presented in Figure 6.12. A correction of 3.0° F should be added to the wet-bulb readings. No correction is needed for the dry-bulb readings. The minus 1-second radio signal is displaced from the minus 1-second position on the trace because the pen which recorded the radio signal was located about 1 inch from the pen which recorded the trace.

Figure 6.13 is an expanded plot of the data obtained at the YFNB-12 for the period of minus 1 minute to plus 5 minutes. The solid lines are based on the data obtained from the charts and have been corrected only for the calibration of the bulbs and the variations in time due to fluctuations in the power supply. The wet- and dry-bulb readings are identified by the symbols indicated on the figure. The dashed lines are the corrected curves, adjusted for the response of the instrument and its associated components. These dashed lines are valid only if the change in temperature at the sensing element is a step

change (Section 5.2.5). During Shot Umbrella, indications are that the surge arrived as a temperature step change at two or possibly three stations—YFNB-12, DD-474, and 55-barge. Relative humidity, corrected for response time, is noted for these stations on Figures 6.4 through 6.6.

In the correction of the data recorded at the YFNB-12 (Figure 6.13), it appears either that the dry-bulb readings overcorrected or the wet-bulb readings undercorrected between 30 and 60 seconds after the burst, since the adjusted wet-bulb temperature lies slightly above the adjusted dry-bulb value. In all probability, the true temperature changes for both bulbs during this period were not the step changes required for the response correction.

It is difficult to gain a complete understanding of the changes occurring within the base surge by examining the data obtained at scattered fixed positions. A more satisfactory approach would be the use of instrumentation that could move with the surge, perhaps at a fixed distance behind the leading edge. However, this technique would be extremely difficult, if not impossible.

Some indication of the changes occurring within the surge may be obtained by studying the peak values of dry- and wet-bulb temperatures recorded just after surge arrival at each station and plotting these as a function of time of occurrence. The magnitudes of the first changes are shown for Shot Umbrella in Figure 6.14.

The figure indicates an initial heating of the lagoon water by the detonation. As during Wahoo, the heating could not be measured exactly, because the surge probably contained a mixture of water originating at the surface, where the temperature was about 1°, and at deeper levels that were colder. When the surge traveled outward, evaporative cooling occurred. The dry-bulb temperature fell below the ambient level about 1 minute after SZT, reaching a minimum soon after 2 minutes. It then rose and gradually approached the ambient value. The wet-bulb temperature rose above the ambient level, probably as a result of the heating by the burst, but dropped toward the ambient value quite rapidly.

Although the times indicated are not precise, the general agreement with theory is excellent. Initially, the base surge was a dense suspension of warm sea water droplets. These droplets warmed the entrained ambient air by conduction and raised its relative humidity by evaporating moisture into it. The warm stage lasted for possibly 60 seconds and the surge was saturated for possibly 100 seconds. Thereafter, the surge relative humidity was reduced by a gradual mixing with the drier external ambient air. In addition, evaporation produced a cooling effect, which became less effective as an increasingly large volume of air was engulfed by the surge. It seems unlikely that the Umbrella base surge could be identified by means of temperature-humidity recorders after about 15 minutes following the burst.

On Shot Umbrella, several of the recorders indicated one or more slight drops in dry-bulb temperature between the time of detonation and the time of surge arrival. Two changes of this nature are shown in Figure 6.13. The temperature drops apparently resulted from the passage of the rarefaction phases of air shock waves, which cooled the air for a brief time.

The rarefaction wave data obtained by Project 1.2 (Reference 29) and the temperature change data obtained by Project 1.3 are summarized in Table 6.3, and are also presented in Figure 6.15. The Project 1.2 records showed the passage of two negative waves at early times. The first wave arrived at the three close-in stations about 0.5 second after the burst and produced a pressure drop in this region (1,747 to 2,070 feet) of the order of 0.1 psi below ambient values. There was no indication of this on the temperature records.

The second negative wave was stronger in magnitude, producing pressure drops ranging from 0.46 psi at the EC-2 to 0.13 psi at the 55-barge. This wave arrived at the EC-2 at 2.6 seconds after the burst. The pressure dropped to a minimum value 1.4 seconds later. The pressure minimum reached the 55-barge 7.1 seconds after the burst. The temperature

drops resulting from the passage of this rarefaction wave were recorded at five stations, extending to Site Keith.

The recorders also registered a third rarefaction wave not found by Project 1.2. This wave may have originated at surface zero about 22 seconds after the burst as the rarefaction phase of a shock wave produced by the collapse of the water cavity. The recorded temperature drops indicate that this wave was approximately of the same order of magnitude as the second negative wave. This wave was not detected at the close-in stations by either Project 1.2 or the temperature recorders, because the surge had already arrived at these stations, making it impossible to differentiate between the effects of the surge and rarefaction wave. For the farther out stations, the Project 1.2 records, which were tape recorded, were not played back to the relatively late times necessary.

The data is consistent with the recorded pressure-versus-time data and with air shock wave theory, which indicates that temperature changes should follow pressure changes and that a pressure wave should broaden as it travels outward. The latter effect accounts for the apparent slowing down of the leading edge of the negative phase as it moved away from the point of origin.

The temperature changes that occurred at the various stations during the passage of the rarefaction phases were calculated by means of the adiabatic relationship for dry air (Reference 40).

$$T_2 = T_1 \left( \frac{P_2}{P_1} \right)^{R/C_p} \quad (6.1)$$

Where:  $T_2$  = final temperature, K

$T_1$  = ambient temperature, K

$P_2$  = final pressure, psi

$P_1$  = ambient pressure, psi

$R$  = gas constant for dry air, 0.237 joules/gm K

$C_p$  = specific heat at constant pressure, 1.00 joules/gm K

Temperature changes calculated by means of Equation 6.1 are included in Table 6.3. Since the Foxboro recording system was not designed to measure the rapid changes that occur during the passage of a shock or rarefaction wave, the data shown in Table 6.3 are not precise. The times of commencement of the temperature drops are probably accurate to within  $\pm 1$  second, but the magnitudes of the temperature drops are not correct because of the relatively slow response of the system. The calculated temperature changes range from 10 to 20 times larger than the recorded values, but the application of a step change correction to the records reduces the difference to about a factor of 3.

The condensation cloud, which appeared on the side of the column 1.8 seconds after SZT, was probably formed by the second rarefaction wave shown on the pressure-time records. The passage of the second wave was also shown by a sudden increase in size of the natural clouds in the area. These changes in cloud appearance started at 4.4 seconds in the vicinity of surface zero, which is consistent with the recorded times of arrival of the second negative wave at the airblast and temperature-humidity stations. There was no evidence of the passage of the third wave at the cloud level.

TABLE 6.1 SUMMARY OF TEMPERATURE AND HUMIDITY RESULTS, SHOT WAIHOO

Station:	DD-593	YC-9	Mea
Ambient value during 1 minute prior to time of detonati			
Dry-bulb temp, °F	82.9	80.9	81.9
Wet-bulb temp, °F	74.2	74.1	74.2
Relative humidity, percent	67	73	70
Time of first change:			
Dry-bulb temperature, seconds	130	160	
Wet-bulb temperature, seconds *	137 to 147	159 to 165	
Peak value during first change:			
Dry-bulb temperature, °F	85.7	81.2	
Wet-bulb temperature, °F	77.7	75.7	
Time of occurrence of peak value:			
Dry-bulb temperature, seconds	140	169	
Wet-bulb temperature, seconds	158	156	
Time of base surge arrival:			
Visual, seconds	140	-	
Photographic, seconds	130 to 169	161 to 176	
Time of return to ambient temperature, minutes	21.9	15.8	
Length of record after zero time, minutes	147	106	

\* Times of wet-bulb temperature change are approximate, since wet-bulb readings were taken at intervals of 6 to 9 seconds.



TABLE 6.2 SUMMARY OF TEMPERATURE AND HUMIDITY RESULTS, SHOT UMBRELLA

Station:	YFNB-12	DD-474	55-barge	DD-593	Site Irwin	Site Jams	Site Keith	Mean
Ambient values during 1 minute:								
Prior to time of detonation:								
Dry-bulb temperature, °F	82.6	82.1	81.6	82.0	2.7	11.7	82.1	82.1
Wet-bulb temperature, °F	75.9	74.6	74.9	75.1	75.3	71.5	75.1	75.1
Relative humidity, pct	73	71	73	72	71	71	73	72
Time of first change:								
Dry-bulb temperature, seconds	30	19	63	46	147	259	—	—
Wet-bulb temperature, seconds	30 to 41	14 to 24	60 to 66	84 to 93	146 to 156	253 to 269	—	—
Peak value during first change:								
Dry-bulb temperature, °F	84.1	83.6	75.2	78.2	79.7	80.0	81.5	—
Wet-bulb temperature, °F	80.4	—	77.3	76.3	76.1	75.2	—	—
Time of occurrence of peak value:								
Dry-bulb temperature, seconds	38	22	137	162	198	329	581	—
Wet-bulb temperature, seconds	53	—	72	107	160	291	—	—
Time of base surge arrival:								
Visual, seconds	—	16	60	87	155	210	—	—
Photographic, seconds	29 to 32	17	57 to 61	54 to 69	111 to 145	—	—	—
Time of return to ambient temperature, minutes								
30	—	—	25	25	14	13.6	—	—
Length of record after zero time, minutes								
80	—	0.6	85	57	73	19	88	—

TABLE 6.3 TEMPERATURE AND PRESSURE DROPS ASSOCIATED WITH THE PASSAGE OF RAREFACTION WAVES, 510T UMBRELLA  
A and B represent separate pressure gage records.

Station	Distance from Surface Zero feet	Pressure Drops (Project 1.2)				Temperature Drops			
		Time of		Pressure Drop psi	Calculated Temperature Drop °F	Time of		Uncorrected Temperature Drop °F	
		Start sec	Minimum sec			Start sec	Minimum sec		
EC-2 B	1,660	-	0.53	0.13	1.4	-	-	-	-
B		2.2	4.0	0.46	5.4	-	-	-	-
A		2.7	4.6	0.17	1.8	-	-	-	-
DD-474 A	1,892	-	0.51	0.07	0.72	-	-	-	-
A		2.6	4.1	0.39	4.1	3	7	0.2	-
21-barge A	2,070	-	0.51	0.07	0.72	-	-	-	-
B		-	0.47	0.07	0.72	-	-	-	-
A		2.8	4.1	0.34	3.6	-	-	-	-
B		-	3.9	0.42	4.5	-	-	-	-
WNE-12	2,340	-	-	-	-	3	5	0.2	-
		-	-	-	-	25	27	0.2	-
DD-592 A	2,969	-	4.9	0.23	2.5	-	-	-	-
55-barge A	5,704	-	7.1	0.13	1.4	-	-	-	-
B		-	7.1	0.13	1.4	5	9	0.1	-
		-	-	-	-	30	32	0.1	-
DD-593	7,523	-	-	-	-	10	12	0.1 to 0.2	-
		-	-	-	-	37	42	0.1	-
Site Irwin	11,700	-	-	-	-	45	50	0.1 to 0.2	-
Site James	14,760	-	-	-	-	6	64	3.1	-
		-	-	-	-	83	-	3.1	-
		-	-	-	-	188	-	3.3	-
Site 1215th	18,780	-	-	-	-	40	43	0.2	-
		-	-	-	-	116	122	0.1	-

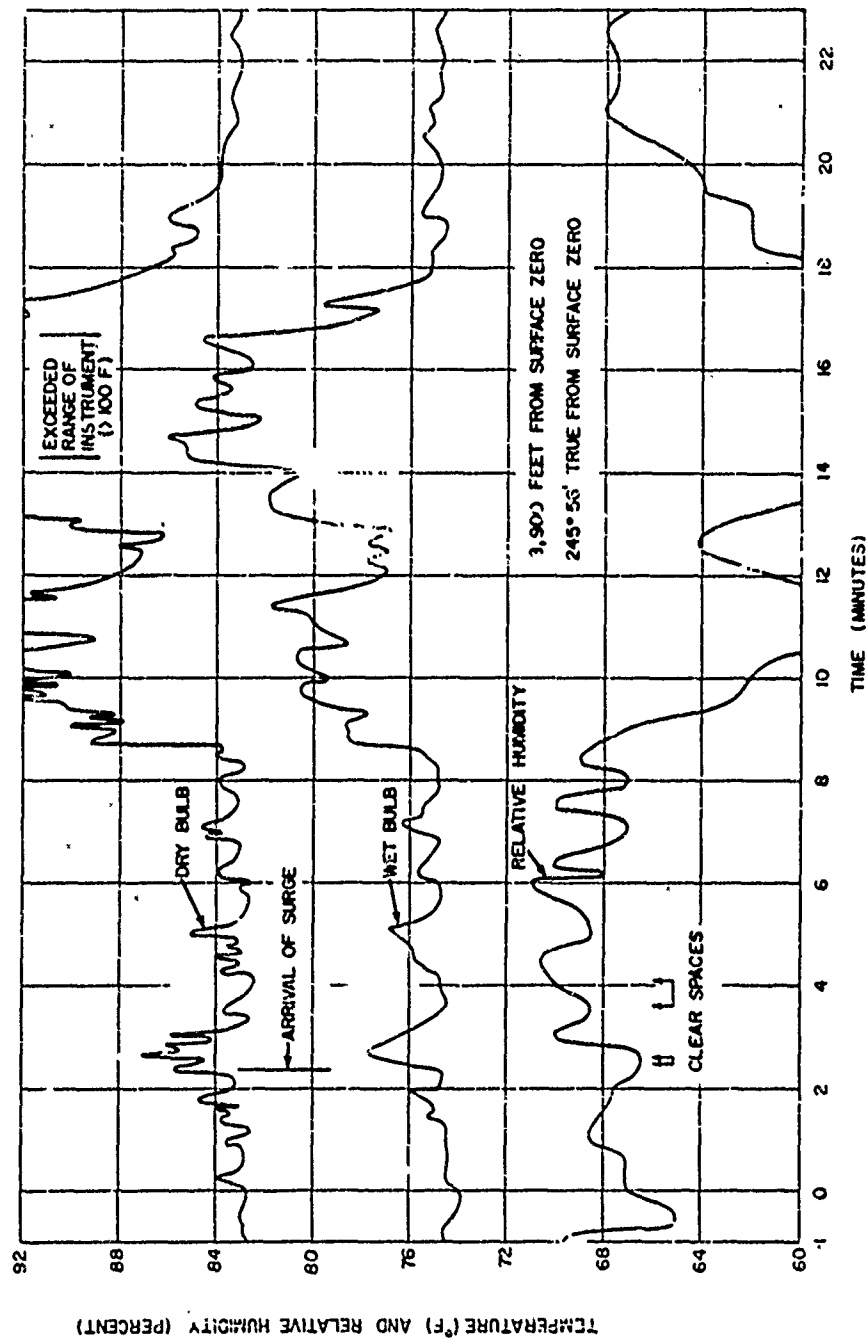


Figure 6.1 Temperature and relative humidity recorded at: DD-503, Shot Wahoo.

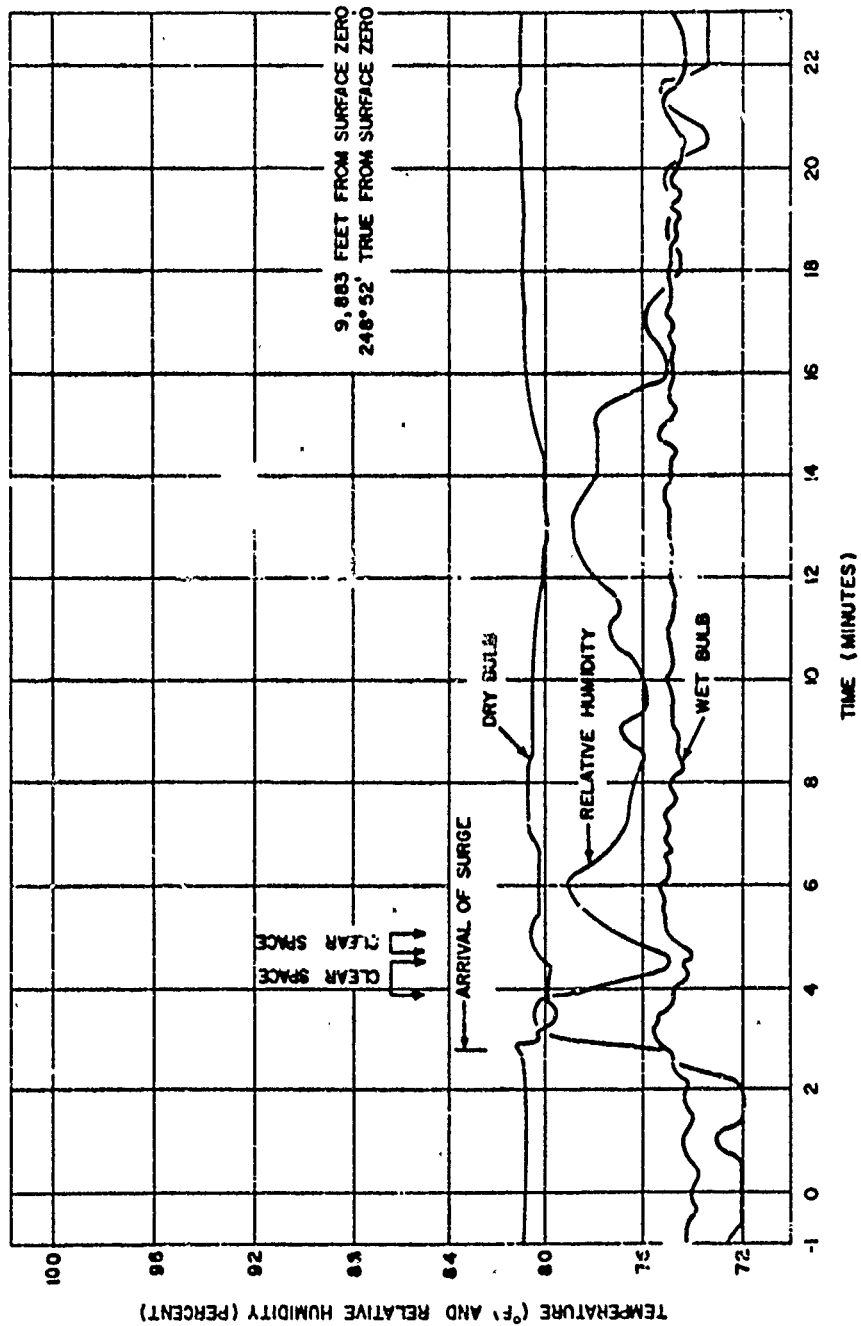


Figure 6.2 Temperature and relative humidity recorded at YC-9, : 10t Wahoo.

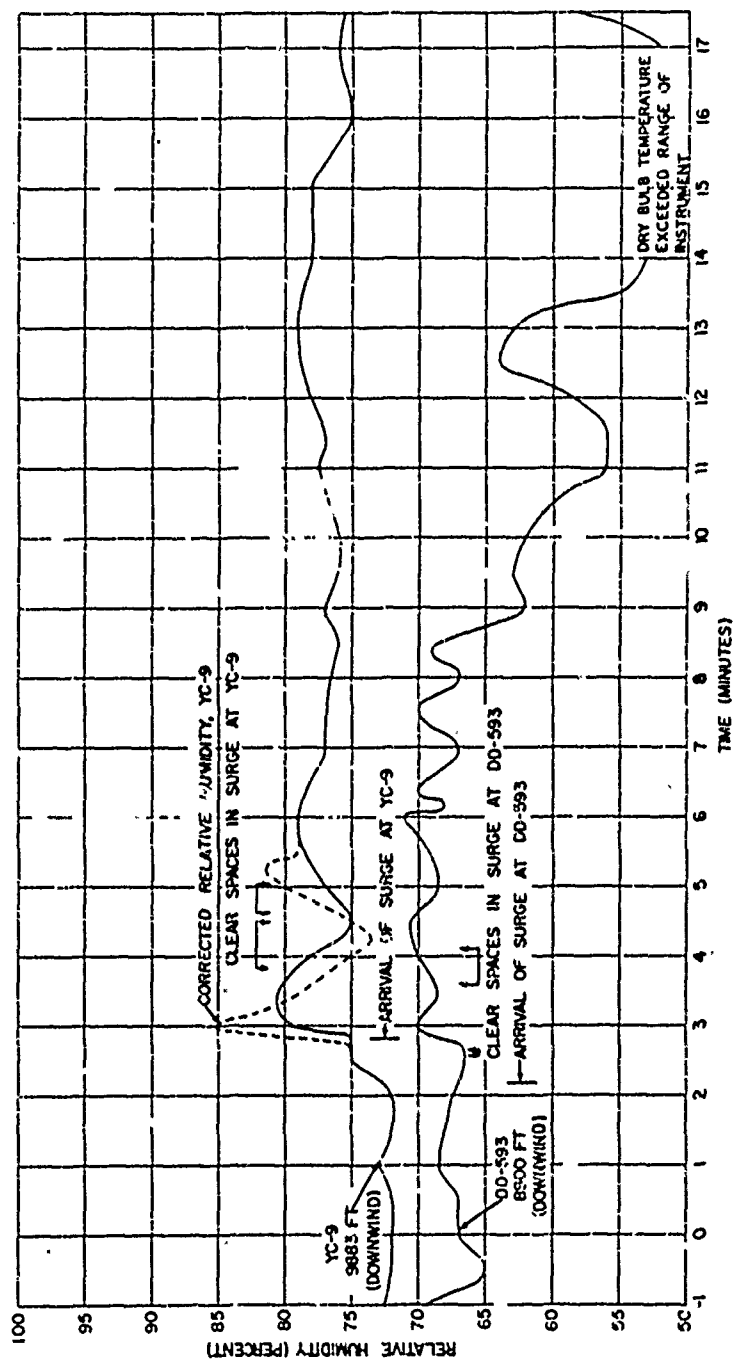


Figure 6.3 Relative humidity, Shot Wahoo.

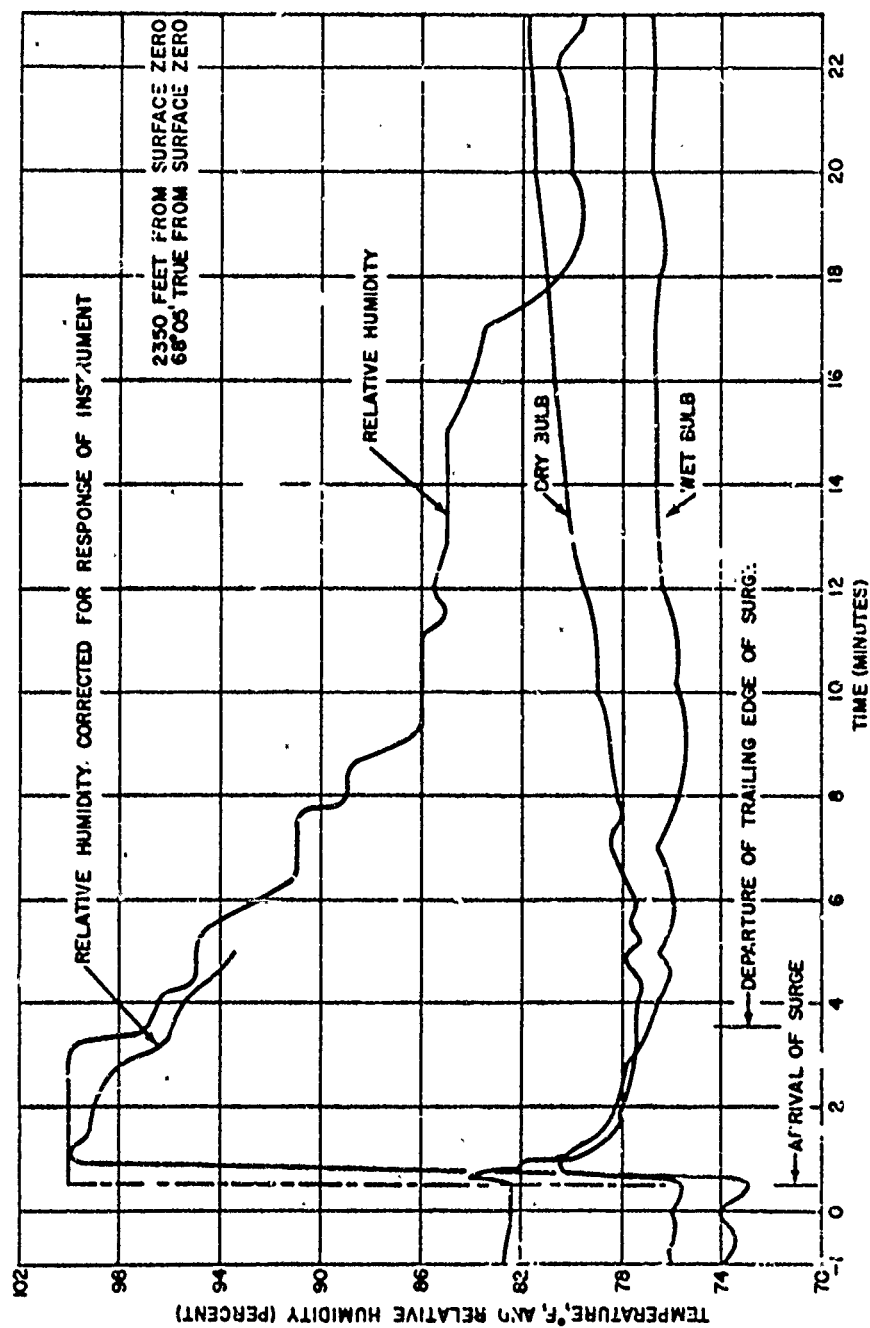


Figure 6.4 Temperature and relative humidity recorded at YFNB-1, Shot Umbrella.

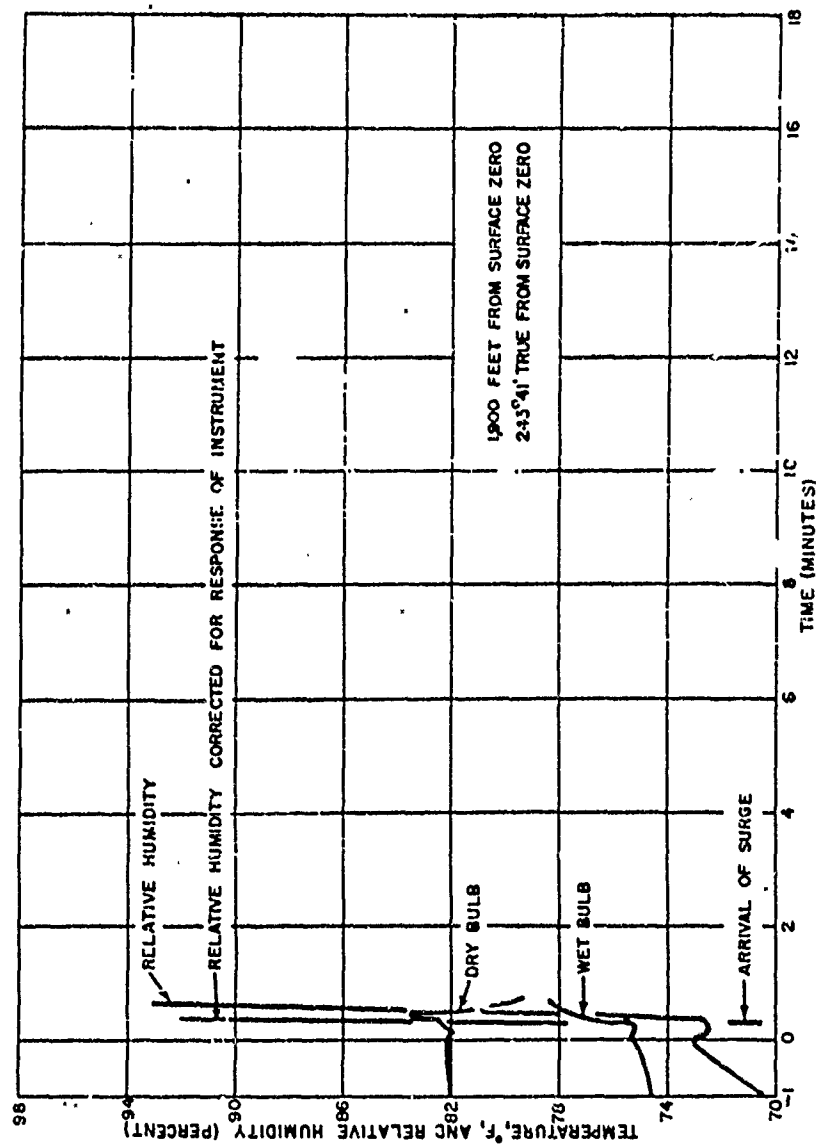


Figure 6.5 Temperature and relative humidity recorded at: DL-474, Shot Umbrella.

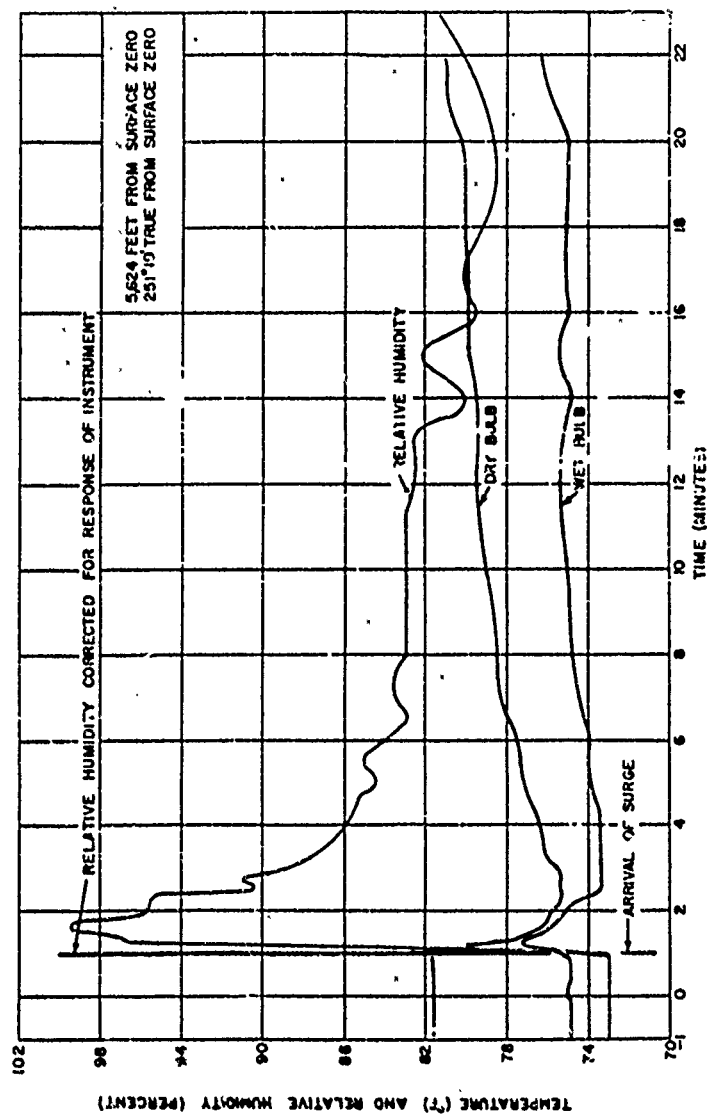


Figure 6.6 Temperature and relative humidity recorded at 55 barge, Shot Umbrella.



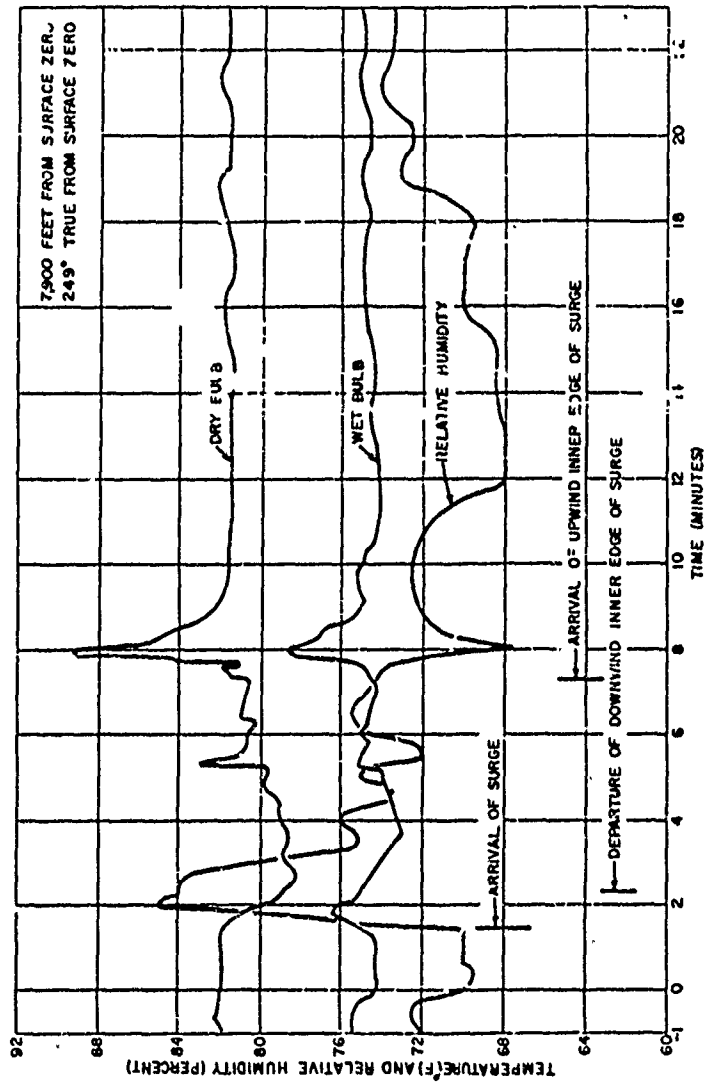


Figure 6.7 Temperature and relative humidity recorded at DD-593, Shot Umbrella.

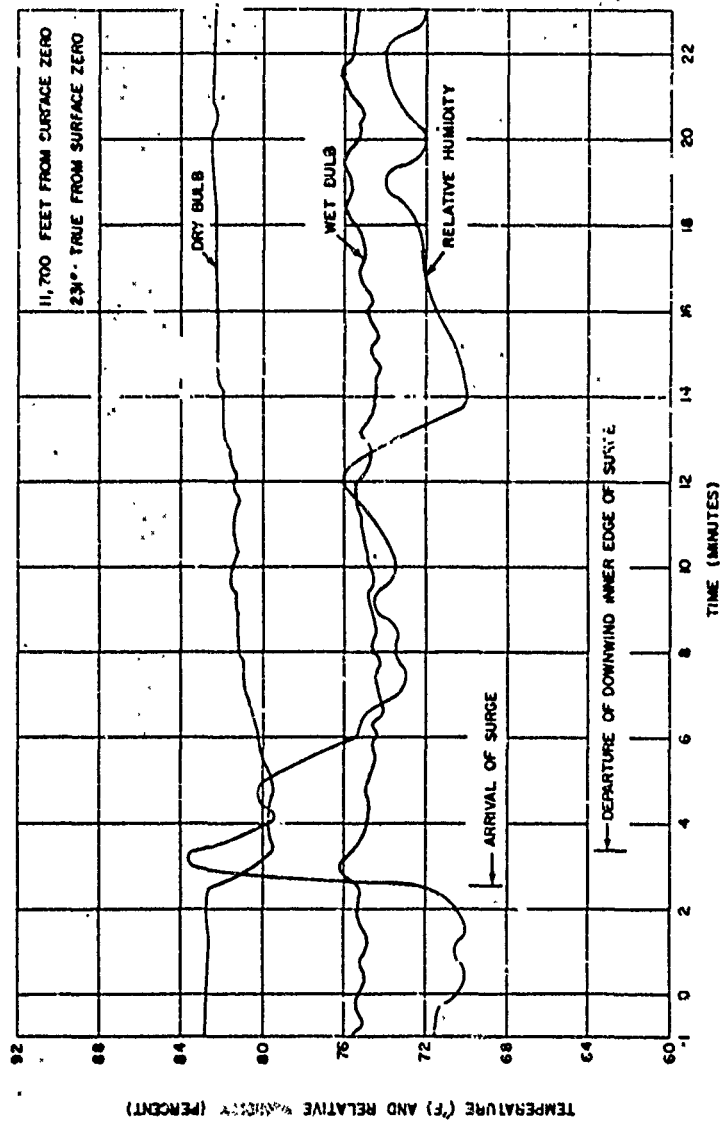


Figure 6.8 Temperature and relative humidity recorded at Site Irwin, Shot Umbrella.

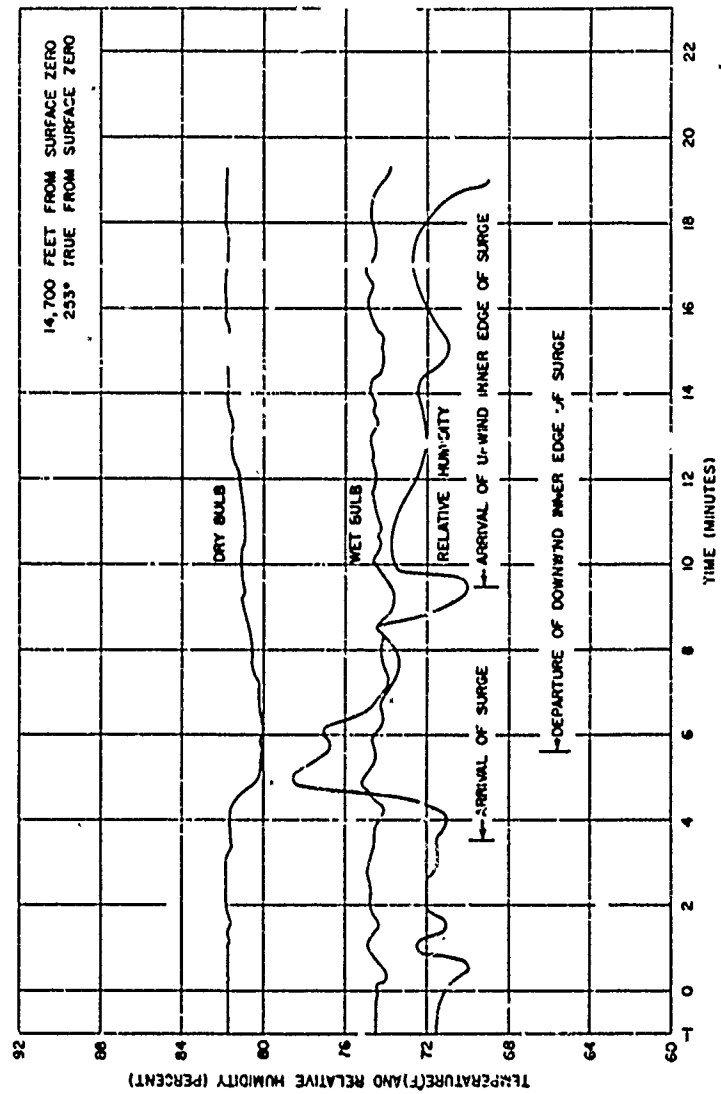


Figure 6.9 Temperature and relative humidity recorded at Site James, Shot Umbrella.

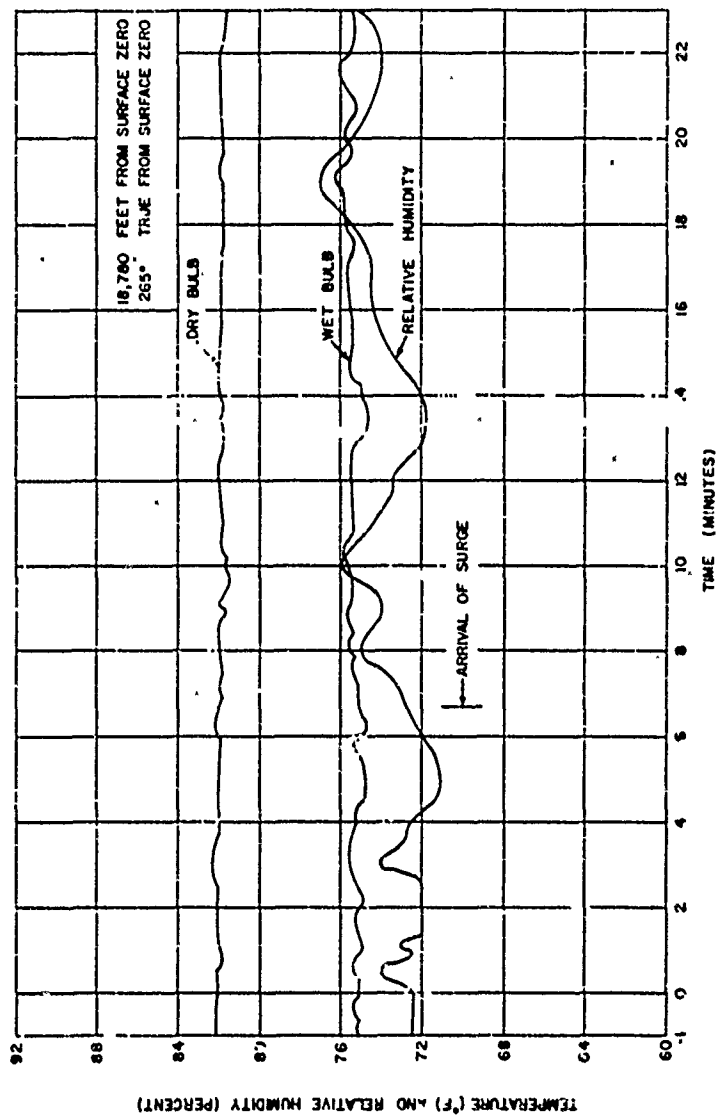


Figure 6.10 Temperature and relative humidity recorded at Site Keith, Shot Jmbre.la.



**Figure 6.11 Relative humidity. Shot Umbrell2.**

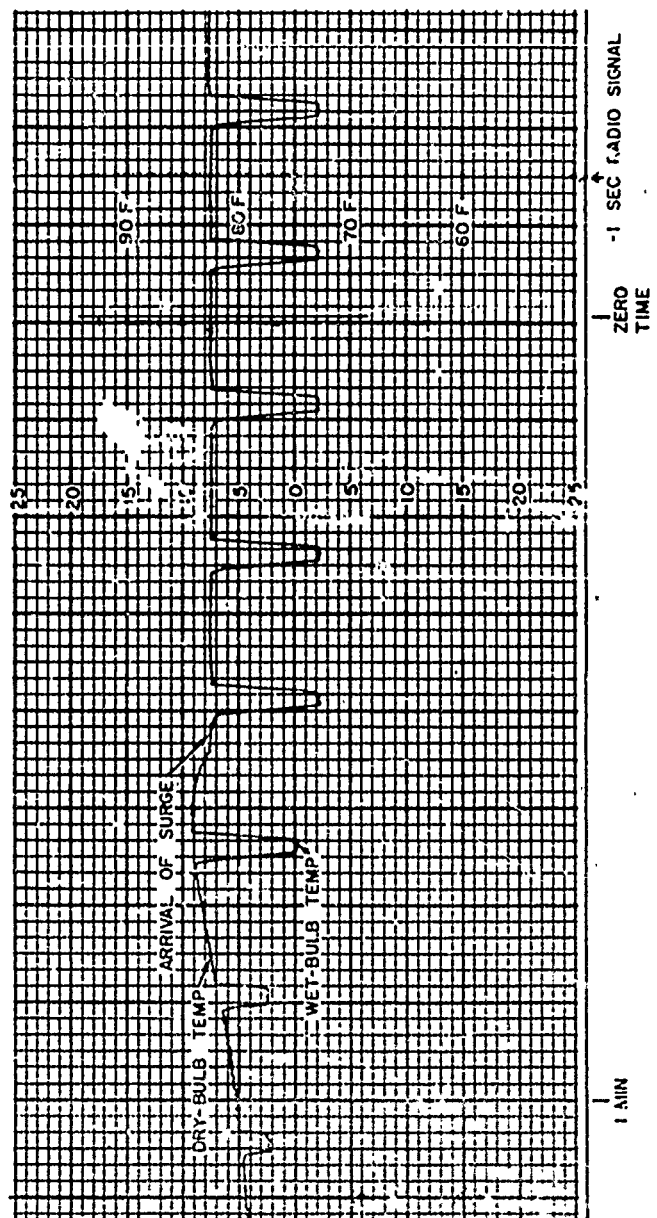


Figure 6.12: Reproduction of a portion of original record obtained on YFN2-12, Shot Umbrella.

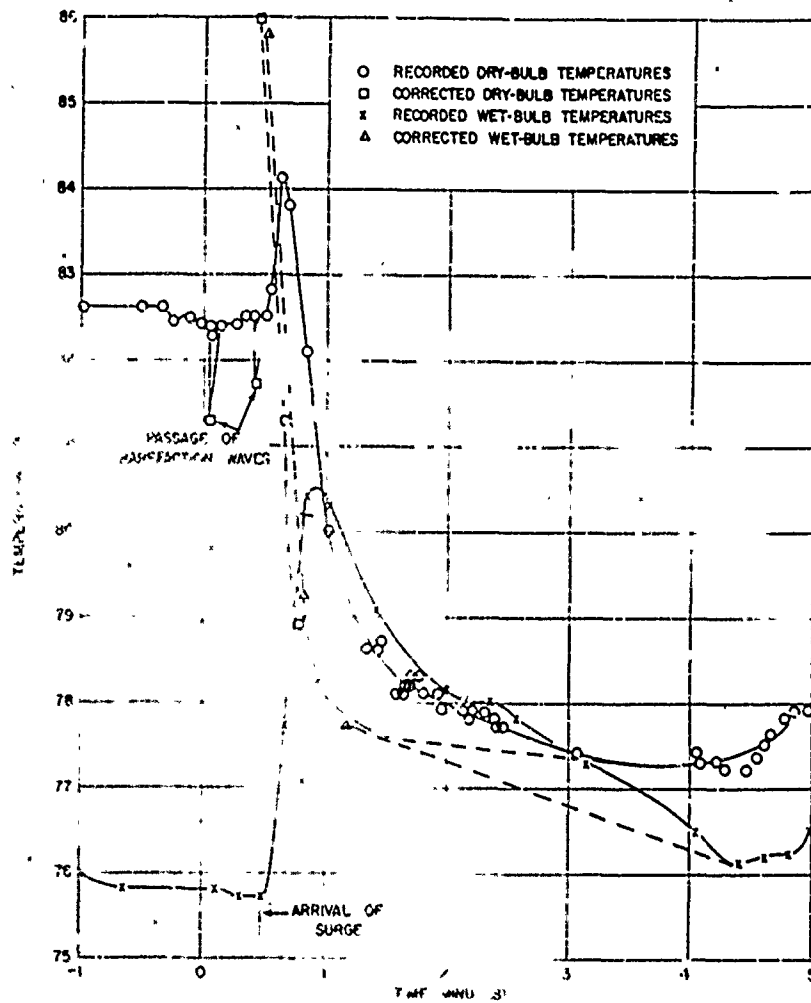


Figure 6-13 Instrument response to variation of temperatures recorded at YFNB-12, station 1000000

CONFIDENTIAL

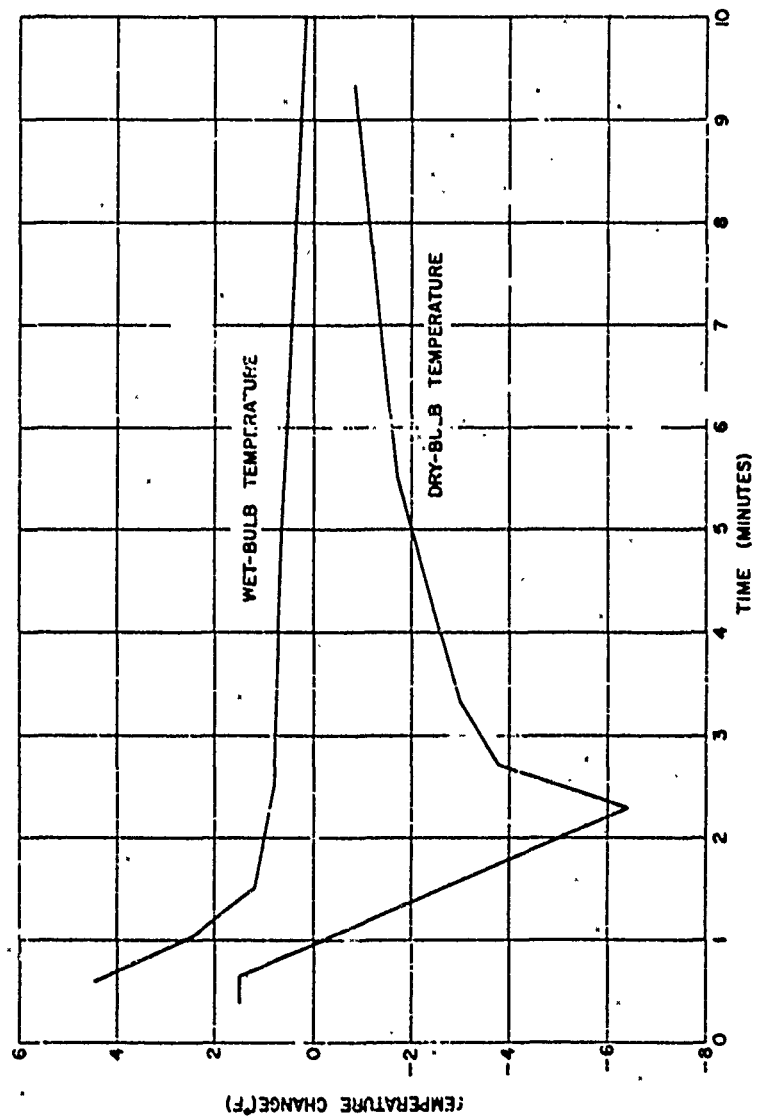


Figure 6.14 Peak wet- and dry-bulb temperature changes immediately after base surge arrival, Shet Umbrella.



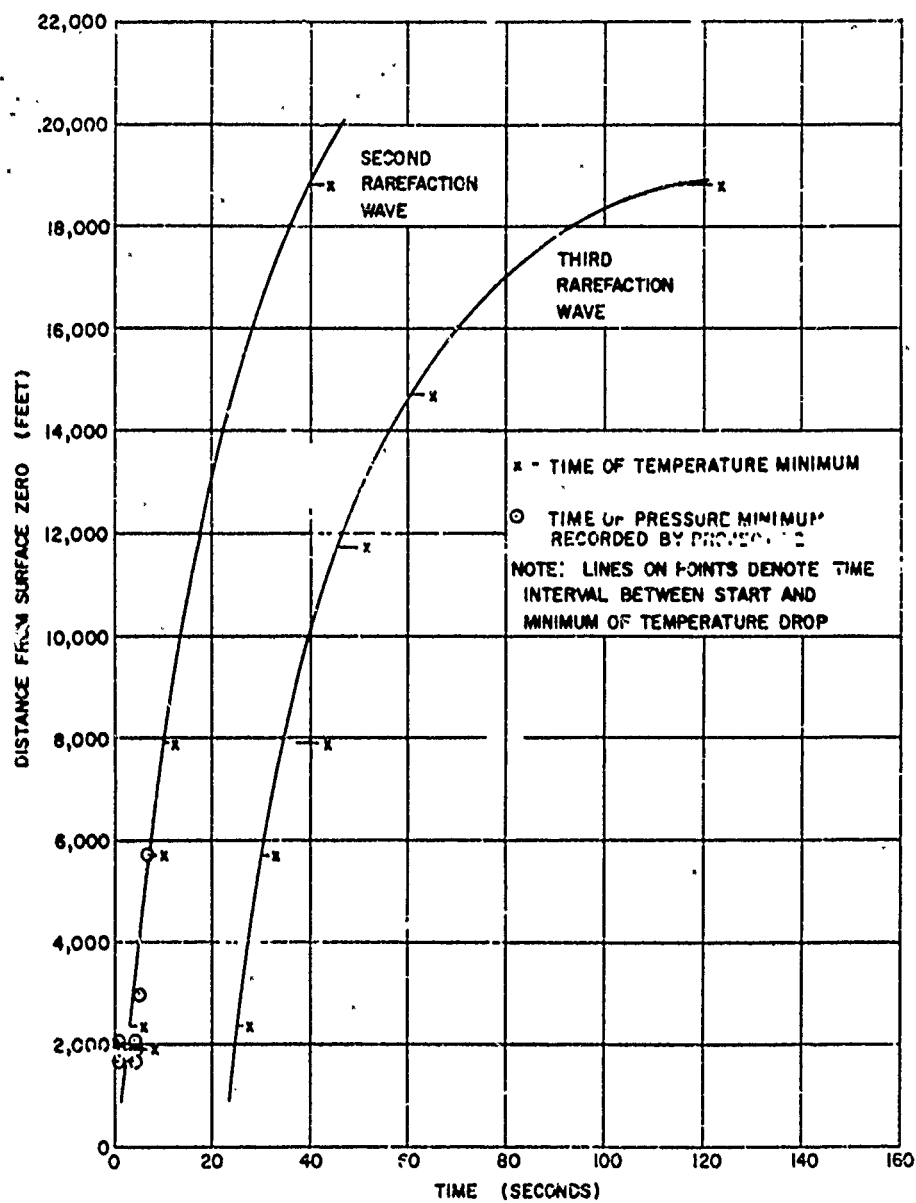


Figure 6.15 Temperature and pressure drops recorded on Shot Umbrella.

## Chapter 7

### COMPARISON OF HARDTACK RESULTS WITH HIGH-EXPLOSIVE AND NUCLEAR DATA

#### 7.1 SPRAY DOMES

The spray dome provides information concerning the shock wave produced by an under-water explosion. Furthermore, it is capable of damaging low-flying aircraft. Initial dome velocities are measured to evaluate the shock wave effects, but a knowledge of the complete height-versus-time history of the spray is needed to assess the hazard to aircraft.

To evaluate the applicability of Equation 1.4 in practice, the vertical rise of the center of the spray domes formed by 300-pound TNT charges has been measured in NOL experimental programs. These tests included charge depths ranging from 10 to 30 feet in relatively deep water. In terms of geometrical scaling ( $\lambda_c$ ), the depths ranged from 1.50 to 15.0 ft/lb<sup>1/3</sup>. Initial dome velocities were obtained by plotting h/t versus time, fitting a straight line, and extrapolating to zero time, as was done for the Wahoo dome. In the height plots, the time interval that was used to determine the slope of the line started between 0.2 and 0.3 second after SZT and lasted for 0.5 second or longer.

According to Equations 1.1 and 1.4, the initial velocity of the water surface directly above a TNT explosion should be

$$V_0 = \frac{6.22 \times 10^6}{\rho U} \left( \frac{W^{1/3}}{R} \right)^{1.13} \quad (7.1)$$

This relationship is shown graphically in Figure 7.1 for comparison with the observed values of  $V_0$  obtained from photographs of the 300-pound TNT explosions. The agreement is good, particularly in the range of  $\lambda_c$ 's between 1.5 and 10 ft/lb<sup>1/3</sup>. The scatter at shallow depths of burst is probably due to measurement difficulties, resulting from the early appearance of plume effects. The lack of agreement at the lower shock pressures ( $\lambda_c > 10$  ft/lb<sup>1/3</sup>) may be attributed to a neglect of the so-called breaking pressure  $P_b$  in Equation 1.4. This appears in Equation 1.5 in the term  $144 P_b / \rho U$ . The nature and magnitude of this term are not known, since Equations 1.4 and 1.5 apply only to the water surface and not to the spray rising above it and masking it. In practice, only the top of the spray can be measured. Fortunately, this gives useful results.

The magnitude of  $P_b$  to use in spray dome studies is best determined by employing Equation 1.5 and solving for  $P_b$  when the observed  $V_0$  is different from that indicated by Equation 1.4 or when no spray is observed ( $V_0 = 0$ ). With this approach,  $P_b$  is essentially an empirical correction factor whose physical meaning is obscure.

The average of the values of  $P_b$  that will produce agreement between Equation 1.5 and the  $V_0$  values that are less than indicated by Equation 1.4, at depths greater than  $\lambda_c = 10$  ft/lb<sup>1/3</sup> in Figure 7.1, is 444 psi. This is in almost exact agreement with an average value of 450 psi obtained by calculating  $P_b$  at the edge of the spray dome (where  $V_0 = 0$ ) from 325-pound TNT charges (Reference 41), and is not greatly different from the average value of 584 psi obtained by the same method from the NOL 300-pound TNT data.

It seems possible that the  $P_b$  effect increases with depth of burst for deep explosions. Some tendency in this direction is shown by Figure 7.1. The data in References 41 and 42 also shows an increasing percentage difference between the observed and theoretical velocities predicted by Equation 1.4 with increasing depth. Charges of amatol weighing 300 pounds produced no spray when fired at a  $\lambda_c$  of 20 ft/lb<sup>1/2</sup>. This implies a  $P_b$  of 1,400 psi for this scaled depth.

As a general rule, Equation 1.4 may be safely used for charges of several hundred pounds between geometrically scaled depths of 1.5 and 10 ft/lb<sup>1/2</sup>. The proper procedure is uncertain at  $\lambda_c$  values greater than 10 ft/lb<sup>1/2</sup>, since some measurements are in agreement with Equation 1.4 and others fall below it. The subject requires further study, because the use of  $P_b$  is undoubtedly an oversimplification.

The retardation  $f$  was also calculated for the rise of the center of the spray domes produced by 300-pound TNT charges. These are shown in Figure 7.2 as a function of  $\lambda_c$ . The scatter is of the order of 20 percent, but the following expression provides a fairly good representation of the data:

$$f = 268 \lambda_c^{-1} \quad (7.2)$$

$$(\text{valid for } 2 < \lambda_c < 16 \text{ ft/lb}^{1/2})$$

This can be interpreted as indicating that relatively small drops are produced in the spray domes from shallow shots, since these are decelerated rapidly by atmospheric drag. The large drops formed by deep explosions suffer little atmospheric drag. The retardation should reach a lower limit of 16 ft/sec<sup>2</sup>, which indicates the effect of gravity alone. For this reason, Equation 7.2 is valid only to a  $\lambda_c$  of 16 ft/lb<sup>1/2</sup>. At greater scaled depths, a constant  $f$  of 16 ft/sec<sup>2</sup> should be employed.

The values of  $f$  determined at the centers of the spray domes were 30 ft/sec<sup>2</sup> for Shot Wahoo and about 20 ft/sec<sup>2</sup> for Shot Wigwam. Both fell well below the TNT values, indicating that Equation 7.2 is not valid for nuclear explosions.

For tactical studies, it is necessary to consider the shape of the dome and its rate of rise at all points. For a TNT explosion, the initial velocity of the surface of the dome as a function of distance  $r$  along the surface can be calculated from Equation 7.1. The shape of the dome at early times may be approximated by taking the ratio of initial velocities along the surface to the initial velocity at surface zero, as follows:

$$\frac{V_0(r)}{V_0(0)} = \cos \delta \left( \frac{c}{R} \right)^{1.13} \quad (7.3)$$

Where:  $V_0(r)$  = initial spray velocity at a given dome radius,  $r$ , ft/sec

$V_0(0)$  = initial spray velocity at surface zero, ft/sec

Since  $\cos \delta = c/R$ , this reduces to

$$V_0(r) = V_0(0) \cos^{2.13} \delta \quad (7.4)$$

An expansion of Equation 7.4 in terms of  $\tan \delta$ , which is equal to  $r/c$ , gives the following (Reference 12):

$$V_0(r) = V_0(0) \left[ 1 + \left( \frac{r}{c} \right)^2 \right]^{-1.07} \quad (7.5)$$

Equations 7.3 through 7.5 are valid for both TNT and nuclear explosions.

If the rising spray can be represented by Equation 1.9, the maximum height at any  $r$  is indicated by

$$h_{\max} = \frac{V_0^2}{4f} \quad (7.6)$$

Where:  $h_{\max}$  = maximum height of spray, feet

On this basis, if  $f$  is assumed to be constant, the shape of the spray dome at its greatest height should be represented approximately by

$$h_{\max}(r) = h_{\max}(0) \left[ 1 + \left( \frac{r}{c} \right)^2 \right]^{-2.13} \quad (7.7)$$

A comparison of the shape of the Wahoo dome at 1-second intervals with curves calculated using Equations 7.5 and 7.7 is presented in Figure 7.3. In general, the agreement with Equation 7.5 is good at  $r/c$  values less than 1. At greater dome radii, the Wahoo curves tend to shift toward the Equation 7.7 curve. Although the Wahoo curves occasionally exceed the limits of the two theoretical curves near the center, the latter provide a useful bracket that can be obtained quickly when the central  $V_0$  and  $h$  values are known.

This treatment provides a means for comparing the spray domes from different bursts. However, a comparison of the Wahoo results with TNT data, for bursts at the equivalent  $\lambda_c$  (2.18 ft/lb<sup>1/3</sup>), would be possible in only a limited manner, because the bubble effects are different. Although  $\lambda_c$  for Wahoo was 1.30,  $\lambda_c$  for a 300-pound TNT explosion at the given  $\lambda_c$  is only .628, which is about half the Wahoo value. The relatively shallow HE bubble pushes the water surface upward through the spray to form a hemispherical mound in the center, before the dome is fully developed.

Photographs of 300-pound TNT explosions at scaled depths of 1.79 and 2.39 ft/lb<sup>1/3</sup> are shown in Figure 7.4. These conditions bracket Shot Wahoo, scalewise. In the shallower burst, a dark central jet, possibly resulting from the travel of gaseous explosion products up the charge support cable, was visible within milliseconds of the explosion. This jet rose rapidly above the dome. In both cases, the bulging of the dome, as a result of the expansion of the relatively shallow bubble, was clearly visible by 0.2 second after SZT.

A well-developed primary spray dome was observed during Shot Wigwam—a 32-kt explosion at a depth of 2,000 feet. The primary dome reached a maximum diameter of about 14,000 feet and had reached a central height of 160 feet when a second spray dome, formed by the first bubble pulse, rose above it (Reference 6). The average initial spray dome velocity measured at surface zero on five photographic records was 115 ft/sec, which was 33 percent higher than the theoretical velocity of 86.7 ft/sec. Similar results were obtained to a dome radius of 1,600 feet.

A comparison of the observed Wigwam spray dome profiles with possible theoretical shapes is made in Figure 7.5. The agreement between the curves and the data is not as good as on Shot Wahoo. In one case, the height is 40 percent greater than the simple theory indicates. This result is consistent with the unusually high initial spray dome velocities recorded on Wigwam.

Both Wahoo and Wigwam were detonated when the ocean surface was extremely rough. This probably accounts for the fact that the spray dome velocities were higher on these nuclear tests than on HE tests, since the latter are rarely conducted in such conditions. In the analysis of the Wigwam data, the exceptionally spiky appearance of the dome and the broad scatter of the measurements were noted (Reference 6). The irregularities in the water surface seemed to have a relatively stronger influence on the wide, shallow Wigwam dome than on the Wahoo dome, which was narrower and higher.

The spray domes formed by shallow HE bottom bursts, scaled geometrically to Shot Umbrella, have not been studied in detail, because the domes are short lived and are rapidly overridden by the expanding column and plumes. At this scaled depth, the effect is more pronounced than shown in Figure 7.4.

Because of the importance of yield determinations on nuclear bursts, the spray dome method employed on Shot Umbrella (Section 4.3) was used for estimating the effective hydrodynamic yield of Shot Baker during Operation Crossroads. The central spray-dome height was measured on several Baker films; the most reliable record showed a spray velocity of 4,700 ft/sec for the period from 0.006 to 0.039 second (Reference 21). This gave a  $P_{\text{eff}}$  of 32.4, which is consistent with shock wave predictions for a distance of 90 feet from a 24-kt nuclear burst. This yield value is within about 2 percent of the reported radiclechemical yield of 23.5 kt, which is evidence that the spray dome velocity method is reliable for the determination of yields of shallow nuclear bursts.

The Baker height-versus-time curve, which was used for the spray dome analysis, showed an upward acceleration at 0.075 second after SZT. This possibly was evidence of blowout, which may have commenced near the surface at approximately 0.06 second after SZT. As a result, the spray dome height-versus-time measurements were too brief in duration to permit the employment of the h/t-versus-t technique that has been used for deeper bursts.

## 7.2 PLUMES AND VISIBILITY RISE SURGE

In order to compare the Wahoo plume with HE plumes, geometrical scaling of the bubble may be employed as an approximate scaling technique. For Wahoo,  $\lambda_c^2$  was 1.30. The NOL 300-pound TNT tests closest to this condition were fired at depths of 25 and 30 feet, where  $\lambda_c^2$  is equal to 1.15 and 1.42 respectively. At both depths, a pronounced central vertical jet rose above the spray dome, originating at the surface about 0.9 second after SZT. The time of origin of this plume was about 0.1 second after the observed first bubble periods of 0.78 and 0.80 second for 300-pound TNT charges at these depths (Reference 43). The reported migration during the first period for charges fired at depths of 25 and 30 feet was about 15 and 25 feet respectively (Reference 43). These approximate values show that the collapsed bubble was close to the surface, and the jet originating at the bottom of the bubble should, therefore, be able to penetrate the water above it to produce the observed vertical plume. Radial plumes appeared at about the same time, resulting from the reexpansion of the bubble just beneath the surface. These phenomena are illustrated for the 30-foot depth in Figure 7.6.

Although the Wahoo bubble probably also migrated to a position close to the surface during its first oscillation, there was no pronounced vertical plume on Wahoo. This difference indicates that the deep HE tests in the field may have little value for the direct scaling of nuclear plumes.

The average radial and vertical growth of the Wahoo and Wigwam plumes is compared in Figure 7.7. The height-versus-time curves are very similar in appearance, although the Wigwam burst occurred at a depth of 2,000 feet, and the bubble oscillated at least three times during the 10 seconds before plume effects appeared. The Wigwam plumes appeared to radiate from a point beneath surface zero. The Wahoo plumes originated about 5 seconds earlier than the Wigwam plumes, apparently from above the original surface.

The maximum height of the Wigwam plumes (1,450 feet) was consistent with the estimated initial velocity at the surface of 300 ft/sec (Reference 6), providing that gravity was the only retarding force. This is to be expected, as there is little atmospheric retardation of large plumes. Since the Wahoo curve is similar to the Wigwam curve and the maximum height is within 50 feet of the Wigwam height, the Wahoo vertical plumes, which may have started at a greater initial height, possibly had a lower initial velocity.

The Wahoo plumes expanded radially at a greater rate than the Wigwam plumes and attained a greater maximum collapsed diameter (3,800 feet as compared to 3,100 feet). A close examination of the Wigwam plumes (Reference 6) showed that there was an initial

group of vertical plumes and a later group of radial plumes, which appeared at lower levels. The second group spread laterally at a greater rate than the first and expanded beyond them at 22 seconds after SZT.

Though the Wigwam yield was 32 kt, the first maximum bubble radius was calculated to be 376 feet, which is almost identical to the 384-foot maximum bubble radius calculated for Wahoo. However, there is evidence that most of the steam in the Wigwam bubble condensed during its upward migration and that the water surrounding the bubble continued to rise in the form of a vortex ring (Reference 17). A vortex ring would have a central velocity greater than the translational rate of the entire mass, which could account for the relatively high velocity of the Wigwam plumes. The Wahoo bubble undoubtedly lost some steam during its collapse but seemed to reexpand above the surface in a roughly spherical shape, thereby driving the surrounding water outward in symmetrical plumes. The Wahoo and Wigwam plumes had almost the same overall volume; this might be attributed to an upward transport by buoyant forces of roughly equivalent masses of water. Although the mechanisms are not understood, the result is possibly connected with the almost identical volumes of the fully expanded bubbles.

In both cases, a group of irregular plumes appeared above the surge after the first mass had subsided. These plumes were believed to result from the oscillation of the surface. The Wahoo late plume was 950 feet high whereas the Wigwam late plume attained a height of 770 feet.

The base surge formed by 500-pound TNT explosions is tenuous and is difficult to measure. It is doubtful that the limited surge data available from these tests, at submergence factors similar to that of Wahoo, is of value for extrapolation to the nuclear scale, particularly since the generating plumes are different in structure.

The Wigwam base surge was similar to the Wahoo surge in general appearance. However, it expanded more slowly and was smaller in size, as shown by the average radial growth curves in Figure 7.9. This would indicate that less liquid water remained airborne following the collapse of the Wigwam plumes than on Wahoo, a result that could have been caused by differences in structure of the plumes.

A comparison of the Umbrella column and plumes with HE surface phenomena for the same scaled depth ( $\lambda_c = 0.595 \text{ ft/lb}^{1/3}$ ) shows a major difference. This is the appearance of a black smoke crown on the HE tests, which represents the blowout of explosion products when the expanding gas bubble ruptures the water surface. Although a nuclear smoke crown would not necessarily be black, a well-defined cauliflower cloud, similar to that during Shot Baker, would be expected if blowout occurred. No such cloud appeared on Shot Umbrella. This result, combined with the relatively low intensity of nuclear radiation recorded before the emergence of the base surge, indicates that the nuclear bubble did not rupture the water surface above the burst when the bubble pressure was high enough to cause an outward flow of fission products.

Under comparable conditions, the amount of blowout of an explosion should decrease with increasing depth until a depth is reached at which no blowout occurs. This trend is indicated by a shrinkage in the smoke crown size and may be examined by using the ratio of the maximum smoke crown diameter  $S_{\max}$  to the maximum column diameter  $D_{\max}$ . In very shallow HE tests, the smoke crown is clearly defined, and the average ratio of  $S_{\max}$  to  $D_{\max}$  decreases from about 4 at a  $\lambda_c$  of  $0.15 \text{ ft/lb}^{1/3}$  to about 3 at a  $\lambda_c$  of  $0.50 \text{ ft/lb}^{1/3}$  (Reference 1). The data for greater scaled depths is limited, but a more rapid decrease in  $S_{\max}/D_{\max}$  occurs. The scaled depth at which no black smoke appears is not known exactly; however, it is roughly  $1.0 \text{ ft/lb}^{1/3}$  for TNT charges weighing between 100 and 600 pounds.

Airblast data from conventional underwater explosions is also of interest here, because the blowout of bubble gases on a shallow burst produces a strong shock wave. The strength

of this wave decreases rapidly between scaled depths of zero and  $0.5 \text{ ft}/\text{lb}^{1/3}$ , then decreases slowly. The wave becomes relatively unimportant, though observable, at a  $\lambda_c$  of  $0.81 \text{ ft}/\text{lb}^{1/3}$  (Reference 44). This result is consistent with the smoke crown evidence.

TNT charges fired on the bottom, at depths geometrically scaled to Shot Umbrella, are in the region where blowout effects change rapidly with increasing depth, and the plume data shows considerable scatter. As examples, the column and smoke crown formed by a 600-pound TNT explosion on the bottom in 5.58 feet of water ( $\lambda_c = 0.535 \text{ ft}/\text{lb}^{1/3}$ ) and a 4,200-pound TNT explosion on the bottom in 9.25 feet of water ( $\lambda_c = 0.508 \text{ ft}/\text{lb}^{1/3}$ ) are shown in Figure 7.9. In both cases, black smoke can be seen to emerge above the column. Although these examples are shallower than Umbrella, scalewise, they are the best approximations to Umbrella that are currently available.

The surface phenomena of Shot Baker are shown in Figure 7.10 in order to illustrate the differences from the Umbrella results. (Shot Baker was detonated at a depth of about 90 feet.) The cauliflower cloud on Baker can be attributed to the shallower depth of burst ( $\lambda_c = 31.5 \text{ ft}/\text{kt}^{1/3}$  as compared to  $75.0 \text{ ft}/\text{kt}^{1/3}$  for Shot Umbrella). The differences in the dimensions of the phenomena are shown in Figure 7.11, where it can be seen, for example, that the maximum radius of the Baker cauliflower cloud was about three times as great as the maximum radius of the Umbrella plume. The Baker and Umbrella height-versus-time curves are similar for the first 25 seconds of development. After this time, a central white plume, which possibly was an extension of the column, rose above the Baker cauliflower cloud.

The sides of the Baker column were virtually straight and were perpendicular to the water surface after the early stage of expansion and before the column started to collapse. HE tests scaled to Baker and Umbrella also form perpendicular cylindrical columns whose maximum diameter  $D_{\max}$  can be measured without great difficulty.

As a result, equations were developed for scaling HE maximum column diameters, and these were converted to nuclear bursts by using an adjustment factor obtained from the Baker result (Chapter 1). However, the Umbrella column was not vertical; in fact, it narrowed down about 300 feet above the surface and then gradually widened out above this up to where it merged with the plume. It was not possible to establish objectively a  $D_{\max}$  that would be comparable to the values obtained for HE and Baker. In addition, the measurements of the growth of the Umbrella column neck were not similar to the column growth curves for HE shots geometrically scaled to Umbrella.

Equation 1.36 predicts a  $D_{\max}$  of 1,550 feet for Umbrella. This is equal to the averaged diameter of the Umbrella column and plume about 6 seconds after the burst, when the lower part of the column was starting to fall. The prediction, therefore, is consistent with the overall size, though it would be difficult to obtain such a number, for scaling purposes, by direct measurement of the Umbrella photographs on the basis of the rules used for the HE and Baker column measurements. Additional knowledge of the detailed phenomena might make possible the formulation of a more general technique for obtaining  $D_{\max}$ .

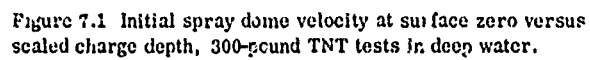
It is clear that the column and plume phenomena of Umbrella and Baker were radically different and that the tests belong in separate categories. These may be termed "shallow-non-blowout" for Umbrella and "shallow-blowout" for Baker or "shallow" and "very shallow" in analogy with the terms employed for deep bursts.

The mechanism of base surge formation was similar on Umbrella and Baker, in that, in both cases, the leading edge of the surge seemed to originate as a spill-out of material from the base of the column. This material possibly came from the lip of the expanding cavity in the water, which was hidden by the spray in the column. The spray in the collapsing column then flowed outward; this was probably the main source of the surge material. Fallout also added water droplets to the surge in both tests, though the fallout was more centrally located on Umbrella than on Baker. In the latter test, large masses of water fell from the cauliflower cloud, which extended well beyond the column.

The average base surge radius-versus-time curves for Umbrella and Baker are compared in Figure 7.12. (The Baker curve is based on recent measurements of the photographs at NOL and extend beyond the values previously summarized in Reference 1.) The Baker surge grew more rapidly and probably reached a greater size than the Umbrella surge, although the record is too short to show the final value. The physical appearance and behavior of the Umbrella and Baker base surges differed radically after the first minutes of development. As shown in Figure 7.10, the Baker structure was relatively complex at 134 seconds after the burst. At this time, a layer of new clouds was forming above the base surge and rainfall was visible within the surge. The Umbrella surge did not lift the ambient air enough to produce a new cloud deck, and the surge droplets gradually evaporated.

A considerable amount of base surge data has been obtained from HE tests at depths scaled geometrically to Umbrella and Baker (Reference 1). This information was used to demonstrate the validity of the Froude scaling technique for base surge studies (Appendix). When the scaled curves were compared, the HE and nuclear results were in good agreement at early times but differed at late times. Consequently, the HE results are useful for the study of surge phenomenology but not for direct extrapolation to the nuclear scale.





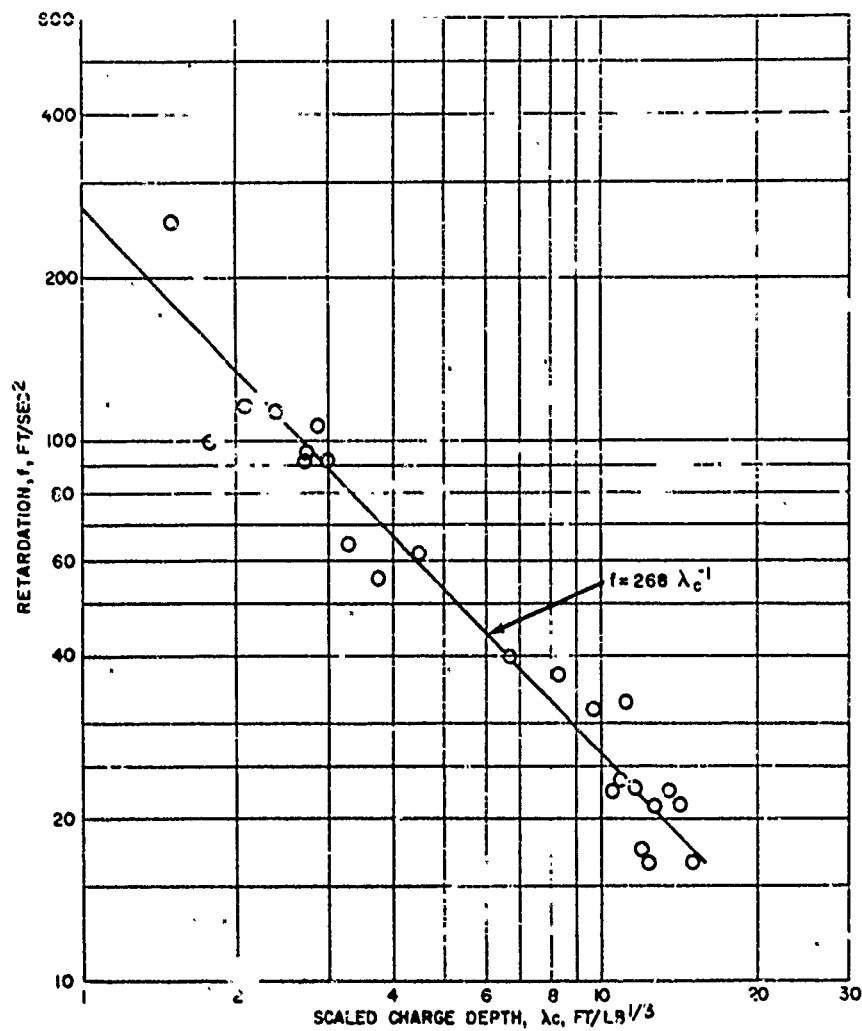


Figure 7.2 Spray dome retardation factor at surface zero versus scaled charge depth, 300-pound TNT tests in deep water.

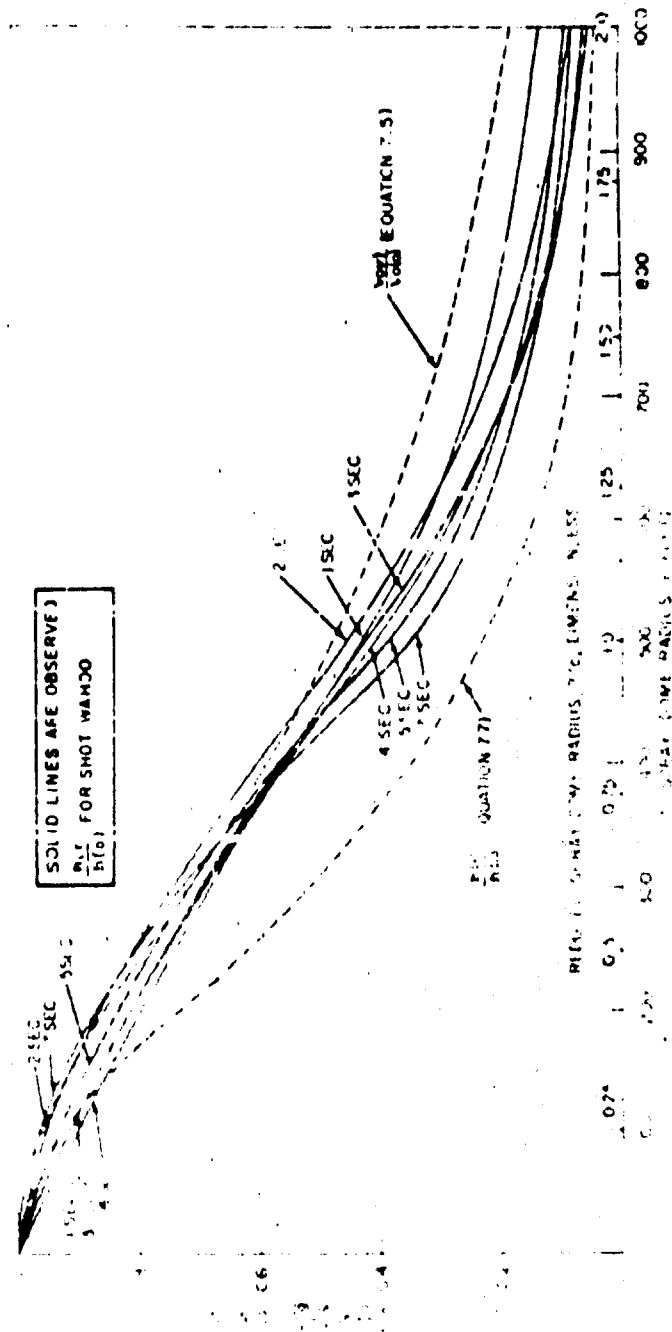
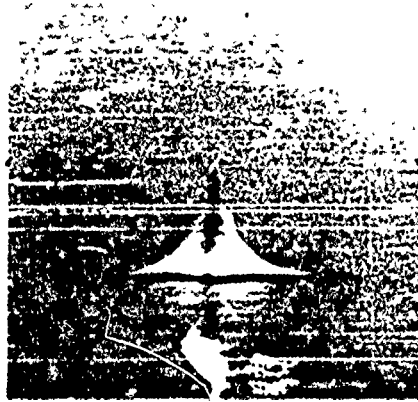


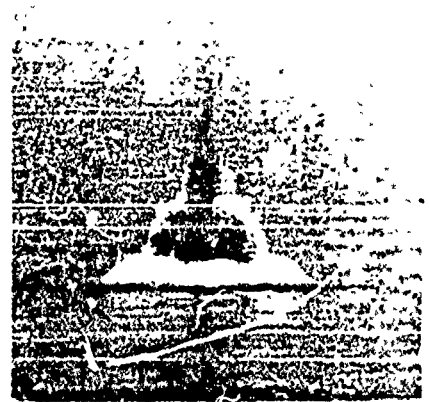
Figure 1. Spray data profiles for various time intervals.

Best Available Copy

CONFIDENTIAL

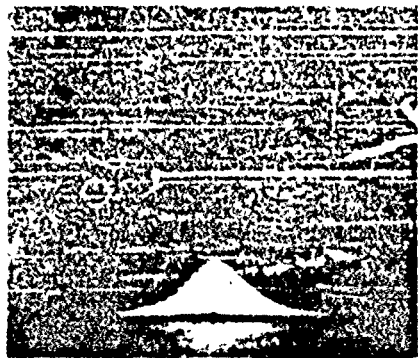


0.07 SECOND

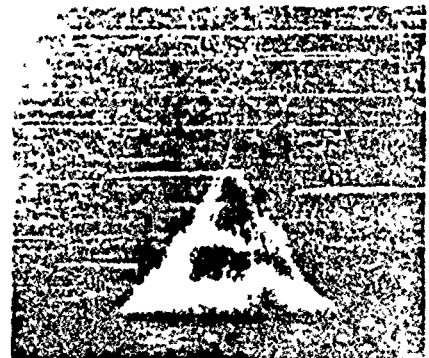


0.21 SECOND

$$\lambda_c = 1.79 \text{ FT/LB}^{1/3}$$



0.11 SECOND



0.41 SECOND

$$\lambda_c = 2.39 \text{ FT/LB}^{1/3}$$

Figure 7.1 Spray plumes from 500-gram TNT tests at the same scale depth for  $\lambda_c = 1.79$  and  $2.39$ .

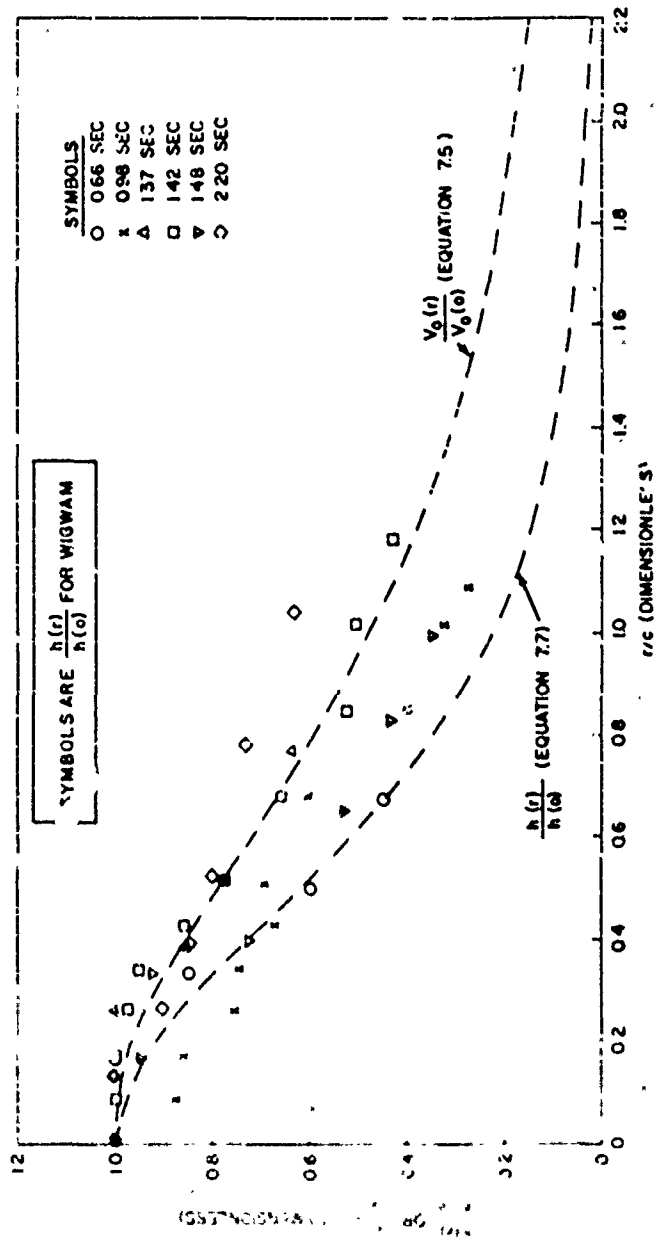
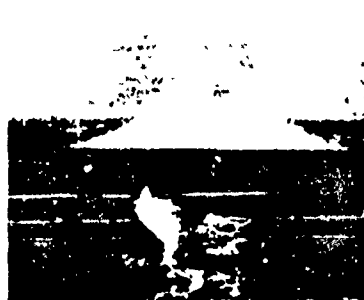


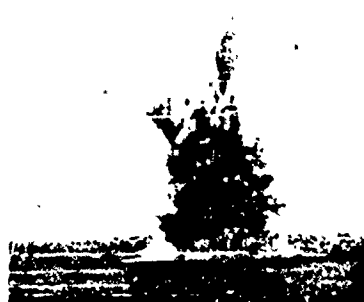
Figure 7.5 Comparison of spray dome profiles with theory, Shot Wigwam.



0.07 SECONDS



1.18 SECONDS



1.55 SECONDS



3.05 SECONDS

$$\lambda_c^1 = 142$$

Figure 7.6 Plume formation by a 300-pound TNT explosion at a depth of 3 feet.

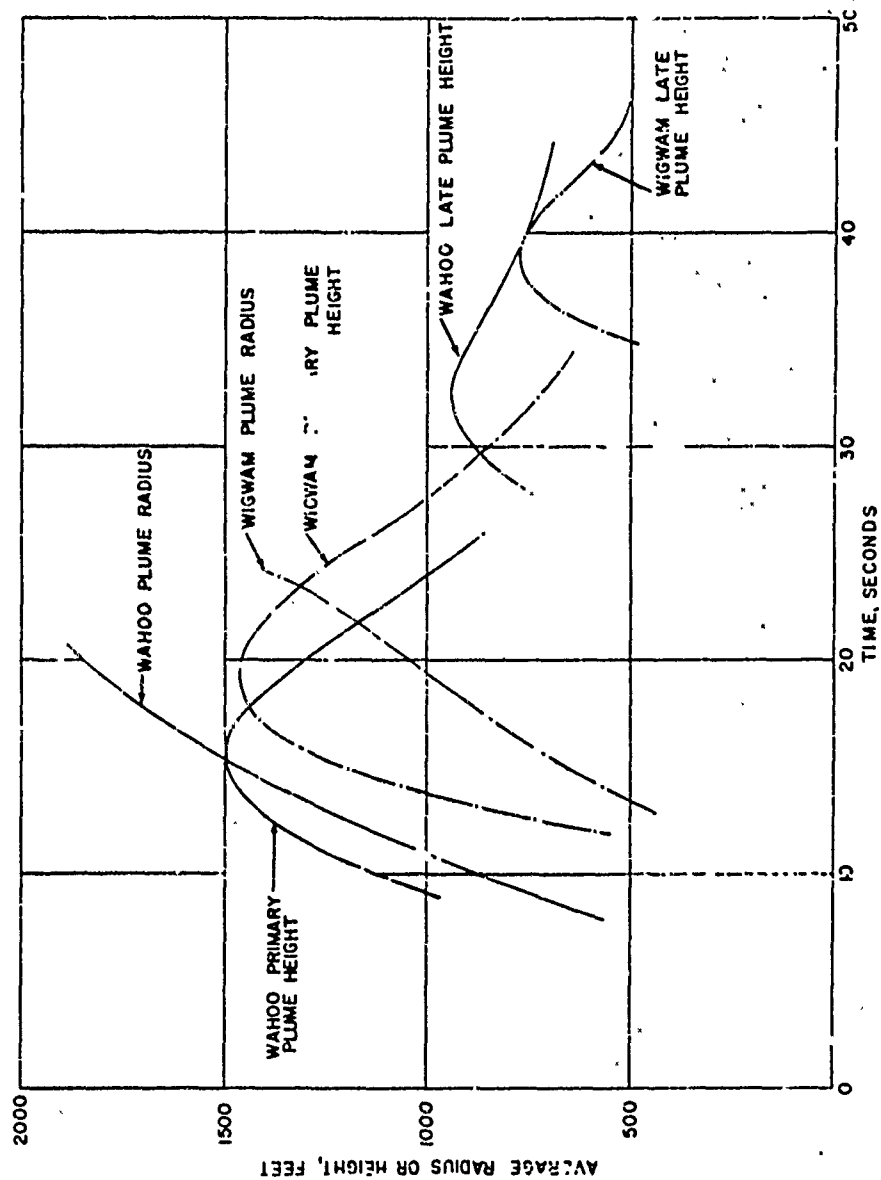


Figure 7.7 Comparison of Wahoo and Wigwam plume growth.

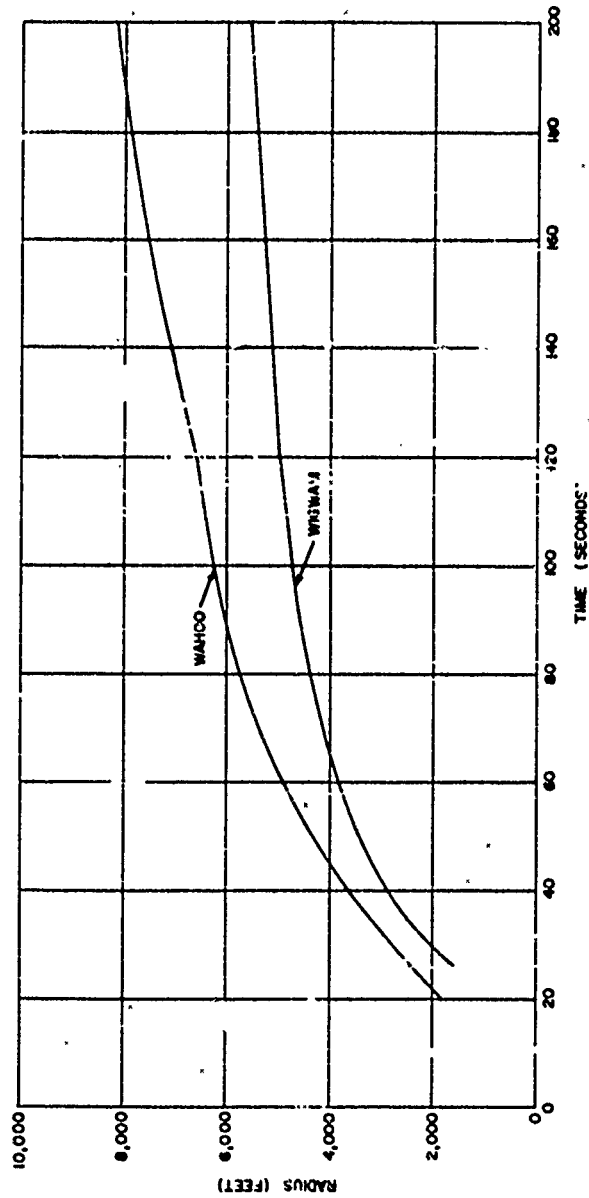


Figure 7 8 Comparison of Wahoo and Wigwam average base surge growth.





0.1 SECOND  
CHARGE WEIGHT 600 LB



0.5 SECOND  
 $\lambda_c = 0.535 \text{ FT/LB}^{1/3}$



0.2 SECOND  
CHARGE WEIGHT 4200 LB



1.0 SECOND  
 $\lambda_c = 0.508 \text{ FT/LB}^{1/3}$

Figure 7.9 Column and smoke crown formation by HE tests  
approximately scaled to Shot Umbrella



18 SECONDS



134 SECONDS

Figure 7.10 Surface phenomena, Shot Baker.

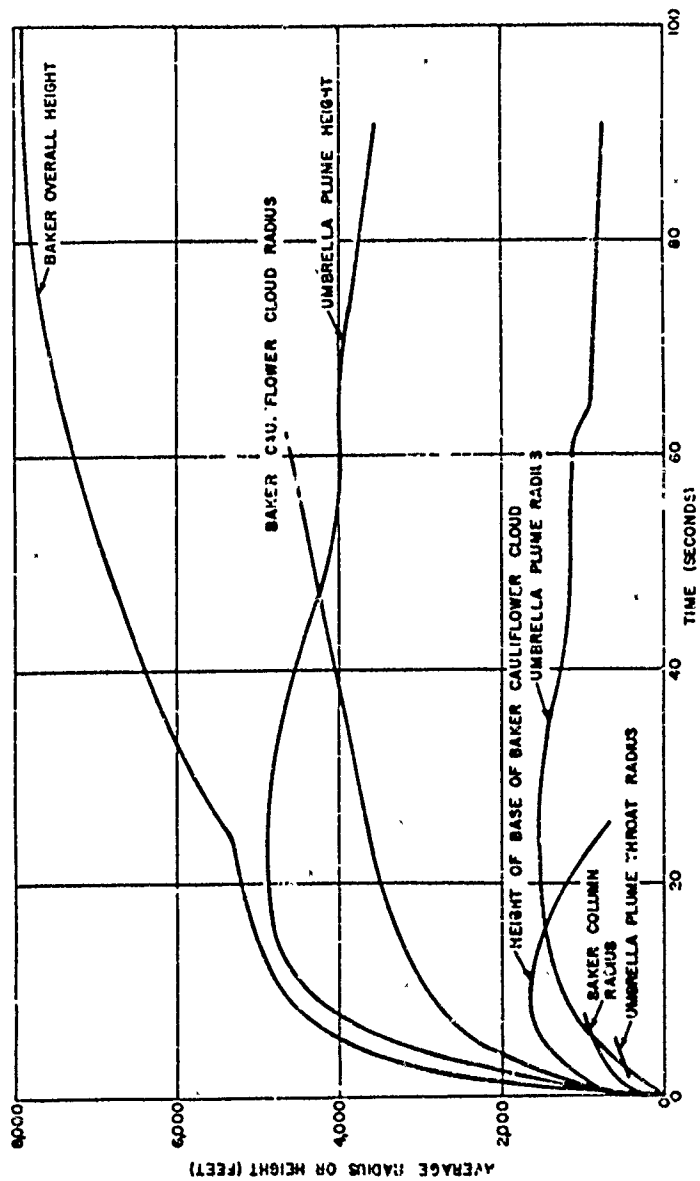


Figure 7.11 Comparison of Baker and Umbrella plume growth.

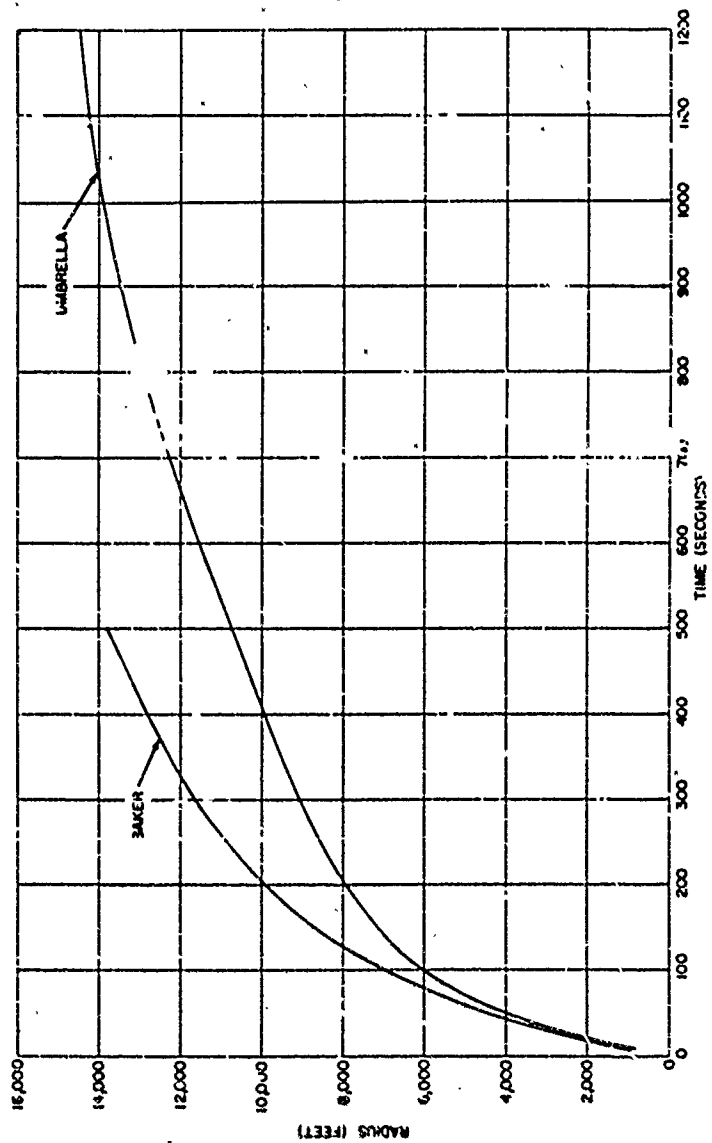


Figure 7.12 Comparison of Umbrella and Baker average surge growth.

## Chapter 8

### SCALING TO OTHER YIELDS AND DEPTHS FOR THE DEVELOPMENT OF SAFE DELIVERY TACTICS

A primary objective was the collection of effects data that could be used for developing tactics for the safe delivery of nuclear antisubmarine weapons and for predicting the lethal ranges of the weapons. In this chapter, the use of the surface phenomena data for this purpose will be considered. The possible offensive use of surface plume and cloud effects for inflicting damage or spreading radiological contaminants will not be treated here, because only limited attention has been given to this subject.

#### 8.1 GENERAL CONSIDERATIONS

In order to develop suitable tactics for the delivery of an existing or proposed nuclear weapon, it is necessary to estimate the nature and magnitude of all the damaging effects for the expected burst environment. If a warhead has been tested under water at one or two depths, as in Operation Hardtack, the problem exists of extrapolating the results to other possible depths of burst. A more difficult problem is the extension of the existing data to a device in the design stage with an expected yield greatly different from the yields of tests conducted in the past. When uncertainty exists in the data or scaling methods, assumptions are usually made that bias the predictions toward greater safety. Consequently, predictions of phenomena made for estimates of safe distances for delivery vehicles may differ from predictions made for other purposes.

Data is available on the surface phenomena of four underwater nuclear tests with yields ranging from 8 to 32 kt and depths ranging from about 90 to 2,000 feet. The initial conditions and scaling parameters are listed in Table 8.1. Each test listed lies in a different depth category, as defined in previous sections of this report. These have been termed "very shallow (blowout)," "shallow (non-blowout)," "deep," and "very deep."

If predictions of the phenomena at other yields and depths are required, the first step is to determine the depth category of the condition of interest. Predictions may then be made, using the appropriate nuclear test in Table 8.1 as a prototype. It is believed that predictions can be made with a reasonable degree of confidence for yields ranging from 1 to 100 kt. However, because of the lack of detailed theoretical knowledge of the surface phenomena at the present time, extrapolations to yields considerably smaller or larger than the above specified range must be made with considerable caution.

For surface phenomena predictions for safe delivery, an additional category of "near surface" burst may be established to include bursts that are so shallow that the layer of water above them is vaporized by the explosion. The phenomena of this type of burst and the associated hazards are unknown. Reference 23 indicates that the following equation can be used to provide an approximate boundary between near surface and very shallow bursts.

$$c = 21 Y^{1/3}$$

(8.1)

The five categories and four defining equations are shown graphically in Figure 8.1. Because this figure was prepared for use in safe delivery considerations, it has been conservatively assumed that a burst at a geometrically scaled depth shallower than Umbrella ( $\lambda_c = 75 \text{ ft/kt}^{1/3}$ ) would be in the blowout region. Probably, the true transitional depth between blowout and containment of the bubble while its pressure exceeds atmospheric pressure lies somewhere between the Umbrella and Baker scaled depths. This has been estimated to be at a  $\lambda_c$  of 60 ft/kt<sup>1/3</sup> (Reference 23), although no direct experimental verification exists.

## 8.2 SPRAY DOME

If delivery of an underwater weapon is to be accomplished by a low-flying aircraft, the rising spray dome is a possible hazard. For practical purposes, the time interval between a burst and the appearance of spray is negligible, since this depends on the speed of the underwater shock wave, which is rarely less than 5,000 ft/sec. The maximum extent of the spray dome formed by an HE or nuclear burst may be estimated by using the following equation

$$\delta = 85.3 - 2.30 \lambda_c \quad (8.2)$$

Where:  $\delta$  = angle with the vertical of a line from the point of burst to the edge of the spray dome, degrees.

The measurements on which this is based are presented in Figure 8.2, which shows the general consistency between HE and nuclear data. For the nuclear bursts, an equivalent yield of 0.667 times the radiochemical yield has been used (Reference 10). Equation 8.2 is probably not valid beyond the range of  $\lambda_c$  indicated in Figure 8.2.

If a need exists for spray dome heights as a function of time for a deep burst, initial spray velocities may be calculated by means of Equation 1.4. The peak shock wave pressures at the surface may be obtained by means of Equation 1.10 if the pressures are less than 3,000 psi, or from Reference 17 if the pressures are greater than 3,000 psi. On the basis of the Umbrella evidence, the yield of a bottom burst should be doubled for the calculation of initial spray velocities, when safety is the prime consideration. Spray dome height-versus-time calculations at any radius may be made for deep shots by employing the Wahoo retardation factors at the same values of dimensionless dome radius  $r/c$ . Equation 3.4 can be expressed in the following form for this purpose.

$$t = 30 c^{-0.5} \frac{r}{c} \quad (8.3)$$

Equation 8.3 is valid only to a dimensionless radius  $r/c$  of 1.26. An upper limit of dome heights may be estimated by assuming that gravity is the only retarding force.

If the depth of burst is great enough to permit one or more bubble oscillations beneath the original surface level, a secondary spray dome hazard will exist. In the absence of other information, it may be assumed, for safety considerations, that this could occur at submergence factors  $\lambda_c$  greater than that of Shot Wahoo. Secondary dome phenomena are not well understood. However, these domes should originate when the explosion bubble pulses reach the surface, and, as on Wigwam, can be about five times as high as the primary spray dome. They should not extend beyond the edge of the primary dome.

The initial spray velocity at the center of the primary Wigwam dome was about 50 percent higher than expected. The reason for this behavior is not known. However, to allow for possible occurrences of this nature and the normal scatter in results, a 50-percent safety factor should be added to calculated initial spray velocities for nuclear bursts.

No procedure for shallow bursts has been established, except for the determination of maximum spray dome extent by means of Equation 8.2, because of the early emergence of the plumes.

### 8.3 PLUMES

A second hazard to delivery vehicles is the rapidly expanding mass of plume produced by an underwater burst. The scaling of Wahoo and Wigwam plume growth is shown in reduced form in Figure 8.3 as the prototypes for deep and very deep bursts, respectively. To scale these data, all radii, heights, and times were divided by the cube root of the yield, which is equivalent to pressure-inertia scaling of the motion (Appendix). This is an approximation based on the successful use of this type of scaling for HE tests. In reality, gravity also affects the motion, but the neglect of gravity does not appear to introduce a serious error, if the range of charge weights under consideration is not excessive.

The plume radius and height data employed as a basis for Figure 8.3 were maximum values because of the safety requirement. The reduced data may be converted to other yields in the deep and very deep categories by multiplying the values by the cube root of the desired yield. To facilitate this procedure, the scaled values are summarized in Table 8.2.

The time of plume origin increases in stepwise fashion with depth of burst. It may be assumed that the time of plume origin coincides with the time of collapse of the oscillating bubble at the end of its final pulsation beneath the surface. A technique for calculating the migration and periods of nuclear bubbles is presented in Reference 23. Since the Wahoo curves in Figure 8.3 are based on a test where the bubble oscillated once before the eruption of the plumes, they are not strictly applicable to a condition in which a nuclear explosion is deep enough to permit two complete bubble oscillations. However, in the absence of such prototype data, the Wahoo curves may be used, providing that the calculated curves for the deeper condition are shifted by adding the period of the second bubble pulsation to the calculated times.

If a nuclear bubble oscillates three times, it falls in the category of very deep bursts represented by Operation Wigwam. However, the third collapse of the Wigwam bubble appeared to occur several hundred feet beneath the surface. For a burst that occurs at a shallower scaled depth than Wigwam, but deeper than indicated by Equation 8.28, the calculated plume curves should be adjusted by subtracting a correction factor. The minimum time of plume eruption for a very deep burst would be the sum of the three periods of bubble pulsation.

For the shallow blowout condition, the column, cauliflower cloud, and heavy liquid fallout must be considered. The scaling of the Baker plume growth is shown in Figure 8.4, reduced by the cube root of the yield. The reduced data may be employed in the same manner as for plumes from deep and very deep bursts. For this purpose, the scaled values are listed in Table 8.2. In the absence of other information, the maximum radius of heavy fallout at Baker may be scaled geometrically. This value was about 4,500 feet.

Maximum values of the Umbrella plume curves are included in Figure 8.4 and summarized in Table 8.2, to be employed as prototype data for shallow bursts that do not produce blowout. For safety considerations, the relatively narrow column neck may be ignored, though it undoubtedly has importance in the development of theories of explosion phenomenology.

In the shallow ranges of depths, it seems advisable to assume that the plumes appear instantaneously at the time of burst. Although the plumes may appear as much as a few seconds later in the case of a large yield at the greatest depth in the shallow range, no methods have been developed for predicting the plume times for shallow bursts.

If a burst occurs in the near surface range defined by Equation 8.1, the surface cloud phenomena would be expected to consist primarily of fallout. The existing techniques for the scaling of surface burst fallout may be employed in this range (Reference 45).

The plumes are capable of doing physical damage by direct contact with a delivery vehicle. In addition, their rapid expansion disturbs the air beyond their visible boundaries. Because of the general lack of reproducibility of plume phenomena the curves given in Figures 8.3 and 8.4 may be considered accurate to  $\pm 30$  percent.

In addition, a buffer zone of  $\pm 50$  percent is recommended for avoidance of the violent air motions beyond the column and plumes. A buffer zone, possibly overlapping these, should also be established for protection from nuclear radiation originating in the column and plumes (Reference 31).

#### 8.4 BASE SURGE

Since the base surge is highly radioactive, it is of considerable importance to be able to predict its growth for the development of weapon delivery tactics for both ships and low-velocity aircraft, i.e., helicopters. It will be assumed that the base surge radial growth for the low velocity tests conducted may be employed as prototype data.

The Wigwag base surge was similar to the Wahoo surge in general appearance, though it was smaller in size, as shown by the crosswind radial growth curves in Figure 7.9. Although no base surge scaling studies have been done for HE tests of deep bursts, it seems reasonable to assume that the Froude technique is valid at the early stage of surge growth for the deep nuclear tests as well as for shallow bursts. A measurement of the maximum plume height or the collapsed plume diameter would seem to be logical choices as characteristic lengths for scaling the radial growth of the surge. However, the plumes are generally irregular in shape and not reproducible. In the absence of good statistical data, these parameters cannot be used.

Since the nuclear plume dimensions appear to be related to the dimensions of the bubble at the end of its first expansion, it seems reasonable that the maximum bubble radius  $A_{max}$  would be suitable as a characteristic length for scaling the base surge radial growth for deep bursts. The Froude scaling of the Wahoo and Wigwag crosswind surge data is presented in Figure 8.5 and Table 8.4. To convert these values to another yield,  $A_{max}$  may be calculated by means of Equation 1.25. Then, the tabulated values of reduced radius should be multiplied by  $A_{max}$  and the tabulated values of reduced time multiplied by the square root of  $A_{max}$ . If the condition of interest falls in the category of a deep burst, the reduced Wahoo data should be used as the prototype values. For a very deep burst, Wigwag is the appropriate prototype.

In order to predict the rate of growth of base surges for nuclear bursts in the very shallow range, the Froude scaling technique has been used with the maximum column diameter  $D_{max}$  as the characteristic linear dimension. This was not possible on Shot Umbrella, because a comparable  $D_{max}$  could not be measured. However, it may be assumed that the  $D_{max}$  of 1,550 feet predicted for Umbrella by means of Equation 1.36 represents an effective  $D_{max}$ , which indicates the efficiency of the Umbrella column in producing a base surge. Physically, this value possibly represents an average plume diameter, which cannot be measured objectively by photographic methods.

The Baker and Umbrella surge radius-versus-time curves, reduced in terms of Froude scaling as indicated above, are presented in Figure 8.6. The similarity between the two curves is striking, although the Umbrella curve extends to a scaled time of 29.5 sec/ft<sup>1/2</sup> whereas the Baker curve ends at a scaled time of 11.1 sec/ft<sup>1/2</sup>. In view of the slight differences between the two curves at early times, it is recommended that a single curve, obtained from the higher values where the two curves exist, be employed as a prototype



for all shallow bursts. Scaled values for this single curve are listed in Table 3.1.

To use these values to obtain a base surge curve for a particular event and depth in the very shallow (blowout) or shallow (non-blowout) region,  $D_{max}$  may be calculated from Equation 1.35 or 1.36. The second step is the multiplication of scaled radii by  $D_{max}$  and scaled times by the square root of  $D_{max}$ . The surge radii used in Figures 3.5 and 3.6 and Table 3.1 are averages. They are probably accurate to  $\pm 20$  percent.

Because of the use of different scaling laws for plumes and base surge phenomena, the calculated curves may overlap. In these cases, the curve showing the greater radius should be used for safety.

In any tactical situation involving the use of ships, the effect of the wind on the base surge is extremely important. The motion of the downwind leading edge of the surge may be obtained by adding the wind speed to the average curve. The motion of the trailing upwind edge did not appear to follow any simple pattern on the four nuclear tests; however, on both Shots Wahoo and Urhela, the upwind surge curve could be approximated by subtracting half the windspeed from the average surge radial growth rate. In all the nuclear tests, the trailing edge of the surge reached a maximum extent, then remained stationary or moved downwind at a rate slower than the windspeed, though usually attaining the speed of the wind at a later time. As a general rule-of-thumb, subtracting half the windspeed from the average surge curve should provide a curve adequate for establishing safe distances upwind from a burst.

The nuclear test data curves show the growth of the visible base surge. It is believed that these curves accurately show the extent of the surge, even at late times when the edges are evaporating. In no case do the curves presented in this report show the maximum surge growth, although a leveling off can be seen. In the absence of better information, the curves can be extrapolated to include the growth of the invisible surge by fitting a hyperbolic equation to the data.

For safety from nuclear radiation originating in the base surge, a buffer zone extending beyond the edge of the surge cloud should be established.

The vertical growth of the base surge has not been studied in detail. On Wigwag, Wahoo, and Urhela, the surge tops tended to fluctuate between 1,000 and 2,000 feet after an initial rapid rise. On Baker, the behavior was similar for the 2 minutes following the burst, after which the surge height increased rapidly as a result of new condensation and cloud development in the surge and the air above it.

No simple rule can be established for surge height predictions. At early times, the vertical growth probably depends mainly on the turbulent motion of the surge. At later times, atmospheric turbulence, temperature, and relative humidity at altitudes up to a few thousand feet become important. In general, 2,000 feet is probably a good order of magnitude estimate for the 1- to 100-kt range for tropical regions when the relative humidity is below 70 percent. At a higher relative humidity, extensive vertical development might occur. If an atmospheric temperature inversion exists in the area of the burst, this would probably inhibit the vertical growth of a base surge.

TABLE 8.1 UNDERWATER NUCLEAR EXPLOSION TESTS

Category	Operation	Shot	Yield kt <sub>TC</sub>	Depth of Burst feet	Depth of Water feet	Maximum Bubble Radius feet	$\lambda_c$ ft/kt <sup>1/3</sup>	$\lambda'_c$
Very shallow (blowout)	Crossroads	Baker	23.5	90	180	865	115	0.104
Shallow (non-blowout)	Hardtack	Umbrella	8	150	150	520	75	0.284
Deep	Hardtack	Wahoo	9	500	1,000	384	240	1.30
Very deep	Wigwam	Wigwam	32	2,000	15,000	376	631	5.33

TABLE 8.2 REDUCED PLUME DATA, SHOTS UMBRELLA, WAHOO, AND WIGWAM

Height		Bubble or Plume Radius		Height		Bubble or Plume Radius	
$t/Y^{1/3}$	$h/Y^{1/3}$	$t/Y^{1/3}$	$r/Y^{1/3}$	$t/Y^{1/3}$	$h/Y^{1/3}$	$t/Y^{1/3}$	$r/Y^{1/3}$
sec/kt <sup>1/3</sup>	ft/kt <sup>1/3</sup>	sec/kt <sup>1/3</sup>	ft/kt <sup>1/3</sup>	sec/kt <sup>1/3</sup>	ft/kt <sup>1/3</sup>	sec/kt <sup>1/3</sup>	ft/kt <sup>1/3</sup>
Shot Umbrella:							
0	0	0	0	5.5	2,335	5.5	715
0.5	460	—	—	6.0	2,360	6.0	735
1.0	810	1.0	240	6.5	2,380	6.5	755
1.5	1,135	1.5	335	7.0	2,400	7.0	770
2.0	1,410	2.0	410	7.5	2,425	7.5	790
2.5	1,650	2.5	475	8.0	2,455	8.0	805
3.0	1,850	3.0	530	10.0	2,370	10.0	810
3.5	2,020	3.5	560	11.0	2,475	11.0	810
4.0	2,145	4.0	625	12.0	2,475	12.0	810
4.5	2,240	4.5	660	12.5	2,475	12.5	810
5.0	2,300	5.0	690	—	—	—	—
Shot Wahoo:							
4.3	526	4.3	382	7.2	798	7.5	752
4.5	556	4.5	410	—	—	8.0	800
5.0	645	5.0	480	—	—	8.5	842
5.5	705	5.5	543	—	—	9.0	880
6.0	750	6.0	600	—	—	9.5	911
6.5	780	6.5	654	—	—	9.6	919
7.0	794	7.0	705	—	—	—	—
Shot Wigwam:							
3.47	104	3.88	90	5.5	448	6.5	340
3.5	110	4.5	182	6.0	459	7.0	380
4.0	235	5.0	229	—	—	7.5	420
4.5	345	5.5	270	—	—	7.89	486
5.0	412	6.0	305	—	—	—	—

TABLE 3.3 REDUCED NUCLEAR PLUME DATA, SHOT BAKER

Height		Column or Plume Radius		Radius of Cauliflower Cloud		Height of Base of Cauliflower Cloud	
$t/Y^{1/2}$	$h/Y^{1/2}$	$r/Y^{1/2}$	$R/Y^{1/2}$	$t/Y^{1/2}$	$r/Y^{1/2}$	$t/Y^{1/2}$	$h/Y^{1/2}$
sec/kt <sup>1/2</sup>	ft/kt <sup>1/2</sup>	sec/kt <sup>1/2</sup>	ft/kt <sup>1/2</sup>	sec/kt <sup>1/2</sup>	ft/kt <sup>1/2</sup>	sec/kt <sup>1/2</sup>	ft/kt <sup>1/2</sup>
1.0	1,080	0.74	99	0.65	650	0.7	345
2.0	1,430	0.1	112	2.0	960	0.9	392
3.0	1,610	0.2	113	4.0	1,075	1.0	418
4.0	1,700	0.3	165	6.0	1,159	1.2	455
5.0	1,750	0.4	175	8.0	1,250	1.4	480
6.0	1,790	0.5	205	10.0	1,320	1.6	533
8.0	1,875	0.8	225	12.0	1,375	1.8	525
10.0	1,985	1.0	242	14.0	1,470	2.0	542
12.0	2,125	1.2	257	16.0	1,485	2.2	558
14.0	2,290	1.4	270	18.0	1,540	2.4	570
16.0	2,320	1.6	285	20.0	1,590	2.6	578
18.0	2,430	1.8	298	21.0	1,610	2.8	582
20.0	2,515	2.0	310	-	-	3.0	585
22.0	2,555	2.2	322	-	-	3.2	585
24.0	2,650	2.4	337	-	-	3.4	585
26.0	2,690	2.51	342	-	-	3.5	585
28.0	2,725	-	-	-	-	-	-
30.0	2,750	-	-	-	-	-	-
31.5	2,760	-	-	-	-	-	-

TABLE 3.4 REDUCED NUCLEAR BASE SOURCE DATA

Shot Baker-Umbrella		Shot Wahoo		Shot Wigwam	
$t/(D_{max})^{1/2}$	$R/D_{max}$ *	$t/(A_{max})^{1/2}$	$R/A_{max}$ †	$t/(A_{max})^{1/2}$	$R/A_{max}$
sec/ft <sup>1/2</sup>		sec/ft <sup>1/2</sup>		sec/ft <sup>1/2</sup>	
0.25	0.68	1.02	4.66	1.34	4.18
1.0	2.00	2.0	9.20	2.0	7.31
2.0	3.35	3.0	12.5	3.0	10.0
3.0	4.15	4.0	14.8	4.0	11.5
4.0	4.70	5.0	16.2	5.0	12.5
5.0	5.11	6.0	17.2	6.0	13.2
6.0	5.46	7.0	18.3	7.0	13.7
8.0	6.06	8.0	19.4	8.0	14.2
10.0	6.60	9.0	20.4	9.0	14.4
12.0	7.04	10.0	21.2	10.0	14.7
14.0	7.42	10.20	21.2	10.31	14.9
16.0	7.78				
18.0	8.09				
20.0	8.35				
22.0	8.60				
24.0	8.83				
26.0	9.03				
28.0	9.22				
30.0	9.35				
30.5	9.37				

\*  $D_{max}$  is defined by Equations 1.35 and 1.36.†  $A_{max}$  is defined by Equation 1.25.

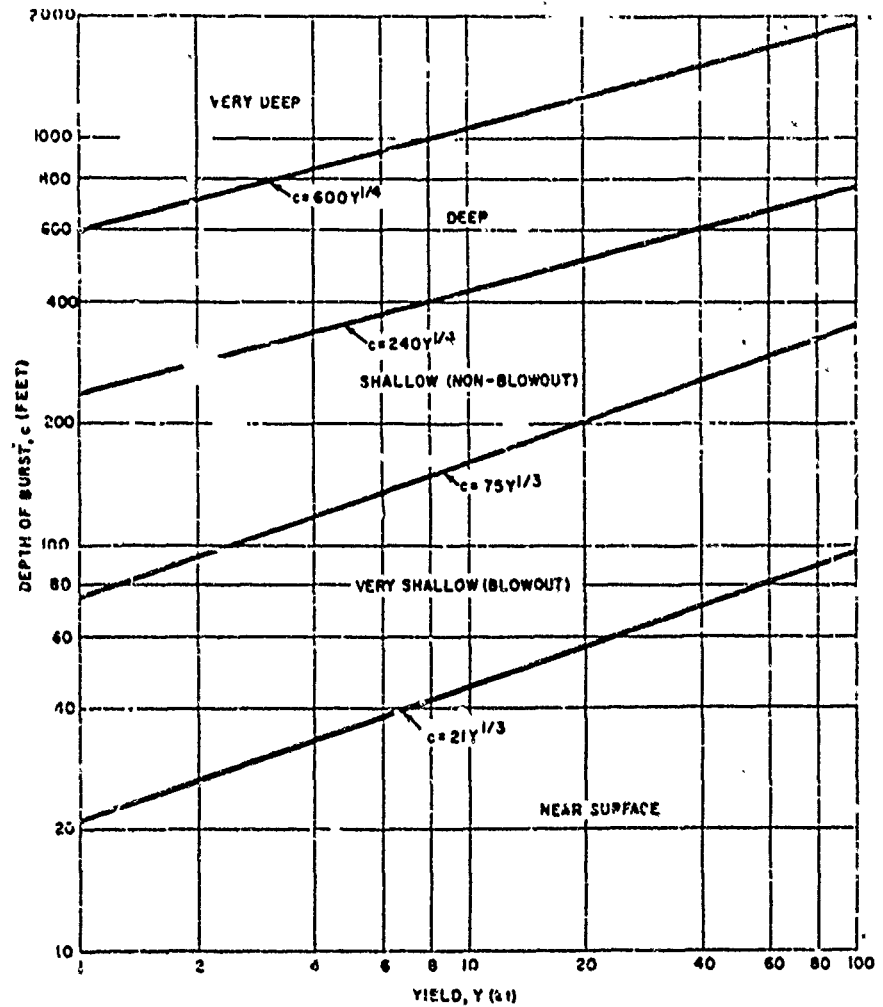


Figure 8.1 Depths of burst for different explosion categories established for safe delivery.

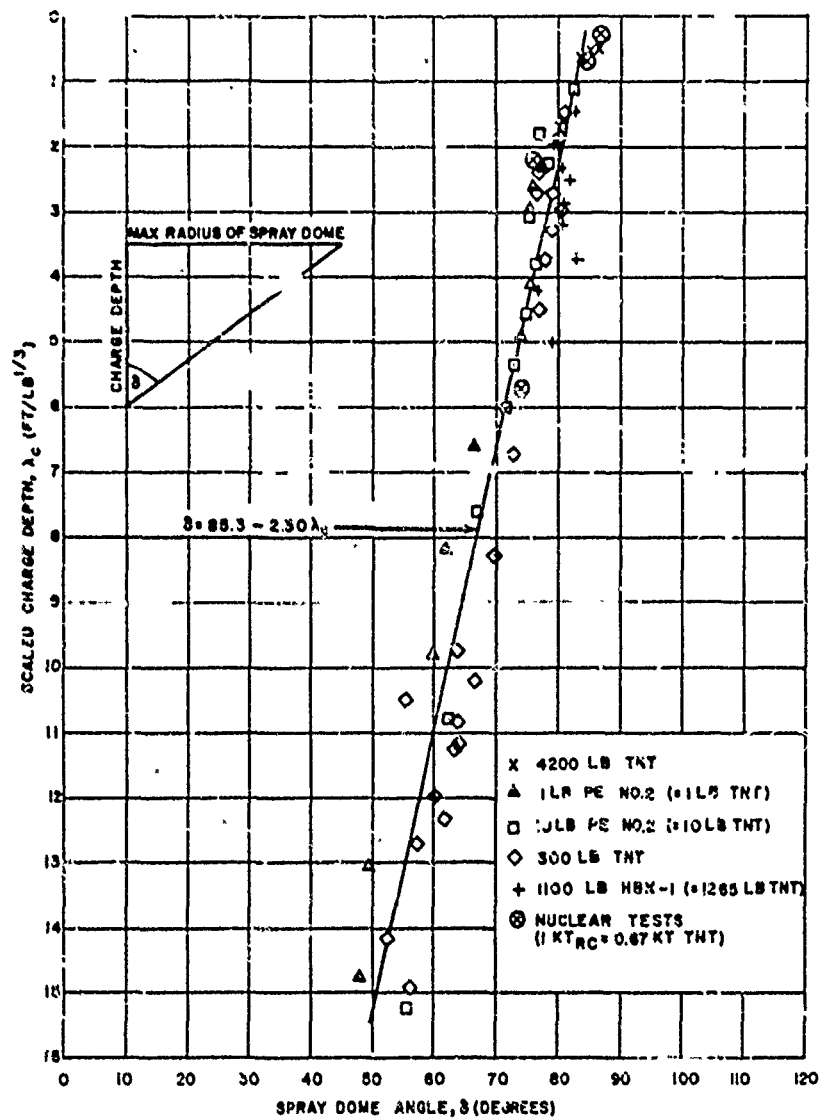


Figure 8.2 Spray dome angle versus scaled charge depth.

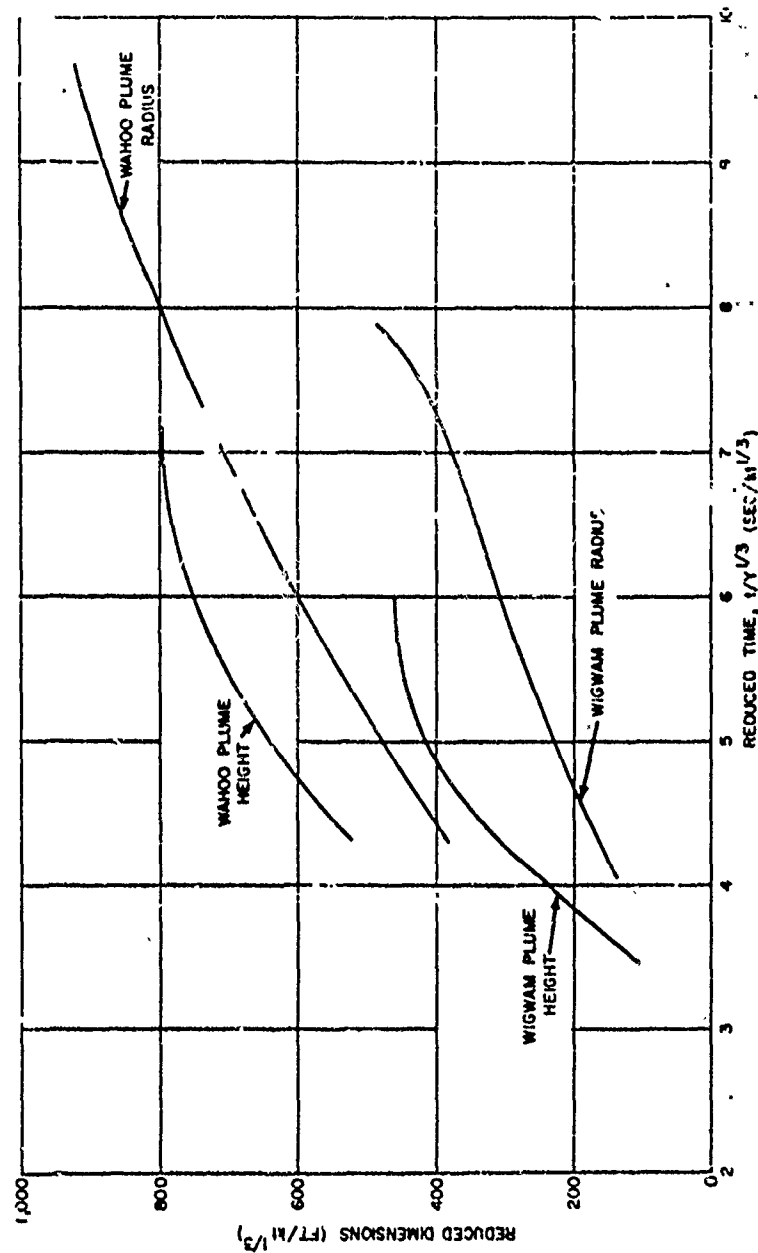


Figure 8.3 Scaling of Wahoo and Wigwam plume growth.

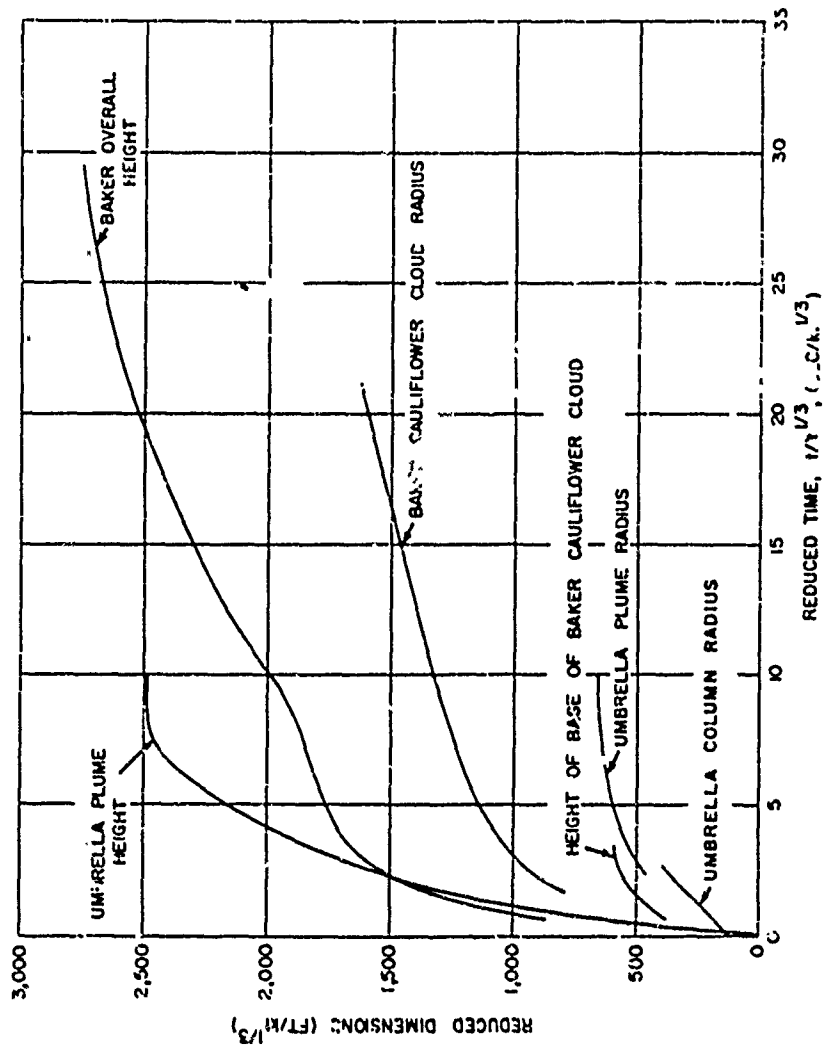


Figure 8.4 Scaling of Umbrella and Baker plume growth.

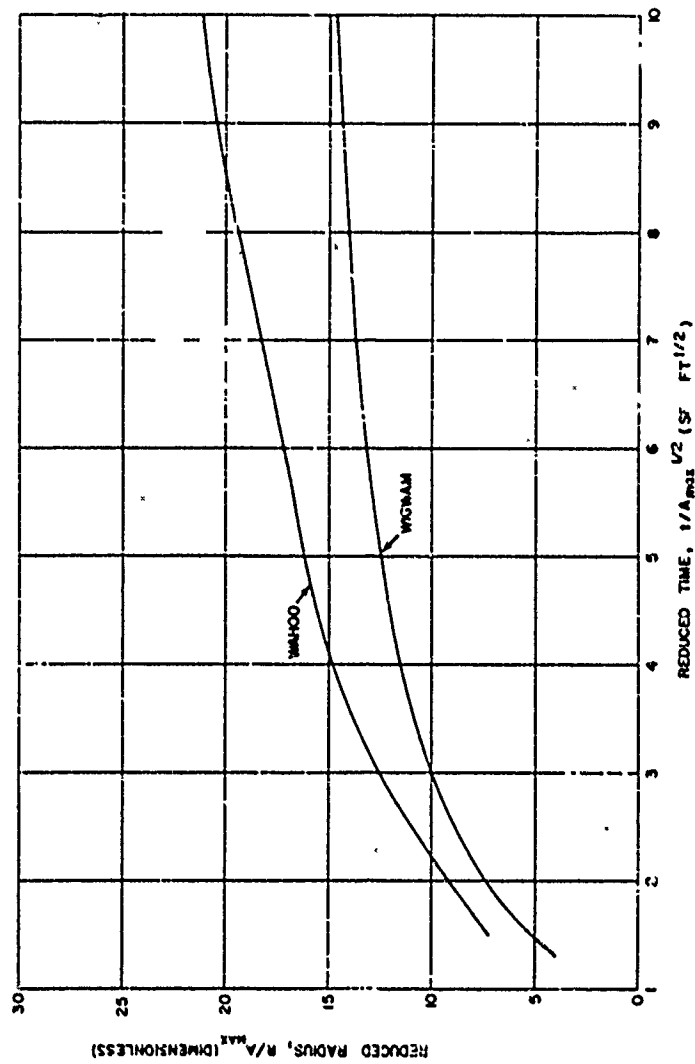


Figure 8.5 Froude scaling of Wahoo and Wigwam: average base surge growth.



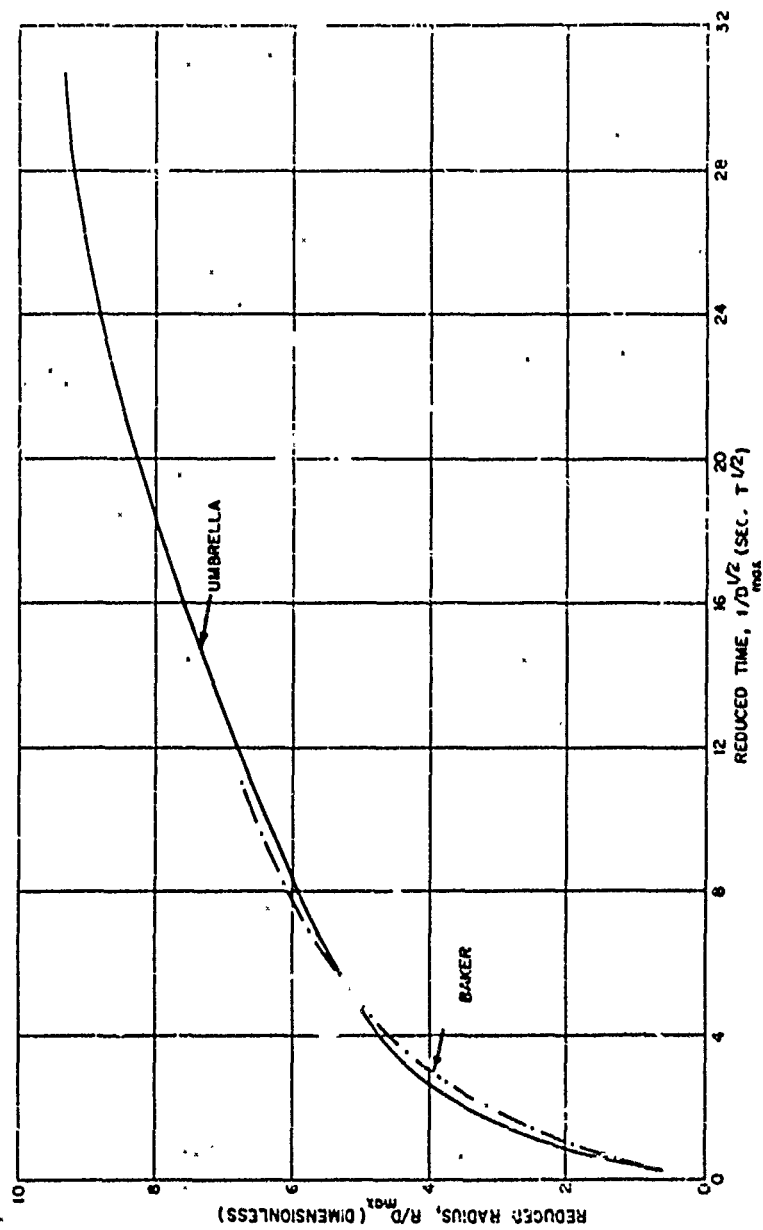


Figure 8.6 Froude scaling of Umbrella and Baker average base surge growth.

## CONCLUSIONS AND RECOMMENDATIONS

### 9.1 CONCLUSIONS

The results of Operations Crossroads and Wigwam demonstrated the value of photographic analysis for obtaining both indirect information about an underwater nuclear explosion and the accompanying shock wave and bubble phenomena, as well as direct information concerning the visible spray and cloud effects. This was also clearly shown by the results of Shots Wahoo and Umbrella in Operation Hardtack.

The slicks, spray domes, and spray rings gave visual evidence of the passage of underwater shock waves. They helped to identify the sources of these waves on Shots Wahoo and Umbrella. The initial vertical velocities of the Wahoo dome were used to calculate peak underwater shock pressures along the surface; the resulting values ranged from 1 to 14 percent higher than indicated by theory. On both shots, an effort was made to calculate the yields of the bursts by means of an initial dome velocity technique. This provided a value of 8.9 kt on Umbrella, which was 11 percent higher than the radiochemical determination, and gave a result of 11 kt on Wahoo, which was 22 percent higher than the radiochemical yield. In both cases, the difference between spray dome and radiochemical yield increased with increasing distance from surface zero.

In general, the measurements from the four nuclear shots indicate a tendency for initial spray dome velocities to be higher than predicted by the theory currently in use. On Shot Baker of Operation Crossroads, the shallowest burst, the difference was negligible; however, the difference increased with increasing depth, reaching a value of 33 percent on Wigwam. It is believed that surface roughness contributed to this result. Possibly, the effect of surface roughness on the spray dome is the same at all depths of burst, and this effect becomes relatively strong for very deep bursts, such as Wigwam, where the initial dome velocities were low and the spray dome was relatively broad and flat.

In view of the lack of a full understanding of the variations that occur in initial spray dome velocities, both as functions of dome radius and depth of burst, it does not seem advisable to employ these measurements for primary yield determinations in underwater nuclear tests. However, the method is a useful check, and, in the absence of other information, could provide an approximate yield.

The photographs proved to be particularly useful for identifying the origins of the shock waves and pressure pulses in air. This was done by correlating the times these pulses arrived at Project 1.2 stations with timed photography of the phenomena. In addition, qualitative evidence of the passage of compression and rarefaction waves was obtained from photographs of changes in the natural clouds in the area.

The plume phenomena of Shot Wahoo were similar in general appearance to those of Shot Wigwam but markedly different from the plume effects of HE tests at depths selected for similarity of bubble behavior. The latter produced high central vertical jets instead of the symmetrical, roughly hemispherical masses of plumes observed on the nuclear tests.

Shot Umbrella produced a tall, roughly cylindrical plume, which did not resemble the cauliflower clouds formed by the shallower Shot Baker and by HE tests scaled geometrically to Shot Umbrella.

In general, these results imply that HE tests have limited value for the direct extrapolation of plume phenomena to the nuclear scale. Although small-scale tests have provided an insight into plume effects, Operation Hardtack demonstrated that these tests alone were not adequate to provide a full understanding of nuclear burst effects.

During Shots Wahoo and Umbrella, considerable information on the growth and drift of the basic surge was acquired. The surges tended to move in the direction of the wind and at the same speed as the wind, except for the trailing upwind edge, which showed evidence of frictional retardation. Average radial growth curves were obtained which provide a basis for the prediction of basic surge development for bursts in the same depth categories as Wahoo and Umbrella.

On both shots, the temperature-humidity records indicated an initial heating of the lagoon water by the detonation. On Umbrella, the surge was at 100-percent relative humidity for possibly 100 seconds after the burst, after which it gradually mixed with the drier external ambient air. After 60 seconds from the burst, the surge was cooler than the surrounding atmosphere as a result of the process of evaporation of the water droplets it contained. After about 15 minutes had elapsed, the Umbrella surge cloud was essentially at the ambient temperature and humidity.

The results of Operation Hardtack, combined with the results of Shots Baker and Wigwam, cover a wide range of experimental conditions. It is now felt that, although the phenomena are not thoroughly understood, predictions can be made with a reasonable degree of confidence for yields between 1 and 100 kt, using the results of the four nuclear tests. No predictions could not be made with confidence prior to Operation Hardtack.

## 9.2 RECOMMENDATIONS

A result of major significance was the dissimilarity between the Umbrella column and plume phenomena and the surface phenomena of HE tests at depths scaled geometrically to Umbrella. Because of the failure of the Umbrella bubble contents to emerge through the water surface at high pressure, both the air shock wave and early (prebase surge) nuclear radiation were less than anticipated.

Since these effects are extremely important for the delivery of underwater weapons in shallow water by ships and aircraft, additional work is needed to obtain a better understanding of the mechanism of blowout and to determine the nature of the scaling relationship.

On the nuclear scale, it would be desirable to obtain surface phenomena data from one or more tests at scaled depths between those for Shots Baker and Umbrella. These would aid in determining the transitional depth between the very shallow (blowout) and shallow (non-blowout) conditions. Of secondary interest in regard to surface phenomena, but extremely useful, would be a nuclear burst intermediate between Wahoo and Wigwam, possibly at a depth permitting the bubble to oscillate twice before breaking the surface. A surface burst would also provide data needed for filling a gap in the existing knowledge. These should all be in the range between 1 and 100 kt. However, because of the uncertainties in the prediction of effects at greater or lesser yields, tests in the fractional kiloton range and at the megaton scale should also be considered.

In the event of future nuclear tests, it is essential that photography be fully utilized as an experimental tool. To attain the maximum benefit from photography, extensive well-planned coverage combined with calm water and relatively clear skies is needed. The latter are difficult to achieve in the geographical areas usually employed for nuclear testing, but climatological data are helpful for selecting the most suitable months. Specific recommendations concerning photography are included in Chapter 2.

In view of the moratorium on underwater nuclear testing at this time, it is recommended that a maximum effort be made to provide the understanding of the surface phenomena of

underwater nuclear bursts by all available experimental and theoretical methods. The emphasis should be on shallow bursts, as indicated above.

In general, the differences between HE results and nuclear burst effects may be attributed to three major causes: the relatively large physical size of the nuclear phenomena, the relatively low-energy-density of an HE charge, and the differences between a nuclear and an HE bubble.

To examine the effects of physical size, HE effects may be studied with a wide range of charge weights. In the past, many surface phenomena experiments have been conducted on a laboratory scale with charges weighing less than 1 gram, and a considerable effort has gone into field experiments in the range between 1 pound and about 2 tons. One test was conducted with 45 tons of TNT. However, the early phases of column formation, the rupture of the water surface by the expanding bubble, and the blowout of explosion products or inflow of air have not been studied in detail. If these phenomena were investigated with charges weighing from about 0.1 gram to possibly 25 tons, a considerable insight would be gained into the effects of the physical size of the experiment on the blowout process. Using the theory of instability (Reference 14) as a starting point, it should be possible to develop adequate scaling laws for blowout from HE. High-speed photography and the employment of pressure probe signals to record values within the plume, column, and bubble would be important tools.

The problem of applying these results to nuclear bursts is more difficult. In this case, the theory of the formation, growth and internal structure of a bubble would play a major role. This theoretical work is considerably advanced as a result of work done for Operation Wigwam. Experimental techniques that may be useful here are the employment of an accelerated vacuum tank to provide adequate scaling of the migration of a nuclear bubble, the use of sparks or exploding wires to produce a steam bubble from a point source, the use of special chemical explosives that contain a large quantity of water of crystallization to produce a steam bubble, and the use of chemical explosives that have bubble-to-shock-wave energy ratios similar to nuclear explosions.

The base surge also requires further study, particularly in regard to the effects of meteorological conditions on the growth and dissipation of the surge. Although Shots Baker and Umbrella were detonated in the same geographical area and during approximately the same season (Baker was fired on 25 July and Umbrella on 10 June), the surge development and dissipation mechanisms were radically different on these tests. This was attributed to the higher relative humidity and greater atmospheric instability during Shot Baker. However, much greater extremes are possible, if bursts occur in different latitudes. It seems likely that a surge rainout would produce relatively high deposits of radioactive materials on ships or other targets, while the passage of an evaporating surge would leave a relatively light deposit. A surge cloud that remains visible for a long period, such as might occur in the Arctic, could probably be identified visually until its radioactivity had been reduced to a low level. This would reduce the likelihood of inadvertently entering the contaminated air, as could have occurred, for example, on a burst such as Wigwam, where the surge became invisible to surface ships about 4 minutes after the burst, yet contained relatively high dosage levels 21 minutes after the burst. In the absence of nuclear tests, theoretical and laboratory approaches are essential for a better understanding of the effects of meteorological conditions on a base surge, because not all of the full-scale phenomena can be simulated with HE tests.

## Appendix

### PRINCIPLES OF HYDRODYNAMIC SCALING OF UNDERWATER EXPLOSION PHENOMENA

In engineering projects, it is common practice to study the performance of a small-scale replica (model) of the large-scale structure (prototype) that is to be built. Some examples are model dams, breakwaters, ships, and aircraft. In these cases, it is also necessary to model the flow of water or air around the structure or vehicle. If a model test is performed properly, valuable information about the prototype can be obtained at a relatively low cost. The same principles that are employed in engineering model studies can also be used for modeling a large underwater explosion with a small one.

The simplest scaling concept is that of geometrical similarity. This implies that the parts of a model have the same shape as the corresponding parts of the prototype. In other words, all dimensions in the model are some constant multiple of the analogous dimensions in the prototype.

For a shallow underwater explosion in which the explosive composition and density are the same in model and prototype, and a spherical charge is used, the following three lengths completely determine the initial conditions:

$d$  = water depth

$c$  = charge depth

$r_0$  = charge radius

Figure A.1 illustrates the experimental conditions for a 0.2-scale model of a shallow underwater explosion. The subscripts m and p are used to designate the model and prototype, respectively. The length scale factor  $k_l$  is defined as follows:

$$k_l = \frac{l_m}{l_p}$$

Where:  $l$  = any linear dimension.

In this case:

$$k_l = \frac{c_m}{c_p} = \frac{d_m}{d_p} = \frac{r_{0m}}{r_{0p}} = \frac{2}{10}$$

Points that correspond to each other in model and prototype are called homologous points. If  $z$  is the vertical coordinate and  $r$  the radial coordinate for the example given in Figure A.1, then

$$z_m = k_l z_p$$

$$r_m = k_l r_p$$

When fluid flow occurs, it is necessary to employ the concept of homologous times. The motion of the model and prototype are kinematically similar if homologous particles be at homologous points at homologous times.

For example:

$$w_m = \frac{dz_m}{dt_m}$$

$$w_p = \frac{dz_p}{dt_p}$$

Where:  $w$  = vertical component of velocity

$t$  = time

Combining these equations gives

$$\frac{w_m}{w_p} = \left( \frac{dz_m}{dz_p} \right) \left( \frac{dt_p}{dt_m} \right) = \left( \frac{dz_m}{dz_p} \right) \left( \frac{dt_p}{dt_m} \right)$$

If  $k_w$  = vertical velocity scale factor, and

$k_t$  = time scale factor,

it follows that:

$$k_w = \frac{k_z}{k_t} = \frac{k_l}{k_t}$$

The scaling of accelerations is developed in the following way:

$$\frac{dw_m}{dt_m} = \frac{d^2z_m}{dt_m^2}$$

$$\frac{dw_p}{dt_p} = \frac{d^2z_p}{dt_p^2}$$

Where:  $\frac{dw}{dt}$  = vertical component of acceleration.

Combining these equations yields

$$\frac{dw_m}{dt_m} / \frac{dw_p}{dt_p} = \frac{d^2z_m}{dt_m^2} / \frac{d^2z_p}{dt_p^2}$$

If  $k_a$  = acceleration scale factor, it follows that

$$k_a = \frac{dw_m}{dt_m} / \frac{dw_p}{dt_p}$$

Since

$$\frac{d^2z_m}{dt_m^2} / \frac{d^2z_p}{dt_p^2} = \left( \frac{d^2z_m}{d^2z_p} \right) \left( \frac{dt_p^2}{dt_m^2} \right)$$

$$k_p = \frac{k_p}{k_t} = \frac{k_p}{k_t}$$

Also  $k_a = \frac{k_w}{k_t} = \frac{k_w}{k_t}$

In order to maintain geometric and kinematic similarity between flow patterns, the ratios between the forces acting on corresponding fluid parcels in model and prototype must be the same. The following are some of the forces commonly encountered in the fluid flow surrounding an underwater explosion, expressed in general form:

$$\begin{aligned} \text{Pressure force} &= pA = \rho l^2 \\ \text{Inertia force} &= ma = \rho v^2 l^2 \\ \text{Gravity force} &= mg = \rho l^3 g \\ \text{Viscous force} &= \mu \frac{dv}{dx} A = \mu v l \\ \text{Surface tension force} &= Tl \end{aligned}$$

Where:  $p$  = pressure

$A$  = area

$a$  = acceleration

$m$  = mass

$\rho$  = density

$v$  = radial velocity

$g$  = acceleration due to gravity

$\mu$  = coefficient of viscosity

$T$  = surface tension

If any two of the above forces govern the flow phenomenon being considered, dynamic similarity may be maintained by keeping the ratio of these forces the same in the model and prototype. The force ratios are expressed as dimensionless numbers, such as the following:

$$\text{Reynolds number} = \frac{\text{inertia force}}{\text{viscous force}} = \frac{v l \rho}{\mu}$$

$$\text{Pressure coefficient} = \frac{\text{pressure force}}{\text{inertia force}} = \frac{p}{\rho v^2} \text{ or } \frac{\Delta p}{\rho v^2}$$

$$\text{Froude number} = \frac{\text{inertia force}}{\text{gravity force}} = \frac{v^2}{l g} \text{ or } \frac{1}{l^2 g}$$

$$\text{Weber number} = \frac{\text{inertia force}}{\text{surface tension force}} = \frac{\rho v^2 l}{T}$$

Where:  $\Delta p$  = pressure difference.

If  $\rho$ ,  $\mu$ ,  $\Delta p$ ,  $T$ , and  $g$  are the same in both model and prototype, the following scale factors can be derived:

Reynolds scaling  $k_v = k_l^{-1}$ ,  $k_t = k_l^2$ ,  $k_a = k_l^{-3}$

Pressure scaling  $k_v = 1$ ,  $k_t = k_l$ ,  $k_a = k_l^{-1}$

Froude scaling  $k_v = k_l^{1/2}$ ,  $k_t = k_l^{1/2}$ ,  $k_a = 1$

Weber scaling  $k_v = k_l^{-1/2}$ ,  $k_t = k_l^{3/2}$ ,  $k_a = k_l^{-2}$

An example of the application of this technique to an underwater explosion problem, consider a parcel of water in the expanding column formed by a shallow burst. The horizontal component of motion is determined mainly by the inertia of the water and the difference between the pressure inside the column and the atmospheric pressure. The pressure difference changes continuously as a result of the expansion of the column until the column breaks apart and pressures are equalized.

If a large-scale explosion is properly scaled with small-model tests that are designed to simulate the radial expansion of the column, and column radius-versus-time data is obtained, the following results should be obtained:

Since  $k_t = k_l$ , all times will be reduced by a factor of 0.2 in a 0.2-scale model.

Since  $k_v = 1$ , the velocities of flow will be the same on all scales.

Since  $k_a = k_l^{-1}$ , the accelerations will be five times as great in a 0.2-scale model as in the prototype.

In addition, if each set of radius-versus-time data is reduced by dividing each measurement by the length scale factor  $k_l$ , and the values are plotted as  $r/k_l$  versus  $t/k_l$ , all points should lie on the same curve. This scaled curve may then be used to predict the actual radius-versus-time curves for an untested condition.

The radial flow of the base surge formed by an underwater explosion is governed by gravity and inertia forces at early times. Therefore, Froude scaling laws should be obeyed by this phenomenon. In this case, velocities and times are reduced by 0.45 in a 0.2-scale model, and accelerations are the same on all scales. A common curve for all radius-versus-time data may be obtained by dividing radii by  $k_l$  and times by  $k_l^{1/2}$ . Figure A.2 illustrates how the radius-versus-time, velocity-versus-time, and acceleration-versus-time curves look for a hypothetical case where pressure-inertia scaling is valid, and for the same case if Froude scaling is valid.

If more than two forces are important in the experiment, exact scaling is impossible, and some compromises must be made. In some cases, the medium must be changed in order to obtain a proper ratio of forces.

If the phenomena are more complex than indicated above, but the variables involved can be listed, it is possible to calculate a set of dimensionless products that may be maintained constant or varied systematically in a series of tests to obtain useful engineering curves (Reference 46).

Model laws may also be established by making use of the differential equations of motion for the phenomena of interest, providing these equations are known. Since the same equation should be valid for both the model and the prototype, the scale factor relationship required to make both of these the same may be determined by algebraic manipulation.

Another method for deriving laws of similarity from differential equations is to express the equations in dimensionless form. An example of this is the development of the scaling laws for the migration of explosion bubbles (Reference 9). This derivation showed that  $Z/W^{1/4}$  must be the same in model and prototype for the proper scaling of bubble migration and provided a method for calculating the migration.

The geometrical scaling considered at the beginning of this appendix is based on the size



of the unexploded charge. For scaling the plume phenomena of deeper bursts, it may be desirable to provide geometrical scaling of the explosion bubble at the end of its initial expansion. It is not possible to fulfill both of these objectives in the same experiment unless special test equipment, such as an accelerated tank, is constructed.

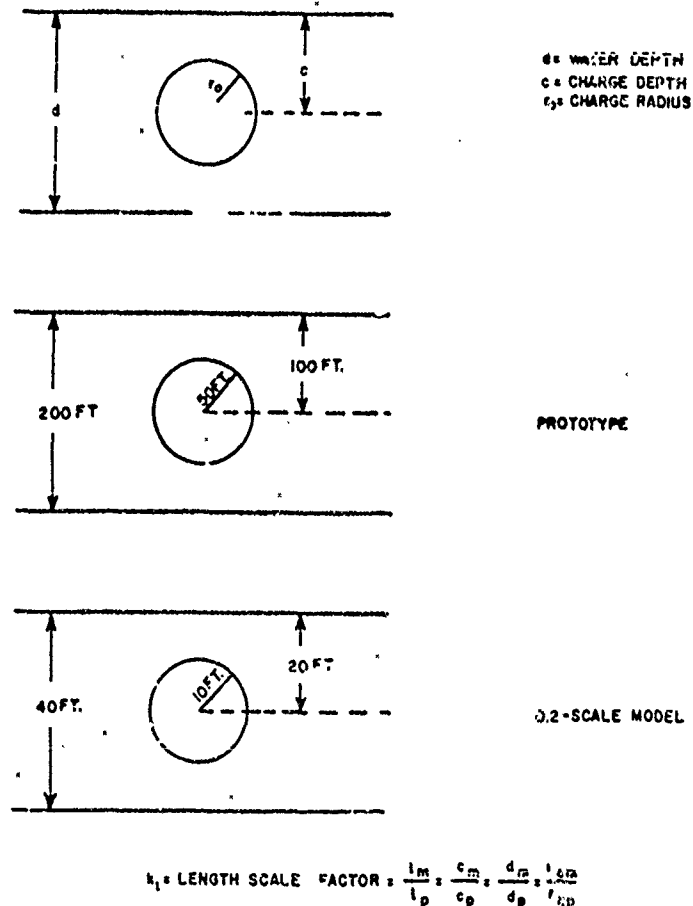
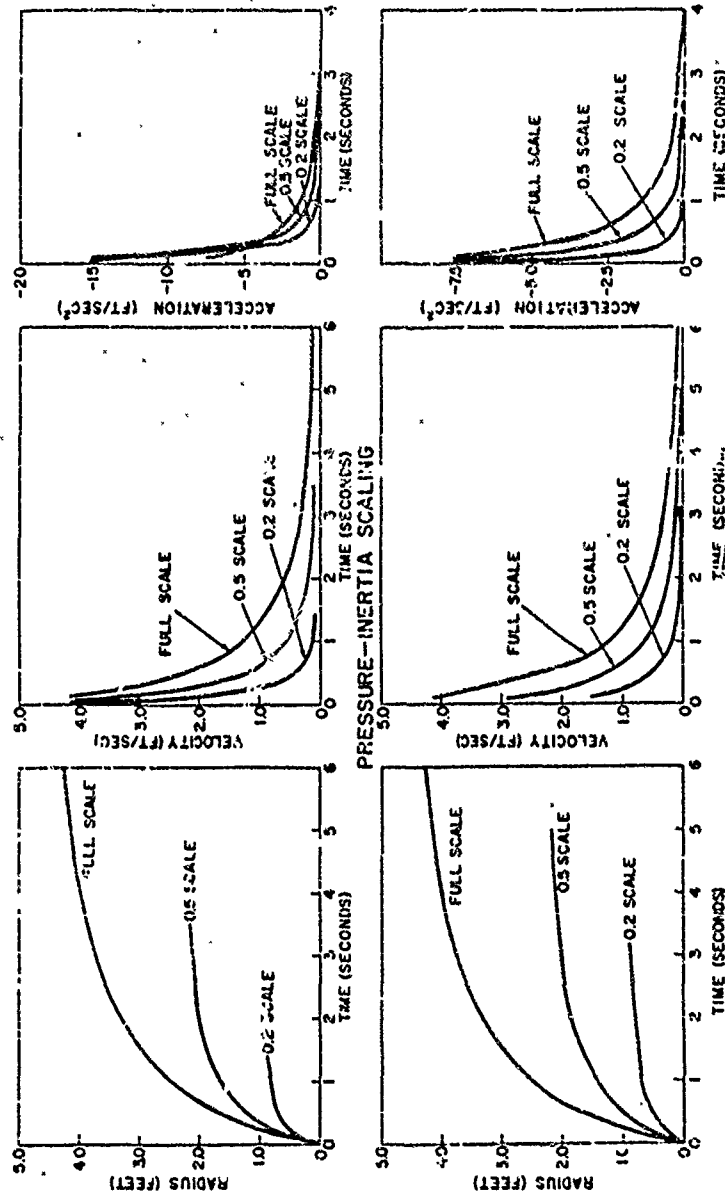


Figure A.1 Geometrically scaled model of shallow underwater explosion.



# INERTIA-GRAVITY (FROUDE) SCALING

Figure A.2 Comparison of scaling techniques.

# REFERENCES

1. M. L. Milligan and G. A. Young; "The Scaling of Base Surge Phenomena of Shallow Underwater Explosions"; NavOrd Report 2987, AFSWP-484, May 1954; U.S. Naval Ordnance Laboratory, Silver Spring, Maryland; Confidential.
2. G. A. Young, et al.; "Effects of the Explosion of 45 Tons of TNT Under water at a Depth Scaled to Test Baker"; NavOrd Report 3624, AFSWP-415, December 1954; U.S. Naval Ordnance Laboratory, Silver Spring, Maryland; Unclassified.
3. G. E. Hudson; "The Analysis of Data from Some Small Explosives in Shallow Water"; Contract NORD 14663, August 1956; New York University, New York 53, N. Y.; Confidential.
4. A. B. Arons, et al.; "Further Investigation of the Base Surge"; NavOrd Report 2144, June 1951; U.S. Naval Ordnance Laboratory, Silver Spring, Maryland; Confidential.
5. R. L. Willey, et al.; "Base Surge Measurements by Photography"; Project 1.1c, Operation Castle, WT-903, September 1955; U.S. Naval Ordnance Laboratory, Silver Spring, Maryland; Secret Restricted Data.
6. G. A. Young, et al.; "Photographic Measurements of Surface Phenomena"; Project 1.5, Operation Wigwag, WT-1009, October 1956; U.S. Naval Ordnance Laboratory, Silver Spring, Maryland; Confidential.
7. W. Wunderlich; "Introduction to the Theory of Underwater Explosions"; Chemical-Physical Research Institute of the German Navy, David W. Taylor Model Basin Translation 208, July 1948; Confidential.
8. G. A. Young; "A Method for Estimating the Initial Gamma Radiation Dosage from an Underwater Burst of a Nuclear Weapon"; NavOrd Report 4215, May 1953; U.S. Naval Ordnance Laboratory, Silver Spring, Maryland; Confidential Formerly Restricted Data.
9. R. H. Cole; "Underwater Explosions"; 1943; Princeton University Press, Princeton, N. J.; Unclassified.
10. H. G. Sney and J. F. Butler; "Shock Wave Parameters for Nuclear Explosions Under Water"; NavOrd Report 4500, May 1957; U.S. Naval Ordnance Laboratory, Silver Spring, Maryland; Confidential Formerly Restricted Data.
11. H. Kolsky, et al.; "Splashes from Underwater Explosions. Part II, Domes from Deep Charges"; Report UNDEX-163, 17 October 1945; Imperial Chemical Industries Limited, Great Britain; Confidential.
12. A. H. Kell; "Introduction to Underwater Explosion Research"; UERD Report 12-10, December 1956; Underwater Explosion Research Division, Norfolk Naval Shipyard, Portsmouth, Virginia; Confidential.
13. E. H. Kennard; "Explosive Load on Underwater Structures as Modified by Bulk Cavitation", 1956; Underwater Explosion Research, Volume III, The Damage Process, Office of Naval Research, Washington, D. C.; Unclassified.

14. G.I. Taylor, "The Instability of Liquid Surfaces When Accelerated in a Direction Perpendicular to Their Planes"; Proceedings of the Royal Society of London, 1950, Vol. A201, Pages 192-196; Unclassified.

15. T. E. Holland; The George Washington University Research Laboratory, Contract No. DA-18-064-404-CML-8, Quarterly Progress Report No. 14, 15 May 1956; Fort Detrick, Frederick, Maryland; Confidential.

16. H. Kolsky, et al.; "Splashes from Underwater Explosions, Part I, Shallow Charges", Report UNDEX-118, 1 December 1944; Imperial Chemical Industries Limited, Great Britain; Confidential.

17. H.G. Snay, et al.; "Predictions of Underwater Explosion Phenomena"; Project 1.1, Operation Wigwam, WT-1004, May 1956; U.S. Naval Ordnance Laboratory, Silver Spring, Maryland; Secret Restricted Data.

18. E.H. Kennard; "Underwater Explosions—A Summary of Results"; Report C-534, February 1951; David W. Taylor Model Basin, Washington, D.C.; Confidential.

19. F. Swift, et al.; "Underwater Pressures from Underwater Bursts"; Project 1.1, Operation Hardtack, WT-1606, August 1960; U.S. Naval Ordnance Laboratory, Silver Spring, Maryland, Waterways Experiment Station, Vicksburg, Mississippi; Confidential Formerly Restricted Data.

20. F.B. Porzel, et al.; "Yield and Energy Partition of Underwater Bursts"; Project 1.11, Operation Hardtack, WT-1616; Armour Research Foundation, Chicago, Illinois; Confidential Formerly Restricted Data.

21. "Report of the Technical Director"; Volumes I and II; Operation Crossroads, May 1947; Armed Forces Special Weapons Project, Washington, D.C.; Secret Restricted Data.

22. H.G. Snay, et al.; "Small Scale Experiments to Determine Migration of Explosion Gas Globes Towards Submarines"; NavOrd Report 2280, 1 July 1952; U.S. Naval Ordnance Laboratory, Silver Spring, Maryland; Confidential.

23. H.G. Snay; "The Hydrodynamic Background of the Radiological Effects of Underwater Nuclear Explosions"; NavWeps Report 7323, 29 September 1960; U.S. Naval Ordnance Laboratory, Silver Spring, Maryland; Confidential.

24. H.G. Snay; "Possibilities of Studying Bubble Migration on a Small Scale; Fourth Conference on Research on Ship Protection Against Underwater Explosions, 4-6 December 1951"; BuShips Report NavShips 250-423-14, July 1952; Bureau of Ships, Washington, D.C.; Confidential.

25. P.M. Fye, et al.; "A Symposium on the Base Surge"; NavOrd Report 2825, 1 April 1953; U.S. Naval Ordnance Laboratory, Silver Spring, Maryland; Confidential.

26. M.B. Hawkins, et al.; "Determination of Radiological Hazard to Personnel"; Project 2.4, Operation Wigwam, WT-1012, 8 May 1957; U.S. Naval Radiological Defense Laboratory, San Francisco, California; Official Use Only.

27. J.W. Winchester, et al.; "Characteristics of Ocean Bottom for Shots Wahoo and Umbrella, Including Umbrella Crater"; Project 1.13, Operation Hardtack, WT-1618; February 1961; U.S. Navy Hydrographic Office, Washington, D.C.; Confidential Formerly Restricted Data.

28. "R&G Data Summary", To be published by Edgerton, Germeshausen, and Grier, Inc., Boston, Massachusetts, Confidential Formerly Restricted Data.

29. P. Hanlon and H. B. Benefield; "Air Blast Phenomena from Underwater Bursts"; Project 1.2, Operation Hardtack, WT-1607, February 1960; U.S. Naval Ordnance Laboratory, Silver Spring, Maryland; Confidential Formerly Restricted Data.
30. W. C. Zuke; "Laboratory Sealing of Underwater Nuclear Explosion Bubbles"; Na. Weps Report 6707, 21 October 1960, U.S. Naval Ordnance Laboratory, Silver Spring, Maryland; Confidential Formerly Restricted Data.
31. E. C. Evans III and T. H. Shirasawa; "Characteristics of the Radioactive Cloud from Underwater Bursts"; Project 2.3, Operation Hardtack, WT-1621; U.S. Naval Radiological Defense Laboratory, San Francisco, California; Secret Restricted Data.
32. M. M. Bigger, et al.; "Shipboard Radiation from Underwater Bursts"; Project 2.1, Operation Hardtack, WT-1619, U.S. Naval Radiological Defense Laboratory, San Francisco, California; Confidential.
33. H. G. Houghton and W. H. Radford; "On the Local Dispersion of Natural Fog"; Papers in Physical Oceanography and Meteorology, October 1938, Vol. 6, No. 3, Published by The Massachusetts Institute of Technology, Cambridge, Massachusetts and Woods Hole Oceanographic Institution, Woods Hole, Massachusetts; Unclassified.
34. J. C. Johnson; "Physical Meteorology"; 1954; The Technology Press of the Massachusetts Institute of Technology and John Wiley and Sons, Inc., New York, New York, and Chapman and Hall, Limited, London, England; Unclassified.
35. H. U. Sverdrup, et al.; "The Oceans", 1946, Prentice-Hall, Inc., New York, New York; Unclassified.
36. C. H. Keith and A. B. Arons; "The Growth of Sea-Salt Particles by Condensation of Atmospheric Water Vapor"; Journal of Meteorology, June 1954, Vol. 11, No. 3, Pages 173 through 184; Unclassified.
37. A. B. Arons and C. F. Kientzler; "Vapor Pressure of Sea-Salt Solutions"; Transactions of the American Geophysical Union, October 1954, Vol. 35, No. 5, Pages 722 through 723; Unclassified.
38. C. F. Marvin; "Psychrometric Tables"; W. B. No. 235, 1941; U.S. Department of Commerce, Weather Bureau, Unclassified.
39. W. E. K. Middleton and A. F. Spilhaus; "Meteorological Instruments", 1953, University of Toronto Press, Toronto, Canada; Unclassified.
40. F. A. Berry, et al.; "Handbook of Meteorology"; 1945; McGraw-Hill Book Company, Inc., New York, New York, Unclassified.
41. D. A. Wilson, et al.; "The Determination of Peak Pressure of an Underwater Explosion from a Study of the Initial Dome Velocity"; Underwater Explosion Research, Volume II, The Gas Globe, 1950; Office of Naval Research, Washington, D. C.; Unclassified.
42. R. R. Halverson and R. S. Price; "Dome-Velocity Method of Determining Depth of Explosion as Applied to a Series of Mark 54 Depth Charges Statically Planted Over a Wide Range of Depths"; OSRD Report No. 4810, 15 February 1945; Woods Hole Oceanographic Institution, Woods Hole, Massachusetts; Confidential.
43. C. P. Slichter, et al., "Measurement of Bubble-Rise Phenomena: I. Mark 54 Depth Charges, TNT Loaded"; NDRC Report No. A-364, OSRD Report No. 6242, March 1946; Woods Hole Oceanographic Institution, Woods Hole, Massachusetts; Confidential.

41. J. F. Pittman: "Characteristics of the Air Blast Field Above Shallow Underwater Explosions"; NavOrd Report 5106, 3 December 1958; U.S. Naval Ordnance Laboratory, Silver Spring, Maryland; Confidential.

45. "The Nature of Radioactive Fallout and Its Effect on Man"; Hearings Before the Special Subcommittee on Radiation of the Joint Committee on Atomic Energy, 85th Congress; Parts 1 and 2, May and June 1957; U.S. Government Printing Office, Washington, D.C.; Unclassified.

46. H. L. Langhaar; "Dimensional Analysis and Theory of Models"; 1951; John Wiley and Sons, Inc., New York, New York and Chapman and Hall, Limited, London, England; Unclassified.

## DISTRIBUTION

### Military Distribution Category 15

#### ARMY ACTIVITIES

- 1 Deputy Chief of Staff for Military Operations, D/A, Washington 25, D.C. ATTN: Dir. of DMAR
- 2 Chief of Research and Development, D/A, Washington 25, D.C. ATTN: Atomic Div.
- 3 Assistant Chief of Staff, Intelligence, D/A, Washington 25, D.C.
- 4 Chief of Engineers, D/A, Washington 25, D.C. ATTN: ENGRS
- 5 Chief of Engineers, D/A, Washington 25, D.C. ATTN: ENGRS
- 6 Chief of Engineers, D/A, Washington 25, D.C. ATTN: ENGRS
- 7-9 Commanding General, U.S. Central Army Command, Ft. Monmouth, Va.
- 10 Director of Special Weapons, U.S. Army, Headquarters AFMPC, Ft. Bliss, Tex. ATTN: Capt. Chester I. Peterson
- 11 President, U.S. Army Artillery, D. C. 25, Ft. Sill, Okla.
- 12 President, U.S. Army Air Defense Command, Ft. Bliss, Tex.
- 13 Commandant, U.S. Army Command and General Staff College, Ft. Leavenworth, Kansas, ATTN: ANCHVCS
- 14 Commanding General, Chemical Corps Training Command, Ft. McClellan, Ala.
- 15 Commanding General, The Engineer Center, Ft. Belvoir, Va. ATTN: Asst. Chd. Engr. School
- 16 Director, Armed Forces Institute of Pathology, Walter Reed Army Med. Center, 625 16th St., NW, Washington 25, D.C.
- 17 Commanding Officer, U. S. Army Research Lab., Ft. Knox, Ky.
- 18 Commandant, Walter Reed Army Inst. of Res., Walter Reed Army Medical Center, Washington 25, D.C.
- 19-21 Commanding Officer, Chemical Warfare Lab., Army Chemical Center, Md. ATTN: Tech. Library
- 22 Commanding General, Engineer Research and Dev. Lab., Ft. Belvoir, Va. ATTN: Chief, Tech. Support Branch
- 23 Director, Waterways Experiment Station, P.O. Box 631, Vicksburg, Miss. ATTN: Library
- 24 Commanding General, Aberdeen Proving Grounds, Md. ATTN: Director, Ballistics Research Laboratory
- 25 The Research Analysis Corp., 5935 Arlington Rd., Bethesda, Md.
- 26 President, Beach Erosion Board, Corps of Engineers, U.S. Army, 201 Little Falls Rd., N.W., Washington 10, D.C.
- 27 Commander-in-Chief, U.S. Army Pacific, APO 550, San Francisco, Calif. ATTN: Ordnance Officer

#### NAVY ACTIVITIES

- 28-30 Chief of Naval Operations, D/A, Washington 25, D.C. ATTN: OP-0383
- 31 Chief of Naval Operations, D/A, Washington 25, D.C. ATTN: OP-31
- 32 Chief of Naval Operations, D/A, Washington 25, D.C. ATTN: OP-75
- 33 Chief of Naval Operations, D/A, Washington 25, D.C. ATTN: OP-51
- 34 Chief of Naval Operations, D/A, Washington 25, D.C. ATTN: OP-5031
- 35-36 Chief of Naval Research, D/A, Washington 25, D.C. ATTN: Code 811
- 37 Chief, Bureau of Naval Weapons, D/A, Washington 25, D.C. ATTN: 111-1
- 38 Chief, Bureau of Ordnance, D/A, Washington 25, D.C.
- 39 Chief, Bureau of Ships, D/A, Washington 25, D.C. ATTN: Code 423
- 40 Chief, Bureau of Supplies and Accounts, D/A, Washington 25, D.C.
- 41 Chief, Bureau of Yards and Docks, D/A, Washington 25, D.C. ATTN: 1-40

- 42 Director, U.S. Naval Research Laboratory, Washington 25, D.C. ATTN: Mrs. Katherine S. Cass
- 43-44 Commander, U.S. Naval Ordnance Laboratory, White Oak, Silver Spring 19, Md.
- 45 Commanding Officer and Director, Navy Electronics Laboratory, San Diego 32, Calif.
- 46 Commanding Officer, U.S. Naval Mine Defense Lab., Panama City, Fla.
- 47-48 Commanding Officer, U.S. Naval Radiological Defense Laboratory, San Francisco, Calif. ATTN: Tech. Info. Div.
- 49-50 Commanding Officer and Director, U.S. Naval Civil Engineering Laboratory, Port Hueneme, Calif. ATTN: Code 131
- 51 Commanding Officer, U.S. Naval School's Command, U.S. Naval Station, Treasure Island, San Francisco, Calif.
- 52 Superintendent, U.S. Naval Postgraduate School, Monterey, Calif.
- 53 Commanding Officer, U.S. Naval School, U.S. Naval Base, Bay West, Fla.
- 54 Commanding Officer, U.S. Fleet School, San Diego 47, Calif.
- 55 Officer-in-Charge, U.S. Naval School, CMC Officers, U.S. Naval Construction No. Center, Port Hueneme, Calif.
- 56 Commanding Officer, Nuclear Weapons Training Center, Atlantic, U.S. Naval Base, Norfolk 11, Va. ATTN: Nuclear Warfare Dept.
- 57 Commanding Officer, Nuclear Weapons Training Center, Pacific, Naval Station, San Diego, Calif.
- 58 Commanding Officer, U.S. Naval Damage Control Training Center, Naval Base, Philadelphia 12, Pa. ATTN: ABC Defense Course
- 59 Commanding Officer, Naval Air Material Center, Philadelphia 12, Pa. ATTN: Technical Data Br.
- 60 Commanding Officer, U.S. Naval Medical Research Institute, National Naval Medical Center, Bethesda, Md.
- 61-62 Commanding Officer and Director, David W. Taylor Model Basin, Washington 25, D.C. ATTN: Library
- 63 Commanding Officer and Director, U.S. Naval Engineering Experiment Station, Annapolis, Md.
- 64 Commander, Norfolk Naval Shipyard, Portsmouth, Va. ATTN: Underwater Explosions Research Division
- 65 Commander, U.S. Marine Corps, Washington 25, D.C. ATTN: Code 4014
- 66 Director, Marine Corps Landing Force, Development Center, MCRD, Parris, Va.
- 67 Commanding Officer, U.S. Naval SIG School, U.S. Naval Air Station, Alameda, Brunswick, Ga.
- 68 Chief of Naval Operations, Department of the Navy, Washington 25, D.C. ATTN: OP-0383
- 69-71 Chief, Bureau of Naval Weapons, Navy Department, Washington 25, D.C. ATTN: NR-1

#### AIR FORCE ACTIVITIES

- 72 Air Force Technical Application Center, H. H. S. J., Washington 25, D. C.
- 73 Sq. USAF, ATTN: Operations Analysis Office, Office, Vice Chief of Staff, Washington 25, D. C.
- 74-75 USAF, Washington 25, D.C. ATTN: AFPCN-101
- 76 Director of Research and Development, DCS/D, USAF, Washington 25, D.C. ATTN: Guidance and Weapons Div.
- 77 USAF, Washington 25, D.C. ATTN: Bio-Def. Res. Med. Division
- 78 Commander, Tactical Command, Langley AFB, Va. ATTN: Doc. Security Branch
- 79 Commander, Sq. Air Research and Development Command, Andrews AFB, Washington 25, D.C. ATTN: RDM-4

84 Commander, Air Force Ballistic Missile Div. HQ, AFB, Air Force Unit Post Office, Los Angeles 45, Calif. ATTN: VEBOT  
 91 Commander, AF Contract Research Center, L. G. Hancock Field, W. Hford, Mass. ATTN: CRCT-2  
 92-96 Commander, Air Force Special Weapons Center, Kirtland AFB, Albuquerque, N. Mex. ATTN: Tech. Info. & Eval. Div.  
 97-98 Director, Air University Library, Maxwell AFB, Ala.  
 99 Commander, Lowry Technical Training Center (TV), Lowry AFB, Denver, Colorado.  
 100-102 Commander, Wright Air Development Center, Wright-Patterson AFB, Dayton, Ohio. ATTN: WACAT (For WACB)  
 103-104 Director, USAF Project RAND, VLA: USAF Liaison Office, The RAND Corp., 1700 Main St., Santa Monica, Calif.  
 105 Commander, Air Technical Intelligence Center, USAF, Wright-Patterson AFB, Ohio. ATTN: APCIB-131a, Library  
 106 Assistant Chief of Staff, Intelligence, HQ, USAF, APO 611, New York, N.Y. ATTN: Directorate of Air Targets  
 107 Commander-in-Chief, Pacific Air Force, APO 953, San Francisco, Calif. ATTN: PFCIB-48, Base Recovery

#### OTHER DEPARTMENT OF DEFENSE ACTIVITIES

108 Director of Defense Research or Engineering, Washington 25, D.C. ATTN: Tech. Library  
 109 Chairman, Armed Services Explos. Safety Board, DOD, Building 7-7, Gravelly Point, Washington 25, D.C.  
 110 Director, Weapons Systems Evaluation Group, Room 1B660, The Pentagon, Washington 25, D.C.

111-114 Chief, Defense Atomic Support Agency, Washington 25, D.C. ATTN: Document Library  
 115 Commander, Field Command, DASA, Sandia Base, Albuquerque, N. Mex.  
 116 Commander, Field Command, DASA, Sandia Base, Albuquerque, N. Mex. ATTN: FCTO  
 117-118 Commander, Field Command, DASA, Sandia Base, Albuquerque, N. Mex. ATTN: FCTV  
 119 Commander-in-Chief, Strategic Air Command, Offutt AFB, Neb. ATTN: OASB  
 120 U.S. Documents Officer, Office of the United States National Military Representative - SNAF, APO 55, New York, N.Y.

#### ATOMIC ENERGY COMMISSION ACTIVITIES

121-123 U.S. Atomic Energy Commission, Technical Library, Washington 25, D.C. ATTN: For DAA  
 124-125 Los Alamos Scientific Laboratory, Report Library, P.O. Box 1663, Los Alamos, N. Mex. ATTN: Helen Redman  
 126-130 Sandia Corporation, Classified Document Division, Sandia Base, Albuquerque, N. Mex. ATTN: E. J. Smyth, Jr.  
 131-140 University of California Lawrence Radiation Laboratory, P.O. Box 808, Livermore, Calif. Attn: Lewis G. Craig  
 141 Division of Technical Information Extension, Oak Ridge, Tenn. (Master)  
 142-143 Division of Technical Information Extension, Oak Ridge, Tenn. (Suppl.)